Dissertation

submitted to the

Combined Faculty of Mathematics, Engineering and Natural Sciences

of Heidelberg University, Germany

for the degree of

Doctor of Natural Sciences

Put forward by

M.Sc. Florian Volker Nicolai

Born in Karlsruhe, Germany

Oral examination: 24th October 2023

Shaping and characterisation by dispersion scan of ultrafast mid-infrared pulses and the effect of the CNN stretching vibration on the photoreaction of 2-diazo-1-naphthol-5-sulfonate

Referees: Prof. Dr. Felix Deschler

Prof. Dr. Thomas Pfeifer

Formung und Charakterisierung durch Dispersionsscan von ultraschnellen Mittinfrarotpulsen und Effekt der CNN Streckschwingung auf die Photoreaktion von 2-Diazo-1-Naphthol-5-Sulfonat

Charakterisierung, Kompression und Formung von Mittinfrarotpulsen (MIR-Pulsen) wird in einem Aufbau basierend auf einem Pulsformer mit akusto-optischem Modulator (AOM) demonstriert. Charakterisierung der spektralen Phase der Pulse geschieht durch eine AOM-Pulsformer basierte Variante von Dispersionsscan (d-scan). Durch Kombination von d-scan und einem evolutionären Algorithmus werden um 3.2 µm zentrierte, breitbandige MIR-Pulse auf unter 50 fs FWHM Autokorrelation komprimiert. Die Fähigkeiten des Aufbaus bezüglich Pulsformung und –charakterisierung werden demonstriert, indem spektrale Phasen steigender Komplexität auf komprimierte, breitbandige MIR-Pulse aufgeprägt und rekonstruiert werden. Zusätzlich wird der Einfluss der Anregung der C=N=N Streckschwingung auf die Photoreaktion von 2-Diazo-1-Naphthol-5-Sulfonat in Methanol Lösung untersucht. Die C=N=N Streckschwingung wird bis mindestens $v = 3$ durch ultraschnelle MIR-Pulse angeregt. Eine Dissoziation des Moleküls im elektronischen Grundzustand wird nicht beobachtet. Die Vibrationsanregung klingt innerhalb von 20 ps ab. Experimente zur schwingungsvermittelten Photodissoziation zeigen, dass die Quantenausbeute der Photoreaktion durch die Schwingungsvoranregung um mindestens 10% erhöht ist im Vergleich zur Molekülanregung mit einem bloßen Ultraviolett-Puls. Dies wird durch einen vergrößerten Franck-Condon Überlapp zwischen der Flanke der Potentialhyperfläche des elektronischen Grundzustands mit dem reaktiven Teil der Potentialhyperfläche des elektronisch angeregten Zustands erklärt.

Shaping and characterisation by dispersion scan of ultrafast mid-infrared pulses and the effect of the CNN stretching vibration on the photoreaction of 2-diazo-1-naphthol-5-sulfonate

Characterisation, compression and shaping of mid-infrared (MIR) pulses are demonstrated in an acousto-optic modulator (AOM) shaper based setup. Characterisation of the pulses' spectral phase is accomplished via an AOM shaper based variant of dispersion scan (d-scan). By a combination of d-scan and an evolutionary algorithm, broadband MIR pulses centred at 3.2 µm are compressed to below 50 fs FWHM autocorrelation. The shaping and characterisation capabilities of the setup are demonstrated by imprinting and retrieving a set of spectral phases of increasing complexity on compressed broadband MIR pulses. Moreover, the effect of excitation of the C=N=N stretching vibration on the photoreaction of 2-diazo-1-naphthol-5-sulfonate dissolved in methanol is investigated. The C=N=N stretch mode is excited up to at least $v = 3$ by ultrafast MIR pulses. Molecular dissociation in the electronic ground state is not observed. Vibrational excitation decays within 20 ps. Experiments on vibrationally mediated photodissociation show that vibrational pre-excitation increases the photoreaction's quantum yield by at least 10% compared to excitation of the molecule by a mere ultraviolet pulse. This is explained by an increased Franck-Condon overlap of the edge of the electronic ground state's potential energy surface with the reactive part of the potential energy surface of the electronic excited state.

Table of Contents

Table of Contents

List of abbreviations

A	Absorbance
ACT	Autocorrelation trace
AGS	$AgGaS_2$, silver gallium sulphide or silver thiogallate
AOM	Acousto-optic modulator
AWG	Arbitrary waveform generator
BBO	β-BaB_2O_4, β-barium borate
BS	Beamsplitter
c	Concentration or speed of light, depending on context
CA	Coherent artefact
CaF_2	Calcium fluoride
CEP	Carrier-envelope phase
cw	Continuous wave
DFG	Difference frequency generation
DNQ	Diazonaphthoquinone, in this work in particular 2-diazo-1-naphthol-5-sulfonate
d-scan	Dispersion scan
FC	Franck-Condon
FP	Fourier plane
FTIR	Fourier-transform infrared
FW	Fundamental wavelength
FWHM	Full width at half maximum
GDD	Group delay dispersion
GSB	Ground state bleach
GVD	Group velocity dispersion
GVM	Group velocity mismatch
IVR	Intramolecular vibrational energy redistribution
LiF	Lithium fluoride
MCT	Mercury cadmium telluride
MeOH	Methanol
MIR	Mid-infrared

ND   Neutral density

NIR   Near-infrared

NOPA   Non-collinear optical parametric amplifier

OPA   Optical parametric amplification/Optical parametric amplifier

PFID   Perturbed free induction decay

PPMCLN   Periodically poled 5 mol% MgO doped congruent lithium niobate

QPM   Quasi-phase matching

QY   Quantum yield

RF   Radio frequency

SH   Second harmonic

SHG   Second harmonic generation

SPM   Self-phase modulation

S/N   Signal-to-noise ratio

TA   Transient absorption

Ti:Sa   Titanium:sapphire

TL   Transform-limited

TOD   Third-order dispersion

UV   Ultraviolet

UVFS   UV fused silica

VIPER   VIbrationally Promoted Electronic Resonance

Vis   Visible

VMP   Vibrationally mediated photodissociation

VNDF   Variable neutral density filter

WL   White light

ZnSe   Zinc selenide

Number

ε Molar decadic absorption coefficient

φ Phase

ω Angular frequency

I   Motivation

Spectroscopy is a powerful tool to investigate the structure of molecules and the interaction with their respective environment, like a substrate or solvent [1]. A particular useful light source for the task of molecular spectroscopy are lasers, owing among others to their high spectral power density, the good spatial collimation and the coherent properties of the emitted radiation [2]. Continuous wave lasers allow for instance to determine molecular energy levels and the coupling between them, to estimate the lifetime of excited states or to study interaction potentials between molecules in gases [1]. With the advent of pulsed lasers that deliver pulses in the femtosecond range, it even became possible to follow the fundamental process of a chemical reaction, namely the breaking and formation of molecular bonds [3-6]. Observation and steering of chemical reactions on the femtosecond time scale make up the field of femtochemistry. The field was pioneered by Ahmed H. Zewail, who was granted the Nobel Prize in Chemistry in 1999 for his work [7].

Time-resolved experiments with resolution of only several femtoseconds have elucidated a myriad of fundamental processes, including, but certainly not limited to, charge transfer in functional materials [8-10], fundamental isomerisation processes [11] like the ones involved in vision [12-14], or the biological essential process of photosynthesis [15, 16]. In time-resolved spectroscopy, often pulses in the visible (Vis) specral region are employed. From an experimentalist's point of view, working in the Vis spectral region has the advantage that sophisticated optics and detectors are available, frequently off-the-shelf. In addition, the beams involved in the experiment commonly can be seen by bare eye which dramatically faciliates alignment of the setup. On the other side, the Vis spectral range corresponds to electronic transitions. These are spectrally broad and Vis absorption spectra of different molecules do often overlap. From spectra in the Vis region it is challenging do derive information about specific bonds or groups within the molecule [17].

In contrast, vibrational spectra are spectrally narrow and overlap between contributions of atomic subgroups within the same molecule or contributions from different molecules rarely occurs. Consequently, contributions to a vibrational spectrum can usually be well separated and ascribed to a specific atomic group or molecule. The vibrational spectrum of a molecule is thus equivalent to a fingerprint of the molecule [18]. On the one hand, vibrational spectra thus provide structure-specific information about particular atomic groups within a molecule and also give insight into the interaction of the molecule with its environment [17, 18]. Time-resolved vibrational spectroscopy allows to follow the dynamics of selected groups inside a molecule [17]. The spectral region in which vibrational transitions are typically located is the mid-infrared (MIR) region. The MIR spectral region can be roughly located in the range 4000-400 cm^{-1} (2.5-25 µm) [18]. On the other hand, MIR radiation can be employed to specifically excite vibrations of selected molecular bonds. Deposition of vibrational energy in chemical bonds via excitation with ultrashort MIR pulses was demonstrated to lead to bond breaking in the electronic ground state [19-22]. MIR pulses have also been applied to selectively control the functional properties of solids [23]. In combination with pulses in the ultraviolet (UV)/Vis spectral range, MIR pulses can be employed to specifically select one molecular species over another for photoreaction, even if both species exhibit virtually the same UV/Vis absorption spectrum [24].

Control experiments often comprise a pulse shaper. A pulse shaper is able to virtually arbitrarily shape the electric field of the pulse that excites the sample under study. Employed in a feedback-based adaptive control scheme, application of a pulse shaper allows to find pulse shapes which are optimally suited for a specific control task, even

without knowledge of the underlying Hamiltonian [25, 26]. Conversely, having found the optimal pulse shape for a particular task, conclusions can be drawn from the optimal pulse shape on the underlying mechanisms of the system. The spectral phase of the excitation pulse plays a decisive role in those types of experiments since it completely determines the pulse's temporal profile for a given spectrum [27].

The rich amount of information of bond specific dynamics encoded in time-resolved vibrational spectra as well as the possibility to selectively vibrationally excite certain bonds within a molecule makes the use of MIR pulses in principle a powerful tool in spectroscopy. However, the implementation of experiments employing MIR pulses is usually more challenging than the implementation of experiments involving only pulses in the UV/Vis region [17]. One of the reasons for this is that optics or detectors are not as readily available as for the UV/Vis spectral range. Furthermore, the alignment of invisible MIR beams is more demanding and time consuming than corresponding alignment of visible beams. The challenges concerning the implementation of ultrafast time-resolved experiments in the MIR spectral region have so far posed an obstacle for the broad usage of femtosecond MIR pulses for probing and control [17].

The work at hand aims to contribute to the field of femtosecond MIR spectroscopy from two aspects. First, a setup for MIR pulse shaping and characterisation is presented. The presented shaper-based setup comprises the successful implementation of dispersion scan (d-scan) for phase characterisation of MIR pulses. Beside the ability of the setup to provide virtually arbitrarily shaped MIR pulses, the presented setup only calls for minimum additional alignment for experiments that include a pulse shaper anyway. The feature of minimum additional alignment is especially appealing for the MIR spectral region for the reasons outlined above. Second, the effect of selective excitation of a specific vibrational mode on the photodissciation of a technologically relevant molecule in solution is examined. A focus is set on whether molecular dissociation in the electronic ground state is possible for that molecular system and whether the quantum yield of the photoreaction triggered by a UV/Vis pulse can be enhanced by vibrational pre-excitation.

This thesis is organised as follows:

- **Chapter II** presents a non-collinear optical parametric amplifier (NOPA) providing broadband MIR pulses from 800 nm seed pulses. The NOPA is tunable to deliver pulses between 2-5 μm. In Ch. II the focus is set on the NOPA configuration providing pulses centred around 3.2 μm. This configuration provided a particularly broad output spectrum supporting pulses below 20 fs. Furthermore, in that spectral region, stretching vibrations of C-H, O-H and N-H bonds are located [28], so that corresponding pulses are interesting for spectroscopic applications. The MIR pulses generated by the NOPA will be further used in Ch. III.

- In **Chapter III**, the MIR pulses from the NOPA are characterised by an acousto-optic modulator (AOM) pulse shaper based variant of d-scan. D-scan is an especially attractive method for phase characterisation of MIR pulses, since it is set up in an all collinear geometry which reduces the demands on alignment. The setup presented in Ch. III is not only capable of characterisation, but also of virtually arbitrarily tailoring of broadband MIR pulses. The phase shaping and characterisation capabilities of the setup are demonstrated for phases with

increasing complexity. Shapeable, broadband MIR pulses with an autocorrelation FWHM below 50 fs were achieved.

- In **Chapter IV**, transient absorption pump-probe spectroscopy is used to investigate the influence of excitation of a specific vibrational mode on the photoreaction of a technologically relevant molecule. In the case under study, the C=N=N stretching vibration of 2-diazo-1-naphthol-5-sulfonate (DNQ for short) dissolved in methanol is excited by femtosecond MIR pulses. For pure vibrational excitation, the level of excitation of the C=N=N stretch mode is determined. For excitation with a UV/Vis pulse, the quantum yield of the photoreaction is estimated for both UV/Vis only excitation and vibrationally mediated photodissociation. The quantum yield enhancement achieved through vibrational pre-excitation of the C=N=N stretch mode is assessed. The measurements on vibrationally mediated photodissociateion are performed at UV/Vis excitation wavelengths both resonant and off-resonant with the DNQ absorption.
- **Chapter V** provides a summary of the findings of this work and an outlook into the direction where future research could be heading.

Ch. II to IV contain each a separate introduction to the respective topic and a section on the theoretical background, so that they can be read independently of one another. Furthermore, Ch. II to IV are each concluded by a section that summarises the results of the corresponding chapter.

II. 1 Introduction

II Non-collinear optical parametric amplifier for mid-infrared pulse generation

II. 1   Introduction

In ultrafast spectroscopy, a myriad of wavelengths is employed to inspect different systems of interest. Photons in the ultraviolet (UV) and visible (Vis) spectral region for example can induce electronic transitions in a molecule, whereas mid-infrared (MIR) photons are able to excite molecular vibrations. In either case, the excitation wavelength needs to be appropriately tuned to the desired transition of the system under study. It might also be desirable to combine several spectral ranges in one experiment, such as UV/Vis excitation and MIR probing [29] or excitation of different states with various visible pump wavelengths [10].

In the laboratory, there is often one (expensive!) laser source that provides ultrashort laser pulses at a fixed wavelength, such as a Titanium:sapphire (Ti:Sa) regenerative amplifier system generating pulses at 800 nm. In order to obtain pulses at the wavelengths that are needed for the experiment, the pulses from the source need to be converted to the required wavelengths. A widespread method to do this is to use optical parametric amplifiers (OPAs). In an OPA, energy of a high energy pulse from the laser source is transferred to other optical frequencies. In this way, pulses at different wavelengths than the one of the original laser source can be generated. If the geometry of the involved beams is non-collinear, one speaks of a non-collinear optical parametric amplifier (NOPA). The use of OPAs has the advantage that several OPAs on the optical table can be pumped by the same laser source and the outputs of the OPAs can thus be synchronised by optical delay lines. Moreover, the energy for the frequency conversion in the OPA is fully provided by the input optical pump pulse and no electric pumping or the like is required. There has been intensive research on the design and implementation of OPAs/NOPAs and systems generating pulses in the UV [30-33], Vis [34, 35], near-infrared (NIR) [35] and MIR [36-39] have been reported.

In this chapter, a two-stage NOPA for broadband MIR pulse generation is presented. The NOPA was designed and built in the group of Prof. Dr. Giulio Cerullo at Politecnico di Milano and is based on the architecture presented in Refs. [40, 41]. The NOPA was originally designed for 800 nm input pulses with s-polarisation and 100 fs pulse length. The performance of the NOPA with ≈ 100 fs input is reported in Refs. [42, 43].

The Ti:Sa laser system used for the work at hand provided substantially shorter input pulses (≈ 40 fs). Therefore, some minor modifications to the original design were necessary. The modified NOPA presented in this chapter was the source for MIR pulses that were used for the shaping and characterisation measurements that are presented in Ch. III.

In this chapter, some basic concepts underlying nonlinear optics and OPA operation are presented in Sec. II. 2. The actual setup of the two-stage NOPA is presented in Sec. II. 3, where also parameters for the NOPA configuration providing broadband MIR output centred at 3.2 µm are given.

II. 2   Theory

This section introduces the basic concepts that are necessary to understand the operation principles of the NOPA presented in this chapter. The theoretical overview given in this section is based on the instructive treatment of ultrafast OPAs presented in Ref. [44].

The real electric field of a linearly polarised electromagnetic monochromatic wave can be written as

$$E(z,t) = B(z) \cdot \cos(\omega_0 t - k_0 z + \varphi_0)$$

$$= \frac{1}{2} A(z) e^{i(\omega_0 t - k_0 z)} + c.c. \tag{II. 1}$$

The complex amplitude $A(z) = B(z) e^{i\varphi_0}$ contains the real amplitude of the wave $B(z)$ and a constant phase offset φ_0, $c.c.$ denotes the complex conjugate. $A(z)$ is independent of time, since a *monochromatic* wave is considered.

A linearly polarised plane wave propagating through a medium along the z-direction induces a polarisation in that medium

$$P(z,t) = \varepsilon_0 \left[\chi^{(1)} E(z,t) + \chi^{(2)} E^2(z,t) + \chi^{(3)} E^3(z,t) + \cdots \right]$$

$$= P_L(z,t) + P_{NL}(z,t) . \tag{II. 2}$$

For simplicity, the plane wave $E(z,t)$, the polarisation $P(z,t)$ and the susceptibilities $\chi^{(i)}$ have been taken as scalar quantities[1]. The polarisation consists of a part $P_L(z,t)$ that depends linearly on the electric field and a nonlinear term $P_{NL}(z,t)$. The evolution of the electric field inside the medium can then be written as

$$\frac{\partial^2 E(z,t)}{\partial z^2} - \mu_0 \frac{\partial^2 D(z,t)}{\partial t^2} = \mu_0 \frac{\partial^2 P_{NL}(z,t)}{\partial t^2} \tag{II. 3}$$

where $D(z,t) = \varepsilon_0 E(z,t) + P_L(z,t)$ is the electric displacement and μ_0 the magnetic permeability of vacuum. The nonlinear polarisation $P_{NL}(z,t)$ acts as a source term in Eq. II. 3. Since polarisation is a macroscopic separation of charges in a medium, the time-dependent change in polarisation $\frac{\partial^2 P_{NL}(z,t)}{\partial t^2}$ can be understood as accaleration of charges. The contribution to the electric field due to $P_{NL}(z,t,)$ is thus caused by the acceleration of charges owing to nonlinear polarisation [45, 46].

In the following, contributions of the electric field to the polarisation are considered only up to second order and $P_{NL}(z,t)$ thus becomes

$$P_{NL}(z,t) = \varepsilon_0 \chi^{(2)} E^2(z,t) = 2\varepsilon_0 d_{\text{eff}} E^2(z,t) . \tag{II. 4}$$

d_{eff} is an effective nonlinear optical coefficient. It takes into account the nonlinear optical susceptibility of the material and the polarisation of the electric field with respect to the nonlinear medium [47].

Consider the total electric field $E(z,t)$ to be composed of three monochromatic fields with angular frequencies ω_1, ω_2 and $\omega_3 = \omega_1 + \omega_2$

---

[1] This simplification is valid since the polarisation properties of the field and tensor properties of χ can be captured in the effective nonlinear optical coefficient d_{eff}, cf. Eq. II. 4.

$$E(z,t) = \frac{1}{2}\left\{A_1(z)e^{i(\omega_1 t - k_1 z)} + A_2(z)e^{i(\omega_2 t - k_2 z)} + A_3(z)e^{i(\omega_3 t - k_3 z)}\right\} + c.c. \quad \text{(II. 5)}$$

In the following, the convention $\omega_3 > \omega_2 \geq \omega_1$ shall be used. The field at ω_3 is then called pump, the field at ω_2 signal and the field at ω_1 idler. With $E(z,t)$ given as in Eq. II. 5, it follows that the nonlinear polarisation involves all the cross terms between frequencies ω_1, ω_2 and ω_3. Let us assume, however, that only those cross interactions efficiently take place that result in a frequency of ω_1, ω_2 or ω_3. This assumption is justified as in nonlinear wave mixing, phase matching effectively limits the combinations of possible interactions, cf. Sec. II. 2.1. That being said, the remaining terms in the nonlinear polarisation are

$$P_{NL}(z,t) = \varepsilon_0 d_{\text{eff}} A_2^*(z) \cdot A_3(z) \cdot e^{i[\omega_1 t - (k_3 - k_2)z]}$$
$$+\varepsilon_0 d_{\text{eff}} A_1^*(z) \cdot A_3(z) \cdot e^{i[\omega_2 t - (k_3 - k_1)z]}$$
$$+\varepsilon_0 d_{\text{eff}} A_1(z) \cdot A_2(z) \cdot e^{i[\omega_3 t - (k_1 + k_2)z]}$$
$$+c.c. \quad \text{(II. 6)}$$

The driving term of Eq. II. 3 then becomes

$$\frac{\partial^2 P_{NL}(z,t)}{\partial t^2} = -\varepsilon_0 d_{\text{eff}} \omega_1^2 A_2^*(z) \cdot A_3(z) \cdot e^{i[\omega_1 t - (k_3 - k_2)z]}$$
$$-\varepsilon_0 d_{\text{eff}} \omega_2^2 A_1^*(z) \cdot A_3(z) \cdot e^{i[\omega_2 t - (k_3 - k_1)z]}$$
$$-\varepsilon_0 d_{\text{eff}} \omega_3^2 A_1(z) \cdot A_2(z) \cdot e^{i[\omega_3 t - (k_1 + k_2)z]} \quad . \quad \text{(II. 7)}$$

Insertion of II. 7 into Eq. II. 3 and assuming that the complex amplitude $A_i(z)$ changes slowly compared to the oscillation of the field, leads to a set of three coupled wave equations for $A_i(z)$

$$\frac{\partial A_1}{\partial z} = -i\sigma_1 A_2^* A_3 \cdot e^{-i\Delta k z}$$
$$\frac{\partial A_2}{\partial z} = -i\sigma_2 A_1^* A_3 \cdot e^{-i\Delta k z}$$
$$\frac{\partial A_3}{\partial z} = -i\sigma_3 A_1 A_2 \cdot e^{i\Delta k z} \quad \text{(II. 8)}$$

with $\sigma_i = \frac{d_{\text{eff}} \omega_i}{c_0 n_i}$ (c_0: speed of light in vacuum, n_i: refractive index at ω_i) and wavevector mismatch $\Delta k = k_3 - k_2 - k_1$. Eq. II. 8 points out several important things: Firstly, the differential change of the amplitude at one frequency is proportional to the amplitudes at the other two frequencies. Secondly, efficient coupling between the waves over a macroscopic distance only occurs if $\Delta k \approx 0$. $\Delta k = 0$ is the so-called phase matching condition, see Sec. II. 2.1. Thirdly, the role of ω_1 and ω_2, i.e. of signal and idler, is equivalent.

The interaction between different optical fields can also be understood in the photon picture. Energy conservation implies that

$$\omega_3 = \omega_1 + \omega_2 \quad \text{(II. 9)}$$
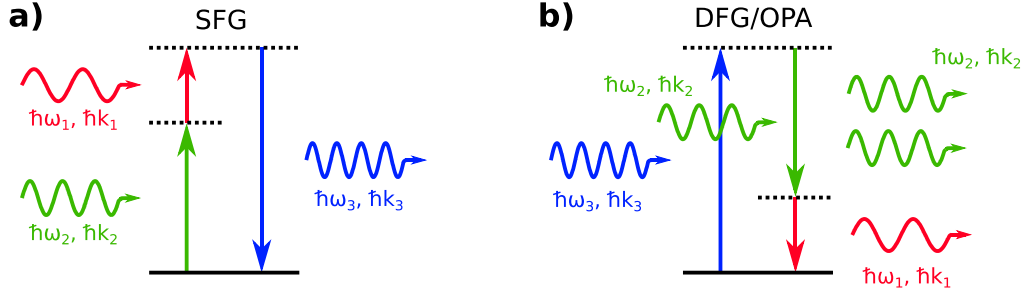
Figure II.1: *Optical parametric processes. a) Sum frequency generation. Two low energy photons are annihilated and a high energy photon is created. b) Difference frequency generation and optical parametric amplification. A high energy pump photon (blue) leads to population of a virtual level (dashed line). A signal photon (green) with lower energy than the pump photon stimulates emission from the high virtual level. In order for the system to decay to the non-virtual initial state (solid line), an additional idler photon (red) needs to be emitted.*

and momentum conservation gives

$$\vec{k}_3 = \vec{k}_1 + \vec{k}_2 \ . \tag{II.10}$$

Note that in Eq. II. 10, $\vec{k}$ is written as a vector quantitiy. This generalisation allows to treat non-collinear beam geometries as well. Fig. II.1 shows schemes of sum frequency generation (SFG), difference frequence generation (DFG) and optical parametric amplification (OPA). If the low frequency photons in SFG are degenerate, the process is called second harmonic generation (SHG). Note that DFG and OPA are very similar processes. The difference lies in the intensities of the fields: If the field at ω_3 is much stronger than the one at ω_1, one speaks of OPA. For comparable intensities of the fields, the process is called DFG.

II. 2.1 Phase matching

It was pointed out above that efficient coupling and thus energy transfer between different optical fields can only occur if the phase matching condition

$$\Delta\vec{k} = \vec{k}_3 - \vec{k}_2 - \vec{k}_1 = 0 \tag{II.11}$$

is fulfilled. In the photon picture, this is a consequence of momentum conservation. In the wave picture of Eq. II. 3, it means that the source term that is responsible for the creation of new frequencies, $\frac{\partial^2 P_{NL}(z,t)}{\partial t^2}$, travels with the same velocity as the newly generated field, so that at each point along the nonlinear material, the newly generated field can interfere constructively with the field that was generated at previous positions, see Fig. II.2 . In the case of collinear beam geometry, the wavevector $\vec{k}$ can be treated as a scalar. Thus, with n_i the refractive index at ω_i, it follows from Eq. II. 11 directly that

$$\omega_3 n_3 = \omega_2 n_2 + \omega_1 n_1 \ . \tag{II.12}$$

For an isotropic material with purely positive or purely negative dispersion, Eq. II. 12 cannot be fulfilled. However, in anisotropic materials Eq. II. 12 can be fulfilled by employing beams with different polarisation and exploitation of birefringence. For this approach, often uniaxial birefringent crystals are employed.
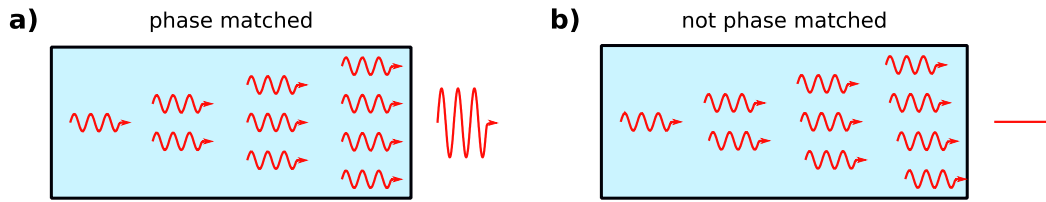
Figure II.2: *Phase matching in a nonlinear medium. a) Phase matched case. The newly generated frequencies all interfere constructively and create a macroscopic output after the medium. b) The phase matching condition is not fulfilled and newly generated frequencies created at different positions along the medium interfere destructively. No macroscopic output of a nonlinearly generated frequency is observed.*

Uniaxial crystals have a distinct direction inside the crystal, the so-called optical axis. Polarisation perpendicular to the optical axis is called ordinary, see Fig. II.3 a). Beams with ordinary polarisation experience a refractive index n_o, whereas beams with a polarisation perpendicular to ordinary, i.e. with extraordinary polarisation, experience a refractive index that depends on the beam's propagation direction with respect to the optical axis. This is illustrated in Fig. II.3 b). The refractive index $n_e(\theta)$ experienced by the extraordinary beam varies between n_o and n_e as

$$\frac{1}{n_e(\theta)^2} = \frac{\cos^2\theta}{n_o^2} + \frac{\sin^2\theta}{n_e^2} \quad . \tag{II.13}$$

θ is the angle between the wavevector $\vec{k}$ of the extraordinary polarised beam and the optical axis of the crystal, see. Fig. II.3 b).
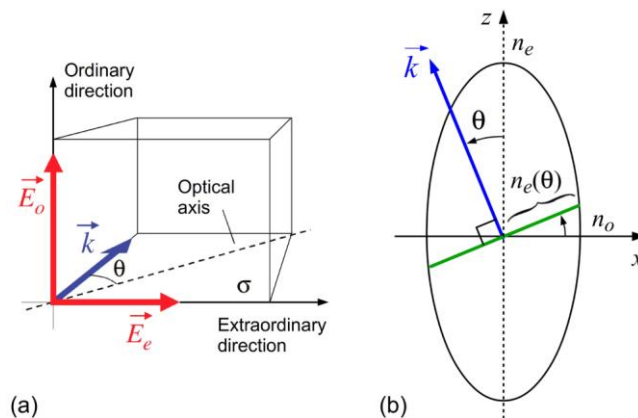
Figure II.3: *a) Definition of ordinary and extraordinary polarisation in an uniaxial crystal. b) Cut through the index ellipsoid of a positive uniaxial crystal ($n_e > n_o$). $n_e(\theta)$ depends on the propagation direction of the beam. The optical axis is in the z-direction. Reprinted with permission from Ref. [44] under the Creative Commons Attribution licence CC BY 3.0.*

9

Type 0	$\omega_1, \omega_2, \omega_3$ have same polarisation
Type 1	ω_1, ω_2 have same polarisation, ω_3 has perpendicular polarisation
Type 2	ω_1, ω_2 are cross-polarised ω_3 has same polarisation as either ω_1 or ω_2

Table II-1: *Different types of phase matching schemes with respect to ordinary and extraordinary polarisation.*

The interplay of different refractive indices at different polarisations often allows to find a value for θ at which Eq. II. 12 can be fulfilled. Depending on the relative polarisation states of pump, signal and idler with respect to ordinary and extraordinary axis, phase matching is categorised in different types, see Tab. II-1.

Another method to achieve phase matching is to periodically switch the sign of d_{eff}. The sign of d_{eff} changes just when the amplitude of the nonlinearly generated total field is about to decrease due to destructive interference between contributions of the newly generated field generated at different positions in the nonlinear medium; i.e. d_{eff} changes when the accumulated phase mismatch $\Delta k \cdot z = \pi$. This type of phase matching is called quasi-phase matching (QPM). The phase matching condition for QPM then includes a grating wavevector $K_g = \frac{2\pi}{\Lambda}$, with Λ the poling period, and reads

$$\Delta k = k_3 - k_2 - k_1 - K_g = 0 \ . \tag{II. 14}$$

QPM is typically of Type 0. Fig. II.4 shows a sketch of a periodically poled crystal, in which the sign of d_{eff} switches periodically.
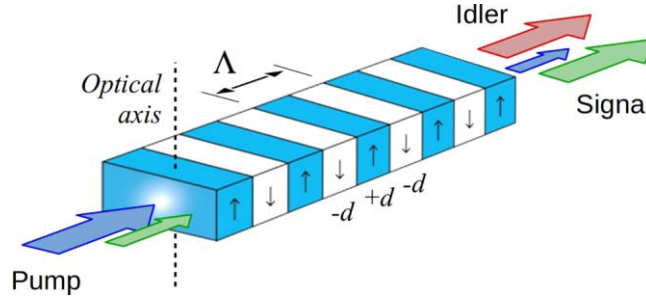
Figure II.4: *Periodically poled nonlinear crystal for QPM. The sign of the effective nonlinear coefficient changes periodically so that efficient wave mixing between the involved frequencies can occur on a macroscopic scale. The poling period Λ is chosen according to the refractive indices of the involved fields. Reprinted with permission from Ref. [44] under the Creative Commons Attribution licence CC BY 3.0.*

II. 2.2 The role of group velocity mismatch

So far, the monochromatic case has been considered with electric fields that extend infinitely long in time. This treatment was sufficient to understand the coupling between different fields and to introduce the concept of phase matching. However, to achieve the large electric fields for which nonlinear conversion actually occurs on a considerable scale, laser *pulses* with high peak intensity are necessary. When dealing with pulses of different frequencies, the temporal overlap between them plays a crucial role, since energy transfer

between the optical fields can only occur if the pulses overlap. A measure for the preservation of temporal overlap between two pulses i and j is the group velocity mismatch (GVM) δ_{ij}

$$\delta_{ij} = \frac{1}{v_{gi}} - \frac{1}{v_{gj}} \quad . \tag{II.15}$$

v_{gi}, v_{gj} are the group velocities of pulses i, j. The GVM indicates the relative temporal shift between the pulses' envelopes after propagation through a certain distance in the material. Consider an OPA process with a pump pulse of FWHM duration τ. The pulse-splitting length

$$l_{j3} = \left| \frac{\tau}{\delta_{j3}} \right| \qquad j = 1,2 \tag{II.16}$$

gives the propagation distance in the nonlinear medium after which the pump has temporally separated from the signal or idler in the absence of gain. If signal and idler temporally walk off in the same direction, i.e. l_{13}, l_{23} are both positive or both negative, the pulse-splitting length limits the crystal thickness that can be employed for amplification.

For the pulse splitting length, only the signal/pump GVM and idler/pump GVM play a role. Conversely, the GVM between signal and idler determines the amplification bandwidth, i.e. the frequency range (around a centre frequency at which $\Delta k = 0$) in which the phase mismatch is sufficiently small to still obtain efficient amplification. The amplification bandwidth is largest if $\delta_{12} = 0$.
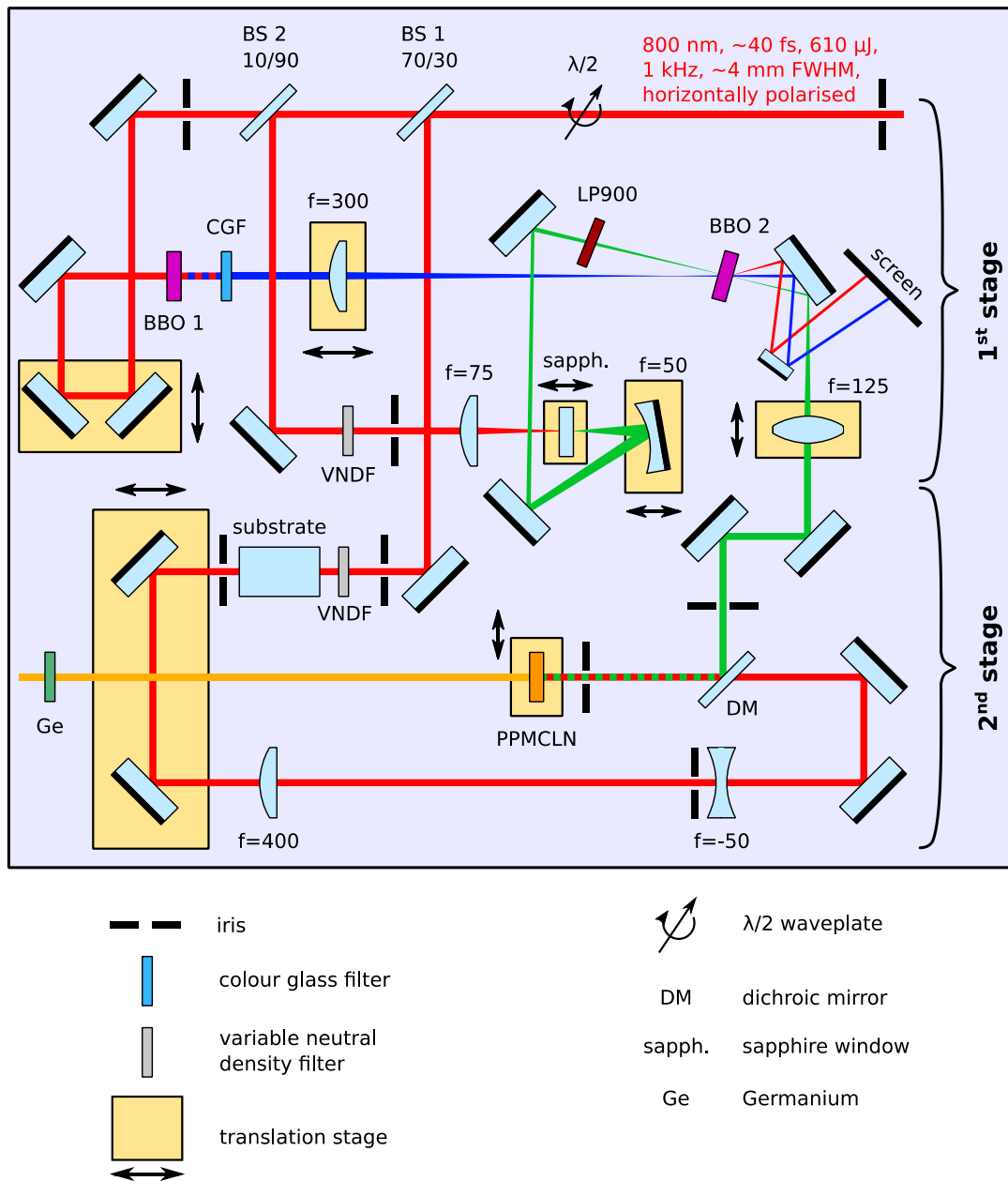
Figure II.5: *Architecture of the NOPA for MIR pulse generation. The NOPA was seeded by a commercial Ti:Sa amplifier system. The NOPA consists of two stages: The first stage generates a NIR seed and the second stage generates the actual MIR radiation. Focal lengths are given in mm. Details on the two stages are given in Sec. II. 3.1 and II. 3.2.*

II. 3   <u>Setup</u>

The optical setup of the NOPA is displayed in Fig. II.5. The NOPA consists of two stages. In the first stage, the seed is generated and pre-amplified. In the second stage, the actual MIR radiation is generated as the idler in an OPA process. The two stages are described in more detail in Sec. II. 3.1 and II. 3.2. If not noted otherwise in Sec. II. 3.1 or II. 3.2, the irises shown in Fig. II.5 only serve for alignment purposes. The input beam for the NOPA was provided

by a commercial Ti:Sa regenerative amplifier system (Coherent Astrella-USP-1K). The input into the NOPA was centred at 800 nm, had a beam diameter of approximately 4 mm FWHM and was horizontally polarised with respect to the optical table. This corresponds to p-polarisation with respect to the NOPA. The input pulses were ca. 40 fs in duration and had an energy of 610 µJ at 1 kHz repetition rate.

Pulse parameters like energy and spectrum which are given in the following for the NIR seed and final MIR pulse correspond to the NOPA configuration that delivers broadband MIR pulses centred at 3.2 µm.

II. 3.1   1st stage: Generation and pre-amplification of the near-infrared seed

The purpose of the first stage of the NOPA is to generate a strong and stable seed in the NIR. The NIR seed from the first stage is then used later in the second stage (cf. Sec. II. 3.2) for the actual MIR generation.

The optical setup of the first NOPA stage is depicted in Fig. II.6 a). First, the polarisation of the NOPA input is turned by a $\lambda/2$-waveplate from p- to s-polarisation[1]. S-polarisation has the advantage that all beams throughout the NOPA lie in one horizontal plane with respect to the optical table. The s-polarised beam is then split by a 70/30 beamsplitter (BS 1 in Fig. II.6 a)). 70% of the energy is reflected towards the second stage, where it serves later as pump beam. The 30% transmitted part is split by a second beamsplitter (BS 2 in Fig. II.6 a)). 10% of the power is reflected and used to generate the NIR seed, whereas 90% of the power (140 µJ) is transmitted. The transmitted part is sent via a delay stage into a β-barium borate (BBO) crystal for SHG (BBO 1, 1 mm thick, Type I, $\theta = 29.2°$). The 800 nm beam is not focused into the BBO crystal, as the generated 400 nm pulse has sufficient energy (23 µJ) even for an unfocused fundamental beam. The 800 nm fundamental is filtered out by a BG39 colour glass filter (CGF in Fig. II.6 a)). An $f = 300$ mm plano-convex lens focuses the 400 nm beam to ca. 2-3 cm in front of the second BBO crystal (BBO 2 in Fig. II.6 a)), where the 400 nm pulse acts as pump for pre-amplification of the NIR signal pulse. Placing the pump beam focus slightly before the BBO crystal increases the beam spot size at the crystal itself. This in turn reduces the risk of burning the crystal and also provides a better overlap of the pump with the NIR signal beam.

The NIR signal beam is generated from the portion of the 800 nm fundamental that is reflected by BS 2. For that purpose, the 800 nm beam is focused by an $f = 75$ mm lens into a 3 mm thick sapphire window for white light (WL) generation. A variable neutral density filter (VNDF) and an iris before the focusing lens allow to tune the incoming pulse energy and to clean the spatial mode of the 800 nm beam, so that stable and homogeneous WL is generated in the sapphire window. The sapphire window is placed on a translation stage so that the focus of the 800 nm beam can be set near to the exit surface of the sapphire window. In this way, the generated WL only needs to propagate through a minimum amount of the sapphire window, which reduces detrimental effects, such as temporal broadening of the WL pulse. The spectrally broad WL seed is focused into a BBO crystal (BBO 2 in Fig. II.6 a), 1 mm thick, Type I, $\theta = 32°$) for pre-amplification with the 400 nm pump. The focusing is done by an $f = 50$ mm spherical mirror via two folding mirrors and a 1 mm thick 900 nm longpass filter (LP900 in Fig. II.6 a)). The latter filters out the 800 nm fundamental as well as visible components of the WL, so that only the desired NIR components of the WL are amplified in BBO 2. The focus position of the WL seed at the BBO crystal can be fine tuned by the translation stage on which the focus mirror is mounted. The

---

[1] With respect to the optical table, this is from horizontal to vertical.

a)

b)
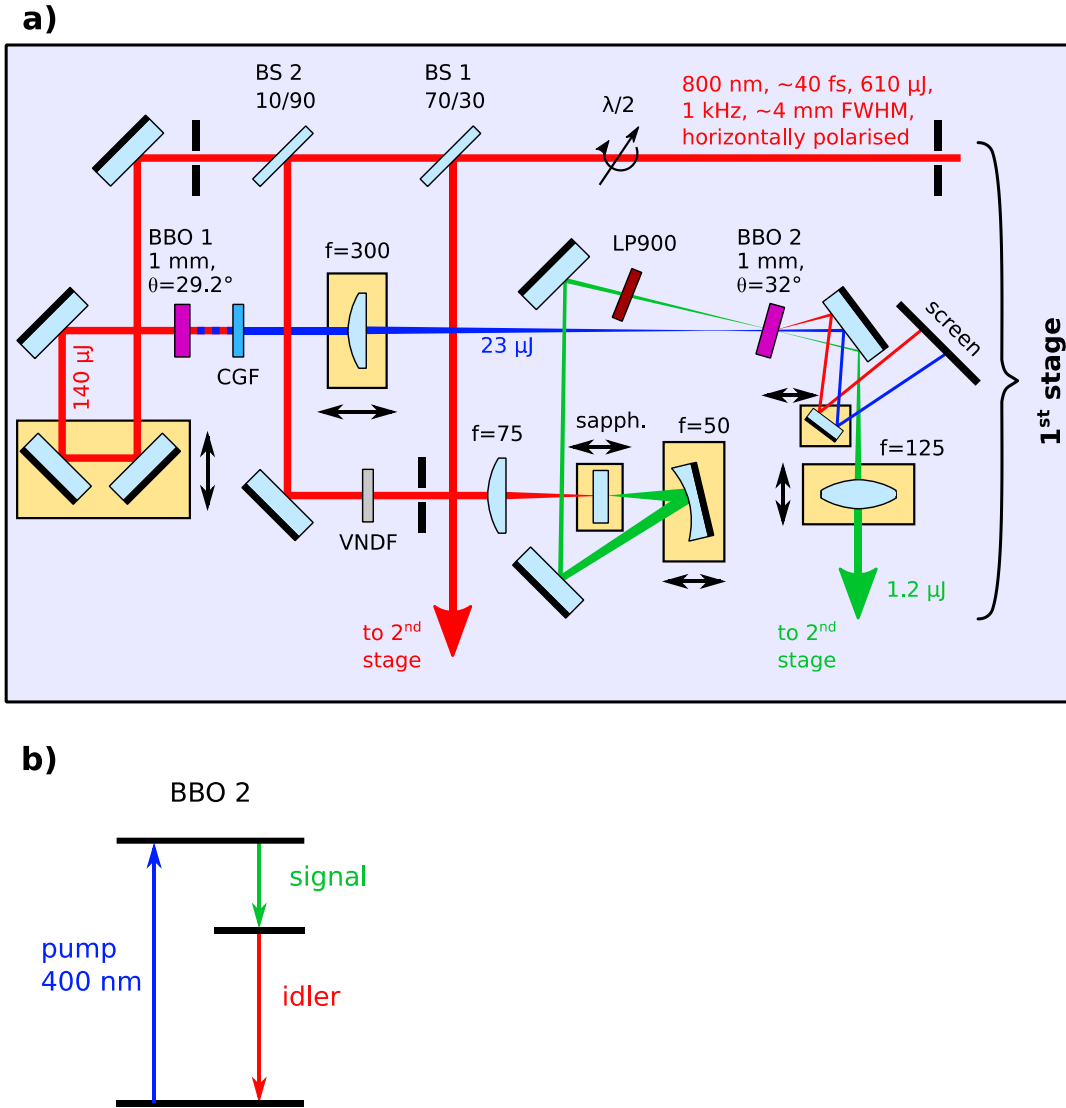
Figure II.6: *First stage of the NOPA. a) Optical setup. See text for details. b) Energy scheme of the OPA process in BBO 2. Note that the signal, represented by green, is actually in the NIR and thus invisible to the bare eye.*

position of the WL focus influences the spatial chirp of the pre-amplified NIR signal, as is detailed in App. A. 1. The timing between NIR seed pulse and 400 nm pump pulse is controlled by the optical delay line in the pump pulse generation path.

In BBO 2, the p-polarised 400 nm pump and s-polarised NIR seed are overlapped non-collinearly. Due to the non-collinearity, pump and idler can be easily spatially separated from the pre-amplified seed after BBO 2. Note that the non-collinearity does not increase the amplification bandwidth, as the group velocity of the signal is larger than the the group velocity of the idler, cf. Ref. [44]. An energy diagram of the pre-amplification of the NIR signal is shown in Fig. II.6 b). In the amplification process with the 400 nm pump, an idler beam around 650 nm is created. If BBO 2 was pumped directly by an 800 nm beam, the resulting idler would be around 3.4 µm. The transmission of BBO, however, significantly drops beyond 2.2 µm. Therefore, the idler at 3.4 µm would be absorbed and efficient amplification of the NIR signal would be prevented, cf. Eq. II. 8. This is why the 800 nm are frequency doubled before acting as pump for the NIR signal.
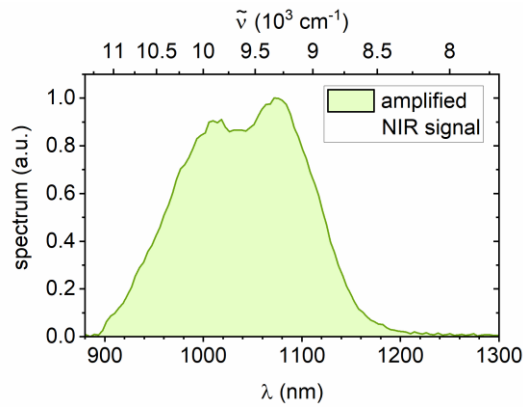
Figure II.7: Spectrum of the pre-amplified NIR signal beam, measured before the 950 nm dichroic mirror of the second stage.

After BBO 2, pump and idler are reflected by a D-shaped mirror onto a screen. Watching the screen is especially useful during alignment of the NOPA, see App. A. 1.

The pre-amplified seed is collimated by an $f = 125$ mm bi-convex N-BK7 lens (Newport KBX067) and had an energy of 1.2 µJ. From autocorrelation measurements, the pre-amplified NIR pulse were estimated to be shorter than 100 fs. A spectrum of the pre-amplified signal is shown in Fig. II.7.

II. 3.2   2nd stage: MIR generation

The generation of the actual MIR beam takes place in the second stage of the NOPA. The MIR beam emerges as the idler from parametric amplification of the pre-amplifed NIR signal with an 800 nm pump pulse.

The collimated pre-amplified NIR signal from the first stage is routed via two stirring mirrors onto a dichroic mirror, see Fig. II.8 a). The dichroic mirror has a separation wavelength of 950 nm and reflects wavelengths above, whereas wavelengths below are transmitted. From the dichroic mirror, the NIR signal is reflected onto a periodically poled 5 mol% MgO doped congruent lithium niobate (PPMCLN) crystal, where it is mixed with the 800 nm pump.

The 800 nm pump is reflected from BS 1 in the first stage towards the second stage. The pump is attenuated by a VNDF to a level below supercontinuum generation in the PPMCLN crystal and thus below the damage threshold of the crystal. The iris before the VNDF cleans the spatial mode of the 800 nm pump. The 800 nm pump pulse is stretched in time by a substrate consisting of 1 cm BK7 glass and 1 cm NaCl in order to match the pulse-splitting length inside the PPMCLN crystal between pump and NIR signal with the thickness of the crystal, cf. Sec. II. 3.2.1. A delay stage allows to control the delay between 800 nm pump pulse and pre-amplified NIR signal pulse. In order to match the beam size of the pump beam with the height of the PPMCLN crystal (2 mm), the pump beam size is reduced by an 8:1 telescope after the delay stage. The telescope consists of an $f = 400$ mm plano convex lens and an $f = -50$ mm bi-concave lens. The iris in front of the bi-concave lens can in principle be used to fine tune the pump spot size at the crystal. However, this was not necessary in the work at hand and thus the iris served only for alignment purposes[1].

The down-telescoped 800 nm pump beam traverses the dichroic mirror and propagates collinearly with the pre-amplified NIR signal beam. The 800 nm pump (130 µJ) and the pre-

---

[1] Note that changing the pump spot size on the PPMCLN crystal by the iris, also changes the divergence of the pump beam. This in turn affects the divergence of the generated MIR beam.

a)

b)

c) fanout structure of periodically poled crystal
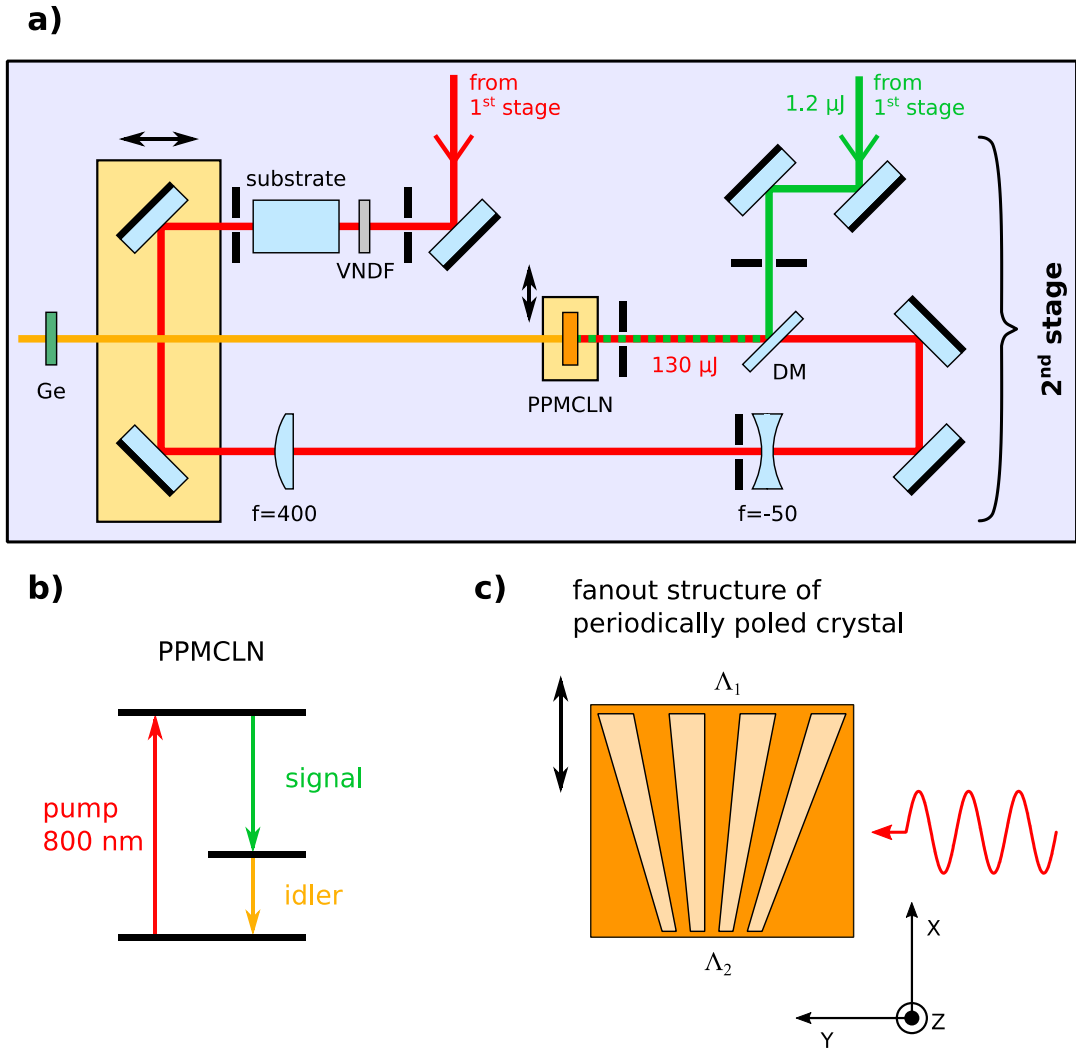
Figure II.8: *Second stage of the NOPA. a) Optical setup. See text for details. b) Energy scheme of the OPA in the PPMCLN crystal. The actual MIR pulse corresponds to the idler. c) Fanout structure of the PPMCLN crystal. The poling period changes from $\Lambda_1 = 23\ \mu m$ on the one side of the crystal to $\Lambda_2 = 20\ \mu m$ on the other side of the crystal. Movement of the crystal perpendicular to the incoming beam (red) optimises the poling period for the involved wavelengths. The movement is denoted by the black double arrow. Dimensions of the crystal are $X \times Y \times Z = 9.6 \times 1.2 \times 2\ mm^3$.*

amplified NIR signal are both s-polarised and interact in the PPMCLN crystal according to Fig. II.8 b). The interaction generates an s-polarised idler in the MIR spectral region. The amplification of the NIR signal is based on QPM in the periodically poled crystal (Type 0 phase matching). The PPMCLN crystal has a fanout structure with a changing poling period along the direction transverse to the input beams, cf. Fig. II.8 c). The poling period varies from 20 µm to 23 µm and can be adjusted by translation of the PPMCLN crystal to match the input spectrum of the NIR signal, cf. Fig. II.10 a). The PPMCLN is anti-reflection coated at the input (800-1300 nm) and output (2000-5000 nm) surface.

The resulting MIR idler co-propagates with the NIR signal and the residual 800 nm pump. A collinear geometry in the second stage is chosen in order to avoid spatial dispersion of the invisible MIR idler and to faciliate later alignment. A Germanium (Ge) window placed at the end of the NOPA filters out the NIR seed and residual 800 nm pump. After the Ge window, the MIR pulse had an energy up to 1.7 µJ. The MIR spectrum after the Ge window is shown
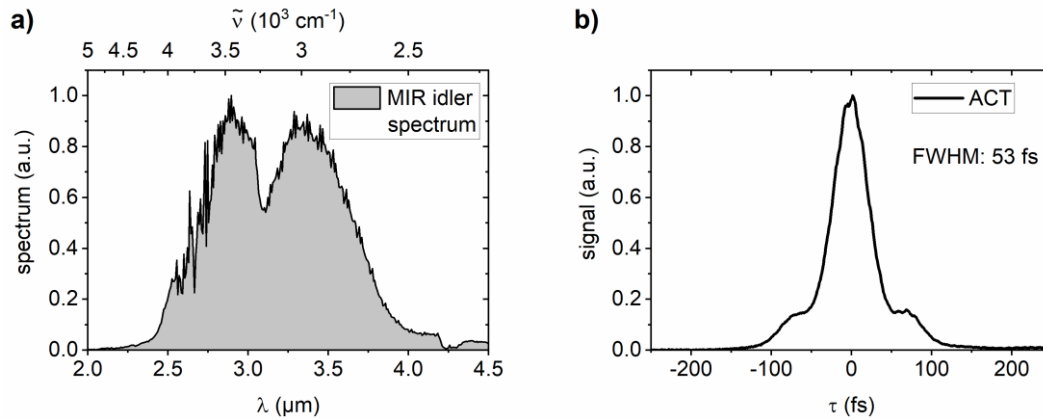
Figure II.9: *a) Spectrum of the MIR idler after the Ge window. The spectrum's centre of mass is at 3.2 µm. The dip around 4.2 µm originates from absorption by CO_2 in the air. b) Autocorrelation measurement of the NOPA MIR output. The shoulders hint at a present third order dispersion.*

in Fig. II.9 a). It was centred at 3.2 µm and spanned from 2.6 to 3.7 µm (FWHM). The MIR spectrum supported a pulse duration as short as 19 fs intensity FWHM, which is less than two optical cycles. However, an autocorrelation measurement of the NOPA MIR output showed that the pulse was approximately twice as long, cf. Fig. II.9 b). The shoulders in the autocorrelation trace (ACT) suggest that there was third order dispersion present in the MIR pulse.

II. 3.2.1 Group velocity mismatches in the PPMCLN crystal

Efficient OPA is possible only if signal and pump pulse have sufficient temporal overlap inside the nonlinear crystal. Fig. II.10 b) shows the GVM between signal/pump (black), idler/pump (blue) and signal/idler pulses (red) in the PPMCLN crystal. As can be seen, the GVM for signal and idler is close to zero near the NIR signal wavelength of 1050 nm, i.e. both NIR signal and newly generated MIR idler travel with the same speed along the crystal. The close to zero signal/idler GVM enables generation of a broadband MIR spectrum, cf. Sec. II. 2.2. In contrast, the GVM between NIR signal and 800 nm pump pulse is ca. -170 fs/mm, which means that for a crystal length of 1.2 mm, the envelopes of signal and pump accumulate a relative delay of 200 fs during propagation through the crystal. To ensure temporal overlap between signal and pump along the whole crystal length, the pump pulse should have a duration similar to that delay. An autocorrelation measurement of the 800 nm pump without any additional substrate in the second stage gave a ACT FWHM of $\tau_{ACT}(\text{no substrate}) = 78$ fs, corresponding to a Gaussian FWHM pulse width of 55 fs. This is well below the 200 fs delay that the pump pulse accumulates relative to the signal during propagation through the crystal. Consequently, without additional substrate in the second stage pump path, there was only weak MIR output observed due to the insufficient temporal overlap. In order to gain a decent energy level of the MIR output pulse, a substrate consisting of 1 cm BK7 and 1 cm NaCl was inserted to stretch the 800 nm pump pulse in time. The measured ACT FWHM of the 800 nm pump increased to $\tau_{ACT}(\text{substrate}) = 218$ fs, i.e. the Gaussian pulse length is longer than 150 fs, comparable to the temporal walk-off due to GVM between signal and pump. The prolonged pump pulse duration gave a decent MIR output of up to 1.7 µJ.

One possibility to further optimise the pump pulse duration could be the usage of a pair of glass wedges that allows to precisely tune the inserted amount of glass.
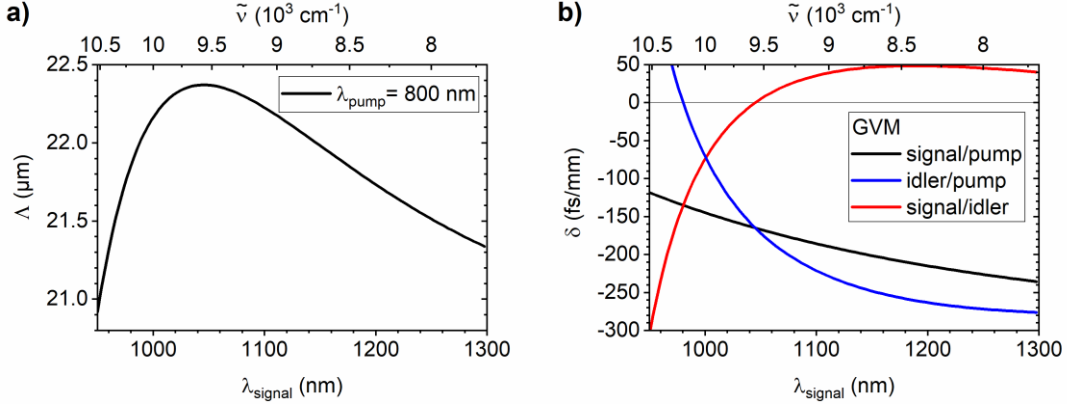
Figure II.10: *a) Poling period Λ for the PPMCLN crystal. b) GVM δ between signal/pump (black), idler/pump (blue) and signal/idler (red) pulses in PPMCLN. In a) and b), the pump wavelength is at $\lambda_{pump} = 800\ nm$. The values were calculated with [48].*

II. 3.2.2 Passive carrier-envelope phase stabilisation of the mid-infrared pulse

The design of the NOPA ensures passive stabilisation of the MIR carrier-envelope phase (CEP). To understand this, the 800 nm NOPA input pulse is assumed to have a CEP φ_0 that varies from shot to shot. In the first stage of the NOPA, the signal is created by WL generation in a sapphire substrate. The dominant process in WL generation is self-phase modulation (SPM). For an input pulse with CEP φ_0, the self-phase modulated pulse after the substrate has a CEP of [49, 50]

$$\varphi_{SPM} = \varphi_0 + \frac{\pi}{2} \ . \tag{II.17}$$

φ_{SPM} is maintained in the seed pre-amplification in BBO 2, which can be seen as a stimulated emission process. In the second stage of the NOPA, the 800 nm pump with CEP φ_0 interacts with the pre-amplified seed with CEP φ_{SPM}, leading to a CEP φ_{MIR} of the MIR idler [49, 50]

$$\varphi_{MIR} = \varphi_0 - \varphi_{SPM} - \frac{\pi}{2} = \varphi_0 - \left(\varphi_0 + \frac{\pi}{2}\right) - \frac{\pi}{2} = -\pi \ . \tag{II.18}$$

φ_{MIR} is thus constant and in particular independent of φ_0, the CEP of the 800 nm input pulse.

It is noted in Ref. [50] that this kind of phase stabilisation does not require interferometric stability of the various beampaths within the NOPA. If the optical path length of one of the beams changes by ΔL, the envelope and carrier wave are shifted by $\Delta t_e = \frac{\Delta L}{v_g}$ and $\Delta t_c = \frac{\Delta L}{v_p}$, respectively, with v_g and v_p the phase and group velocity. This leads to a shift in CEP of

$$\Delta\varphi_0 = 2\pi \frac{\Delta t_e - \Delta t_c}{T}$$

$$= 2\pi \frac{1}{T} \cdot \left(\frac{1}{v_g} - \frac{1}{v_p}\right) \cdot \Delta L$$

$$= \frac{2\pi}{c} \cdot \frac{n_g - n_p}{T} \cdot \Delta L$$

$$= -0.021\,\text{m}^{-1} \cdot \Delta L \qquad\qquad (\text{II.}\,19)$$

where c denotes the speed of light. In the last line of Eq. II. 19, values for the refractive index n_p and group index n_g of air as well as for the period of the carrier wave T have been inserted. Those values have been taken for an optical wave at 3 μm. Eq. II. 19 shows that for a CEP change of e.g. $\Delta\varphi_0 = \frac{\pi}{20}$, the change in optical path length needed to be $\Delta L = 7.5$ m! This is several orders of magnitue beyond any realistic change due to instabilities in the optical path length. Thus, the effect of optical path length instabilities on the CEP can be neglected.

II. 3.3   Spectral tunability of the NOPA

The pulse parameters for pre-amplified NIR signal and MIR idler that are presented above are for a configuration of the NOPA that results in a broadband MIR spectrum centred around 3.2 μm. However, the NOPA is tunable in the whole spectral range of 2-5 μm. A demonstration of the spectral tunability over that range is presented in Ref. [43].

The limits of spectral tunability are set on the long wavelength edge by the separation wavelength (950 nm) of the dichroic mirror which combines pre-amplified NIR signal and pump in the second stage. The difference frequency between 950 nm and 800 nm corresponds to $\lambda_{DFG} = 5070$ nm. Furthermore, PPMCLN is transmissive only up to 5.5 μm [48], which ultimately sets a long wavelength limit to the NOPA.

On the low wavelength side, the efficiency of the WL seed generation in the first stage drops significantly above 1300 nm, so that no appropriate NIR seed is available for DFG with MIR wavelengths below 2 μm. In addition, the Ge filter window at the end of the NOPA is only transmissive above 2 μm.

Within the 2-5 μm range, the NOPA output spectrum can be tuned by:

1. Changing the tilt of BBO 2 in the first stage. This changes the phase matching in the pre-amplification process and thus the amplification efficiency of different wavelengths within the WL spectrum.
2. Adjusting the delay between WL seed and 400 nm pump in the first stage to control which part of the chirped WL seed will be amplified.
3. Changing the transverse position of the PPMCLN crystal in the second stage, i.e. adjusting the periodic poling period Λ and with that the phase matching for DFG.
4. Changing the delay of the 800 nm pump pulse in the second stage. This determines which part of the broadband pre-amplified NIR seed predominantly interacts with the 800 nm pump. Furthermore, the delay of the pump governs which instantaneous frequencies of the chirped pump pulse are active in the parametric amplification.

From the four items listed above, a change of the 800 nm pump delay in the second stage was observed to have the largest effect on the MIR output spectrum.

II. 4   Summary

In this chapter, a two-stage NOPA for broadband MIR pulse generation was presented. The NOPA was pumped by 800 nm, 40 fs pulses with 610 µJ at 1 kHz. The generated MIR pulses were CEP stabilised. Pulse parameters for the NIR seed and MIR output in the configuration providing broadband MIR pulses centred at 3.2 µm were given. The broadband MIR spectrum around 3.2 µm supports a pulse duration of 19 fs. From autocorrelation measurements, the actual pulse duration was determined to be twice as much. The pulses around 3.2 µm had an energy up to 1.7 µJ. Limits of the spectral tunability of the NOPA were discussed and means to tune the output spectrum in the range 2-5 µm were listed.
The MIR output of the NOPA was used for the pulse shaping and characterisation that is presented in Ch. III.

In order to further increase the output energy of NOPA, the 1.2 mm thick PPMCLN crystal could be replaced by a thicker crystal. In this case, also the 800 nm pump in the second stage needed to be further stretched to increase the pulse splitting length between pump and signal/idler so that the thicker crystal length can actually be exploited. It is also conceivable to extend the NOPA by a third stage in which the MIR beam is amplified. In both cases, phase matching restrictions are expected to become more severe and a balance between the spectral broadness and the energy of the MIR pulse needs to be found. This balance depends on the requirements of the actual experiment.

III Mid-infrared pulse shaping and characterisation by acousto-optic modulator based dispersion scan

III. 1 Introduction

The ability to shape ultrashort laser pulses is a valuable tool in spectroscopy. Systematic shaping of pulses has helped to gain insight into the dynamics of biologically [51] and technologically [52] relevant molecules. In particular, shaped pulses in the MIR spectral region have been used to enhance the population in selected vibrational states [53], to control the quantum interference between multiple vibrational excitation paths [54] as well as in FTIR microscopy [55]. Moreover, shaped MIR pulses have found their application in determination of molecular structure and environment at interfaces with sum frequency generation (micro)spectroscopy [56, 57].

In ultrafast spectroscopy, knowledge of the full pulse shape, i.e. its spectral amplitude and phase, provides valuable information. This is especially true if the experiment is based on control of the pulse shape. The pulse's spectrum can usually be directly measured with a spectrometer, whereas determination of the phase is less straightforward. To achieve the latter, a variety of techniques for phase characterisation has been developed throughout the years. Among the most widespread techniques are frequency-resolved optical gating (FROG) [58, 59], spectral phase interferometry for direct electric-field reconstruction (SPIDER) [60, 61] or multiphoton intrapulse interference phase scan (MIIPS) [62, 63].

FROG in its original form is a spectrally resolved autocorrelation whereas SPIDER is based on the interferogram of the pulse to be characterised and a spectrally and temporally shifted copy of itself. Both methods have been successfully used for pulse characterisation from the UV to MIR region [64]. Variants of FROG and SPIDER allow for detection in the Vis region by up- or downconversion with a reference pulse [65-67]. Thus, the signal to be measured can be conveniently detected, even if the pulse itself is in the UV or MIR. In case the experimental setup comprises a pulse shaper, MIIPS represents a convenient alternative for phase characterisation. It is based on iterative pulse compression by compensation of the pulse's group delay dispersion. The phase that finally compresses the pulse thus corresponds to the pulse's original phase.

More recently, another method for phase characterisation has emerged and quickly gained popularity within the community: dispersion scan, or d-scan for short [68]. In d-scan, several known values of dispersion are imprinted on the pulse to be characterised and subsequently, a non-linear signal, such as the second harmonic (SH), is generated. From the resulting two-dimensional trace (dispersion vs. wavelength of the non-linearly generated signal) and an independently measured fundamental wavelength (FW) spectrum, the phase of the pulse can be obtained. Like MIIPS, d-scan employs known phases to determine the pulse's spectral phase. However, d-scan is more reliable for pulse's with complex phases, as it does not rely on the second derivative of the applied test phase [62, 68]. The popularity of d-scan in the Vis and NIR spectral range arises due to its simple inline implementation. A pair of glass wedges is commonly used to imprint the desired dispersion on the pulse and the setup is all collinear. This signfiantly facilitates the alignment, as no separation and recombination of beams or interferometric accuracy is needed. Furthermore, after the characterisation step, the glass insertion can be easily adjusted to compress the pulse. Despite the widespread use of d-scan in the Vis/NIR range, only few examples of pulse characterisation in the MIR spectral range have been reported so far. This is due to the lack

of suitable off-the-shelf MIR optics required for dispersion control, such as chirped mirrors. Reported implementations of d-scan in the MIR range are based on the use of a grating compressor [69] or on discrete dispersion steps. The latter are realized either by inserting a set of windows with different thicknesses into the beam path [70] or by varying the number of passes through the same substrate [71]. Variation of the dispersion of an auxiliary NIR pulse and subsequent sum frequency generation with the MIR pulse of interest has also been published [72].

In this chapter, d-scan is implemented for MIR pulses employing a pulse shaper, which introduces the desired dispersion. For experiments involving a pulse shaper anyway, the proposed method for pulse characterisation only calls for minimum additional optics. Moreover, demands on alignment are reduced by a full collinear geometry. The presented d-scan implementation is also known as chirp scan and has been successfully demonstrated for 800 nm pulses in Ref. [73]. Furthermore, the shaper has the ability to imprint virtually any desired phase onto the pulse.

This chapter is organised as follows: In Sec. III. 2, principles of the d-scan method and pulse shaping are explained. A focus is set on pulse shaping with acousto-optic modulators. Sec. III. 3 presents details on the experimental setup. Sec. III. 4 gives an overview over the methods used to test the capabilites of the setup. The results for phase characterisation and phase shaping are given in Sec. III. 5. This section consists of two parts: First, the general viability of the d-scan implementation is demonstrated by correct retrieval of the phases of substrates that introduce GDDs of different signs. The pulses for this proof of principle demonstration are rather narrowband and are centred around 4.8 μm. In the second part of the results section III. 5, d-scan is applied to broadband pulses around 3.2 μm. For the broadband pulses, compression, phase shaping and retrieval is demonstrated. The broadband pulses are compressed below 50 fs autocorrelation (FWHM) and the imprinted test phases are of different complexity. The results on the broadband pulses have also been published in Ref. [74]. A discussion of the results for the broadband pulses follows in Sec. III. 6. At the end, a conclusion summarises the major findings of the chapter.

III. 2 <u>Theory</u>

III. 2.1 <u>Representation of a laser pulse</u>

As starting point, a mathematical descripton of a laser pulse is presented. The representation presented in this section is based on the description given in Refs.[1] [64, 75-77].

A laser pulse can be described by the temporal evolution of its electric field $E(t)$ at a fixed point in space[2]. If a perfect, sufficiently fast detector existed, that detector could be placed at this spot and could measure the oscillations of $E(t)$. Thus, $E(t)$ is a real valued function of time. The Fourier transform of the electric field in the time domain gives an equivalent description of the pulse in the frequency domain:

---

[1] When comparing the representation of a laser pulse given in different references, care needs to be taken of the convention used in the respective reference. Especially the sign in the exponential of the Fourier transform or the sign of the spectral phase are common candidates to switch between different references.

[2] Here, a linearly polarised pulse is considered and thus $E(t)$ is treated as a scalar quantity.

$$\tilde{E}(\omega) = \mathcal{F}\{E(t)\} = \int_{-\infty}^{\infty} E(t)e^{i\omega t}dt. \tag{III.1}$$

The tilde in $\tilde{E}(\omega)$ denotes that $\tilde{E}(\omega)$ is a complex quantity. Conversely can $E(t)$ be obtained from $\tilde{E}(\omega)$ by inverse Fourier transformation:

$$E(t) = \mathcal{F}^{-1}\{\tilde{E}(\omega)\} = \frac{1}{2\pi} \int_{-\infty}^{\infty} \tilde{E}(\omega)e^{-i\omega t}d\omega. \tag{III.2}$$

The representation of the pulse in the frequency domain is useful, as quantities in the frequency domain are often more easily accessible for measurement or manipulation than quantities in the time domain. Since $E(t)$ is a real valued function, its Fourier transform $\tilde{E}(\omega)$ is Hermitian, i.e. $\tilde{E}^*(\omega) = \tilde{E}(-\omega)$ (* denotes complex conjugation). This also implies that $\tilde{E}(\omega)$ has non-vanishing components for $\omega < 0$.
It might be convenient to consider only the frequency components with $\omega > 0$, especially if one thinks about a measured spectrum (no one can measure a spectrum at negative frequencies or wavelengths). In this case, one can split $\tilde{E}(\omega)$ into its negative and positive frequency components

$$\tilde{E}(\omega) = \tilde{E}^+(\omega) + \tilde{E}^-(\omega) \tag{III.3}$$

with

$$\tilde{E}^+(\omega) = \begin{cases} \tilde{E}(\omega) & for\ \omega \geq 0 \\ 0 & for\ \omega < 0 \end{cases} \qquad \tilde{E}^-(\omega) = \begin{cases} 0 & for\ \omega \geq 0 \\ \tilde{E}(\omega) & for\ \omega < 0 \end{cases}$$

The inverse Fourier transforms of $\tilde{E}^+(\omega)$ and $\tilde{E}^-(\omega)$ are labelled $\tilde{E}^+(t)$ and $\tilde{E}^-(t)$, respectively. $\tilde{E}^+(t)$ and $\tilde{E}^-(t)$ are now complex valued functions and are complex conjugates of each other: $[\tilde{E}^+(t)]^* = \tilde{E}^-(t)$. The real valued, in principle measurable electric field $E(t)$ can be derived from these complex valued quantities by

$$E(t) = \tilde{E}^+(t) + \tilde{E}^-(t)$$
$$= 2\,\mathrm{Re}\{\tilde{E}^+(t)\}$$
$$= 2\,\mathrm{Re}\{\tilde{E}^-(t)\}. \tag{III.4}$$

As complex valued quantities, the representations of the pulse in the time and frequency domain can be written as product of their respective amplitude $|\tilde{E}^+|$ and phase φ

$$\tilde{E}^+(t) = |\tilde{E}^+(t)| \cdot e^{-i\varphi(t)}$$
$$= |\tilde{E}^+(t)| \cdot e^{-i\varphi_0} \cdot e^{-i\omega_0 t} \cdot e^{-i\varphi_a(t)}, \tag{III.5}$$

$$\tilde{E}^+(\omega) = |\tilde{E}^+(\omega)| \cdot e^{i\varphi(\omega)}. \tag{III.6}$$

The temporal phase $\varphi(t)$ is composed of the so-called carrier-envelope-phase φ_0, the phase introduced by the carrier frequency ω_0, and an additional time dependent phase $\varphi_a(t)$. $\varphi_a(t)$ describes variations of the frequency in time and is responsible for changes of the pulse shape, such as temporal broadening of the pulse.

In the frequency representation, the modulus $\left|\tilde{E}^+(\omega)\right|$ can be determined from a measurement of the spectrum, as it is proportional to the square root of the spectral intensity $I(\omega)$: $\left|\tilde{E}^+(\omega)\right| \propto \sqrt{I(\omega)}$.

Hence, information about the spectral amplitude $\left|\tilde{E}^+(\omega)\right|$ and phase $\varphi(\omega)$ equals to full knowledge about the temporal evolution of the pulse.

As $\tilde{E}^+(\omega)$ and $\tilde{E}^+(t)$ are linked via Fourier transforms, their bandwidths are not independent of each other, but are related via the time-bandwidth product

$$\Delta\tau_p \Delta\omega_p \geq 2\pi c_B. \tag{III.7}$$

τ_p denotes the pulse length, i.e. FWHM of the pulse intensity ($I(t) \propto |E(t)|^2$), $\Delta\omega_p$ is the FWHM of the spectral bandwidth $I(\omega)$ and c_B is a constant that depends on the shape of the spectrum. For a Gaussian pulse for example, $c_B = 0.441$. Equality in Eq. III.7 is reached for a so-called transform-limited (TL) pulse. A TL pulse has the shortest possible duration for
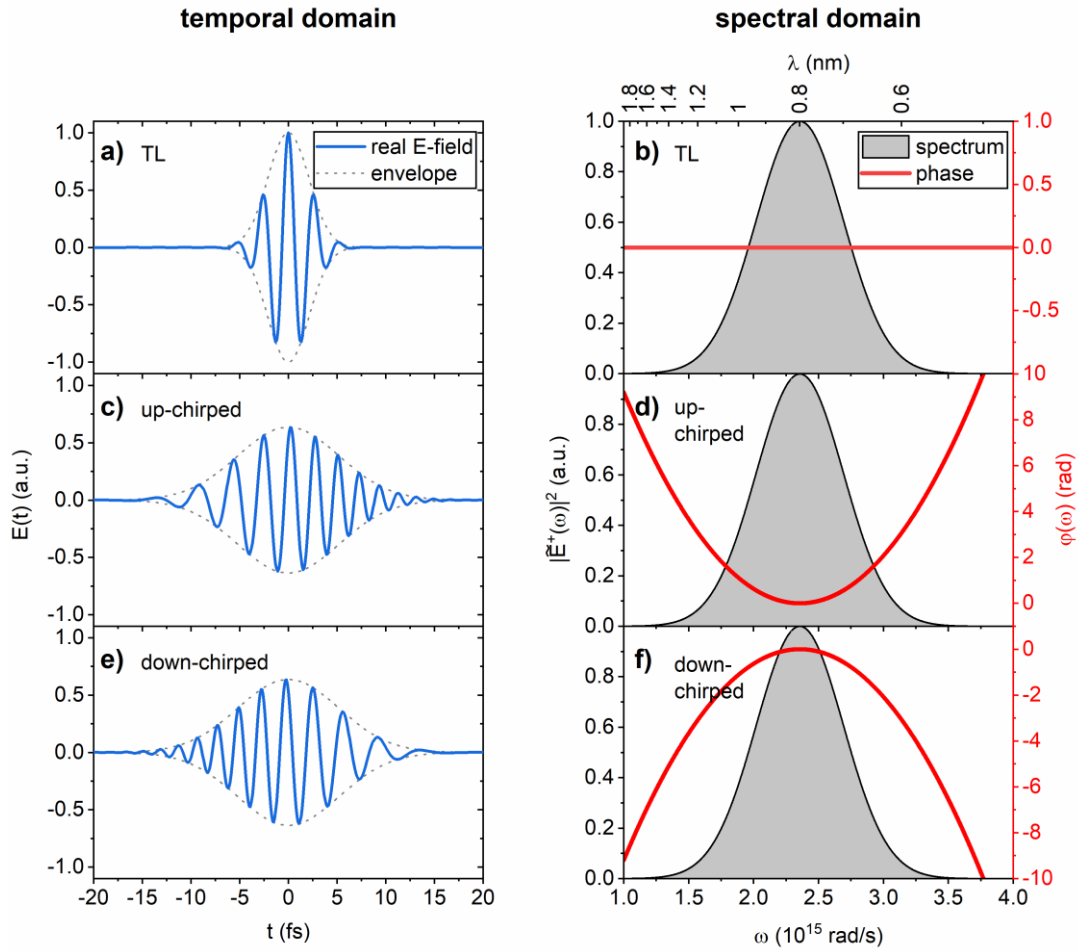
Figure III.1: *Pulses with different spectral phases represented in the time and frequency domain. Left column: representation in the time domain, right column: representation in the frequency domain. a), b) Transform-limited (TL) pulse, c), d) pulse with positive spectral phase ('up-chirped'), e), f) pulse with negative spectral phase ('down-chirped'). Note that the spectra for all three pulses are the same, but the pulses differ in spectral phase. The chirped pulses are stretched in time compared to the TL pulse. Furthermore, the instantaneous frequency changes from low to high for the up-chirped pulse and from high to low for the down chirped pulse.*

a given spectrum. As can also be seen from Eq. III. 7, the larger the spectral bandwidth, the shorter the pulse can theoretically be.

The different forms of representation in time and frequency domain are illustrated in Fig. III.1. There, three pulses with the same Gaussian spectrum, but different spectral phases are shown in both domains. For a given spectrum, a flat phase provides the shortest pulse, i.e. a TL pulse (cf. Fig. III.1 a), b)). For a TL pulse, all frequencies arrive at the same time and the frequency $\omega(t)$ is constant over the whole pulse duration (Fig. III.1 a)). Adding a quadratic phase $\varphi(\omega)$ to the pulse leads to stretching of the pulse in time (Fig. III.1 c) and d)). Furthermore, the instantaneous frequency within the pulse changes: For the pulse with positive spectral phase (so-called up-chirped pulse), the low frequencies precede the high frequencies and vice versa for down-chirped pulses with $\varphi(\omega) < 0$.

In general, the delay of a certain frequency component within the spectrum can be obtained from the spectral phase $\varphi(\omega)$ via the group delay $T_g(\omega)$

$$T_g(\omega) = \frac{\partial \varphi(\omega)}{\partial \omega}. \tag{III.8}$$

In a similar manner, the instantaneous frequency $\omega(t)$ is derived from the temporal phase $\varphi(t)$ via

$$\omega(t) = \frac{\partial \varphi(t)}{\partial t} = \omega_0 + \frac{\partial \varphi_a(t)}{\partial t}. \tag{III.9}$$

It is often appropriate to express the spectral phase as a Taylor expansion around some spectral centre frequency ω_0:

$$\begin{aligned}
\varphi(\omega) &= \sum_{m=0}^{\infty} \frac{1}{m!} \frac{\partial^m \varphi(\omega)}{\partial \omega^m}\bigg|_{\omega_0} \cdot (\omega - \omega_0)^m \\
&= \varphi(\omega_0) + \varphi'(\omega_0)(\omega - \omega_0) \\
&\quad + \frac{1}{2}\varphi''(\omega_0)(\omega - \omega_0)^2 \\
&\quad + \frac{1}{6}\varphi'''(\omega_0)(\omega - \omega_0)^3 + \cdots
\end{aligned} \tag{III.10}$$

- $\varphi(\omega_0)$ is the negative of the carrier-envelope phase φ_0 in temporal domain from Eq. III.5 ($\varphi_0 = -\varphi_0(\omega_0)$) and describes the relative shift in time between pulse envelope and carrier wave.

- The linear phase $\varphi'(\omega_0)$ corresponds to a shift of the pulse envelope in time.

- $\varphi''(\omega_0) = \frac{\partial^2 \varphi(\omega)}{\partial^2 \omega}\big|_{\omega_0} = \frac{\partial T_g(\omega)}{\partial \omega}\big|_{\omega_0}$ is called group delay dispersion (GDD) or chirp.

- $\varphi'''(\omega_0)$ is the third-order dispersion (TOD). A pulse with TOD exhibits post- (pre-) pulses in the time domain for TOD > 0 (TOD < 0).

$\varphi_0(\omega_0)$ and $\varphi'(\omega_0)$ do not change the temporal pulse envelope. Therefore the focus in this work will be on second and higher order dispersion terms. $\varphi''(\omega_0), \varphi'''(\omega_0)$, etc. have units of fs^2/rad, fs^3/rad^2, ... , but those are commonly abbreviated to fs^2, fs^3, etc. [75].

III. 2.2 Pulse shaping in the frequency domain

Controlled manipulation of an ultrafast laser pulse's shape is mostly done in the frequency domain, since any electronic device is orders of magnitude too slow to be controlled on the femtosecond time scale. The spectral domain, however, is much better accessible to the experimentalist and - as has been outlined in the previous section - is fully equivalent to the temporal domain.

Consider a pulse $\tilde{E}_{in}^+(\omega)$ entering some system with spectral transfer function $\tilde{H}(\omega) = \left|\tilde{H}(\omega)\right| \cdot e^{i\varphi_{sys}(\omega)}$. The pulse $\tilde{E}_{out}^+(\omega)$ after transmission through the system can be written as [78]

$$\tilde{E}_{out}^+(\omega) = \tilde{H}(\omega) \cdot \tilde{E}_{in}^+(\omega) = \left|\tilde{H}(\omega)\right| \cdot e^{i\varphi_{sys}(\omega)} \cdot \tilde{E}_{in}^+(\omega). \qquad (\text{III.}11)$$

An easy to implement method to manipulate the pulse shape is to send the pulse through some dispersive material. The phase introduced by propagation through a transparent dispersive medium of length L and refractive index $n(\omega)$ is

$$\varphi_{sys}(\omega) = k(\omega) \cdot L = \frac{\omega}{c} n(\omega) \cdot L, \qquad (\text{III.}12)$$

where $k(\omega) = \frac{2\pi}{\lambda}$ denotes the wavenumber and c the speed of light in vacuum. Second and higher order dispersion stretch an originally TL pulse in time. However, the degree of control over the pulse shape via propagation through substrates is limited.

A much more sophisticated method for pulse shaping is Fourier pulse shaping with a 4f pulse shaper [79]. The basic geometry of a 4f pulse shaper is depicted in Fig. III.2.
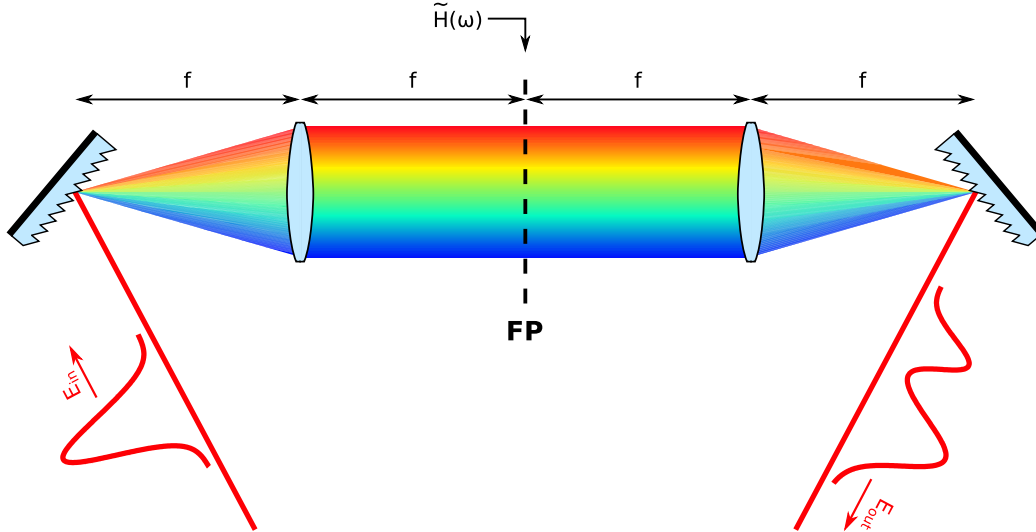
Figure III.2: *4f pulse shaper geometry. An incoming pulse E_{in} is spectrally dispersed by a diffraction grating. Each spectral component is focused by a lens on a different position in the Fourier plane (FP). A spatial light modulator placed in the FP imprints the desired shaping mask $\tilde{H}(\omega)$ on the spatially separated components of $\tilde{E}_{in}^+(\omega)$. After the FP, the spatially separated spectral components are combined again in a reversed manner as they were split. After the shaper, the output pulse E_{out} is modulated. The distance grating $\leftrightarrow$ lens and lens $\leftrightarrow$ FP is the focal length f of the lens, each. Often the lenses are replaced by reflective optics to avoid additional dispersion or chromatic aberrations introduced by the lenses.*

A 4f pulse shaper consists of a diffraction grating that disperses the different frequencies of the incoming pulse, followed by a lens at distance f (the focal length of the lens) from the grating. The lens focuses each frequency of the incoming pulse onto a different position in the focal plane. From Fourier optics one knows that the electric field in the focal plane corresponds to the Fourier transform of the incoming field [46]. That is why the focal plane in a 4f setup is called the Fourier plane (FP). In the FP, a spatial mask can imprint the desired spectral transfer function $\tilde{H}(\omega)$ onto the spatially separated Fourier components of the incoming field $\tilde{E}_{in}^{+}(\omega)$. Such a spatial mask can be realized e.g. by a liquid crystal spatial light modulator or an acousto-optic modulator (AOM). After the FP, another lens and grating are arranged in reversed order to perform an optical inverse Fourier transformation. The output pulse after the second grating is thus modulated according to the mask in the FP.

Depending on the application, the grating might be replaced by other dispersive elements, e.g. a prism, and the lens by other focusing elements, such as a curved mirror.

In a perfect 4f pulse shaper, the spectral resolution is infinitely high. However, in real systems, the spectral resolution is limited either by the smallest spatial features of the mask in the FP or by the finite focal spot size of each frequency component in the FP. The finite spectral resolution results in a maximum time window of the shaped pulse in which the features of the perfect mask (which corresponds to infinite-resolution) can be accurately reflected. Thus, this time window sets an upper bound for the time duration or delay of the shaped pulse. Under the assumption that it is the focal spot size that limits the spectral resolution and that the spatial profile of the beam is Gaussian, the FWHM length of that time window T is given by [78]:

$$T = \frac{4\alpha\sqrt{\ln 2}}{w_0} = \frac{2\sqrt{\ln 2}\, w_{in}\lambda_0}{cd\, cos\theta_{in}} \qquad with\ \alpha = \frac{\lambda_0^2 f}{2\pi cd\, cos\theta_d}. \qquad (III.13)$$

Here, α is the spatial dispersion across the FP (unit cm (rad/s)$^{-1}$), w_0 the radius of the focused beam at the FP, w_{in} the radius of the input beam before the first grating, c the speed of light, d the period of the grating, λ_0 the central wavelength diffracted at angle θ_d from the first grating and θ_{in} is the angle of the incoming beam with respect to the first grating.

III. 2.3 Acousto-optic modulator

An AOM consists of a crystal of optically transparent material with a piezo-electric transducer placed at one end and an acoustic absorber at the opposite end (Fig. III.3). The piezo-electric transducer is driven by a radio frequency (RF) signal and transforms the RF signal into an acoustic wave which propagates along the device with velocity v_{ac}. The absorber at the opposite end prevents the formation of acoustic standing waves. The sound wave induces a refractive index modulation via the photo-elastic effect. A laser beam that impinges on the device is diffracted by the refractive index modulation caused by the acoustic wave. For sufficiently large interaction region between acoustic and optical wave, the AOM operates in the thick grating regime, also known as Bragg regime. The Bragg regime is characterised by high diffraction efficiency and angular selectivity [78]. In the following, a closer look is taken on AOM operation in the Bragg regime.
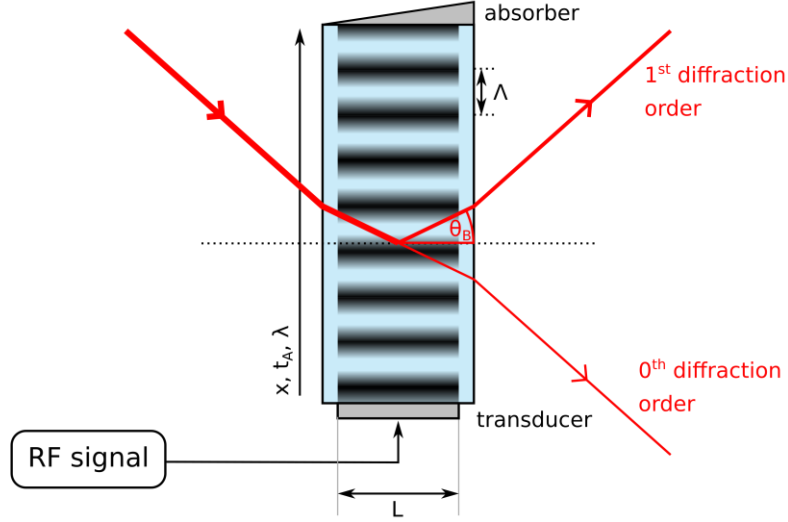
Figure III.3: *Scheme of an AOM. A transducer transforms an RF signal into an acoustic wave that propagates along the AOM crystal. An incoming light beam is diffracted at Bragg angle θ_B by the refractive index modulation induced by the traveling acoustic wave. The phase and amplitude of the RF signal is thus transferred onto the light beam. For illustrational purposes, the magnitude of θ_B is strongly exaggerated.*

Significant diffraction of the light wave from the acoustic wave only occurs if the Bragg condition is fulfilled, i.e. if the angle of incidence of the light corresponds to the Bragg angle θ_B. θ_B (inside the medium) is given by [46]

$$\sin \theta_B = \frac{\lambda_m}{2\Lambda} = \frac{\lambda_0}{2n\Lambda} = \frac{\lambda_0 f_{ac}}{2nv_{ac}}. \tag{III.14}$$

λ_m and λ_0 are the optical wavelength in the medium and in free space, respectively. Λ is the acoustic velocity in the medium, f_{ac} the acoustic frequency and n the refractive index of the medium.

Whether the interaction region between acoustic and optical wave is large enough for the AOM to operate in the Bragg regime is quantified by the Q parameter [80]

$$Q = \frac{2\pi\lambda_m L f_{0,ac}^2}{v_{ac}^2} = \frac{2\pi\lambda_m L}{\Lambda^2}. \tag{III.15}$$

L is the thickness of the interaction region between optical and acoustic wave, $f_{0,ac}$ the centre RF frequency. For $Q \geq 4\pi$, the AOM operates in the Bragg regime [80].

The acoustic wave $\mathcal{A}(t_A)$ can be written as function of the time t_A it takes for the acoustic wave to propagate to position $x(t_A)$ along the AOM aperture [81]

$$\mathcal{A}(t_A) = a(t_A) \cdot \sin\big(\Phi_A(t_A)\big) = a(t_A) \cdot \sin\left(2\pi f_{0,ac} t_A + \Psi_A(t_A)\right). \tag{III.16}$$

Phase $\Phi_A(t_A)$ and amplitude $a(t_A)$ of the acoustic wave, i.e. of the RF signal, are transferred onto the diffracted optical wave [46, 80]. As in a 4f pulse shaper different optical frequencies correspond to different positions $x(\omega)$ along the AOM aperture, a proper scaling between aperture position and optical frequency allows a mapping between phase and amplitude of the acoustic wave and the desired transfer function $\tilde{H}(\omega) = |\tilde{H}(\omega)| \cdot e^{i\varphi_{des}(\omega)}$ [81]

$$\varphi_{des}(\omega) = \pm\Psi_A(x(\omega)). \qquad \text{(III. 17)}$$

The sign depends on whether the beam is diffracted into +1st or -1st order.[1] A method for scaling aperture position to optical frequency is shown in App. B. 1. The relation between acoustic amplitude a and $|\widetilde{H}(\omega)|$ can be approximated by [46, 80, 82]

$$|\widetilde{H}(\omega)| \propto \sin\left(\frac{\pi}{2}\frac{a}{a_{sat}}\right), \qquad \text{(III. 18)}$$

with a_{sat} the saturation acoustic amplitude leading to highest diffraction efficiency. a_{sat} depends on the AOM material and geometry. As long as the acoustic amplitude stays well below a_{sat}, $|\widetilde{H}(\omega)|$ is directly proportional to a.

The spectral resolution of an AOM based 4f pulse shaper is limited either by the minimum acoustic feature size $\Delta x_0 = \frac{v_{ac}}{\Delta f_{ac}}$, with Δf_{ac} the modulation bandwidth of the AOM [80], or by the average spot size of the corresponding optical frequency across the light-sound interaction region [78, 80]. Parameters of the AOM shaper used in this work are given in Sec. III. 3.2.

III. 2.4 Bragg angle correction mask

For efficient diffraction of light by an AOM, the Bragg condition needs to be satisfied with the Bragg angle θ_B inside the AOM medium given by Eq. III. 14. θ_B translates by Snell's law into the corresponding Bragg angle in air

$$\sin\theta_{B,air} = n\sin\theta_B = n\frac{\lambda_m}{2\Lambda} = \frac{\lambda_0}{2\Lambda} = \frac{\lambda_0 f_{0,ac}}{2v_{ac}}. \qquad \text{(III. 19)}$$
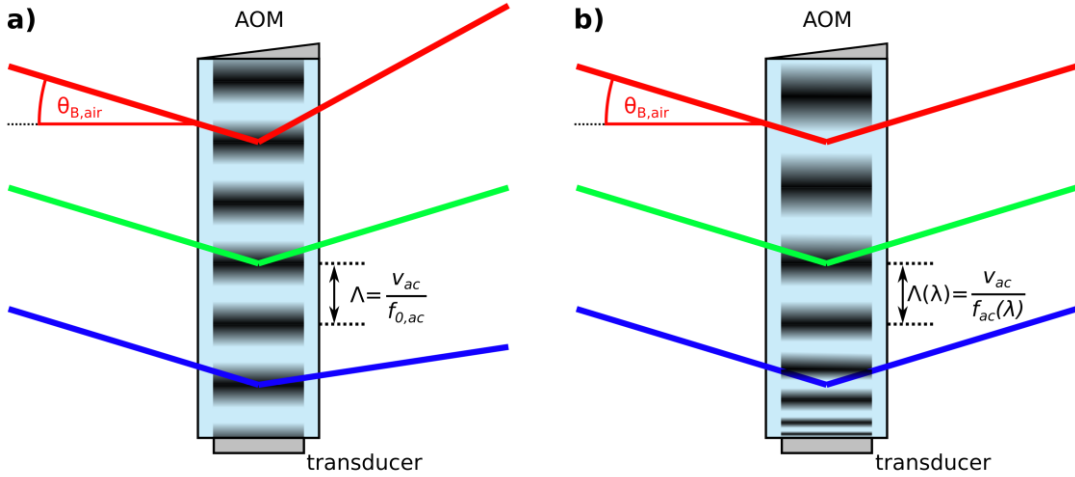
Figure III.4: *Effect of the acoustic wavelength on light diffraction from an AOM. a) A fixed acoustic wavelength leads to a dispersion of diffraction angles for the different optical wavelengths. b) If the acoustic wavelength is adapted to the optical wavelength, the same diffraction angle for all optical wavelengths can be achieved. Adapted with permission from Ref. [83].*

---

[1] In addition to the desired spectral phase $\varphi_{des}(\omega)$, also other spectral phase contributions will be imprinted on the pulse by the AOM. These additional contributions are due to the unmodulated sine wave $\sin(2\pi f_{0,ac}t_A)$, cf. Eq. III. 16, and transmission through the AOM substrate. This point will be examined in Sec. III. 6.1.

The geometry of a 4f setup imposes that all optical wavelengths impinge at the same angle at the AOM. Thus, for a fixed acoustic frequency $f_{0,ac}$, i.e. for an unmodulated sine wave, the Bragg condition can only be fulfilled for one optical wavelength λ_0 and only that wavelength exits the AOM at the same angle as it has entered it. All other wavelengths are diffracted at different angles from the AOM, as shown in Fig. III.4 a). The angular dispersion finally results in unwanted spatial dispersion of the outgoing beam after the shaper which is disadvantageous for efficient pulse shaping [81, 83]. In order to fulfill the Bragg condition for all optical wavelengths, an adapted acoustic wave needs to be applied by the transducer. This is discussed in detail in Ref. [83]. The adapted acoustic frequency ensures that the local acoustic wavelength $\Lambda(\lambda)$ matches the Bragg condition for each optical wavelength λ across the AOM aperture, see Fig. III.4 b). As the incoming angle $\theta_{B,air}$ is the same for all λ, a constant C can be defined as (cf. [83])

$$C = 2v_{ac}\sin\theta_{B,air} = \lambda_0 f_{0,ac} = \lambda f_{ac}(\lambda). \tag{III.20}$$

From this, the matching acoustic frequency is found to be

$$f_{ac}(\lambda) = \frac{\lambda_0 f_{0,ac}}{\lambda}. \tag{III.21}$$

The Bragg angle corrected waveform that is put on the AOM is thus (cf. [83])

$$\mathcal{A}(t_A) = a(t_A) \cdot \sin\big(\phi(t_A) + \Psi_A(t_A)\big) \tag{III.22}$$

with

$$\phi(t_A) = \phi_0 + 2\pi \int_0^{t_A} f_{ac}\big(\tau(\lambda)\big)d\tau. \tag{III.23}$$

The variables denote the same quantities as in Eq. III. 16. ϕ_0 is an initial phase and can be chosen for example so that the acoustic phase of the central wavelength λ_0 vanishes, i.e. $\phi\big(t_A(\lambda_0)\big) = 0$. The mapping $\lambda \leftrightarrow \tau(\lambda)$ is done via v_{ac} and the position vs. frequency calibration presented in App. B. 1.
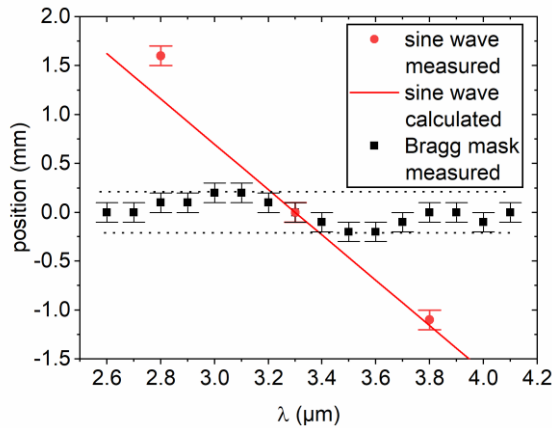
Figure III.5: *Effect of the Bragg angle correction mask on the position of various spectral components at the second grating of the shaper. The scattered points display data measured by a beam profiler. The variation in position for the Bragg mask is 0.4 mm, as indicated by the horizontal dotted lines. The thin red solid line is a calculation for the acoustic unmodulated sine wave based on ray optics. Details on this calculation are given in App. B. 2.*

Fig. III.5 displays the effect of a Bragg angle correction mask on the position of various spectral components for the pulse shaper used in this work. The figure shows that the spatial dispersion is strongly reduced by application of a Bragg mask compared to a pure sine wave.

III. 2.5 Dispersion scan

A laser pulse is completely described by its representation in the spectral domain $\tilde{E}^+(\omega) = |\tilde{E}^+(\omega)| \cdot e^{i\varphi(\omega)}$, cf. Sec. III. 2.1. For the d-scan technique, the retrieval of the phase $\varphi(\omega)$ is based on the addition of several *known* spectral phases $\phi_j(\omega)$ onto the pulse to be characterised, subsequent generation and recording of the second harmonic (SH) spectra[1] for each imprinted dispersion $\phi_j(\omega)$. In this way, a two-dimensional d-scan trace is obtained, as shown in Fig. III.6.

Assuming a flat spectral response of all involved components, the measured SH spectrum is proportional to [68]

$$S(\omega, \phi_j) = |\mathcal{F}\{E_{SH}(t)\}|^2$$

$$= \left| \mathcal{F}\left\{ \left(\mathcal{F}^{-1}\{|\tilde{E}^+(\omega)| \cdot e^{i\varphi(\omega)} \cdot e^{i\phi_j(\omega)}\} \right)^2 \right\} \right|^2. \tag{III. 24}$$

In the above expression $E_{SH}(t)$ is the electric field of the SH in the time domain, which is simply the squared field of the FW spectrum in time domain. The latter is given by an inverse Fourier transform of the original field in the frequency domain modulated by the phase $\phi_j(\omega)$.

In order to retrieve $\varphi(\omega)$, a simulated d-scan trace $S_{sim}(\omega_i, \phi_j)$ is fitted to the measured d-scan trace $S_{meas}(\omega_i, \phi_j)$. The spectra are usually not given as a continuous function of ω, but only on a set of descrete angular frequencies ω_i. For the calculation of $S_{sim}(\omega_i, \phi_j)$, the dependency of the SH spectrum on $\varphi(\omega_i)$, as presented in Eq. III. 24, is taken into account and $\varphi(\omega_i)$ is appropriately parameterised. The spectral amplitude $|\tilde{E}^+(\omega)| \propto \sqrt{I(\omega)}$ is not fitted, but determined via an independent measurement of the FW intensity spectrum $I(\omega)$. The fit seeks to minimize the error function [68]

$$G = \sqrt{\frac{1}{N_i N_j} \sum_{i,j} [S_{meas}(\omega_i, \phi_j) - \mu_i S_{sim}(\omega_i, \phi_j)]^2}. \tag{III. 25}$$

N_i and N_j are the number of frequency points per SH spectrum and the number of applied known phases, respectively. The parameter μ_i accounts for the spectral response of the system. It is updated at each iteration of the fitting procedure and is given by

$$\mu_i = \frac{\sum_j S_{meas}(\omega_i, \phi_j) S_{sim}(\omega_i, \phi_j)}{\sum_j S_{sim}(\omega_i, \phi_j)^2}. \tag{III. 26}$$

The AOM shaper-based d-scan implementation employed in this work is described in the next section.

---

[1] In principle, also other nonlinear generation processes than SH generation can be employed, such as third harmonic generation [84] or self-diffraction [85]. However, SH generation is the most common method used for d-scan.
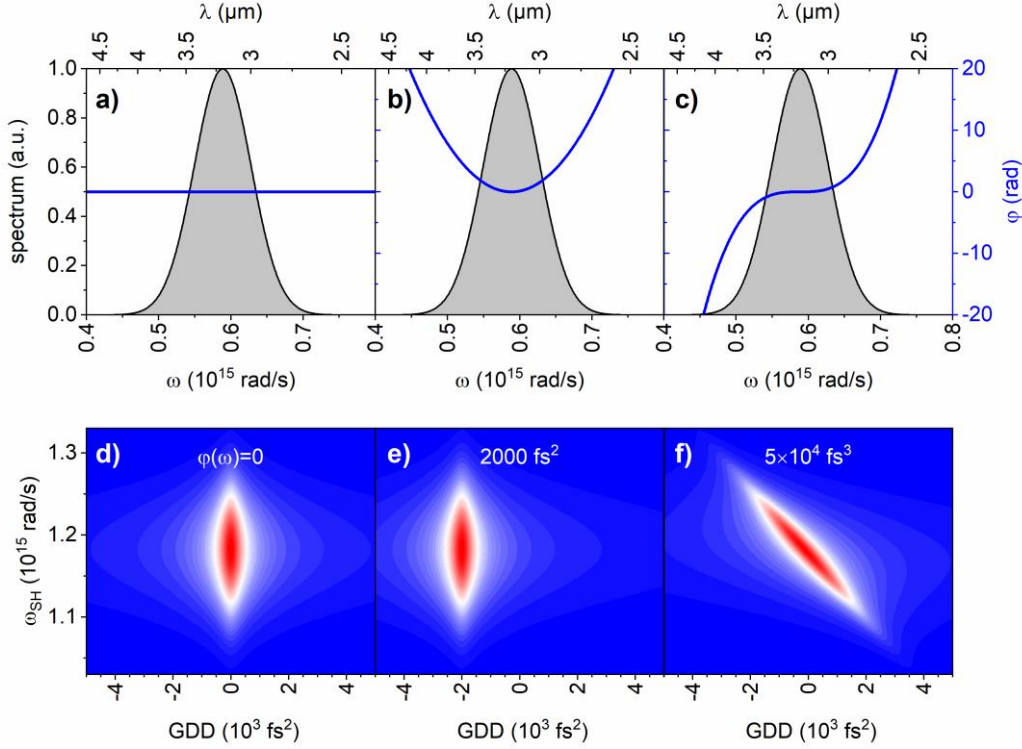
Figure III.6: Top row: Pulses with same spectrum (grey shaded), but different spectral phases $\varphi(\omega)$ (blue). Bottom row: D-scan traces of the pulses in the top row. The pulse with the flat phase gives a signal centred around zero GDD (a) and d)), a pure second order phase shifts the signal to the corresponding opposite GDD (b) and e)) and a TOD leads to a tilt of the trace (c) and f)). In the shown case, the imprinted known spectral phases $\phi_j(\omega)$ are pure second order GDDs. The d-scan traces were simulated with the lab2 package [86].

III. 2.6 AOM shaper-based d-scan

In this work, d-scan is realised with an AOM pulse shaper. Fig. III.7 displays the working principle of the shaper based d-scan. The pulse shaper imprints some phase ϕ_{AOM} onto the incoming unshaped pulse. The shaped pulse has a phase φ. In the example depicted in Fig. III.7, ϕ_{AOM} just cancels the initial phase of the incoming pulse, so the shaped pulse has a flat phase. In order to perform d-scan, the shaper also imprints a set of pure quadratic phases $\phi_j(\omega)$ around a centre frequncy ω_0

$$\phi_j(\omega) = \frac{1}{2} c_j (\omega - \omega_0)^2 \qquad (III.\,27)$$

onto the shaped pulse. For each of the $\phi_j(\omega)$, the SH spectrum is measured and in this way, a d-scan trace is obtained.

The shaper-based variant of d-scan is also called chirp scan. Implementations of chirp scan in the NIR and Vis spectral region are reported in Refs. [73, 87].
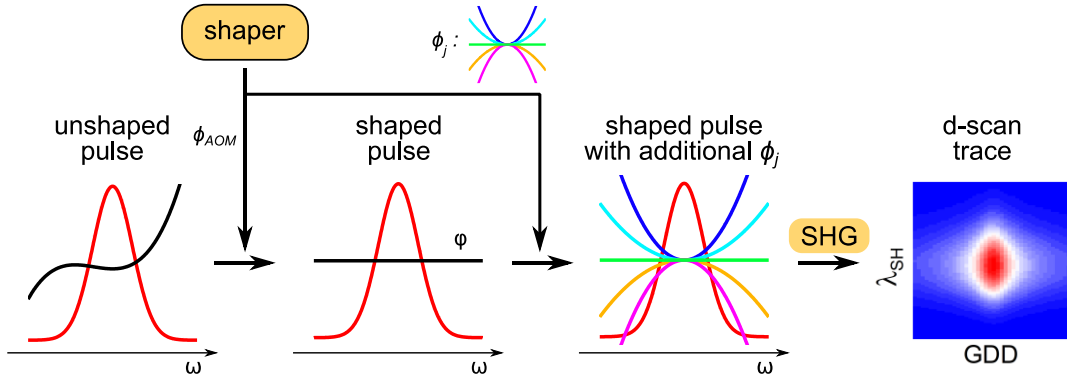
Figure III.7: *Schematics of the shaper-based d-scan. The AOM shaper imprints a phase ϕ_{AOM} onto an initially unshaped pulse. The shaped pulse has a spectral phase φ. In addition to ϕ_{AOM}, the shaper also imprints several quadratic phases ϕ_j onto the shaped pulse for d-scan characterisation (represented by the parabolas of different colours). Taking SH spectra for the various ϕ_j gives the d-scan trace. The separation between ϕ_{AOM} and ϕ_j is done to show the conceptual difference between them; in the experiment, both are imprinted in the same device as $\phi_{AOM} + \phi_j$. Reproduced with permission from Ref. [74].*

The recorded d-scan trace, together with an independently measured spectrum of the fundamental wavelength, is evaluated by a retrieval algorithm[1] in order to determine the spectral phase φ of the shaped pulse. In the present work, the retrieval algorithm almost exclusively uses a Nelder-Mead algorithm [88] to minimise the G-error. $\varphi(\omega)$ is parameterised by its values at certain frequencies and $\varphi(\omega)$ is obtained by a spline interpolation in between those frequency knots. At first, the spacing of the frequency knots is coarse, and only the coarsely spaced frequency knots are optimised by the fit. When the algorithm converges or gets stuck, the spacing between the frequency knots is decreased, cf. Ref. [89].

If the measured d-scan trace shows features that are indicative of a Taylor phase, such as shift, tilt or curvature of the trace [73], $\varphi(\omega)$ is first parameterised by a Taylor series with 40 coefficients to get a first estimation for the phase. As soon as the retireval algorithm stagnates or converges for the Taylor representation, the phase is parameterised by its values at a set of certain frequencies and the procedure outlined above takes place. In this manner, deviations from a pure Taylor phase can be represented as well.

III. 2.7 Shaper-based autocorrelation

By application of the mask

$$\widetilde{H}(\omega) = \cos\left(\frac{\omega\tau}{2}\right) = \left|\cos\left(\frac{\omega\tau}{2}\right)\right| \times \exp\left\{i \cdot \underbrace{\arg\left[\cos\left(\frac{\omega\tau}{2}\right)\right]}_{0\ or\ \pi}\right\} \qquad \text{(III. 28)}$$

the AOM pulse shaper generates two replicas of the input pulse separated by time τ [90]. Double pulse creation thus involves both amplitude and phase modulation of the input

---

[1] A Python code for pulse retrieval was written in our group. The code was mainly developed by Niklas Müller and modified by myself.

pulse. By variation of τ, the created double pulses can be readily used to record a collinear interferometric autocorrelation trace (ACT) with the signal of the generated SH [75, 91, 92]:

$$
\begin{aligned}
I(\tau) &= \int_{-\infty}^{\infty} |[E(t) + E(t - \tau)]^2|^2 \, dt \\
&= \int_{-\infty}^{\infty} |2A^4(t) + 4A^2(t)A^2(t - \tau) \\
&\quad + 4A(t)A(t - \tau)[A^2(t) + A^2(t - \tau)] \cos[\omega\tau + \varphi_a(t) - \varphi_a(t - \tau)] \\
&\quad + 2A^2(t)A^2(t - \tau) \cos[2\{\omega\tau + \varphi_a(t) - \varphi_a(t - \tau)\}]| \, dt.
\end{aligned}
$$

$$\text{(III. 29)}$$

$A(t)$ is the electric field's envelope with $E(t) = A(t) \cos\big(\omega_0 t + \varphi_a(t)\big)$. The peak ($\tau = 0$) to background ($\tau = \infty$) ratio for the interferometric ACT is 8:1. By filtering out the cosine terms in Eq. III. 29, one gets the expression for an intensity ACT with a peak to background ratio of 3:1.

As in the double pulse creation also amplitude modulation is involved, good care was taken to operate the AOM in the linear regime when taking shaper-based interferometric ACTs, cf. Sec. III. 2.3. Furthermore, the correct separation τ between the pulses was independently confirmed by autocorrelation measurements with an autocorrelator using a mechanical delay stage.

III. 2.8 Evolutionary algorithm

Evolutionary algorithms are a means to optimise the outcome of an experiment, even if there is only little knowledge about the underlying mechanisms that lead to the desired outcome. An evolutionary algorithm requires a suitable feedback signal to quantitatively judge the experimental outcome in order to adjust the control quantity. That control quantity might be for example the phase of a laser pulse and the success of the experiment
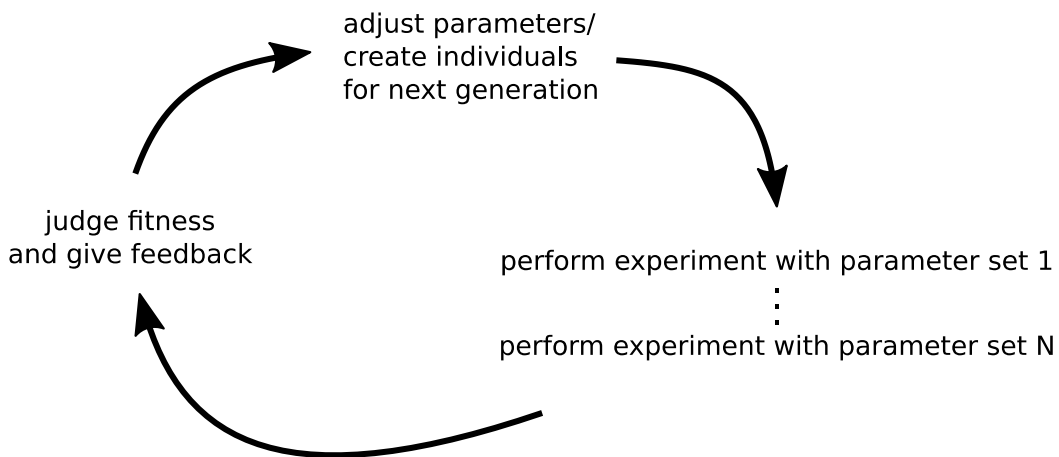
Figure III.8: *Working principle of an evolutionary algorithm. A set of N parameters, i.e. N individuals, form a generation. Each parameter set is tested by the experiment. The experimental outcome is judged by its fitness with respect to the desired outcome. The individuals of the next generation are created on basis of the fittest individuals from this judgement and the whole procedure is repeated.*

might be judged by the strength of the pulse's SH signal. Evolutionary algorithms mimic biological evolution. A set of parameters is used to describe the control quantity. Each set of parameters is called an "individual" and several individuals make up a "generation". The experiment is then performed multiple times, each time with a different set of parameters of the control quantity, i.e. a different individual, in action. Each individual of a generation is thus tested and judged by its fitness concerning the desired experimental outcome [93]. The best, i.e. fittest, individuals are the starting point for the next generation. Fig. III.8 shows a scheme of the described procedure.

In this work, an evolutionary algorithm is employed to find the phase of the spectral wings of the broadband MIR pulses. The SH signal serves as feedback and the pulse shaper is used to test several phases [93, 94].

For determination of the phase of the spectral wings by the evolutionary algorithm (blue and red wing separately), only the spectral fraction of interest transmits the shaper and generates the SH signal, all other spectral parts are blocked by the pulse shaper. The spectral phase is parameterised by a third order Taylor expansion and optimal values for GDD and TOD are sought, the central frequency is set to the centre of gravity of the respective spectral wing. The spectral wings that are optimised by the evolutionary algorithm have a small spectral overlap with the region that is characterised by d-scan. By comparison of the phases found in that overlap region with both d-scan and evolutionary algorithm, a linear phase can be determined to properly concatenate the phases of the central region - determined by d-scan - and the spectral wings - determined by the evolutionary algorithm. In order to avoid kinks, the concatenated phase is smoothed by a Savitzky-Golay filter. More details on the implementation of the evolutionary algorithm are given in App. B. 3.

III. 3   Experimental details

III. 3.1 Optical setup

The setup for pulse characterisation and shaping of the broadband MIR pulses centred at 3.2 µm is shown in Fig. III.9. Minor changes in the setup for the pulses centred at 4.8 µm are listed in App. B. 4. The NOPA which was presented in Ch. II acts as the source for MIR pulses. The pulses are centred around 3.2 µm and have an energy of 1.5 µJ at 1 kHz repetition rate. A periscope after the NOPA adjusts the beam height to the level of the pulse shaper and flips the MIR pulses' polarisation from vertical to horizontal. The (slightly diverging) MIR beam from the NOPA is collimated by a CaF_2 lens ($f = 515$ mm). Two mirrors in front of the pulse shaper couple the beam into the pulse shaper. The pulse shaper itself has 4f geometry with an AOM as modulating device. More details on the pulse shaper are given in Sec. III. 3.2. Phase and amplitude modulations are imprinted on the -1st diffraction order. An iris after the pulse shaper acts as spatial filter: The modulated -1st diffraction order passes through the iris, whereas unwanted diffraction orders are blocked. Additionally, a razor blade on a translation stage blocks remnants of the non-diffracted 0th diffraction order that could not be blocked by the iris. Two steering mirrors right after the shaper allow to fine adjust the pointing of the modulated beam. The pulses after the shaper have ca. 400 nJ energy. The modulated MIR beam can either be guided directly into the spectrometer for measurement of the fundamental spectrum, or be focused by a parabolic mirror ($f = 50.8$ mm) into an $AgGaS_2$ (AGS) crystal (Eksma Optics, $\theta = 39°$, $\phi = 45°$) for second harmonic generation (SHG). Before SHG in the AGS crystal, a 50 mm lithium fluoride (LiF) rod (Korth Kristalle GmbH) compensates the GDD that is imprinted on the pulse by

transmission through the AOM germanium (Ge) substrate and by the pure Bragg angle correction phase mask (cf. Ref. [81]). The LiF rod thus counteracts the GDD that is introduced by sole transmission through the "idle" shaper and that is not part of the actual intended phase modulation. Another 50 mm LiF rod is placed in the beam path for measurement of the FW spectrum to account for any wavelength dependent losses caused by transmission through the rod. After SHG in the AGS crystal, the SH beam is collimated by a CaF$_2$ lens (f = 50.0 mm) and the FW is filtered out by a shortpass filter (Laser Components, cut-off wavelength 2.3 μm). The SH beam can either be guided onto an InGaAs photodiode (THORLABS DET10D/M) to record a collinear ACT or to the spectrometer to record the spectra for d-scan. Neutral density filters (not shown in Fig. III.9) are placed before both photodiode and spectrometer to avoid saturation of the devices.
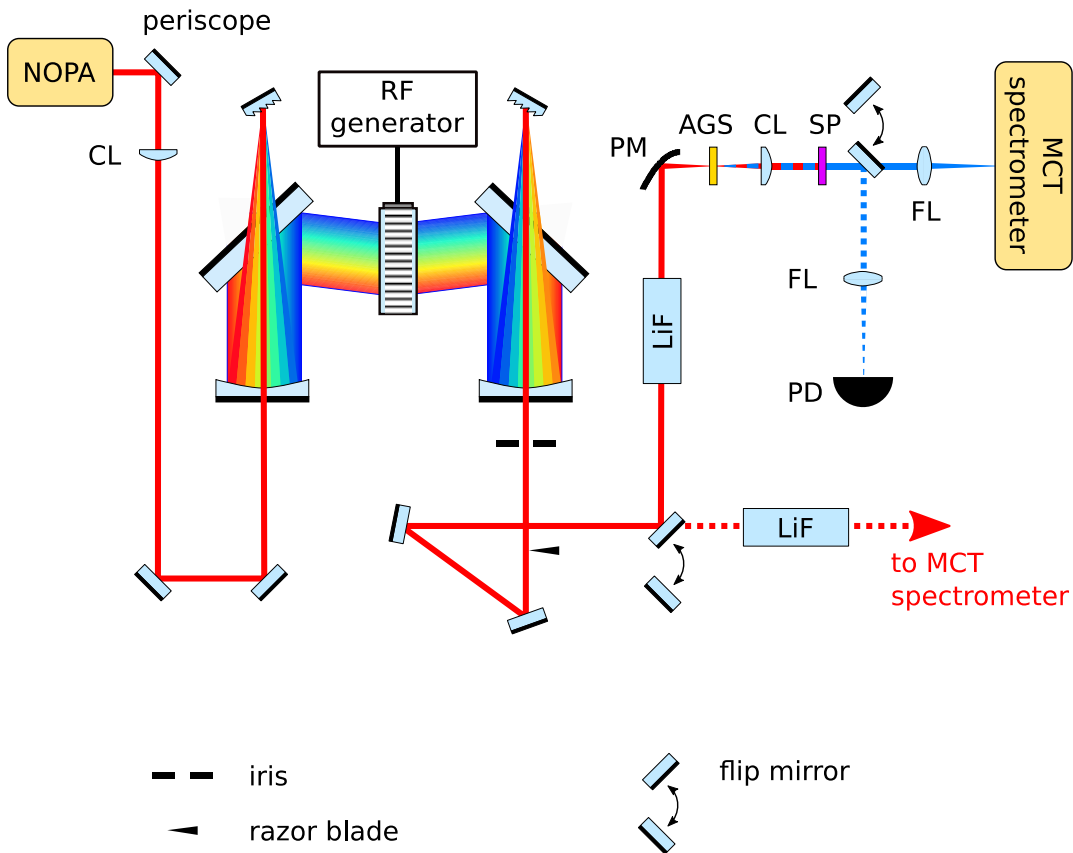
Figure III.9: *Setup for the AOM shaper based d-scan and autocorrelation measurements. The MIR beam from the NOPA is guided into the 4f pulse shaper with the AOM. After the shaper, an iris and razor blade act as spatial filters and block unwanted diffraction orders of the beam. The shaped pulse can either be guided directly to the spectrometer (dashed red line, flip mirror down) or to the AGS crystal for SHG (red solid line, flip mirror up). After SHG, the fundamental wavelength is filtered out by a shortpass filter. The SH is detected either by a spectrometer (blue solid line, flip mirror down) or by a photodiode (dashed blue line, flip mirror up). AGS: AgGaS$_2$, CL: Collimation lens, FL: Focusing lens, LiF: Lithium fluoride rod, PD: Photodiode, PM: Parabolic mirror, RF: Radio frequency, SP: shortpass filter. Adapted with permission from Ref. [74].*

The spectrometer is a spectrograph (Acton Research Corporation, SpectraPro-500i, f = 0.5 m) which employs a mercury cadmium telluride (MCT) array detector with a coated zinc selenide (ZnSe) window. The spectrograph records both the FW as well as the SH spectrum. For the FW spectrum, a 150 grooves/mm grating and for the SH a 300 grooves/mm grating is used. Both gratings are mounted on a grating turret and one can easily switch between them.

Before being fed into the retrieval algorithm, both fundamental wavelength spectrum and d-scan trace are corrected for the transmission efficiency through the system. The corrections include grating and detector efficiency of the spectrograph. For the d-scan trace, transmission through the ND and shortpass filters are considered as well. Spectral efficiency and transmission curves are provided by the manufacturers.

III. 3.2 AOM pulse shaper

The pulse shaper is set up in folded reflective 4f geometry with a Ge AOM as spatial light modulator in the Fourier plane [97, 98]. It consists of gratings with 150 grooves/mm (Richardson Gratings), 6 cm wide cylindrical mirrors with f = 170 mm and 8.5 cm wide folding mirrors. Mirrors and gratings are gold coated. This combination of optics images the

AOM material	Germanium
Active aperture	55 mm
Length of sound-light interaction region	L = 21 mm
Centre optical wavelength	λ_0 = 3200 nm
Refractive index at λ_0	$n(\lambda_0)$ = 4.04
Acoustic centre frequency	$f_{0,ac}$ = 75 MHz
Acoustic bandwidth	Δf_{ac} = 50 MHz
Sound velocity	v_{ac} = 5.50 mm/µs
Bragg angle in medium	θ_B = 0.31°
Bragg angle in air	$\theta_{B,air}$ = 1.25°
Access time	10 µs
Q parameter	Q = 6.2 π
Minimum acoustic feature size	Δx_0 = 110 µm
Average horizontal spot size across interaction region ($\frac{1}{e^2}$ diameter)	$2\overline{w}_0$ = 300 µm
Effective number of pixels over active aperture	180
Time window available for shaping	T = 3.3 ps
Maximum displacement of FP due to FP tilt	0.6 mm
Rayleigh range	z_R = 20 mm

Table III-1: *Parameters of the AOM pulse shaper. For the meaning of the given parameters, see Sec. III. 2.2 and III. 2.3. The Bragg angle θ_B refers to the central wavelength λ_0. Access time is the time it takes for an acoustic wave to propagate across the AOM aperture. For the calculation of $\overline{w}_0$ and z_R, a Gaussian spatial beam profile is assumed. $n(\lambda_0)$ is taken from Ref. [95], v_{ac} from Ref. [96].*

MIR spectrum onto the whole active aperture of the Ge AOM (ISOMET LS600-1109-10-W). The AOM is operated around 75 MHz acoustic carrier frequency and supports a frequency range of 55-105 MHz. The RF waveform is generated by an arbitrary waveform generator (AWG) with 1 GHz sampling rate (Chase Scientific Company, DA11000). Parameters for the AOM pulse shaper are summarised in Tab. III-1.

Tab. III-1 shows that the pulse shaper has effectively 180 pixels over the whole aperture, which is deduced from the average $\frac{1}{e^2}$ diameter spot size of the focused beam at the FP. This is a rather conservative estimation. Using the FWHM definition of the spot size instead, increases the number of pixels to more than 300. In either case, it is the spot size of the focused beam at the FP and not the minimum acoustic feature size Δx_0 which limits the resolution. The broadband MIR spectrum with its wings is distributed over the whole AOM aperture. The 180 effective pixels over the whole aperture correspond to ca. 70 pixels over the FWHM of the spectrum. Furthermore, the Q parameter is well above 4π and thus the AOM operates in the Bragg regime. As the AOM is tilted by the Bragg angle, the FP does not coincide with the median plane of the AOM [64]. However, comparing the maximum displacement of the FP due to that tilt with the Rayleigh range of the focused beam at the FP, reveals that the tilt does not cause a serious issue.

III. 3.2.1 Synchronization between traveling acoustic wave and optical pulse

The acoustic wave that carries the phase and amplitude information for the desired optical pulse shaping is a traveling wave, which means that it needs to be sent anew for each laser pulse. The access time of the acoustic wave (the time it takes for the acoustic wave to travel across the AOM's active aperture) is 10 µs. This implies that the timing between the acoustic wave and the laser pulse train needs to be synchronized. A scheme of that synchronization is shown in Fig. III.10: For each pulse of the laser pulse train, the regenerative amplifier laser system triggers a delay generator (DG535 by Stanford Research Systems, Inc.). This delay generator generates two more signals: A TTL gate signal to activate the RF amplifier[1] and a trigger for the AWG to generate the desired RF waveform. The RF waveform is amplified by the activated RF amplifier and the amplified RF signal generates an acoustic wave that traverses through the AOM. The duration of the RF waveform (10 µs) is set to the access time of the acoustic wave.

The 10 µs access time corresponds to an optical path length of 3 km. It is nearly impossible to delay the optical pulses by such a long distance in the lab. That is why the trigger signal sent by the laser system is delayed by ca. 990 µs to actually match the *next* laser pulse in the 1 kHz pulse train.

The timing stability between acoustic and optical waveform from pulse to pulse is limited by the 1 GHz internal clock rate of the AWG. It is better than $\frac{\lambda_{ac}}{10}$, with λ_{ac} the acoustic wavelength.

---

[1] According to the manufacturer's data sheet, the RF amplifier is not designed for cw operation and its duty cycle must not exceed 25%. The duty cycle is controlled by the RF gate pulse.
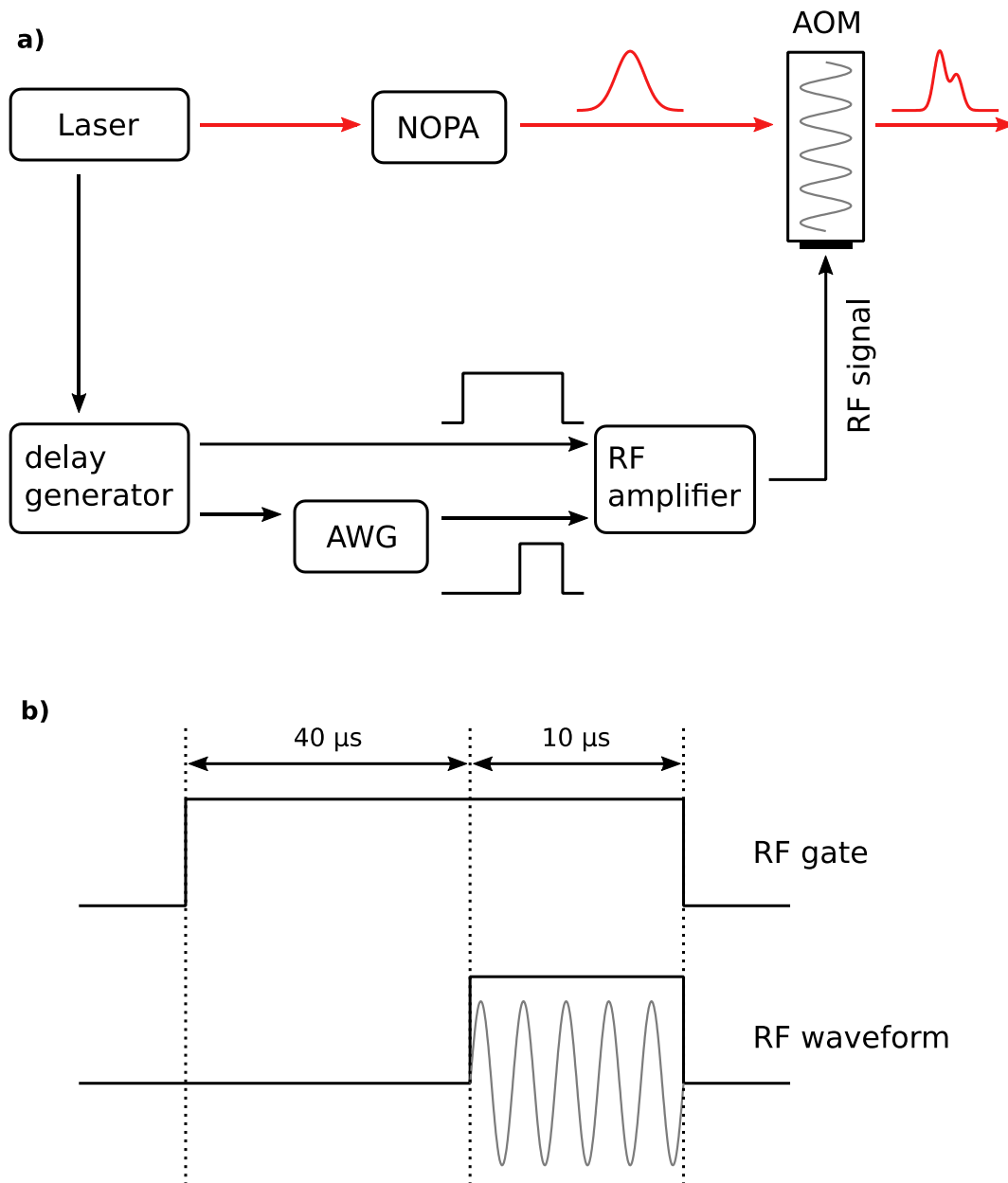
Figure III.10: *a) Scheme of the synchronization between laser pulse and acoustic wave of the modulator. Black lines denote electric signals; red lines represent the optical line. b) Close-up of the timing between RF gate and RF waveform signals that are sent into the RF amplifier. For technical reasons, the RF gate pulse needs to arrive 40 μs prior to the RF waveform. Both signals terminate at the same time. The length of the RF waveform (10 μs) corresponds to the transit time of the acoustic wave through the optical aperture of the AOM. AWG: Arbitrary waveform generator, RF: Radio frequency.*

III. 4   Methods

In order to demonstrate the capabilities of the AOM shaper-based setup, several measurements were carried out. The applicability of the shaper-based d-scan characterisation is first tested in Sec. III. 5.1 for a narrowband pulse centred at 4.8 µm. This is done by retrieving the phases introduced by Ge and LiF substrates. Ge and LiF exhibit GDDs of different signs. The phase imprinted by the substrates is independent of the phase that is added by the AOM shaper. The phases retrieved with the shaper-based d-scan are compared with the theoretically expected phases of the substrates.

After that, d-scan is applied to a broadband pulse centred at 3.2 µm. Compression of the broadband pulse is demonstrated in Sec. III. 5.2. Furthermore, in Sec III. 5.3 several spectral phases of different complexity are imprinted on a compressed broadband MIR pulse by the AOM. The imprinted spectral phases are then retrieved by the shaper-based d-scan method and the result is compared to the applied phases.

Details about the performed measurements are given below.

III. 4.1 Measurements on a narrowband pulse

The narrowband MIR pulse around 4.8 µm was roughly compressed by applying a GDD on the shaper that maximised the SH signal of the shaped pulse. For both the Ge and LiF substrates, two measurements were performed: One with the substrate in the beam path and one reference measurement without substrate. The retrieved phase of the reference measurement was fitted by a third order Taylor phase and that fit was subtracted from the substrate measurement. The difference accounts for the phase imprinted by the respective substrate and was compared to the theoretically expected phase. The latter was calculated from the refractive indices of Ge [99] and LiF [100], respectively , cf. Eq. III. 12 . The substrates used were a 50 mm Ge and a 40 mm LiF rod, respectively.

III. 4.2 Measurements on a broadband pulse

The ability of the implemented d-scan method for phase characterisation is also examined for a MIR pulse with broadband spectrum centred around 3.2 µm. The MIR pulse was compressed in the same way as described in Sec. III. 5.2 and the AOM shaper imprinted several phases on the compressed pulse. The phases of the tailored pulse were characterised by d-scan and the reconstructed phases are compared to the applied phases. For this comparison, a reference phase of the compressed pulse was subtracted from the reconstructed phases of the tailored pulse. The difference is then compared to the phase that was imprinted on the compressed pulse by the AOM shaper. The reference phase of the compressed pulse is given in App. B. 5.

III. 5   Results

III. 5.1 D-scan phase retrieval of substrates for a narrowband MIR pulse

D-scan measurements for narrowband pulses on Ge and LiF substrates are shown in Fig. III.11. The measured phase imprinted by the substrates is compared with the theoretically expected phase. Fig. III.11 c) and f) show the results for Ge and LiF, respectively. In both cases, the agreement between expected and retrieved phase is reasonably well. There are only a few single points that clearly deviate from the expected phase. The expected phase is thus correctly reproduced by the d-scan retrieval.
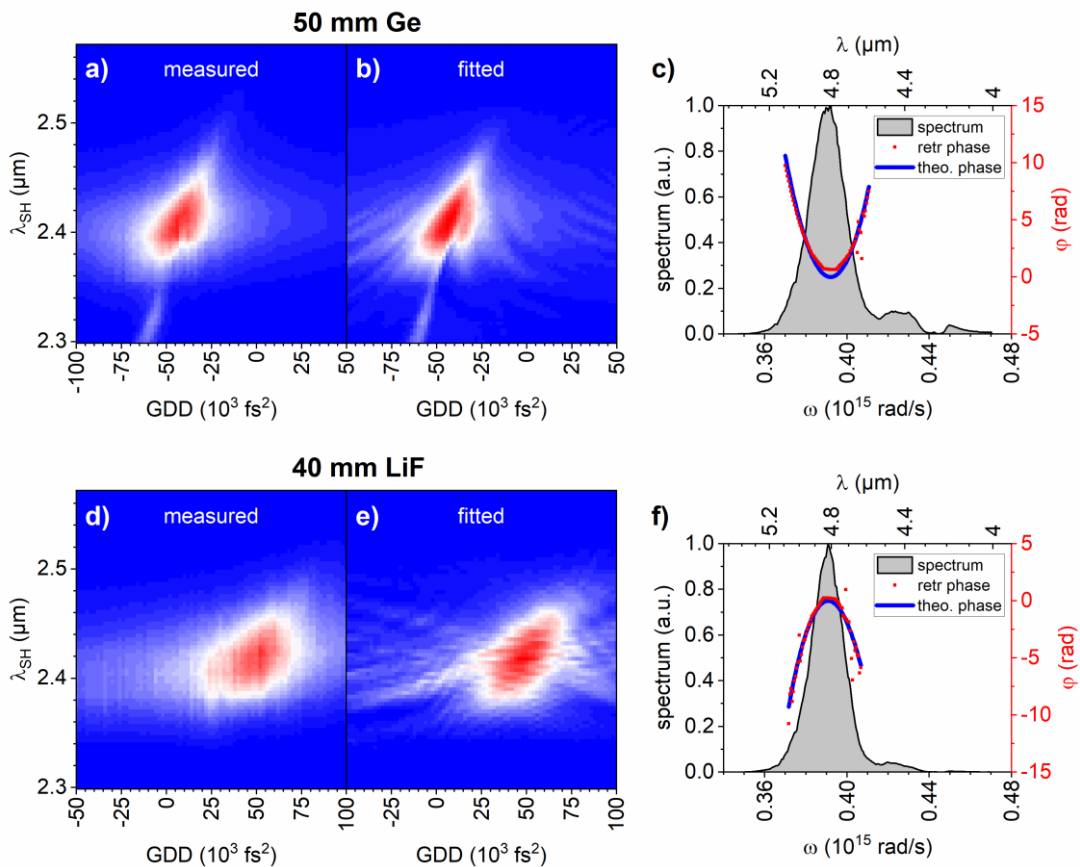
Figure III.11: D-scan results for different substrates. Top row: 50 mm Ge substrate. a), b) measured and fitted trace (retrieval error G=0.0269), c) Comparison of the retrieved phase by d-scan (red scattered) with the theoretically expected phase (blue line). Bottom row: 40 mm LiF substrate. d), e) measured and fitted traces (G=0.0454), f) Comparison of retrieved and theoretically expected phase. In c) and f), the retrieved phase was subtracted by the phase of a reference measurement without substrate in the beam path. The phases are only shown for regions with spectral intensities above 10% of the maximum spectral intensity. The retrieval algorithm sometimes introduces jumps of 2π in the retrieved phase. Those jumps are pure numerical artefacts and have no physical meaning. Thus, for better comparison with the theoretically expected phase, the retrieved phase in c) is shifted by 2π in the region above $\omega=0.408\times10^{15}$ rad/s ($\lambda=4.62$ μm) and in f) above $\omega=0.403\times10^{15}$ rad/s ($\lambda=4.67$ μm).

III. 5.2 <u>Pulse compression of a broadband MIR pulse</u>

In order to compress the broadband MIR pulse, a series of iterative pulse characterisations is performed. After each iteration, the opposite of the obtained phase is imprinted on the pulse for compression. D-scan is used to characterise the phase in the central region of the spectrum. For spectral regions where d-scan is not reliable, an evolutionary algorithm is employed for phase estimation, cf. Sec. III. 2.8. Fig. III.12 shows the results of this iterative pulse compression procedure. Without any additional phase for compression, the pulse possesses a strong third order dispersion of ca. 214 000 fs³ around $\omega_0 = 0.583$ rad/s (Fig. III.12 a),b)). The dominance of third order dispersion can already be seen from the shape of the measured trace, that looks like a tilted line. The phase obtained from the d-scan retrieval is thus fitted by a third order polynomial. After compensation of the retrieved GDD and TOD, the trace does not look like a tilted line any longer (Fig. III.12 d)), which means that the TOD has been successfully compensated. This is confirmed by the reconstructed spectral phase, cf. Fig. III.12 c). An intensity ACT which is deduced from the shaper based interferometric ACT, reveals a FWHM of the ACT around 60 fs after the first compression iteration, cf. Fig. III.12 e). Further correction of the pulse for the phase retrieved in the second iteration removes the C-shaped curvature of the d-scan trace, as is seen by comparison of Fig. III.12 g) with d). The range of the pulse's spectral phase decreases as well, cf. Fig. III.12 f). Consequently, the pulse gets shorter, as is confirmed by the autocorrelation measurement shown in Fig. III.12 h). A Lorentzian fit[1]

$$f(\tau) = y_0 + \frac{2A}{\pi} \frac{\tau_{FWHM}}{4(\tau - \tau_0)^2 + \tau_{FWHM}^2} \tag{III. 30}$$

to the intensity ACT gives a FWHM of the ACT of $\tau_{FWHM} = 46$ fs. More iterations in pulse compression did not help to decrease the pulse length further.

The spectral phases retrieved from the d-scan measurements show scattering and kinks in the spectral region above $\omega = 0.67 \times 10^{15}$ rad/s (below 2.8 µm), cf. Fig. III.12 a), c), f). In this region, the d-scan retrieval is not reliable. This issue will be further discussed in Sec. III. 6.2.

---

[1] The meaning of the parameters are: y_0: offset, A: area under curve for $y_0 = 0$, τ_0: centre position, τ_{FWHM}: FWHM of the curve
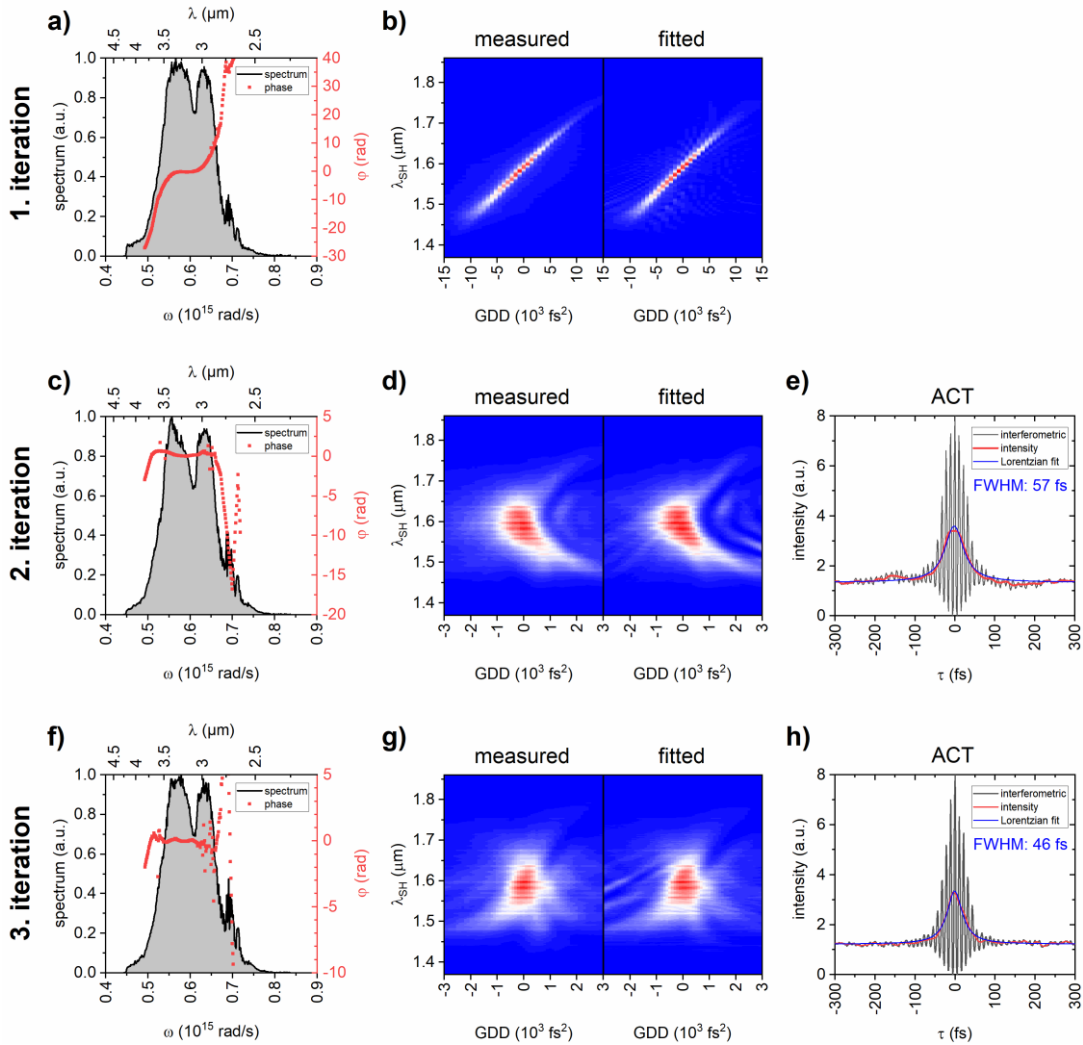
Figure III.12: *Iterative pulse compression of the broadband MIR pulse. a), c), f) fundamental spectra (grey shaded, left scale) and retrieved spectral phases from d-scan (red, right scale) for consecutive iteration steps. Note the decreasing y-scale for the phase from first to third iteration. Spectral phases are not shown for spectral regions with intensities below 10% of the maximum spectral intensity. In f), the retrieved phase is shifted by 2π below 0.52×10^{15} rad/s (3.6 µm) for better visibility. b), d), g) measured (left) and retrieved (right) d-scan traces. Note the larger range in GDD for the first iteration. b) Matrix size for retrieval (frequency × dispersion axis): 321×41, retrieval error G=0.0160, d) matrix size: 321×61, G=0.0280, g) matrix size: 321×61, G=0.0200. e), h) interferometric ACTs (black), the derived intensity ACTs (red) and Lorentzian fits to the intensity ACTs. For the first iteration, there is no ACT shown, as the uncompressed pulse is long and the ACT noisy. Reproduced with permission from Ref. [74].*

III. 5.3 D-scan characterisation of tailored broadband MIR pulses

A compressed broadband MIR pulse serves as basis for further phase tailoring and spectral phases of different complexity are imprinted on it. Fig III.13 shows d-scan measurements for imprinted phases of second (Fig. III.13 a) –f)) and third (Fig. III.13 g) –l)) order dispersion. The traces of second order dispersion of ± 2000 fs^2 show the typical displacement of the SH signal's maximum from zero GDD by ∓ 2000 fs^2. An imprinted third order dispersion results in a trace that resembles a tilted line. The retrieval of the spectral phase works well for the
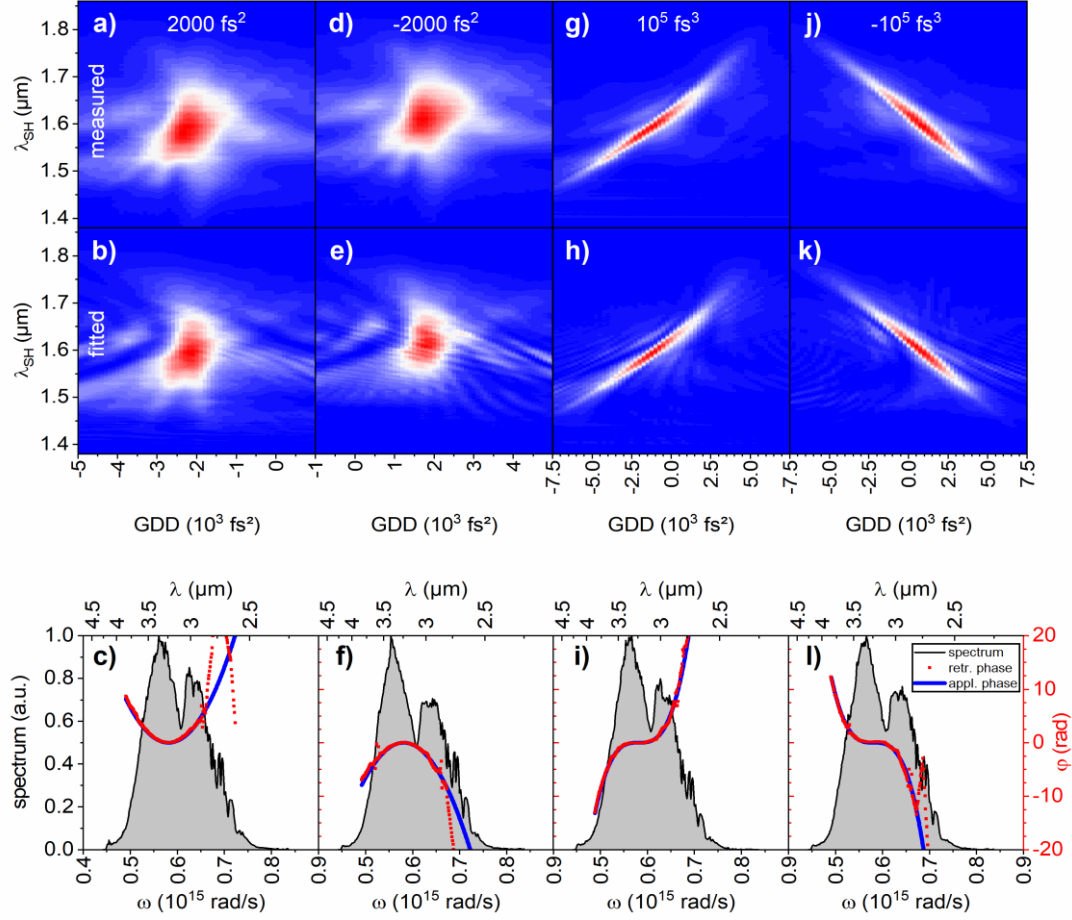
Figure III.13: d-scan measurements of broadband MIR pulses with tailored phases of second (a) -f)) and third (g) -l)) order dispersion. First row: measured traces; second row: fitted traces; third row: fundamental spectra (grey shaded, left scale), reference corrected retrieved spectral phases (red squares, right scale) and the phase applied by the AOM shaper on the compressed pulse (blue solid line, right scale). Spectral phases are not shown for spectral regions with intensity lower than 10% of the maximum spectral intensity. If not noted otherwise, the initial phase guess for the retrieval algorithm was a flat phase. a) -c) applied phase 2000 fs^2, retrieval error G=0.0415, d) -f) -2000 fs^2, G=0.0574. The initial guess for the phase was -2000 fs^2 with 20% noise on the phase. Such a guess can be readily obtained by observing that the d-scan trace is centred around +2000 fs^2. In addition, 1% of the d-scan trace's maximum value was added as noise on the simulated trace during the retrieval. g) -i) 10^5 fs^3, G=0.0201, j) -l) -10^5 fs^3, G=0.0236. The Taylor phases are applied around a central frequency ω_0=0.58×10^{15} rad/s (λ_0=3.24 μm). For better comparison with the applied phase, the retrieved phase in f) (-2000 fs^2) and l) (-10^5 fs^3) was shifted by 2π above ω=0.66×10^{15} rad/s (λ=2.8 μm). Reproduced with permission from Ref. [74].

major part of the broad MIR spectrum, as is demonstrated in the last row of Fig. III.13 by comparison of the (reference corrected) retrieved phase with the phase that is applied by the shaper. Despite the agreement between applied and retrieved phases for the biggest part of the spectrum, the deviation becomes large in the blue edge of the spectrum above $\omega \approx 0.67 \times 10^{15}$ rad/s (below $\lambda = 2.8$ µm). This feature was already observed for the pulse compression in the previous section and will be further discussed in Sec. III. 6.2.

Moreover, fourth order phases of $\pm 2 \times 10^{6}$ fs^4 (Fig. III.14 a) –f)) and a phase corresponding to a 2-colour double pulse (Fig. III.14 g) –i)) were imprinted on a compressed MIR pulse. For the 2-colour double pulse, the separation frequency is at $\omega = 0.58 \times 10^{15}$ rad/s ($\lambda = 3.24$ µm) with the blue part of the spectrum delayed by 500 fs. The phase of the 2-colour double pulse is interesting because its group delay has a discontiniuty at the separation frequency. This discontinuity would make retrieval with MIIPS challenging. Fig. III.14 shows that phase retrieval with d-scan works well for the greater part of the broadband MIR spectrum. Again, significant deviations between applied and retrieved phases are only observed above $\omega \approx 0.67 \times 10^{15}$ rad/s ($\lambda = 2.8$ µm). In addition to d-scan, a shaper based ACT was measured for the 500 fs 2-colour double pulse. The inset Fig. III.14 i) shows the deduced intensity ACT. The ACT confirms the successful creation of the double pulse and thus the shaping fidelity.
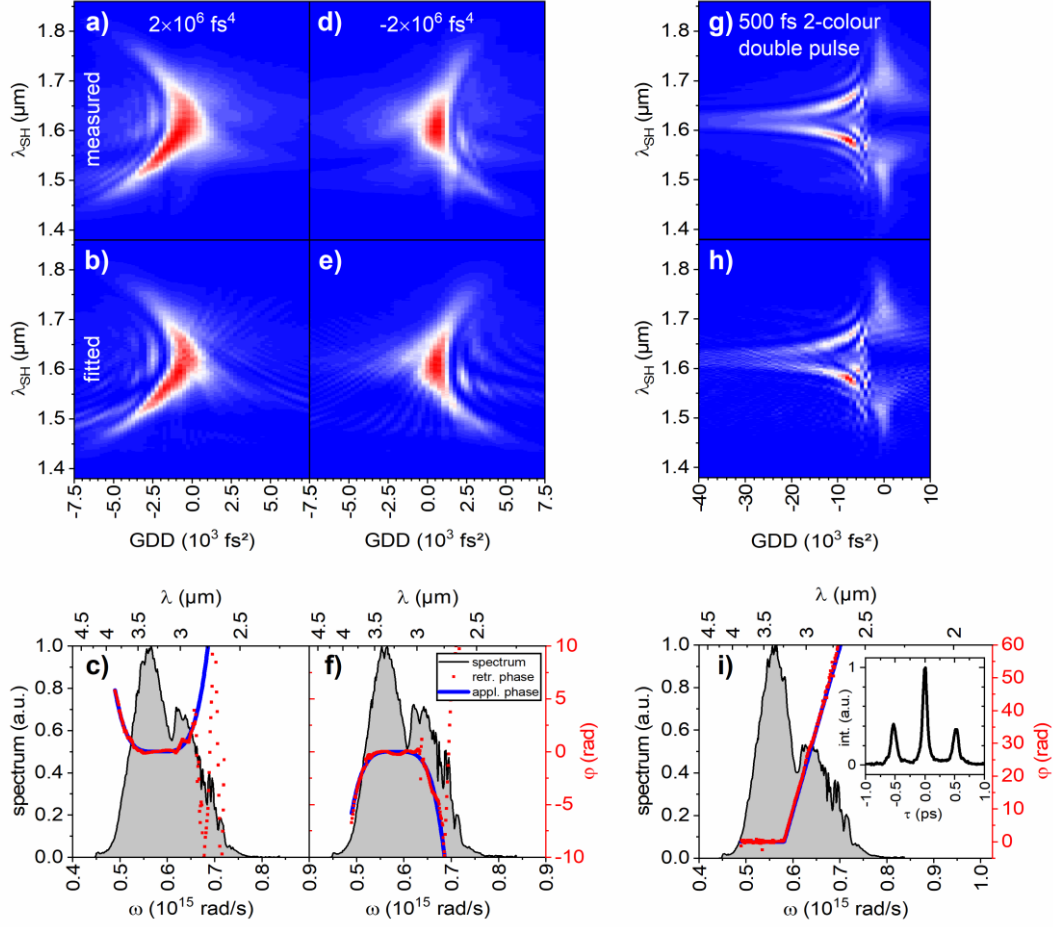
Figure III.14: *d-scan measurements of broadband MIR pulses with tailored phases of fourth order dispersion (a) -f)) and different linear phases in two spectral regions, corresponding to a 2-colour double pulse (g) -i)). First row: measured traces; second row: fitted traces; third row: fundamental spectra (grey shaded, left scale), retrieved spectral phases (red squares, right scale) and the phase applied by the AOM shaper on the compressed pulse (blue solid line, right scale). The reconstructed phase has been corrected for the reference phase of the compressed pulse. The initial phase guess for the retrieval algorithm was a flat phase for all depicted cases and no noise was added on the simulated traces. Spectral phases are not shown for spectral regions with intensity lower than 10% of the maximum spectral intensity. a) -c) applied phase 2×10^6 fs^4, retrieval error G=0.0325, d) -f) -2×10^6 fs^4, G=0.0329. The fourth order dispersion is applied around a central frequency ω_0=0.58×10^{15} rad/s (λ_0=3.24 µm). g) -i) 2-colour double pulse with separation frequency ω=0.58×1015 rad/s (λ=3.24 µm) and 500 fs between the two spectral parts, G=0.0266. The 2-colour double pulse is the only example in this work where a differential evolution scheme [101] instead of the Nelder-Mead algorithm was used for phase retrieval. The inset in i) shows an ACT of the 500 fs double pulse. For f) and i), the retrieved phase was shifted by 2π above ω=0.64×10^{15} rad/s (λ=3.0 µm) and ω=0.67×10^{15} rad/s (λ=2.8 µm). Reproduced with permission from Ref. [74].*

46

III. 6   Discussion

III. 6.1 Phase of a uncompressed broadband pulse

The uncompressed broadband pulse has a strong third order phase contribution after passing through the AOM shaper, see Fig. III.15 b) and Fig. III.12 a), b). This can be understood by following the approach presented in Ref. [81], that is by investigation of the contributions of the different components of the optical setup to the spectral phase. The major contributions come from sole transmission through the AOM 4f shaper setup and the subsequent transmission through the 50 mm LiF rod. Those contributions are depicted in Fig. III.15 a). The contribution of the AOM shaper in turn is composed of the phase imprinted by the 21 mm thick Ge substrate of the AOM and the phase caused by the Bragg angle correction mask. Thus, a phase is imprinted on the pulse by sole transmission throught the AOM 4f shaper setup, even if no active phase shaping is employed. The LiF rod after the shaper partly compensates that phase.
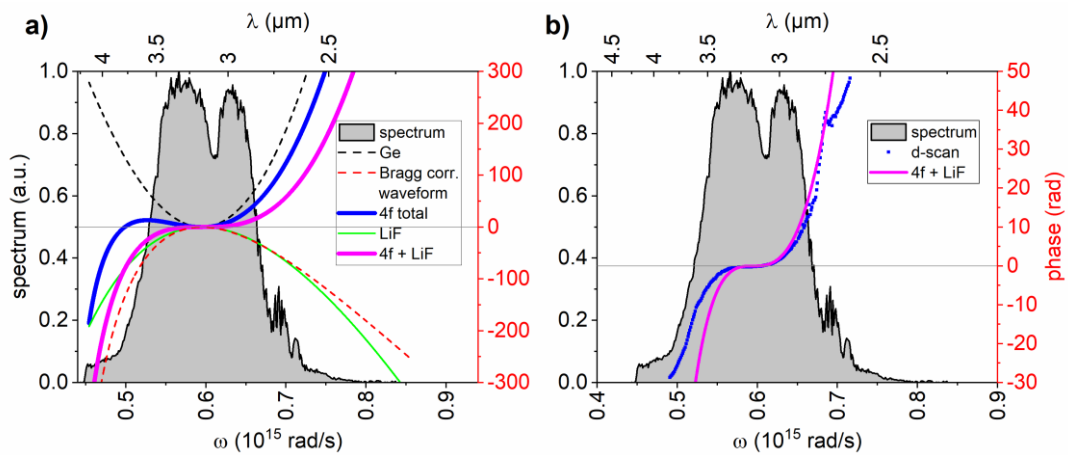
Figure III.15: *a) Different phase contributions of the optical setup. The Ge substrate of the AOM (21 mm thick, black dashed) and the Bragg angle correction mask (red dashed) make up the total phase imprinted on the pulse by sole transmission through the 4f setup (blue solid). The subsequent 50 mm LiF rod (green solid) partly compensates the phase caused by the 4f setup. b) Comparison of the total phase contribution from a) (magenta solid line) and the phase retrieved by the d-scan (blue scattered). The horizontal line at 0 rad is a guide for the eye. Note the different scales for the phase axes in a) and b).*

Tab. III-2 lists the various second and third order contributions to the phase. As can be seen from the table, the second order dispersion of the pulse shaper and the LiF substrate have different signs and the LiF substrate compensates the second order dispersion of the 4f setup really well, leaving a GDD of only 67 fs^2. This is surprisingly low, considering the large amounts of GDD introduced by each single component. The TOD of the 4f setup cannot be cancelled by the LiF substrate, since both TOD values have the same sign and thus add up. Comparing the values for GDD and TOD with the values obtained from the d-scan retrieval shows that the measured pulse after the shaper also has only little GDD, but large TOD. However, the measured TOD value is significantly smaller than the value estimated from investigation of the single components. This can also be seen in Fig. III.15 b), where the retrieved phase by d-scan has a less steep evolution than the phase deduced from the optical components. These findings indicate that there are more contributions to the pulse's

	$\varphi''(\omega_0)$ (fs^2)	$\varphi'''(\omega_0)$ (fs^3)
Bragg mask	- 16 909	219 939
Ge substrate	31 276	72 232
Total 4f setup	14 367	292 171
LiF substrate	- 14 300	79 439
4f setup + LiF	67	371 610
d-scan	529	213 910

Table III-2: *Second and third order contributions to the spectral phase around ω_0=0.595×10^{15} rad/s. The values for the optical setup (top part of the table) were determined by calculation and numerical differentiation of the various phase contributions. The values for d-scan (last line) were obtained by fitting a third order polynomial to the retrieved phase.*

phase than the ones considered in the above investigation and that a phase retrieval by measurement is indeed necessary to correctly determine the pulse's phase.

III. 6.2 Range of reliable region of the d-scan retrieval

The results of the d-scan measurements have shown that the shaper-based d-scan in principle works. The G-errors of the fitted traces are in the lower single-digit percentage range, which is indeed common for d-scan retrieval [101, 102]. However, for the broadband spectrum, the phase retrieval becomes unreliable for the blue part of the spectrum, above ca. 0.67×10^{15} rad/s (below 2.8 μm). The reason for the retrieval breakdown at high frequencies is investigated in this section.
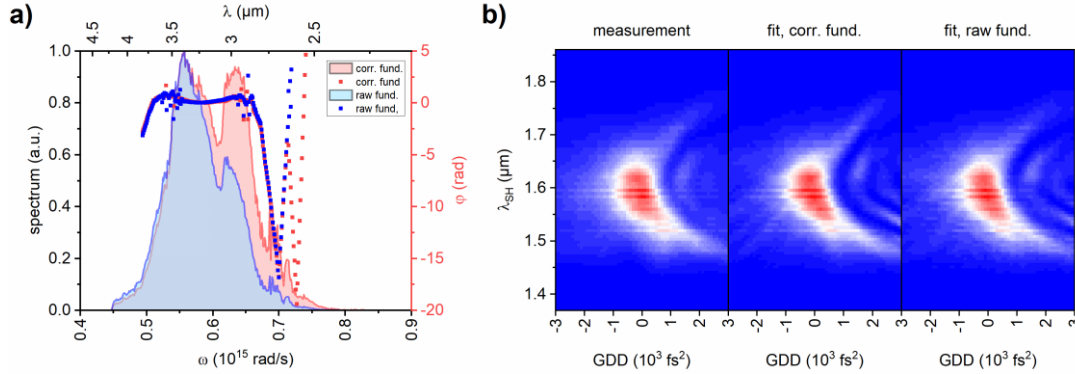
Figure III.16: *Comparison of d-scan retrieval with different fundamental spectra used. a) Raw data of the measured fundamental spectrum (blue shaded, left axis) and fundamental spectrum corrected by the grating efficiency of the spectrograph (red shaded, left axis). The retrieved spectral phases (right axis) are similar for both fundamental spectra (blue dots: retrieval with raw fundamental spectrum, red dots: retrieval with corrected fundamental spectrum). Especially, in both cases, the retrieved phase becomes unreliable above 0.67×10^{15} rad/s (below 2.8 μm). For better comparison, the spectral phase fitted with the raw fundamental spectrum is shifted by 2π below 0.54×10^{15} rad/s (above 3.5 μm). Phases are only shown for spectral regions with intensity higher than 10% of the maximum spectral intensity. b) Measured (left) and fitted traces with both the corrected (middle, G=0.0280) and raw fundamental spectrum (right, G=0.0193) used.*

Beside the trace of the SH spectra, d-scan requires an independently measured spectrum of the fundamental. It is thus examined whether a wrongly calibrated fundamental spectrum causes the retrieval breakdown. Fig. III.16 shows the retrieval for the pulse compression (cf. Fig. III.12 c), d)) performed with two different fundamental spectra given to the retrieval algorithm: The measured raw spectrum (blue shaded in Fig. III.16 a)) and the measured spectrum corrected for the grating and detector efficiency of the spectrograph (red shaded in Fig. III.16 a)). The main effect of the efficiency correction is an amplification of the region above 0.6×10^{15} rad/s (below 3.1 μm). The retrieval error G is slightly better for the raw fundamental spectrum. However, for both raw and corrected fundamental spectra, the retrieved phase looks similar. In particular, the reliable retrieval region does not change for the reduced spectral intensity in the blue part of the raw fundamental spectrum. From this, it can be concluded that a faulty calibration of the fundamental spectrum is not the reason for the retrieval breakdown below 2.8 μm.

It was also examined whether the MIR beam after the AOM shaper exhibits spatial chirp. A highly non-uniform spatial distribution of the frequencies within the MIR beam could prevent successful phase retrieval since not all frequencies of the measured fundamental spectrum could interact with each other in SH generation. The potential interaction of all the fundamental frequencies is however assumed in the retrieval algorithm. Anyway, no spatial chirp could be observed in the MIR beam after the shaper. Details on the spatial chirp measurement are given in App. B. 6.

The MCT detector of the spectrograph uses a coated ZnSe window. This window has extremely low transmission above 1.3×10^{15} rad/s (below 1.5 μm). Therefore, the detected SH spectrum below 1.5 μm is low and noisy. The corresponding frequencies of the fundamental spectrum are hence prone to erroneous phase reconstruction. This point is demonstrated in Fig. III.17: D-scan traces of a pulse with pure fourth order dispersion are simulated [86] both with the full SH spectrum recorded and with the edges of the SH spectrum below 1.5 μm not recorded (Fig. III.17 a), top row). The deviation of the retrieved phase by d-scan from the originally applied fourth order phase is presented in Fig. III.17 c). As can be seen in the figure, the deviation above 0.68×10^{15} rad/s (below 2.8 μm) is much higher for the trace with clipped SH spectrum than for the trace with full SH spectra detected. The same qualitative behaviour is observed for traces with other simulated phases.

For the retrieval of the full d-scan trace, significant deviations are only observed on the edge of the low spectral intensity regime of the fundamental spectrum, cf. Fig. III.17 c). However, the G-errors are similar for both retrievals from the full and the clipped d-scan trace. This means that for the given clipped d-scan trace, the fit algorithm cannot unambiguously retrieve the spectral phase.

It has been shown in the literature that d-scan possesses some tolerance against bandwidth restrictions of SH recording or generation and that the full SH trace is not necessarily needed for complete phase retrieval over the whole fundamental spectral range [103, 104]. This is because the information encoded in the d-scan trace is in part redundant, since a frequency in the fundamental spectrum not only generates a signal at the corresponding SH wavelength, but also at other wavelengths through mixing with different frequencies within the fundamental spectrum. However, for bandwidth limited SH detection, the redundancy of an uncalibrated d-scan trace needs to be sufficiently large in order to successfully retrieve the phase over the full fundamental spectrum [105]. The applied correction of the measured SH spectrum for the detector sensitivity according to the data sheet can in fact
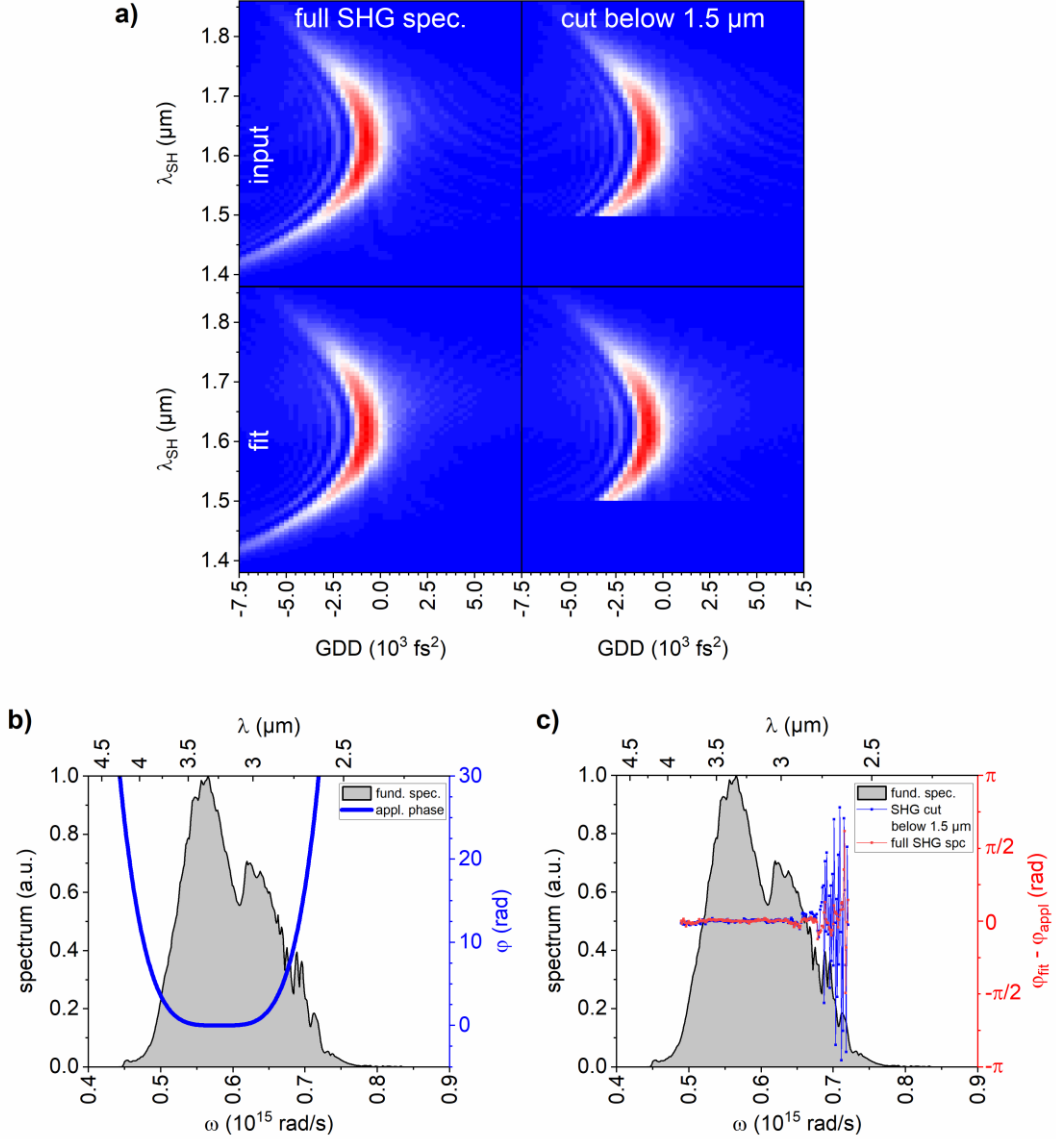
Figure III.17: *Influence of a clipped SH spectrum on the d-scan retrieval. a) Simulated (upper row) and retrieved (lower row) d-scan traces. D-scan traces are simulated with the full SH spectrum recorded (left column, G=0.0119) and the edge of the SH spectrum clipped below 1.5 µm (right column, G=0.0151). No noise was added to the simulated traces. b) FW spectrum (grey shaded, left axis) and pure fourth order Taylor phase $\varphi_{appl} = 2 \times 10^6\,fs^4$ (blue, right axis), that were used for the simulation of the d-scan traces. c) Difference modulo 2π between the retrieved phase φ_{fit} from the simulated d-scan trace and the originally applied fourth order phase φ_{appl} (right axis).The phase difference is evaluated for both the retrieval with the clipped (blue) and full (red) SH spectrum taken into account. In the blue wing of the spectrum, the difference is much larger if the SH spectrum of the d-scan trace is clipped. Phase differences are only shown for spectral regions with intensity higher than 10% of the maximum spectral intensity.*

partly compensate for the low detection efficiency. But this method finally comes to a limit if the measured SH intensity in a large spectral range is too low, since the sensitivity correction leads to strongly amplified noise as well.

The findings of this section suggest that the reason for the unreliable phase retrieval below 2.8 μm is the low transmission below 1.5 μm of the coated ZnSe window of the spectrograph used in the measurements.

III. 6.3 Pulse compression of broadband MIR pulses

The fit of the measured ACT of the compressed pulse of Sec. III. 5.2 gives a FWHM of 46 fs, cf. Fig. III.18 c). The measured fundamental spectrum, however, supports a TL-pulse with 22 fs FWHM. The simulated interferometric ACT [86] of such a pulse is shown in Fig. III.18 a). A Lorentzian fit to the derived intensity ACT of the TL-pulse gives a FWHM of only 28 fs, which is almost half the value of the 46 fs from the measurement. It is not surprising that the measured pulse duration does not correspond to the TL-pulse, as the d-scan cannot retrieve

the phase at the edges of the spectrum and the third order phase estimation from the evolutionary algorithm is not accurate enough to fully compensate the phases of the spectral edges. A much better agreement between simulated and measured ACT can be achieved, when the fundamental spectrum for the simulation is restricted to $(0.49 - 0.66) \times 10^{15}$ rad/s (i.e. 2.8-3.9 μm), cf. Fig. III.18 d). Below 2.8 μm, the d-scan retrieval is erroneous due to the ZnSe window of the detector as discussed in the previous section; above 3.9 μm, the low spectral intensity (below 10% of the spectral maximum) makes accurate phase retrieval also challenging. The fitted 40 fs FWHM of the simulated ACT for a TL-pulse with restricted fundamental spectrum (Fig. III.18 b)) is close to the 46 fs of the measured ACT. The derived intensity ACTs of both the simulations and the measurement are shown all together in Fig. III.18 e). These results indicate that it is the limits of the reliable d-scan retrieval region that prevent compression of the broadband pulse to its transform limit.
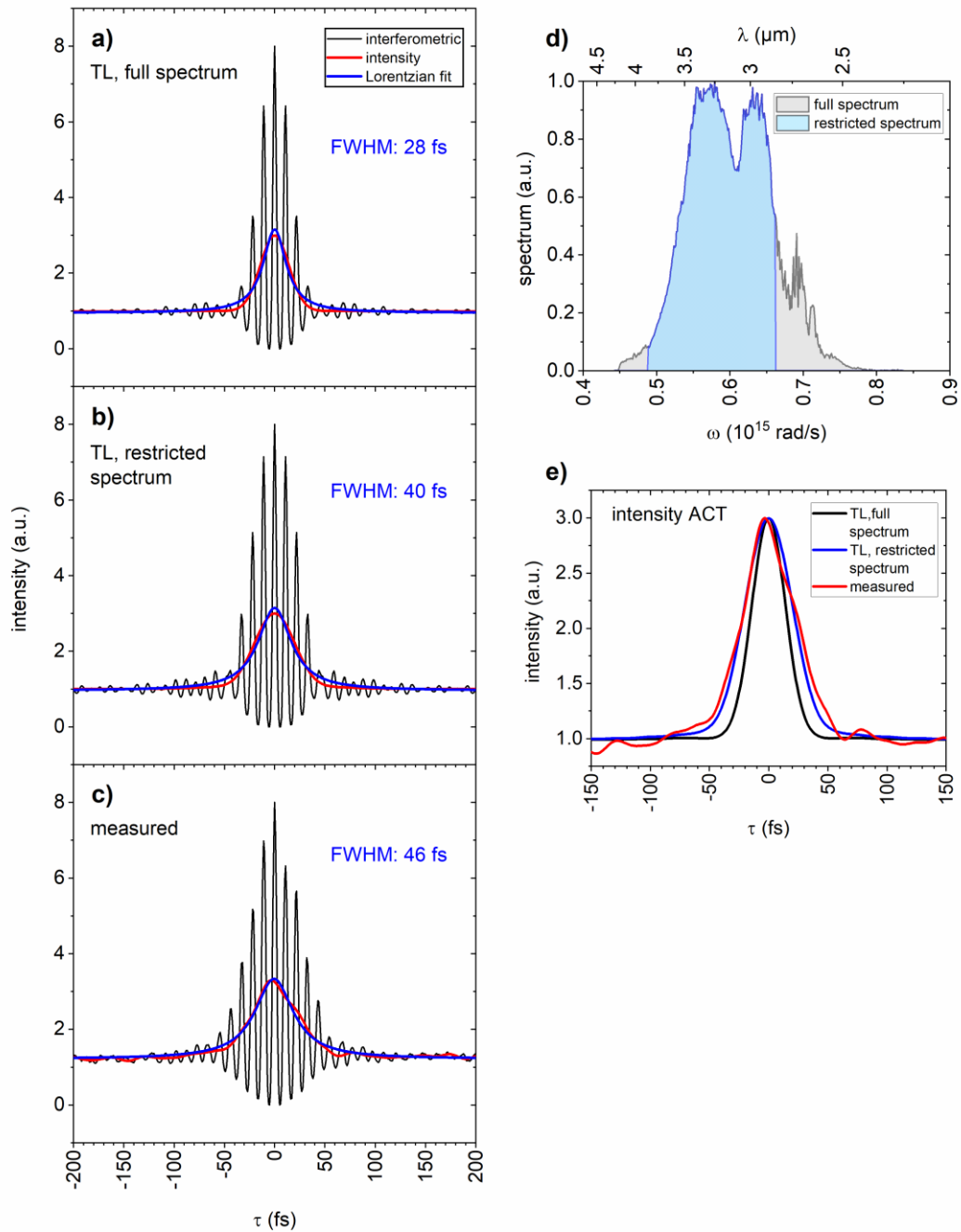
Figure III.18: *Comparison between simulated and measured ACTs. a) Simulated ACT of a TL pulse with the full spectrum taken into account. Black: Interferometric ACT, red: Intensity ACT deduced from the interferometric ACT, blue: Lorentzian fit to the intensity ACT. The FWHM value refers to the Lorentzian fit. b) Simulated ACT of a TL pulse with its spectrum restricted between $\omega = (0.66 - 0.49) \times 10^{15}$ rad/s ($\lambda = 2.8 - 3.9\ \mu m$). c) Measured ACT (cf. Fig. III.12 h)). d) Full spectrum (grey shaded) and restricted spectrum (blue shaded) that are used for the simulations. The restricted spectrum covers the range $\omega = (0.66 - 0.49) \times 10^{15}$ rad/s ($\lambda = 2.8 - 3.9\ \mu m$). e) Direct comparison between the deduced intensity ACTs from a)-c). For better comparison with the simulated ACTs, the measured ACT was downshifted by 0.3.*

III. 6.4 Shape of simple d-scan traces

As was pointed out in Refs. [73, 106], for pulses with sufficiently simple phase $\varphi(\omega)$, the second derivative $\varphi''(\omega)$ of the unknown phase can be directly estimated from the d-scan trace. For that estimation, no retrieval algorithm is needed. The estimation is based on the assumption that only frequencies in close vicinity of ω contribute to the SH signal at 2ω. In this case, the SH signal is maximised, if the second derivative of the applied dispersion $\phi_j''(\omega)$ locally cancels $\varphi''(\omega)$, i.e. $\varphi''(\omega) = -\phi_j''(\omega)$. For a d-scan trace with dispersion $\phi_j(\omega) = \frac{1}{2}c_j(\omega - \omega_0)^2$ and the GDD c_j as scan parameter, the c_j for which $\varphi''(\omega) = -c_j$ can then be readily read off the trace itself by following the course of the SH maxima. This is illustrated in Fig. III.19.

Fig. III.19 a) displays the measured trace of a compressed pulse with an additional phase of -2000 fs^2 imprinted. It is the same measurement as shown in Fig. III.13 d), but with the dispersion axis now in vertical direction and ω_{SH} instead of λ_{SH} plotted. The white line denotes the position of the maxima of the SH signal, simply estimated by eye. The maxima approximately appear at the same GDD c_j for all ω_{SH}. The white line's read off GDD value is

$$c_j = -\varphi''(\omega) = 1.88 \times 10^3 \text{ fs}^2.$$

The applied phase by the shaper was a quadratic phase with $\varphi''(\omega) = -2 \times 10^3$ fs^2. The deviation from the expected phase can be explained by the reference phase of the compressed pulse (see Sec. B. 5), that was not considered in this simple analysis.

The SH maxima in Fig. III.19 b) lie along a line. The white line is again estimated just by eye and intersects zero GDD (white dotted line) at $\omega_{0,SH} = 1.162 \times 10^{15}$ rad/s. The slope is determined via the points marked by the crosses. The expression for the white line thus reads
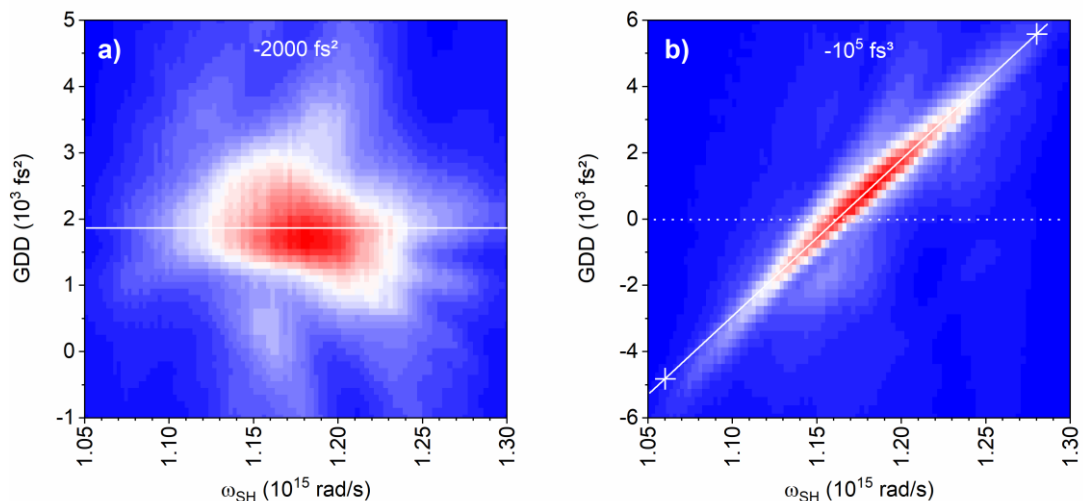
Figure III.19: *d-scan traces of a compressed MIR pulse with additionally imprinted phases of a) -2000 fs^2 and b) -10^5 fs^3. The white line marks the course of maximum SH intensity. In b), the dotted line marks zero GDD and the crosses are used to determine the slope. Note that in contrast to the figures of Sec. III. 5.3, the GDD for phase characterisation is now plotted along the vertical axis and ω_{SH} instead of λ_{SH} is used.*

$$-\varphi''(\omega) = \frac{\left(5586 - (-4822)\right)\frac{\text{fs}^2}{\text{rad}}}{\frac{1}{2}(1.28 - 1.06)\,\frac{\text{rad}}{\text{fs}}} \cdot (\omega - \omega_0)$$

$$= 94\,618\,\frac{\text{fs}^3}{\text{rad}^2} \cdot (\omega - \omega_0). \qquad (\text{III.}\,31)$$

The factor $\frac{1}{2}$ in the denominator appears because the x-axis of the d-scan trace is the SH frequency at twice the value of the fundamental spectrum; $\omega_0 = \frac{1}{2}\omega_{0,SH} = 0.581 \times 10^{15}$ rad/s. Integration of $\varphi''(\omega)$ leads to

$$\varphi(\omega) = -\frac{1}{6} \cdot 94618\,\frac{\text{fs}^3}{\text{rad}^2} \cdot (\omega - \omega_0)^3. \qquad (\text{III.}\,32)$$

The integration constants $\varphi'(\omega_0)$ and $\varphi_0(\omega_0)$ have been set to zero as they cannot be determined by d-scan anyway. The third order Taylor phase determined in this manner agrees well with the applied third order phase by the shaper with $\varphi'''(\omega_0) = -10^5$ fs^3/rad^2 around $\omega_0 = 0.58 \times 10^{15}$ rad/s, cf. Fig. III.13 j)-l).

For both depicted examples, the simple analysis of the measured d-scan traces gives a reasonable estimation for the GDD and TOD values without employing any retrieval algorithm. The estimated values deviate ca. 5% from the expected values. Note that in the simple analysis, the phase of the compressed pulse was not considered at all and no reference phase was subtracted, in contrast to the analysis presented in Sec. III. 5.3.

As mentioned earlier, the method presented in this section only works for sufficiently simple pulses. For a complicated trace as the one of the 2-colour double pulse of Fig. III.14 g), a retrieval algorithm is actually needed. A retrieval algorithm has the further advantage that it can exploit redundancies which are encoded in the d-scan trace by contributions of several fundamental frequencies to the signal at a certain SH frequency.

III. 7   Conclusion

In this section, a versatile setup for pulse shaping and characterisation in the MIR spectral region based on an AOM 4f pulse shaper has been presented. The reconstruction of the MIR pulse's spectral phase was achieved via a shaper-based variant of d-scan. Successful retrieval of the spectral phase introduced by substrates with different signs of GDD was demonstrated for pulses centred at 4.8 µm. Also, phase retrieval has been proven to work well for the greatest part of the broadband spectrum of pulses centred at 3.2 µm. This confirms the setup's fidelity for pulse shaping. However, the retrieval for the broadband pulses breaks down below 2.8 µm. The origin of this breakdown has been identified as the extremely low SH detection sensitivity below 1.5 µm. By a combination of phase retrieval with d-scan in the central part of the spectrum and characterisation by an evolutionary algorithm for the spectral wings, the pulses centred at 3.2 µm can still be compressed and broadband, shapeable MIR pulses with a pulse duration below 50 fs FWHM autocorrelation are achieved.

Beside tackling the low SH detection efficiency beneath 1.5 µm, further improvements of the presented method could aim at the implementation of the retrieval algorithm. The algorithm in its current form can be improved with respect to the phase reconstruction at the very edges of the spectrum, i.e. in regions of low spectral intensity. Possible alternative implementations for d-scan retrieval algorithms are suggested in the literature [107, 108].

The presented AOM shaper-based d-scan implementation represents a convenient alternative for phase characterisation in experiments that involve a pulse shaper anyway. The in-line, all collinear geometry only calls for minimum additional alignment, since no beam splitting, recombination, etc. is required. This makes the setup especially suited for the MIR spectral region, where alignment is much more challenging than for example in the Vis spectral range.

III. 7 Conclusion

IV   Impact of the excitation of the CNN stretching vibration on the photoreaction of 2-diazo-1-naphthol-5-sulfonate

IV. 1   Introduction

It is a chemist's dream to gain control over the behaviour of a molecule, such as the time and place when and where it reacts, to guide its reaction along one or another pathway or to pick only one specific species for reaction out of an ensemble of many different species. One promising route to achieve the goal of control is the use of laser light [109, 110]. Laser light offers an ample set of controllable parameters, such as wavelength or intensity, that can be applied to photochemistry. With the advent of ultrafast laser systems, high intensity laser pulses on the femtosecond time scale became available. This is the time scale on which the core process of a chemical reaction, namely breaking and formation of molecular bonds, occurs [3-5]. Femtosecond laser pulses allow to observe [6, 111] and steer [112] molecular bond breaking and formation. The observation and steering of chemical processes on the femtosecond time scale is called femtochemistry. The field of femtochemistry was pioneered by Ahmed H. Zewail, who was awarded the Nobel Prize for his work in 1999 [7]. Impressive experiments have demonstrated optical control over a large variety of systems. The controlled quantities include molecular motions inside an organic crystal [113], the ratio between different photoisomeric species of biologically relevant molecules [114] and the steering of the energy flow within biologically relevant molecules [51]. Moreover, enhancement of molecular excited state population and vibrational coherence with shaped laser pulses has been demonstrated [115, 116].

In the task of molecular photocontrol, the mid-infrared (MIR) spectral region received special attention. This is because the MIR region is the spectral region in which molecular vibrations can be resonantly excited. A molecule's structure with its specific atomic groups is imprinted on its vibrational spectrum and vice versa, localised site specific vibrations can be induced by MIR radiation of appropriate frequency [17]. The MIR spectral region is thus called molecular fingerprint region, in contrast to the ultraviolet/visible (UV/Vis) region, where molecular spectra are broadband and spectra of different molecules often overlap. On the one hand, MIR spectroscopy reveals structural changes of a molecule or its surroundings [117]. On the other hand, MIR pulses can be applied in the selection of one particular molecular species for photochemistry within a mixture of different species. The latter was demonstrated even for the extreme case of isotopomers [24].

MIR pulses can also be utilised for chemical bond breaking in the electronic ground state by highly exciting a certain vibrational mode. Bond cleavage in this way has been demonstrated for gaseous diazomethane [20], for metal carbonyls in the gas phase [19, 21] and - almost two decades later - also for the liquid phase [22].

In this chapter, the effect of MIR excitation is investigated for a diazonaphthoquinone (DNQ) derivative, namely 2-diazo-1-naphthol-5-sulfonate, cf. Fig. IV.1. When irradiated by UV light, this molecule undergoes a Wolff rearrangement reaction which converts the ketone at the six-membered ring to a ketene at a five-membered ring, cf. Sec. IV. 2.1. The resulting ketene reacts further with the solvent; in the case of water finally to indenecarboxylic acid. This photoreaction makes DNQ derivatives highly relevant for technological applications, since it induces a change from hydrophobic to hydrophilic behaviour of the derivatives.

57
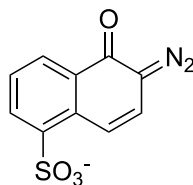
Figure IV.1: *2-diazo-1-naphthol-5-sulfonate, the molecule studied in this chapter.*

For example, DNQ derivatives are used as photoactive components of photoresists. These photoresists mainly consist of novolak (a condensation polymer), solvent and the photoactive component. Pure novolak resin is soluble in an aqueous base developer solution. However, when a small amount of DNQ derivative is added to the novolak resin, the novolak's dissolution speed in the developer solution decreases dramatically. When irradiated by UV light though, the DNQ based inhibitor undergoes the aforementioned photoreaction and the novolak dissolves even faster in the developer solution than pure novolak [118]. In this way, UV irradiation can change the novolak dissolution rate by more than three orders of magnitude [119].

The drastic light induced solubility change is applied in photolithography for the production of integrated circuits [118] or the creation of structures on the sub 100 nm scale [120]. DNQ based photoresists have found their use also in non-lithographic, self-organized pattern formation on silicon wafers [121].

The light induced switching of DNQ derivatives from hydrophobic to hydrophilic behaviour gained attention in medical research as well. DNQ can, for example, be part of micellar nanoparticles that are loaded with drugs. On irradiation and the induced transition of DNQ from hydrophobic to hydrophilic, the micelle structure gets destroyed and the loaded drug is released [122, 123]. Such systems have high potential for on demand drug delivery, as desirable for example in tumor therapy [124, 125]. The drug release can be triggered either by UV light [122, 123] or by NIR light via 2-photon absorption [124, 126-128].

In the work presented here, 2-diazo-1-naphthol-5-sulfonate is the only DNQ derivative that will be investigated. Thus, in the following the abbreviation *DNQ* shall be used to denote 2-diazo-1-naphthol-5-sulfonate in particular.

In this chapter, it shall be investigated whether vibrational excitation of the C=N=N stretch mode of DNQ (i.e. 2-diazo-1-naphthol-5-sulfonate) affects the molecule's Wolff rearrangement reaction to the ketene. In order to do so, a series of transient absorption measurements is performed on DNQ: In a MIR pump/MIR probe experiment, the possibility of molecular dissociation in the electronic ground state is evaluated. Moreover, it is estimated up to which level the MIR pulse in the experiments excites the C=N=N stretch mode. A MIR pump/white light (WL) probe experiment reveals how vibrational excitation of the C=N=N stretch mode affects the DNQ UV/Vis absorption spectrum. The information obtained is then used to tune the UV pump wavelength, which is applied in a combined experiment with MIR pre-excitation and subsequent UV pump. The photoproduct yields for UV excitation of DNQ with and without vibrational pre-excitation are compared. The measurements with MIR pre-excitation and subsequent UV excitation are carried out for two UV pump wavelengths, one at resonance of the DNQ UV/Vis absorption spectrum, one out of resonance at the low energy edge of the absorption.

This chapter is organised as follows: Sec. IV. 2 provides a summary of literature on DNQ's photoreaction mechanism that is relevant for this work (Sec. IV. 2.1), as well as a brief

overview on the anharmonic molecular potential (Sec. IV. 2.2), vibrational ladder climbing (Sec. IV. 2.3) and the Franck-Condon principle (Sec. IV. 2.4). The transient absorption (TA) technique as well as employed postprocessing steps are presented in Sec. IV. 3. Sec. IV. 4 describes the different types of TA experiments listed above in greater detail and elaborates on the respective accesible information. Details on the experimental setup are given in Sec. IV. 5. The results of the various measurements on DNQ are given in Sec. IV. 6 and will be discussed in Sec. IV. 7. The findings are summarised in Sec. IV. 8 and conclusions obtained from the outcome are drawn.

IV. 2   Theory

IV. 2.1 Literature review on DNQ's photoreaction

In this section, a selection of literature on the photoreaction mechanism of DNQ shall be briefly reviewed. This will help to interpret the results presented in Sec. IV. 6. The molecule investigated in this chapter is 2-diazo-1-naphthol-5-sulfonate (DNQ), a diazonaphthoquinone derivative. The pathway of the photoreaction of DNQ dissolved in methanol (MeOH) is shown schematically in Fig. IV.2: Upon UV/Vis photoexcitation, the N_2 group is cleaved from the naphthalene scaffold. The cleavage of the diazo group is followed by ring contraction and formation of a ketene, which is known as Wolff rearrangement [130]. Combination of theoretical [131-133] and experimental [29, 129, 134] work strongly suggests that both a concerted and a stepwise mechanism via a carbene intermediate are operative in the ketene formation. However, experimental studies have shown that the concerted pathway dominates the reaction [129, 134]. For the concerted reaction, the ketene is estimated to form on a time scale of some 100 fs [29, 52, 133]. The ketene further reacts with the solvent to the corresponding enol on a 50 ns time scale [129]. The enol in turn reacts with MeOH to form an ester (not shown in Fig. IV.2).

The carbene intermediate of the stepwise pathway can either react to the ketene or be trapped by the MeOH to form a 2-methoxy-1-naphthol-5-sulfonate [129, 134] (the latter is
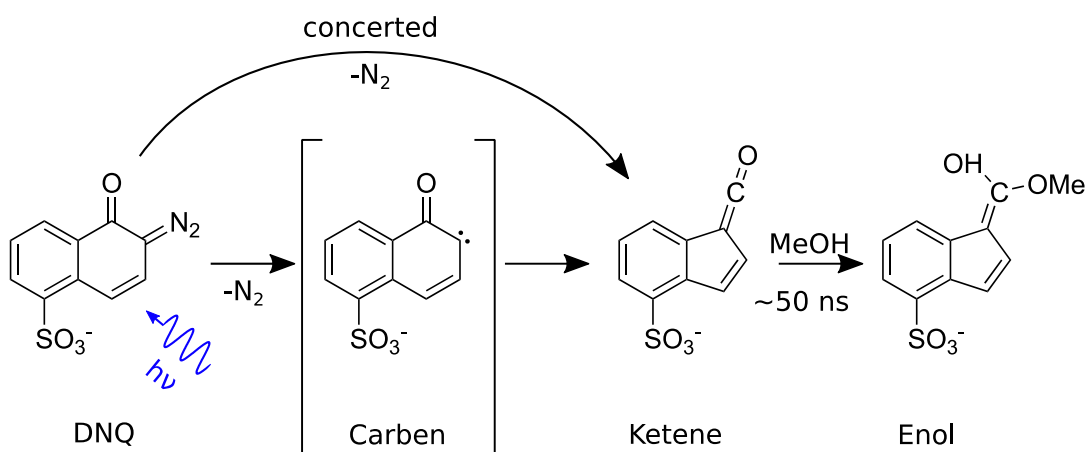
Figure IV.2: *Reaction scheme of DNQ under irradiation with UV/Vis light. Both a dominant concerted and a minor stepwise (via a carbene intermediate) pathway contribute to the reaction. The ketene intermediate reacts further with the solvent MeOH to the corresponding enol on a 50 ns time scale. The following reaction of the enol to the indenecarboxylic ester and a potential reaction of the carbene with MeOH are not shown. For these, see e.g. Ref. [129].*

not shown in Fig. IV.2). The yield of the 2-methoxy-1-naphthol-5-sulfonate side product was found to be less than 10% [129]. A backreaction of the carbene intermediate and N_2 to the original DNQ molecule does not take place [129]. In the stepwise reaction pathway, the ketene is formed from the carbene within a few picoseconds [29, 129].

Theoretical studies on the mentioned photoreaction revealed that the relaxation from the electronically excited state of DNQ occurs via an extended seam of conical intersection, which lies along the C-N stretch coordinate [133]. Whether the photoexcited DNQ molecule decays back to the original reactant or forms a photoproduct depends on the C-N distance at which the wave packet traverses from the electronically excited state to the ground state potential energy surface: For photoproduct formation, the C-N distance needs to be considerably enlarged compared to the configuration at which the wavepacket relaxes back to the original reactant [133]. Furthermore, relaxation from the UV/Vis photoexcited state of DNQ, either into a photoproduct or back to the original reactant, involves out-of-plane bending of the N_2 group [132, 133].

The lifetime of the electronically excited state of DNQ is less than 300 fs [29, 52, 131, 133].

IV. 2.2 Anharmonic potential

Since this chapter is about the influence of vibrational excitation of the C=N=N stretch mode on the photoreaction of DNQ, remarks about molecular vibrations are given in this setion.

For the treatment of molecular vibrations, a commonly applied approximation is the Born-Oppenheimer approximation. The Born-Oppenheimer approximation makes use of the fact that the mass of the electrons is lower than the mass of the nuclei by at least 3 orders of magnitude. The electrons can thus instantaneously follow the motion of the nuclei and immediately adjust to the positions of the nuclei. This allows to factorise the wave function of the molecule (ψ_{mol}) as product of an electronic (ψ_{el}) and nuclear wave function. The nuclear wave function again can be written as product of a vibrational (ψ_{vib}) and rotational (ψ_{rot}) term [135]

$$\psi_{mol} = \psi_{el} \cdot \psi_{vib} \cdot \psi_{rot} \ . \tag{IV.1}$$

Let us have a closer look on the vibrational part of the wave function. The nuclei effectively move in a potential that is created by Coulomb interactions between the nuclei and electrons. The potential V that acts on the nuclei can be expanded in a Taylor series around the nucleis' equilibrium positions [136]

$$V = V_0 + \sum_{i=1}^{3N} \left(\frac{\partial V}{\partial q_i}\right)_0 q_i + \frac{1}{2} \sum_{i,j=1}^{3N} \left(\frac{\partial^2 V}{\partial q_i \partial q_j}\right)_0 q_i q_j + \frac{1}{3!} \sum_{i,j,k=1}^{3N} \left(\frac{\partial^3 V}{\partial q_i \partial q_j \partial q_k}\right)_0 q_i q_j q_k + \cdots \ .$$

$$\tag{IV.2}$$

Here, q_i denote the massweighted displacements of the nuclei from their equilibrium positions[1] and N is the number of atoms in the molecule.

---

[1] For the first atom with mass m_1: $q_1 = \sqrt{m_1} \cdot \Delta x_1, q_2 = \sqrt{m_1} \cdot \Delta y_1, q_3 = \sqrt{m_1} \cdot \Delta z_1$, for the second atom with mass m_2 : $q_4 = \sqrt{m_2} \cdot \Delta x_2, \dots$. $\Delta x_i = x_i - x_{i0}$ etc. is the displacement from the equilibrium position in Cartesian coordinates.

For small displacements, the nuclei experience a harmonic potential. The corresponding vibrational mode n with angular frequency ω_n has equidistant energy levels E_n [136]:

$$E_n = \hbar\omega_n \left(v_n + \frac{1}{2}\right) . \tag{IV.3}$$

For the harmonic oscillator approximation, electric dipole transitions are only allowed between neighbouring vibrational levels [136, 137]: $\Delta v_n = \pm 1$.

For larger displacements, i.e. higher vibrational excitations, however, the anharmonicity of the potential needs to be taken into account. The vibrational energy of the molecule thus reads (without mode degeneracies) [136]

$$E = \hbar\left[\sum_n \omega_n \left(v_n + \frac{1}{2}\right) + \sum_{m,n} x_{m,n} \left(v_m + \frac{1}{2}\right)\left(v_n + \frac{1}{2}\right) + \cdots\right] \tag{IV.4}$$

$x_{m,n}$ are the anharmonic constants. The diagonal elements $x_{n,n}$ describe the anharmonic shifts of a mode n, the off-diagonal elements $x_{m,n}$ are due to couplings between modes n and m. Thus, the vibrational energy levels of a mode are no longer equidistant and also depend on the vibrational excitation of other modes.

An analytic expression for the anharmonic potential of the mode n that is often used, is the one dimensional Morse potential [135, 138], see Fig. IV.3, with

$$V(Q_n) = D_{e,n}\left[1 - e^{-a_n(Q_n - Q_{eq})}\right]^2 . \tag{IV.5}$$

$D_{e,n}$ is the dissociation energy, a_n a constant describing the steepness of the potential and $\left(Q_n - Q_{eq}\right)$ the displacement along the normal mode coordinate Q_n from the equilibrium position Q_{eq}, cf. App. C. 1[1]. All quantities refer to the n-th vibrational mode.

The energy levels of an isolated vibrational mode n, that does not couple to other modes, are then [135]

$$E_n = \hbar\omega_n \left(v_n + \frac{1}{2}\right) - x_e \hbar\omega_n \left(v_n + \frac{1}{2}\right)^2 \tag{IV.6}$$

with the anharmonicity constant $x_e = \frac{\hbar\omega_n}{4D_{e,n}}$.

The frequency of a transition $v_n \rightarrow v_n + 1$ between two vibrational levels depends on the vibrational quantum number v_n and decreases with increasing vibrational excitation v_n

$$\omega(v_n \rightarrow v_n + 1) = \omega_n - 2\omega_n x_e(v_n + 1) \tag{IV.7}$$

For an anharmonic potential, the selection rule $\Delta v_n = \pm 1$ for electric dipole transitions is not that strict any longer and also overtone transitions with $\Delta v_n = \pm 2, \pm 3, \dots$ are allowed. However, even if not completely suppressed, those overtone transitions are still weak. For a 2-atomic molecule, for example, the relative intensities of transitions with $\Delta v = \pm 1 : \pm 2 : \pm 3$ scale like $1 : x_e : x_e^2 : \dots$, x_e is a small number of the order 10^{-2} [135].

---

[1]For a simple 2-atom molecule, there is only one vibrational mode possible and $\left(Q_n - Q_{eq}\right)$ reduces to $\left(R - R_{eq}\right)$, with R the interatomic distance and R_{eq} the interatomic distance at equilibrium.
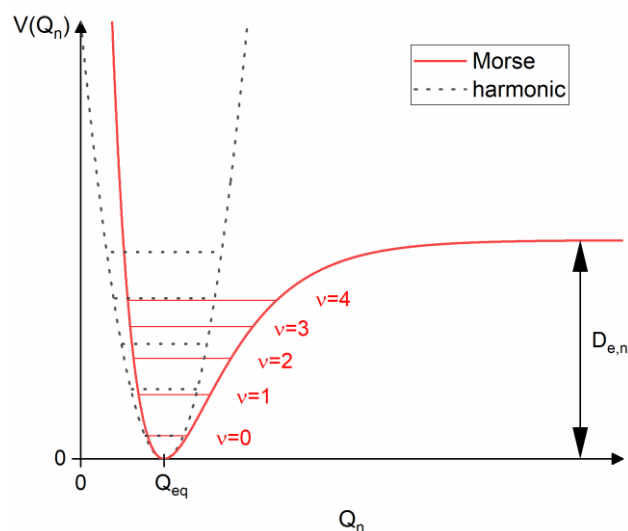
Figure IV.3: *Morse potential and harmonic potential along the normal mode coordinate Q_n. $Q_n = Q_{eq}$ corresponds to the equilibrium position. The vibrational energy levels in case of the Morse potential are not equidistant, in contrast to the vibrational energy levels of the harmonic potential.*

IV. 2.3 Vibrational ladder climbing

An obvious way to achieve excitation of vibrational modes in a molecule is heating. However, by just heating up the molecule, the energy will be distributed statistically among the molecule's various modes [109]. In contrast, a method to drive a molecule to a highly excited level of a certain *selected* vibrational mode is vibrational ladder climbing. Vibrational ladder climbing is a multiphoton process, in which vibrational energy levels are successively excited by a MIR laser pulse that is resonant to the selected mode, cf. Fig. IV.4 [19, 21]. Ultrafast MIR pulses are particularly suited for that task for two reasons. First, they have a broad spectrum that covers the range of transition frequencies of both low and high lying levels. Second, they are short enough to overcome relaxation processes that decrease the population in the desired vibrational levels. Such relaxation processes can be e.g. energy loss to the surrounding solvent or a drain of the energy originally deposited in the selected mode into other modes of the same molecule. The latter is called intramolecular vibrational energy redistribution (IVR).

Ladder climbing can be optimised (suppressed) by using negatively (positively) chirped pulses [21]. For negatively chirped pulses, high frequencies that match the transitions in the lower part of the ladder, interact first with the molecules; whereas low frequencies, corresponding to higher lying vibrational transitions, only interact with the molecules when there is already some population in intermediate levels. A slight redshift of the excitation spectrum with respect to the fundamental $v = 0 \rightarrow v = 1$ transition is also beneficial for ladder climbing to high levels [20, 21].

The pictorial description given in the above paragraph can also be understood in terms of density matrix elements. It is pointed out in Refs. [115, 116] that the absorption rate from a lower to an upper state is proportional to the product of the real electric field and the imaginary part of the coherence $\rho_{v+1,v}$ between these states
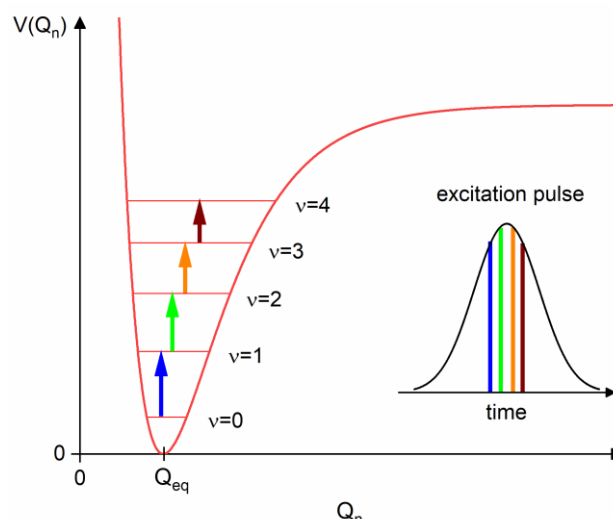
Figure IV.4: *Ladder climbing mechanism for an anharmonic potential. The excitation to high vibrational levels occurs via stepwise absorption of multiple photons. The transition frequencies between adjacent vibrational levels decrease with higher excitation (indicated by the red-shifting colour of the arrows). Ladder climbing can be enhanced by adjusting the excitation pulse shape to the sequence of the vibrational mode's transition frequencies, as indicated by the inset.*

$$\frac{d(\rho_{v+1} - \rho_v)}{dt} \propto E(t) \cdot \text{Im}(\rho_{v+1,v}) \ . \tag{IV.8}$$

ρ_{v+1} and ρ_v denote the population in the upper and lower state, respectively. If $E(t)$ is in resonance with the absorption, the coherence varies slowly and the product on the right hand side of Eq. IV.8 has positive sign for the largest part of the pulse duration. This is the case if the instantaneous frequency evolves according to the decreasing transition frequencies with larger v, i.e. for a negatively chirped pulse. In consequence, population is efficiently transferred from the lower to the upper state. In contrast, if $E(t)$ is out of resonance, the right hand side of Eq. IV.8 frequently switches sign and efficient popultion transfer from lower to upper state is prevented.

In the extreme case, vibrational ladder climbing can even result in bond breakage and thus in molecular dissociation without electronic excitation [19-22].

IV.2.4 Franck-Condon principle

In Sec. IV.2.2 it was pointed out that for vibrational transitions of a molecule within the *same* electronic state, transitions with $\Delta v = \pm 1$ are favoured. Transitions between *different* electronic states are also accompanied by a change of the vibrational excitation of the molecule, $v'' \rightarrow v'$, with v'' and v' the vibrational quantum number in the electronic ground and excited state, respectively. However, there are no strict selection rules concerning the change in vibrational quantum number for those vibronic transitions. For dipole transitions, the transition probability between different vibrational states $P_{v'' \rightarrow v'}$ is rather proportional to the Franck-Condon integral [135, 139]:

$$P_{v''\to v'} \propto \left| \int_{-\infty}^{\infty} \psi_{vib,v''}(\vec{R})\psi_{vib,v'}(\vec{R})dV \right|^2 . \qquad (IV.9)$$

$\vec{R}$ is the set of all nuclear coordinates and the integration extends over the volume of the molecule. Eq. IV.9 has a simple physical interpretation: The transition probability depends on the overlap between the vibrational wavefunctions in the electronic ground and excited state, see Fig. IV.5 . The electronic transition in Fig. IV.5 does not change the internuclear distances, i.e. it happens vertically. This is a consequence of the Born-Oppenheimer approximation, which is rooted in the fact that the electrons move much faster than the nuclei. Thus, the nuclei will not change their position during the electronic transition, but will only afterwards take their new equilibrium positions.
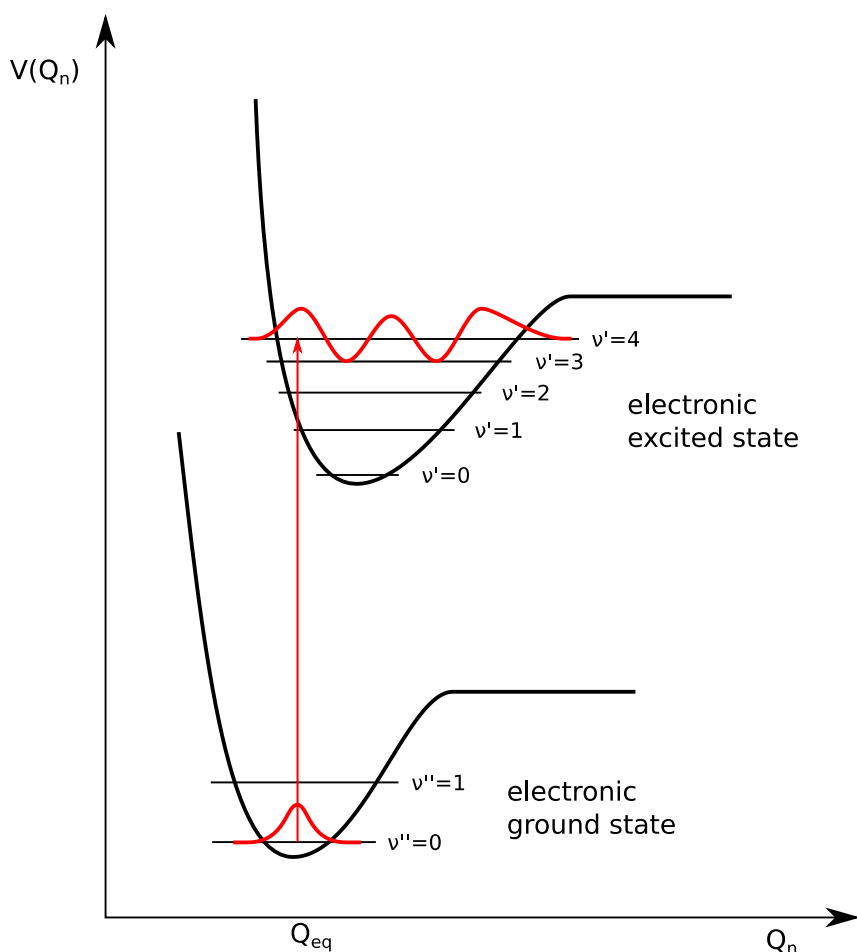
Figure IV.5: *Franck-Condon principle. An electronic transition is accompanied by a change in the vibrational state. The strength of the transition depends on the wave function overlap of the initial vibrational state with the final vibrational state. In the depicted example, there is a strong overlap for the transition $v'' = 0 \to v' = 4$. On the timescale of the electron excitation, the spatial structure (bond distances and angles) of the molecule does not change. Q_{eq} denotes the equilibrium position in the electronic ground state.*

IV. 3   Measurement technique: Transient absorption

IV. 3.1   Priciple of transient absorption

TA spectroscopy is a technique to monitor photoinduced changes in the absoprion spectrum of a sample and follow those changes in time. This can provide valuable information about a photoreaction's dynamics, such as the lifetime, characteristic absorption features and decay routes of excited states.

In a classical TA experiment, two pulses are involved: A strong pump pulse and a weak probe pulse. The time delay τ between pump and probe pulse can be scanned. The pump induced changes in the sample's absorption spectrum at given τ, $\Delta A(\lambda, \tau)$, are assessed by recording the spectrum of the probe pulse after the sample with and without precedent pump pulse [16]

$$\Delta A(\lambda, \tau) = A(\lambda, \tau)_{\text{pump on}} - A(\lambda, \tau)_{\text{pump off}}$$

$$= -\log_{10}\left(\frac{I(\lambda, \tau)_{\text{pump on}}}{I(\lambda, \tau)_{\text{pump off}}}\right) \tag{IV.10}$$

A is the absorbance of the sample and I the intensity of the probe pulse recorded by the detector. The switching between *pump on* and *pump off* can be realized by a mechanical chopper wheel that blocks every other pump pulse. For τ much longer than the cross correlation between pump and probe pulse, the measured transient spectrum $\Delta A(\lambda, \tau)$ is a superposition of several contributions (cf. Fig. IV.6) [16, 140]:

1. Ground state bleach (Fig. IV.6 a)): The pump has driven some molecules in the sample volume from the ground state to an excited state. Thus, there are fewer molecules left in the ground state that can absorb the probe pulse. In consequence, the absorption of the sample decreases. The shape of the ground state bleach corresponds to the negative of the molecule's stationary absorption spectrum.

2. Stimulated emission (Fig. IV.6 b)): The probe pulse can stimulate emission from the populated excited state back to the ground state. As the emitted photons propagate in the same direction as the probe pulse, the recorded intensity on the detector increases.

3. Excited state absorption (Fig. IV.6 c)): The excited state population of the sample molecules can be excited to an even higher lying level by the probe pulse and the absorption at the corresponding transition wavelength increases.

4. Contributions by newly emerging photoproduct (Fig. IV.6 d)): If the pump pulse triggers a photoreaction, the emerging photoproduct will have its own absorption spectrum and the probe pulse can induce transitions of the photproduct molecules. This leads to increased absorption at wavelengths where the photoproduct absorbs more than the reactant and to decreased absorption where the product absorbs less than the reactant, similar to excited state absorption and ground state bleach, respectively.

As the probe pulse is weak compared to the pump pulse, the probe does not significantly alter the population distribution generated by the pump pulse.

The aforementioned contributions to the TA signal are observed in a sample that exhibits absorption at the pump wavelength. However, when pump and probe pulse overlap in time, there is a TA signal even in transparent media. This signal is the so-called coherent
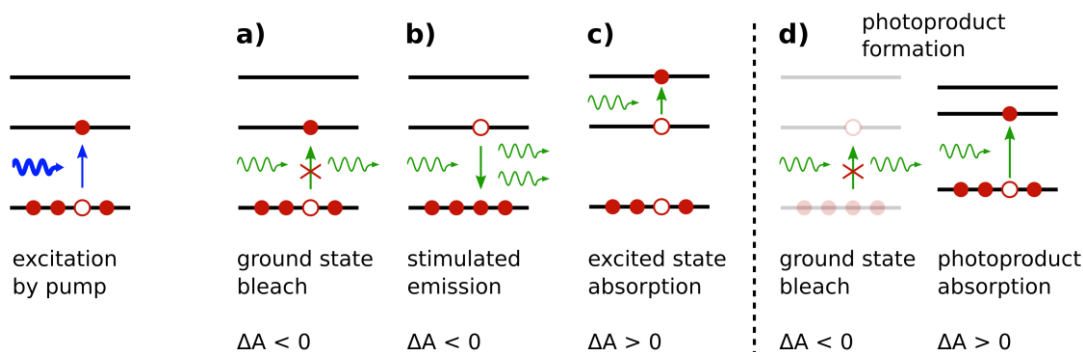
Figure IV.6: Contributions to the TA signal. The pump pulse (blue) induces a transition in the molecule (left). The molecule's absorption spectrum is then examined by a probe pulse (green) and changes via several mechanisms: a) Ground state bleach, b) stimulated emission, c) excited state absorption. If a photoproduct is formed (d)), the photoproduct has its own absorption spectrum that affects the detected probe pulse spectrum (right in d)). After photoproduct formation, the converted molecule in general no longer absorbs at the original wavelengths of the reactant, leading to a bleach signal (left in d), fainted).

artefact (CA). Three mechanisms are the source of the CA at pump-probe overlap. Those are two-photon absorption, stimulated Raman amplification and cross-phase modulation [141].

Another type of CA arises when the phase relaxation time of an absorption is longer than the probe pulse length. This type of CA is called perturbed free induction decay (PFID) [142, 143]. PFID only occurs for $\tau < 0$, i.e. when the probe pulse arrives at the sample before the pump pulse. Due to the long dephasing times of vibrational transitions, PFID is mostly observed in experiments with IR or MIR probe pulses.

The CA usually is an unwanted contribution to the recorded TA trace, as it distorts the kinetic signal of the sample molecule around time zero. Nevertheless, the measurement of the CA at pump-probe overlap in pure solvent provides useful information about the experimental setup. From the CA measurement, the cross correlation between pump and probe pulse can be estimated, and with that the instrument response function. Furthermore, the measured TA trace of the sample can be corrected for group delay dispersion (GDD) that is introduced by optics in the setup, as will be illustrated in the next section.

IV. 3.2 Time zero correction

A TA experiment aims to observe the changes in a sample at delay τ after excitation by the pump pulse. It is therefore convenient to set the arrival time of the pump pulse to $\tau = 0$. The induced changes are probed by a (spectrally broad) probe pulse. Ideally, the probe pulse would be transform limited and all its spectral components would arrive at the sample simultaneously. However, the reality in the lab often looks differently and the probe pulse shows considerable temporal dispersion. This leads to a slanted wavelength vs. delay representation of the TA trace, as shown in Fig. IV.7 (left), which makes further analysis cumbersome.

Fortunately, the recorded TA trace can be corrected for that distortion. This is done by measuring a trace of the CA in pure solvent. The CA trace only has contributions when pump and probe pulse overlap in time, cf. Fig. IV.7 (middle). A 3rd order polynomial is fitted to the CA trace to determine the time of pump/probe overlap at each wavelength:
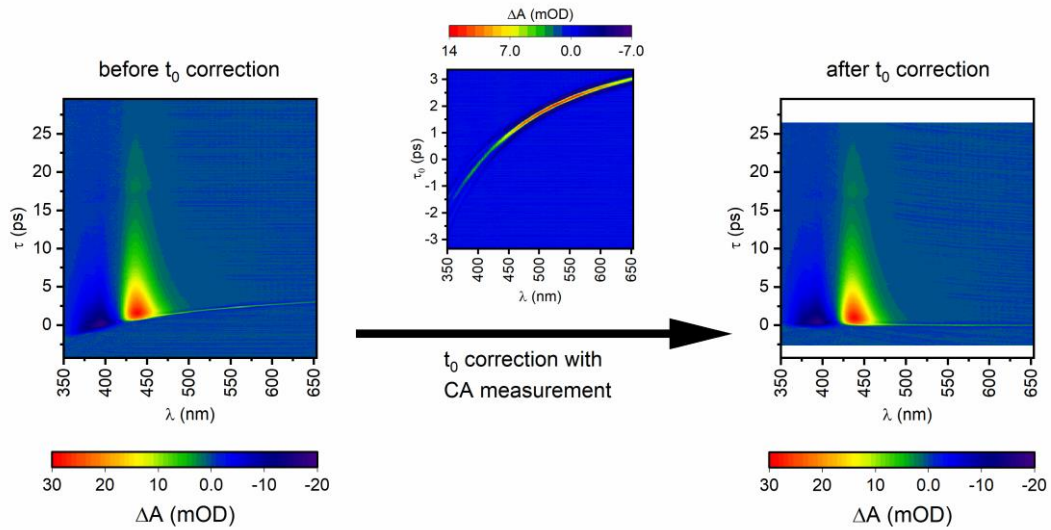
Figure IV.7: *Time zero (t_0) correction of a TA trace. Left: TA trace before t_0 correction. Dispersion of the probe pulse is clearly visible. Middle: Measurement of the CA gives a reference of temporal overlap between pump and probe pulse. Note the different scaling compared to the sample traces. Right: TA trace after t_0 correction. The TA signal starts at $\tau = 0$ for all wavelengths. Note the clipping at the edges of the delay axis.*

$$\tau_0(\lambda) = \sum_{n=0}^{3} a_n \lambda^n \quad . \tag{IV.11}$$

The time axis that was determined in the measurement, $\tau_{meas}(\lambda)$, is then corrected for $\tau_0(\lambda)$ to give the corrected time axis

$$\tau(\lambda) = \tau_{meas}(\lambda) - \tau_0(\lambda) \tag{IV.12}$$

In this way, the transients at each wavelength are shifted in time separately, according to the time delay of the respective spectral component of the probe pulse. Thus, the resulting TA trace is corrected for the probe pulse's dispersion. In addition, pump and probe overlap at $\tau = 0$, cf. Fig. IV.7 (right).

IV. 3.3 Baseline correction

The recorded TA trace might be contaminated by contributions that have nothing to do with the dynamics of the sample under investigation. Such contributions could arise for example from scattered pump light that reaches the detector without having interacted with the probed sample volume. Consequently, those kind of contributions give a constant spectral offset to the TA trace. Subtracting a spectral baseline rectifies the measured TA trace from these contaminations. The baseline is obtained by averaging the recorded values in an adequate range before time zero for each wavelength separately.

IV. 3.4 Post-pulse correction

For the experiments that will be presented in Sec. IV. 6.2, it was found that in the t_0 corrected MIR pump/WL probe TA trace, a prominent feature is visible around 18 ps, where the magnitude of the signal increases again (Fig. IV.8 a)). Consequently, the transients show a bump at that delay (Fig. IV.8 b)). This bump is not due to any molecular dynamics, but
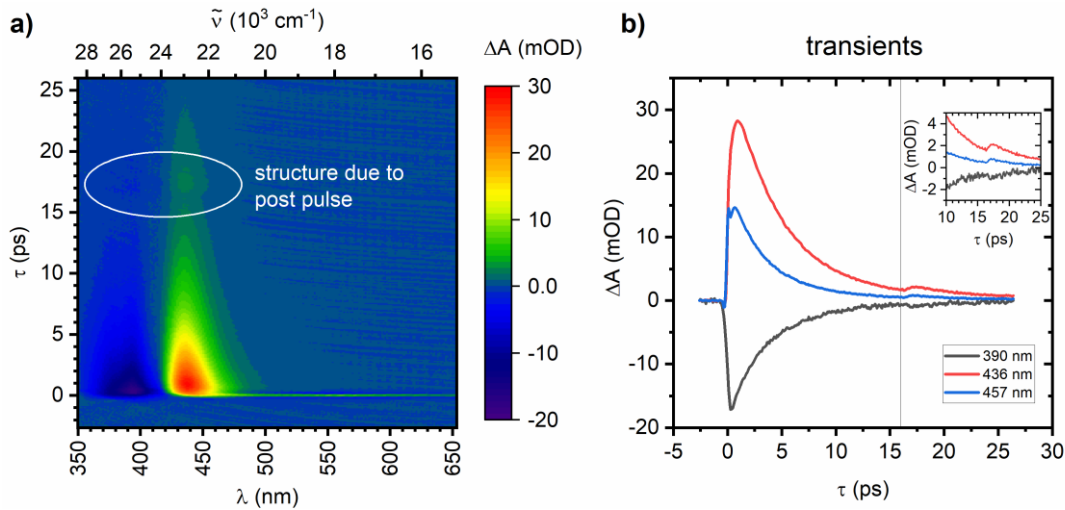
Figure IV.8: *a) MIR post-pulse contaminated TA trace. A feature with increased signal magnitude is visible around 18 ps. b) The post-pulse manifests itself as bump in the transients. The vertical line at 16 ps is a guide for the eye. The inset shows a close-up view of the bumps.*

originates from a weak, unwanted MIR post-pulse. This was confirmed by measurements with the flow cell filled with the solvent only. These revealed a second, weaker CA around 18 ps. Furthermore, similar features were also visible in the MIR pump/MIR probe traces, i.e. the unwanted pulse must come from the MIR and not from the WL. The time delay between main pulse and post-pulse suggests that the post-pulse comes from a reflection within the MIR generating AGS crystal in the TOPAS NDFG stage, cf. Sec. IV. 5.1.
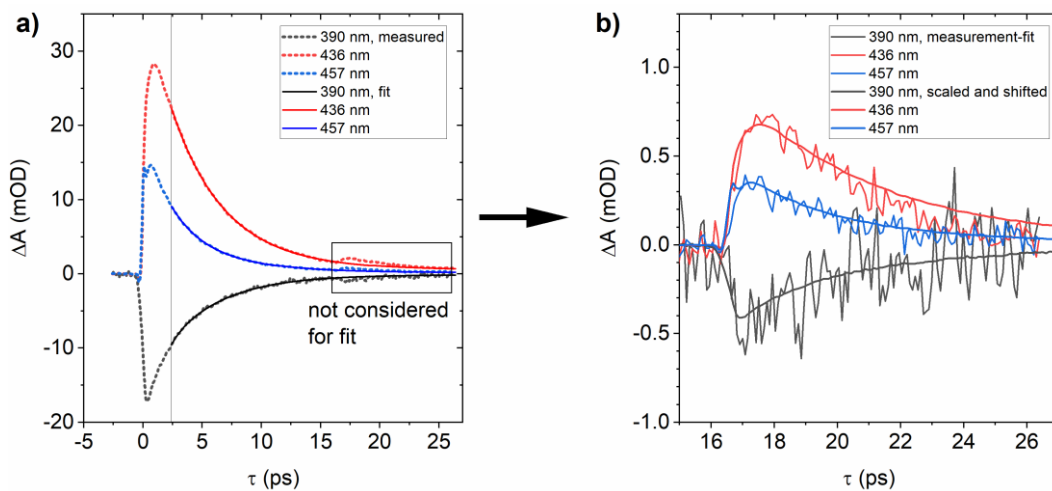
Figure IV.9: *a) Measured transients (dotted) and corresponding fits (solid line) in order to extrapolate the transients triggered by the main pulse to delays with post-pulse contamination. A biexponential function with offset is used as fit function and only data points after $\tau = 2.4$ ps (vertical line) are used for the fits. Delays with a significant contribution of the post-pulse (16-26 ps) are also not considered for the fit. b) Contributions of the post-pulse to the transients, calculated as the difference between the measured transients and the extrapolation done by the fits in a). Also shown are the corresponding scaled and time shifted transients from earlier delays. The scaling factor of 0.024 and time shift of 16.6 ps are the same for all wavelengths.*

As the post-pulse most likely originated from the MIR generation stage, there was no easy way to spatially separate it from the main pulse; the post-pulse would have always been present in the measurements. Thus, the measured traces were later corrected for that post-pulse in the following way: The measured trace is a superposition of the dynamics triggered by the main pulse and the artefacts introduced by the post-pulse. Since the post-pulse causes the same dynamics as the main pulse previously, the post-pulse artefact can be seen as a scaled and time shifted version of the transient initiated by the main pulse. The measured trace can thus be corrected for the post-pulse by subtracting a scaled and time shifted version of itself from each single transient.

Fig. IV.9 illustrates that the post-pulse contribution can indeed be excellently approximated by scaling and time shifting the transient at earlier delays: Three measured transients are fitted by a biexponential fit with offset. For the fit, only data points are considered that are well beyond any CA and do not include post-pulse features. There is no physical meaning attributed to this fit, it is only to extrapolate the transient triggered by the main pulse to delays where the transient is contaminated by the post-pulse in order to have an idea how it would look like without the unwanted post-pulse. Fig. IV.9 b) shows that the difference between the measured transients and the fits, i.e. the contributions of the post-pulse, can
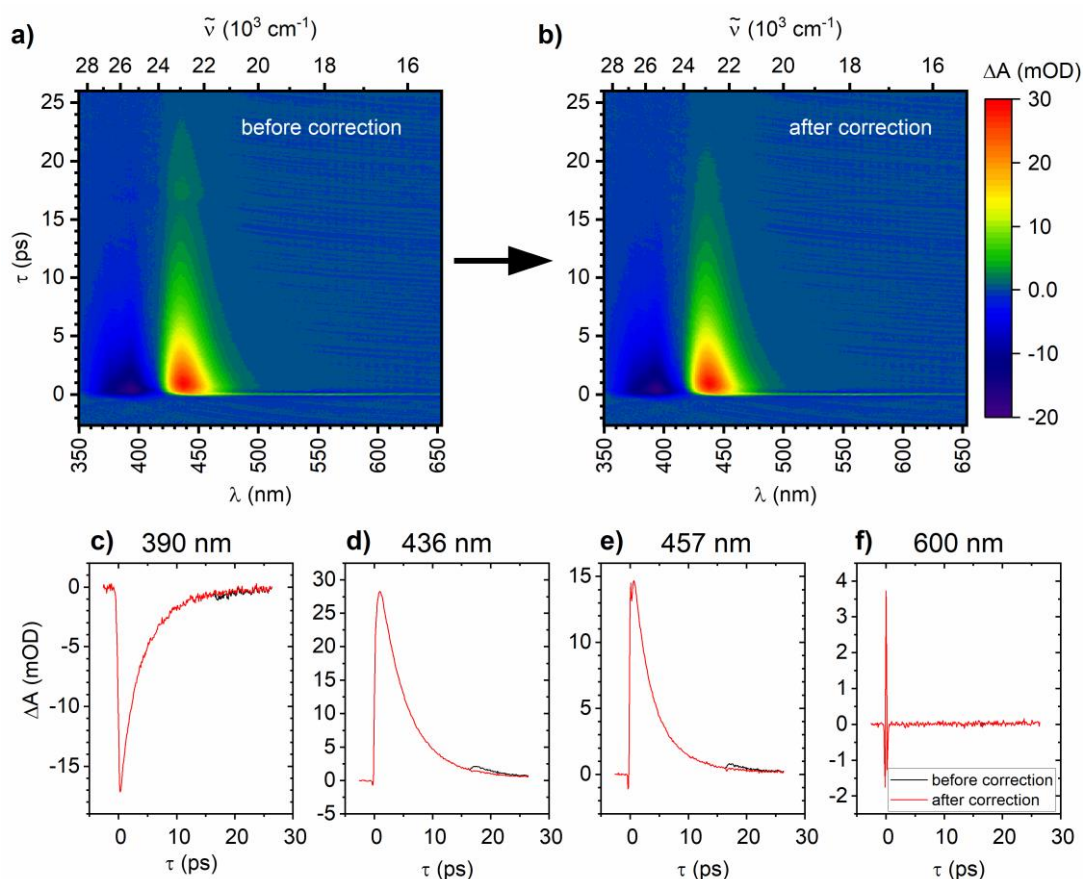
Figure IV.10: *a) t_0 corrected TA trace before post-pulse correction. b) Trace after post-pulse correction. The correction was done by subtracting a scaled and time shifted replica of each transient from itself. The scaling factor and time shift are the same for every transient. c)-f) Chosen transients before (black) and after (red) post-pulse correction. On the one hand, the bump caused by the post-pulse is successfully removed by the correction (c)-e)). On the other hand, the correction does not introduce new artificial features (f)).*

be well described by a scaled and time shifted version of the corresponding transients before the post pulse. Fig. IV.10 shows the non-post-pulse-corrected trace face to face with the corrected trace.

IV. 4 Methods

In order to investigate the question how excitation of the C=N=N stretch mode influences the photoreaction of DNQ, different types of TA experiments were performed. Each single experiment is supposed to answer a certain aspect of this question. The different partial aspects can then be merged to give a picture about the impact of the C=N=N stretch vibration on DNQ's photoreaction. An overview of the experiments that have been performed and which aspect they are expected to answer is given in this section.

In total, pulses in three spectral regions have been employed:

- Broadband MIR pulses centred at 4.8 μm (2100 cm^{-1}). These were used for vibrational excitation of the C=N=N stretch mode. Furthermore, they were also used as probe for both the transient vibrational population of the reactant and the formation of the ketene photoproduct, which as well shows characteristic vibrational features in this spectral region.
- WL pulses spanning from below 350 nm to well above 600 nm. These were used as probe.
- UV pulses promoting the DNQ molecules from the electronic ground state to the electronic excited state. Those pulses were centred at 393 nm and 433 nm, respectively. The excitation pulse around 433 nm will be called UV pulse in this chapter, even though it is already in the visible. This is, firstly, to better distinguish it from the visible WL probe pulse and secondly, to have a common naming of the pulses around 393 nm and 433 nm, which both serve to excite DNQ from the electronic ground state to the electronic excited state.

The combination of these distinct laser pulses to the individual types of TA experiments is described in the following.

IV. 4.1 MIR pump/MIR probe

As described in Sec. IV. 2.1, a UV/Vis photon can induce a photoreaction, in which the N_2 group is cleaved from the DNQ molecule. In this photoreaction, the DNQ molecule is excited to the electronically excited state by the UV/Vis photon. It is desirable to know whether the cleavage of the N_2 group is also possible without the DNQ molecule entering the electronically excited state, but staying in the electronic ground state all the time. A possible scheme for such an elecronic ground state reaction is vibrational ladder climbing, see Sec. IV. 2.3. To this aim, it seems reasonable to choose the C=N=N stretching vibration for excitation (around 2118 cm^{-1} [29]), as it is the N_2 group that shall finally be cleaved from the DNQ. Cleavage of the N_2 group by vibrational excitation of the C=N=N stretch mode has been demonstrated in experiments on diazomethane (CH_2N_2) in the gas phase. In that experiment, 5-6 vibrational quanta in the C=N=N stretch mode were necessary to dissociate CH_2N_2 into CH_2 and N_2 [20].

In order to figure out whether N_2 cleavage in the electronic ground state via vibrational ladder climbing is possible in DNQ as well, DNQ was excited by a MIR pulse around 2118 cm^{-1}. 2118 cm^{-1} corresponds to the transition $v = 0 \rightarrow v = 1$ of the C=N=N stretching vibration [29]. The MIR pump pulse's spectrum was broad enough to cover the expected range of excitation frequencies necessary for population of high vibrational states. The MIR spectrum was also slightly red shifted with respect to the DNQ absorption maximum, see Fig. IV.11 c). The population of the vibrational levels of the C=N=N stretch mode was probed by a MIR probe pulse. Furthermore, the MIR probe was able to detect a potentially emerging ketene, which exhibits an absorption band at 2128 cm^{-1} [29], see Fig. IV.11 c). MIR pump and probe were generated in the same source and were separated by a beamsplitter, see Sec. IV. 5.1. Their spectra were thus degenerate.
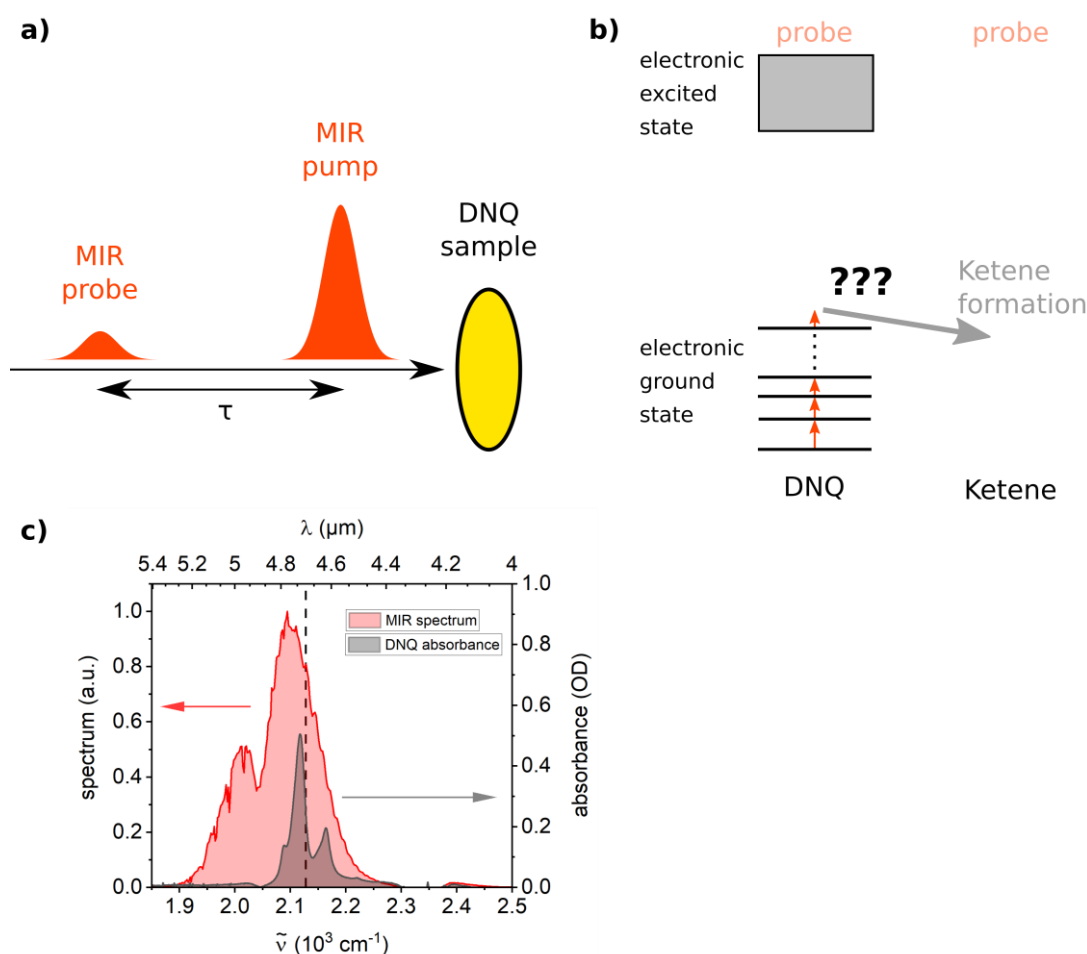
Figure IV.11: *Scheme of the MIR pump/MIR probe experiment. a) Pulse sequence. Pump and probe are separated by delay τ. b) Involved energy levels. Excitation only happens in the electronic ground state. The spectrally broad MIR probe is able to probe both the occupation of different vibrational energy levels of DNQ and a potentially emerging ketene photoproduct. The electronically excited state is not involved in this experiment. c) MIR spectrum (red, left axis) and DNQ MIR absorption spectrum (grey shaded, right axis). The dip around 2040 cm^{-1} in the measured MIR spectrum comes from absorption of MeOH in the sample cell. The DNQ absorption spectrum has its main peak at 2118 cm^{-1} and exhibits side peaks. The dashed line indicates the position of a potentially emerging ketene band.*

IV. 4.2 MIR pump/WL probe

To address the question whether vibrational excitation of the C=N=N stretch mode influences the electronic absorption of DNQ, a TA experiment with a MIR pump and WL probe pulse was carried out. Special attention was given to which parts of the UV/Vis absorption spectrum are affected the most by vibrational excitation in the electronic ground state. The excitation spectrum of the MIR pulse was virtually the same as in Sec. IV. 4.1.

The steady state UV/Vis absorption spectrum of DNQ in MeOH shows several peaks of absorption: around 400 nm, between 310-325 nm and a strongly rising edge below 290 nm. However, the WL pulses available in the experiment could only reliably probe the spectral region above 350 nm, as depicted in Fig. IV.12 c).

The information gained in this measurement was used later in a vibrationally mediated photodissociation (VMP) experiment to tune the excitation wavelength of a UV/Vis pump pulse accordingly in order to enhance the ketene photoproduct formation by MIR pre-excitation, see Sec. IV. 4.4.
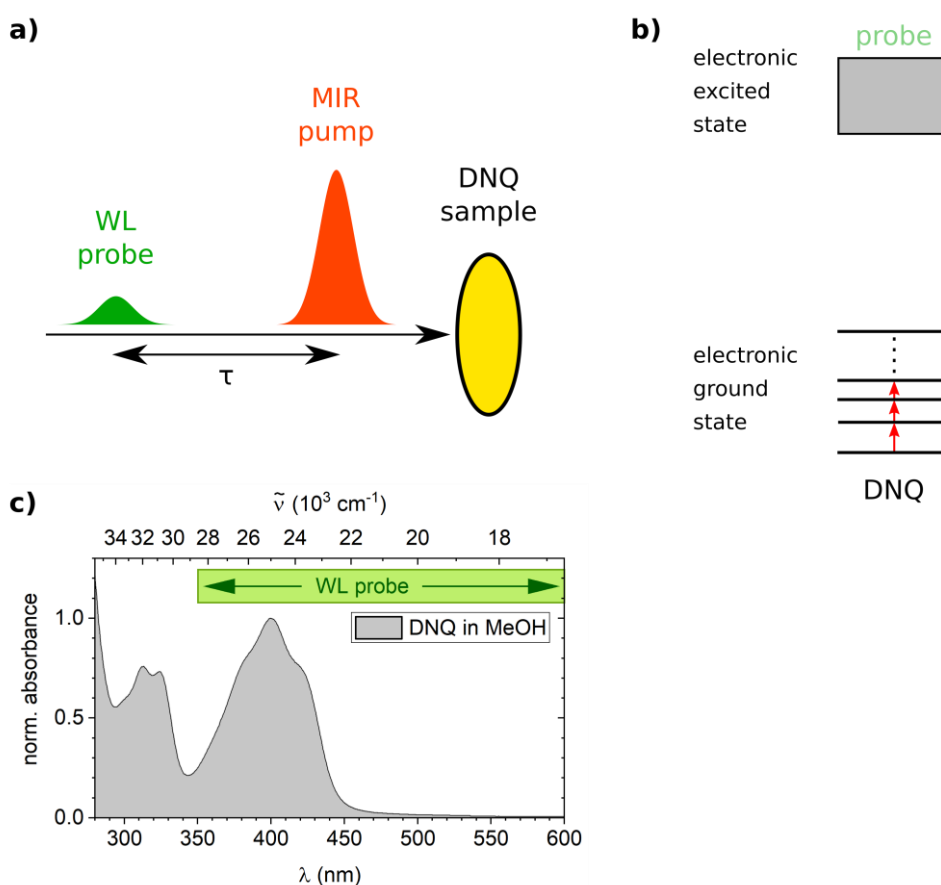
Figure IV.12: *Scheme of the MIR pump/WL probe experiment. a) Pulse sequence. b) Involved energy levels. The WL probing occurs between the electronic ground and excited level. c) UV/Vis absorption spectrum of DNQ in MeOH. The spectrum is normalised to the absorbance at 400 nm. The green bar denotes the range of the WL probe spectrum.*

IV. 4.3 UV pump/WL probe

In order to identify the features that are imprinted on the WL probe spectrum by the photoreaction of DNQ to ketene, a TA measurement with a UV pump and WL probe pulse was performed, see Fig. IV.13. No MIR pulses were involved in this experiment. This measurement will later help to interpret the results of a VMP experiment with combined vibrational pre-excitation and electronic excitation, cf. Sec. IV. 4.4. As will be shown in Sec. IV. 6.3, ketene formation can be probed indirectly with WL via a non-recovering bleach of the DNQ absorption.
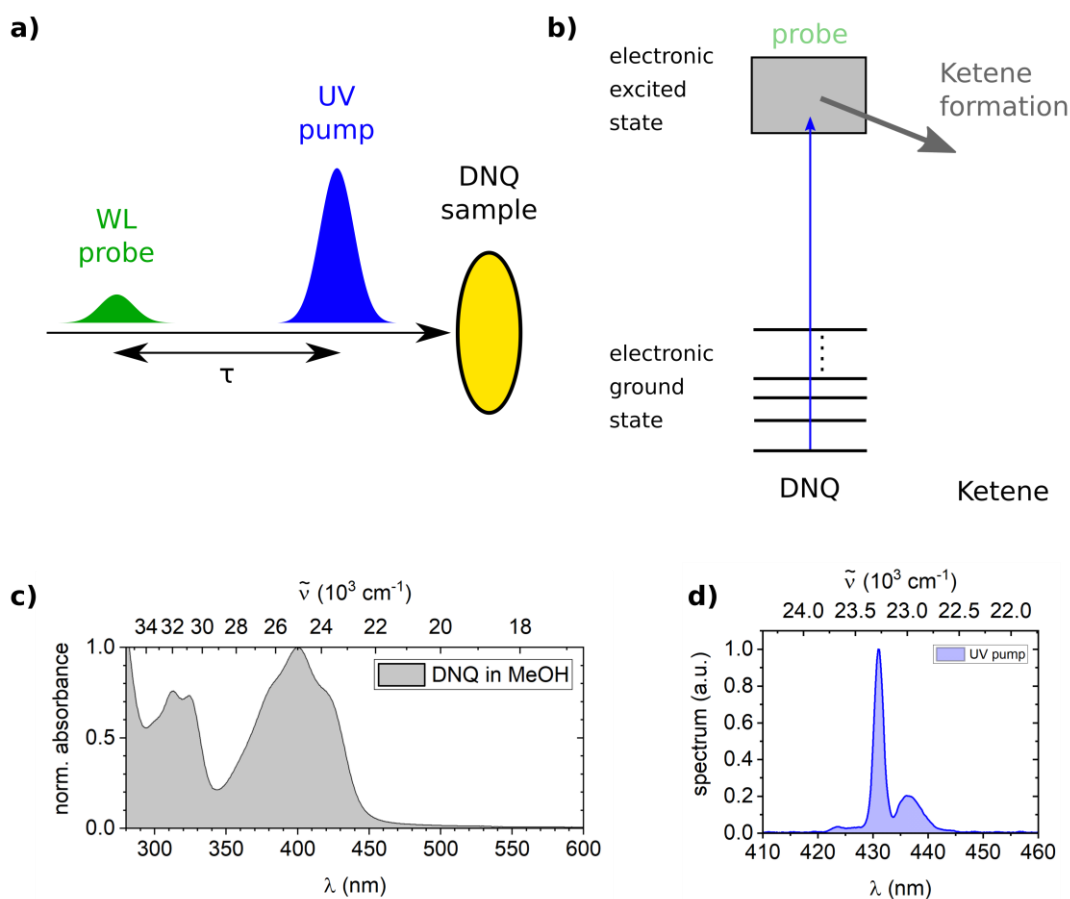
Figure IV.13: *Scheme of UV pump/WL probe experiment. a) Pulse sequence. b) Involved energy levels. The UV pulse triggered the reaction DNQ to ketene. The WL probed the bleach of the DNQ. c) UV/Vis absorption spectrum of DNQ. d) UV excitation spectrum. The excitation wavelength was set to the edge of the DNQ absorption spectrum.*

IV. 4.4 MIR pre-pump/UV pump/WL probe

To finally find out whether vibrational pre-excitation of the C=N=N stretch mode of DNQ can enhance or suppress ketene formation in the UV induced photoreaction, the photoproduct yield was compared for UV induced reactions with and without vibrational pre-excitation. To this aim, a VMP experiment with MIR pre-pump, UV pump and WL probe was performed and measurements with the MIR pre-pump blocked and open were taken. The pulse sequence applied for a VMP measurement with MIR pre-pump is shown in Fig. IV.14 a). A MIR pulse excites the C=N=N stretching vibration. At time t after the MIR excitation, a UV pulse promotes the DNQ molecules to the electronically excited state. After
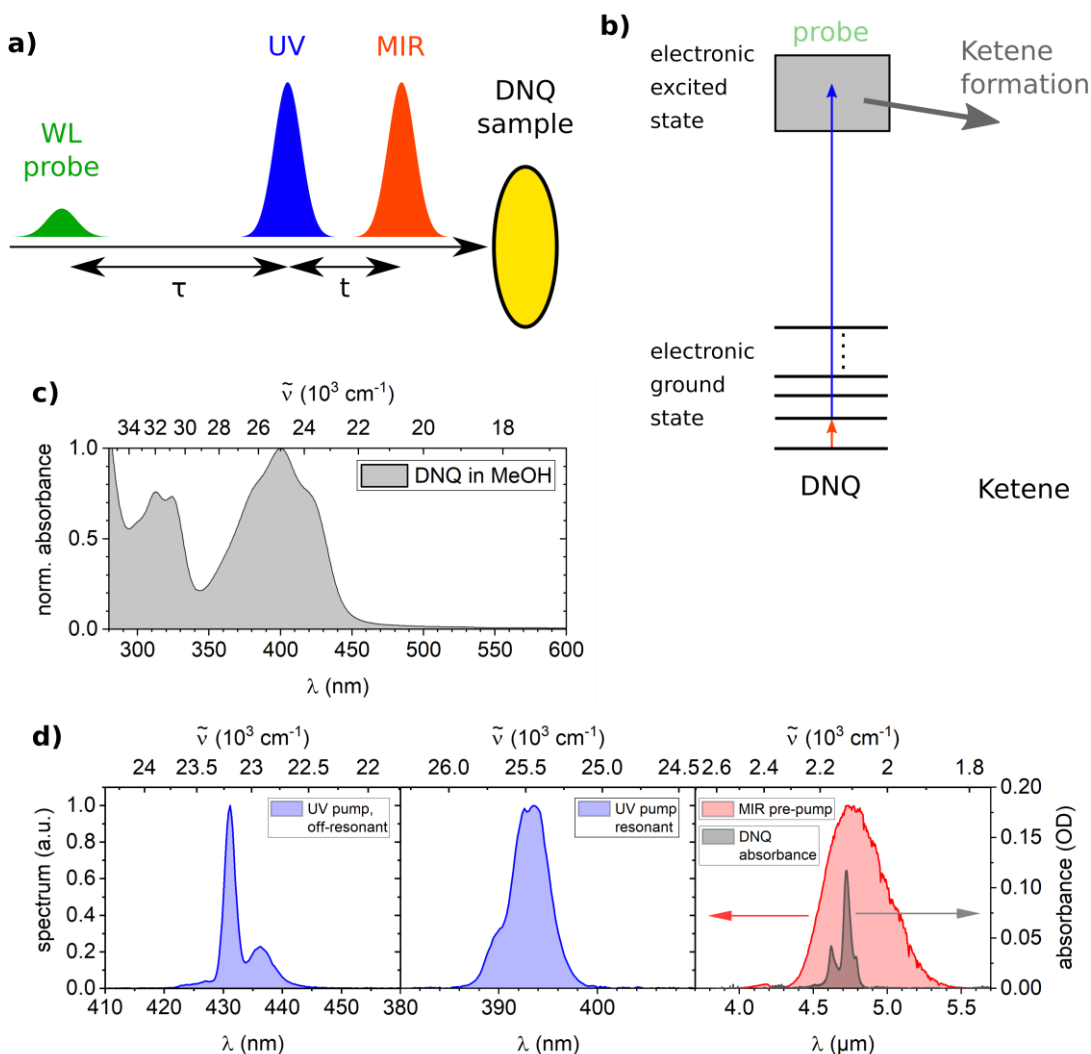
Figure IV.14: *Scheme of the MIR pre-pump/UV pump/WL probe VMP experiment. a) Pulse sequence. Two pulse delays are in action: The delay between MIR pre-pump and UV pump is denoted t, whereas the delay between UV pump and WL probe is denoted by τ. Positive t means that the MIR pulse arrives before the UV pulse at the sample; for negative t, the UV pulse arrives first. b) Involved energy levels. The MIR pre-pump first populates a vibrational energy level in the electronic ground state, from which the UV pump excites the molecules into the electronic excited state. In the figure, MIR excitation to the first vibrational level is shown, but excitation to other vibrational levels is also possible. Ketene formation takes place from the electronic excited state. The WL pulse probes the bleach of the DNQ. c) UV/Vis absorption spectrum of DNQ. It has a peak around 400 nm. d) Excitation spectra. Left: UV excitation spectrum at the edge of the DNQ absorption. The UV pump pulse spectrum has a double peak structure with the stronger peak at 431 nm and the weaker one at 436 nm. The spectrum's centre of mass is at 433 nm. Middle: UV excitation set to the peak of the DNQ absorption. The spectrum was centred at 393 nm. Right: MIR pre-pump spectrum (red, left y-axis) and MIR DNQ absorption (grey, right y-axis). Note that the x-axis shows wavelength and not wavenumber. In contrast to Fig. IV.11, there is no dip at 4.9 μm (2040 cm^{-1}), as the spectrum was measured before passing through the flow cell filled with MeOH. The lower DNQ absorbance compared to Fig. IV.11 is due to lower concentration used in the measurements with WL probe.*

electronic excitation, part of the DNQ molecules form the respective ketene. The change in absorbance is probed by a WL pulse at delay τ after the UV pulse. The corresponding Jablonski diagram is displayed in Fig. IV.14 b). The broadband MIR spectrum (Fig. IV.14 d)) was centred at 4.8 μm and reached beyond 5 μm. As will be shown in Sec. IV. 7.1.1, the MIR spectral width thus enables vibrational excitation to levels with $v > 1$.

The change in photoproduct yield due to vibrational pre-excitation was determined for several delays t between MIR pre-pump and UV pump.

Details on how comparability between the measurements with and without MIR pre-pump and between the different delays t was ensured are given in Sec. IV. 5.2.

The experiment was carried out for two different UV pump wavelengths, $\lambda_{UV} = 433$ nm and $\lambda_{UV} = 393$ nm, as shown in Fig. IV.14 d). $\lambda_{UV} = 433$ nm is at the wing of the DNQ absorption spectrum, whereas $\lambda_{UV} = 393$ nm is close to its maximum, see Fig. IV.14 c). Moreover, it will be shown in Sec. IV. 6.2, that these two λ_{UV} differ with regards to the MIR pre-excitation. A MIR pre-excitation has a contrary effect on the absorption at these two UV wavelengths: A MIR pre-excitation increases the absorption at the off-resonant $\lambda_{UV} = 433$ nm, whereas the vibrational pre-excitation decreases the absorption at resonant $\lambda_{UV} = 393$ nm.

IV. 4.5 MIR pre-pump/UV pump/MIR probe

A similar VMP experiment as described in Sec. IV. 4.4 was performed to confirm the results of the MIR pre-pump/UV pump/WL probe measurement. This time, the WL probe was replaced by a MIR probe, cf. Fig. IV.15.

In the experiment with WL probe, the photoproduct formation could be probed indirectly via the non-recovering bleach of the DNQ absorption band around 408 nm. Knowledge about the DNQ photoreaction from literature links the non-recovering DNQ bleach to ketene formation, cf. Sec. IV. 2.1. However, there is no distinct band present in the WL spectral region that can be directly and unambiguously identified as ketene. To validate the interpretation of the non-recovering bleach band around 408 nm as ketene formation, a measurement was performed with the WL probe pulse replaced by a MIR probe pulse. This had the advantage that the emerging ketene could be probed directly via its specific C=C=O stretching vibration at 2128 cm⁻¹ (4699 nm) [29]. The excitation scheme of DNQ was the same as described in Sec. IV. 4.4, with the UV pump pulse off-resonant with the DNQ steady state absorption.
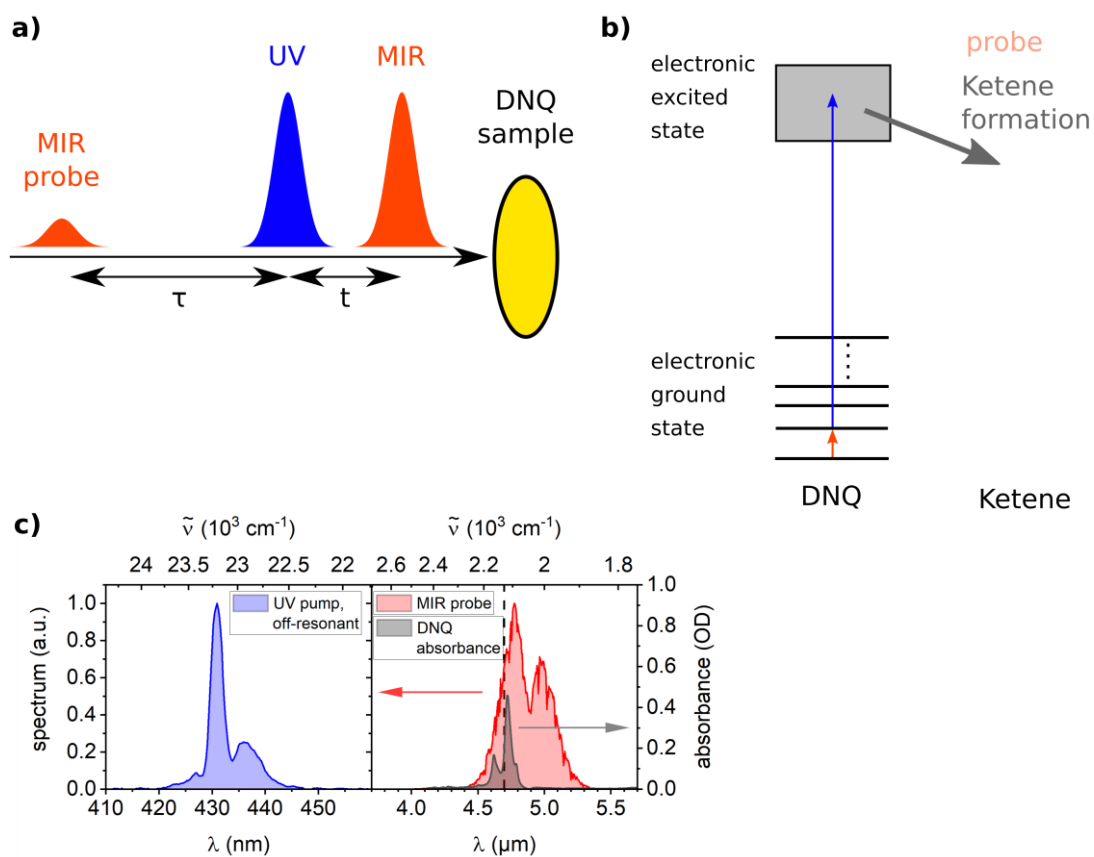
Figure IV.15: *Scheme of the MIR pre-pump/UV pump/MIR probe VMP experiment. a) Pulse sequence. b) Involved energy levels. The excitation scheme is the same as in Fig. IV.14, but now the MIR probe pulse probed directly the vibration specific for the emerging ketene. c) Pulse spectra. Left: UV excitation spectrum (blue). The spectrum's centre of mass was 433 nm. Right: MIR probe spectrum after transmission through MeOH filled sample cell (red, left y-scale) and DNQ absorption spectrum (grey, right, y-scale). The black dashed line denotes the absorption of the emerging ketene.*

IV. 5   Experimental details

IV. 5.1   Setup

For the various TA experiments presented in this chapter, in total four beams were needed at the sample stage

1. MIR pump,
2. MIR probe,
3. UV pump,
4. white light (WL) probe.

Not all of the beams were used at the same time. A sketch of the experimental setup is shown in Fig. IV.16. The fundamental pulses for all following conversion processes were provided by a commercial Ti:Sa regenerative amplifier system (Coherent Astrella-USP-1K),
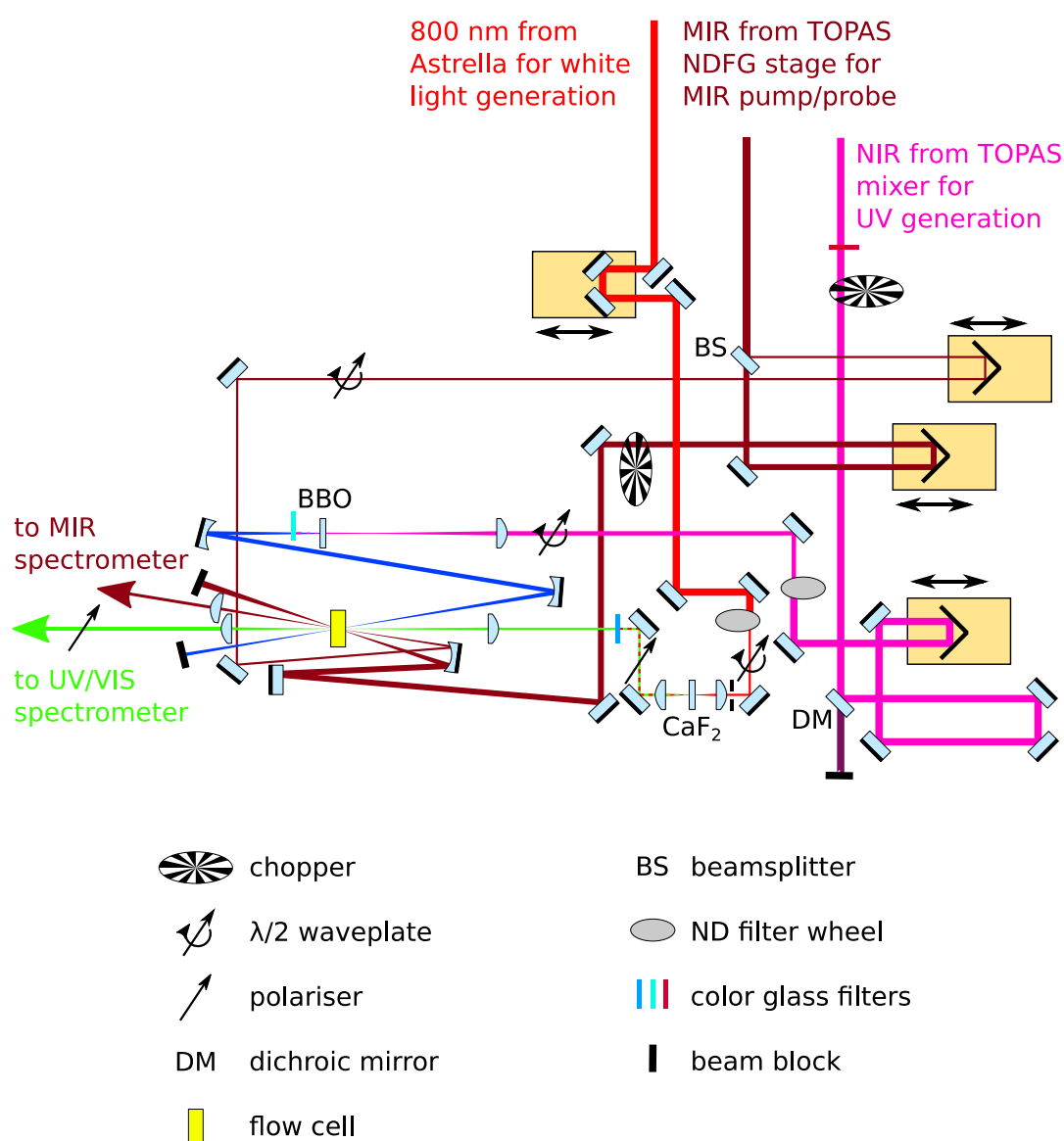
Figure IV.16: *Setup for the TA experiments. For the various measurements, four beams are needed in total at the sample stage, but at most three of them were used at the same time. See text for more details.*

providing linear horizontally polarised pulses at 800 nm with 7 mJ energy at 1 kHz repetition rate. Depending on the compression, the pulses can be as short as 35 fs. However, for the following experiments the compression was optimised for maximum MIR output of the NDFG stage. Telescopes and beamsplitters (not shown in Fig. IV.16) were used to provide proper pulse energies and beam diameters for subsequent non-linear conversion processes. The $1/e^2$-radii of the spot sizes that will be stated below were determined by knife-edge measurements.

MIR pump

The MIR pulses were generated by a commercial optical parametric amplifier (OPA) system (Light Conversion TOPAS-800) with subsequent non-collinear difference frequency generation of signal and idler (Light Conversion NDFG stage). The TOPAS was pumped by 800 nm, 1.8 mJ pulses from the Astrella. The emerging signal and idler pulses had a total energy of 0.4 mJ and were centred around 1.4 µm and 2.0 µm, respectively. The difference frequency generation took place in an AGS crystal (1 mm thick, $\theta = 39°$) and the emerging horizontally polarised MIR pulses were centred around 4.8 µm, with an energy of 9 µJ and pulse length of 120 fs. Signal and idler were spatially separated from the DFG MIR beam and had been blocked. 98% of the MIR beam's energy were transmitted by a beamsplitter (BS) into the MIR pump path. The MIR pump beam was sent via a delay stage and was chopped by a mechanical chopper wheel. The MIR pump was finally focused by a f = 75 mm spherical gold-coated mirror (Thorlabs CM254-075-M01) into the sample. The MIR pump pulses reaching the sample cell were horizontally polarised and had an energy of ca. 5-7 µJ. The $1/e^2$-radius of the MIR pump spot at the sample position was approximately 60-70 µm. After transmitting the sample, the MIR pump beam was blocked.

MIR probe

The MIR probe pulses were generated by the same OPA/DFG system as the MIR pump pulses. MIR pump and probe beams were separated by a BS which transmitted 98% of the incoming beam power into the MIR pump path whereas 2% were reflected into the MIR probe path. After propagating via a delay stage, the polarisation of the MIR probe pulses was turned by a $\lambda/2$-waveplate to magic angle (54.7°) with respect to the horizontal axis. The MIR probe pulses were focused by the same f = 75 mm spherical mirror as the MIR pump pulses into the sample. 100 nJ of MIR probe energy arrived at the sample. After the sample, the MIR probe beam was collimated by an f = 100 mm plano-convex CaF_2 lens and guided to a Czerny-Turner spectrograph (Acton Research Corporation, SpectraPro-500i) with a 2x32 pixels MCT array detector (InfraRed Associates, Inc.). The grating used in the spectrograph had 150 lines/mm, which lead to a resolution of 6.9 nm/px. ND filters were placed in front of the spectrograph to avoid saturation of the detector.

UV pump

A second TOPAS-800 system in combination with an additional mixing crystal (both by Light Conversion, not shown in Fig. IV.16) delivered NIR pulses that were later frequency doubled in a BBO crystal to generate the desired UV pulses. The beam from the TOPAS mixing crystal traversed a RG-715 colour glass filter that blocked any visible components present in the beam. The beam was chopped by a mechanical chopper wheel. Afterwards, the NIR pulses were reflected by a dichroic mirror (Thorlabs DMLP1180), whereas the co-propagating signal and idler pulses passed that mirror and were blocked. The NIR pulses travelled through a delay line and were focused by an f = 200 mm CaF_2 lens slightly in front of a BBO

crystal (EKSMA Optics, 1 mm thick, $\theta = 29.2°$, $\phi = 90°$) for second harmonic generation. The preceding ND filter wheel and $\lambda/2$-waveplate (B. Halle 600-1200 nm achromatic waveplate) were for energy and polarisation adjustment of the NIR pulses. After the BBO crystal, the fundamental NIR pulses were blocked by a 1 mm BG42 colour glass filter. The transmitted UV pulses were collimated by a spherical $f = 200$ mm aluminium-coated mirror (Thorlabs CM-254-200-G01), before an $f = 150$ mm aluminium-coated spherical mirror focused them into the sample. Depending on the experiment, the UV pulses were centred at 433 nm or 393 nm, respectively. In both cases, they were polarised horizontally. The pulse energies arriving at the sample were 1.3 µJ for 433 nm and 1.4 µJ for 393 nm, respectively. The UV pulse energies were below the threshold of WL generation in the CaF_2 windows of the sample cell. From CA measurements with the WL pulses, it was deduced that the UV pulses were shorter than the MIR pulses, i.e. shorter than 120 fs. The $1/e^2$-radius at the sample position was measured to be approximately 70 µm. After the sample, the transmitted UV beam was blocked.

WL probe

800 nm pulses from the Astrella system propagated via a delay stage and were focused by an $f = 50$ mm plano-convex CaF_2 lens (Thorlabs LA5183) into a 2 mm thick CaF_2 window (by Korth Kristalle) for WL generation. Before the 800 nm pulses were focused into the CaF_2 window, their energy was attenuated by an ND filter wheel and iris to 600 nJ. The iris additionally cleaned the spatial mode of the 800 nm beam profile. The polarisation direction of the linearly polarised 800 nm fundamental and the orientation of the CaF_2 window were adjusted so that the generated WL was polarised at magic angle (54.7°) with respect to the horizontal. To avoid damage to the CaF_2 window, a motorised holder permanently moved the window in the plane perpendicular to the 800 nm beam propagation direction. The generated WL was collimated by another lens, which was identical to the focusing lens. Subsequently, the WL polarisation was cleaned by a Glan polariser (B. Halle). A 5 mm KG5 colour glass filtered out the 800 nm fundamental. The WL reached down to 320 nm and had an energy of 2 nJ. An $f = 100$ mm UVFS plano-convex lens (Newport SPX022) focused the WL pulses into the sample to a $1/e^2$-radius of 60-70 µm. After the sample, the WL beam was collimated by an $f = 100$ mm CaF_2 plano-convex lens and routed into a spectrograph with a 256 pixels photodiode array detector. The resolution of the spectrograph was 1.3 nm/px. For experiments involving a UV pump pulse (horizontally polarised), an analyser turned to vertical polarisation was placed after the WL collimation lens to reduce scattering from the UV pump into the spectrograph.

Delay stages

For two beam pump-probe measurements, the pump-probe delay τ was scanned by moving the delay stage of the pump beam. For the three beam measurements with MIR pre-pump and UV pump it was the delay stage of the probe that was moved to scan τ, in order to ensure that the delay t between MIR pre-pump and UV pump was well defined.

Sample cell

The DNQ in MeOH solution was circulated through a flow cell by a peristaltic pump. The flow cell consists of two 2 mm CaF_2 windows with a 100 µm spacer in between. The flow rate of the peristaltic pump is large enough to exchange the sample volume several times within 1 ms. The total sample volume used for one measurement was approximately 10 ml.

IV. 5.2 Comparability of the measurements with MIR pre-pump on and MIR pre-pump off

For the determination of the photoproduct formation enhancement through vibrational pre-excitation, cf. Sec. IV. 4.4 and IV. 6.4, it is crucial that the measurements with MIR pre-pump on and MIR pre-pump off are comparable, i.e. that the experimental conditions are the same for both. This was achieved by a suitable chopper scheme as is presented in Fig. IV.17. The UV pump was chopped with 500 Hz and the MIR pre-pump was chopped with 250 Hz. The recorded spectra were then accordingly sorted and the corresponding TA traces with MIR pre-pump on and MIR pre-pump off were calculated. In this way, both traces with *MIR on* and *MIR off* were taken during the same sweep of the WL probe delay stage, so that any potential long term drifts in laser power etc. affected both traces likewise.
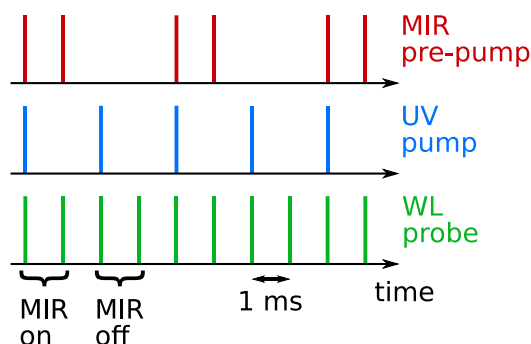
Figure IV.17: *Pulse scheme for the MIR pre-pump/UV pump/WL probe VMP experiment. The UV pump was chopped at 500 Hz, the MIR pump at 250 Hz. The repetition rate of the laser was 1 kHz. The spectra were then sorted to get TA traces with MIR on and MIR off.*

Furthermore, in the course of the measurement, the MIR-UV delays t were taken in an interleaved manner. This means that the delays from $t = -4$ to 20 ps were not taken in an ascending order, i.e. first taking all scans for $t = -4$ ps, then taking all scans for $t = -2$ ps, then for $t = 0$ ps and so on. Instead, the measurement was actually performed by taking half of the scans for $t = -4$ ps, then half of the scans for $t = 1$ ps, then for $t = 0$ ps, for $t = 5$ ps, $t = -2$ ps, $t = 10$ ps, $t = 2.5$ ps and $t = 20$ ps. The other half of the scans was taken in reversed order for t and in the end, all scans were averaged at each t for *MIR on* and *MIR off* separately to get the corresponding traces. In this way potential drifts during the course of the measurement - like a slightly changing ratio of MIR and UV pump energies or a small change in beam overlap - did not distort the measured time dependence of the product yield enhancement with MIR-UV delay t as much as they would have if the MIR-UV delays t would have been scanned in a strictly ascending order.

To find the time overlap between MIR and UV pulse, the WL pulse was used as reference, as there was a distinct CA for MIR/WL as well as for UV/WL that could be used for this purpose.

IV. 5.3 Sample preparation

For the experiments shown, DNQ was measured in MeOH solution. The solution was prepared by dissolving DNQ powder in MeOH in a sonifier for ca. 40 minutes. The sample was handled under red light and was kept in brown glass bottles to avoid photodegradation. 50 mM solutions were used for the TA measurements with MIR probe, 13 mM solutions for measurements with WL probe.

DNQ powder was available from previous experiments performed in our group as sodium 2-diazo-1-naphthol-5-sulfonate (CAS: 2657-00-3, Quzhou Rundong Chemical Co., Ltd). DNQ is a monohydrate, the available powder was used without further purification.

To check whether the DNQ powder that was still available in our group had degraded over time, an FTIR spectrum of this powder dissolved in MeOH was compared to a spectrum of a MeOH solution prepared with newly bought DNQ powder (CAS: 2657-00-3, AK Scientific, Inc.; distributed by Carbolution Chemicals GmbH). Both spectra showed the same characteristic absorption lines with same amplitude and lineshape. There was no absorption line visible in one spectrum which was not visible in the other one. This is also consistent with AK Scientific's data sheet [144] on DNQ. The data sheet states that DNQ is stable under the conditions under which it had been stored. Thus, the DNQ powder that was available in our group has not suffered from significant degradation and therefore, was used for the following experiments.

IV. 5.4 Steady state absorption spectra

Steady state absorption spectra of DNQ in MeOH were measured in the MIR spectral region by an FTIR spectrometer (PerkinElmer Spectrum 400) and in the UV\Vis\NIR region by a spectrophotometer (Shimadzu UV-1800).

IV. 6   Measurements and results

IV. 6.1 MIR pump/MIR probe TA

A TA trace for the MIR pump/MIR probe experiment on DNQ is displayed in Fig. IV.18. In the measurement shown in Fig. IV.18, a maximum pump-probe delay τ of nearly 60 ps was covered. The 2D map shows three main features: Reduced absorption around 2118 cm^{-1}, which corresponds to bleaching of the ground state, together with two bands of increased
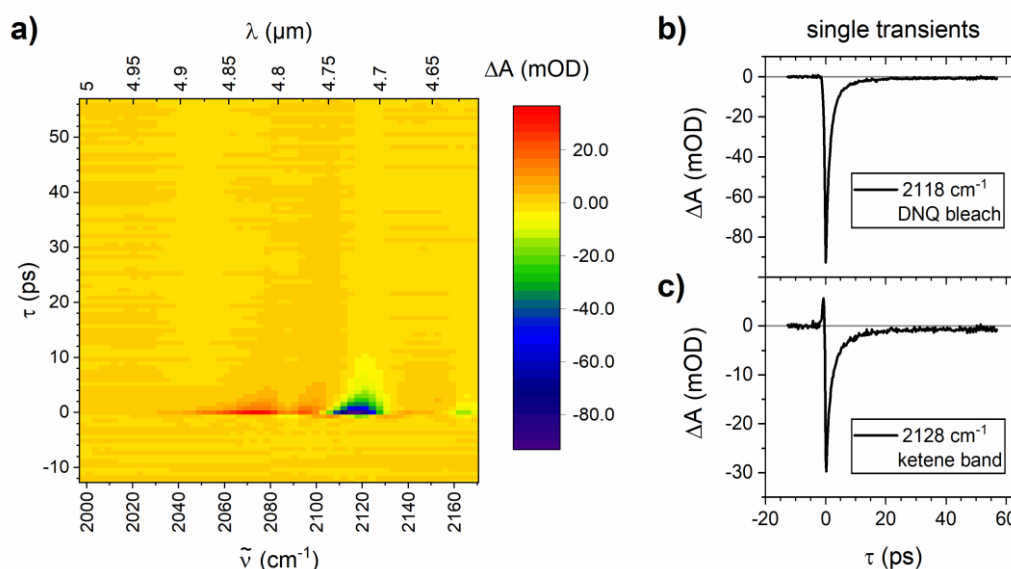
Figure IV.18: a) MIR pump/MIR probe TA trace with pump-probe delays up to nearly 60 ps. The trace is corrected for a MIR post-pulse, see Sec. IV. 3.4 for details. b) Transient at 2118 cm^{-1}, corresponding to the spectral position of the GSB of the C=N=N stretching vibration of DNQ. c) Transient at 2128 cm^{-1}, corresponding to the spectral position of the C=C=O stretching vibration of ketene.

absorption around 2100 cm^{-1} and 2076 cm^{-1}. The two latter bands are redshifted with respect to the ground state bleach (GSB) and are assigned to vibrationally excited states of the C=N=N stretch mode of DNQ. The weaker negative feature at 2164 cm^{-1} also corresponds to GSB. It is caused by a side peak of the structured absorption spectrum, see Fig. IV.11 c). All those features decay within 20 ps. Afterwards, there is no structure in the TA trace visible any more. Especially, the ΔA signal of the GSB at 2118 cm^{-1} fully recovers to zero (Fig. IV.18 b)), indicating that all of the DNQ molecules that were excited by the MIR pump pulse return to the vibrational ground state of DNQ. Furthermore, there is no persisting positive signal at 2128 cm^{-1} visible (Fig. IV.18 c)). Such a signal would indicate formation of ketene and thus cleaving of the N$_2$ group from the DNQ molecule.

An additional measurement with shorter maximum pump-probe delay τ, but increased time resolution was performed, see Fig. IV.19. The increased time resolution allows for a better determination of the highest vibrational excitation level of the C=N=N stretch mode that is achieved by the MIR pump. The trace in Fig. IV.19 displays the same features of GSB and absorption of vibrationally excited states as the one shown Fig. IV.18 a). Below 2040 cm^{-1}, there are at first glance no features visible beside some CA at t$_0$. In addition, hyperbola shaped features before t$_0$, in the range $\tau = -5$ ps to $\tau = 0$ ps, are now more pronounced, especially between 2060-2120 cm^{-1}. These correspond to PFID, which is caused by the long coherence times of vibrations [142, 143].

The maximum vibrational excitation, however, cannot be readily read off the measured trace in Fig. IV.19. This is because the measured signal contains a *structured* GSB contribution. Correction of the measured ΔA for the structured GSB will be discussed in Sec. IV. 7.1.1 and the maximum excited vibrational level will be inferred.
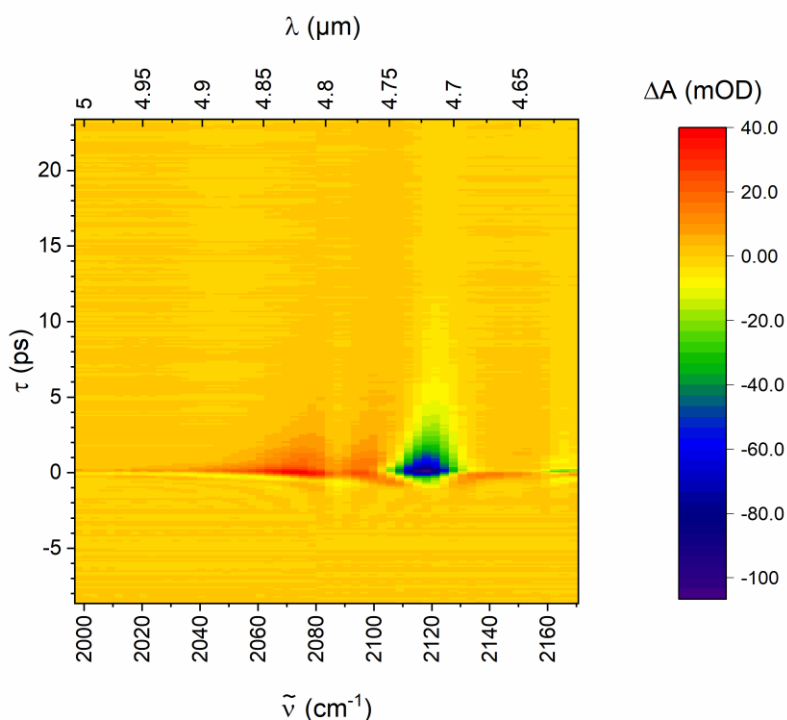
Figure IV.19: *MIR pump/MIR probe TA trace with increased time resolution. The trace is corrected for a MIR post-pulse, see Sec. IV. 3.4 for details.*

IV. 6.1.1 <u>Attempts to optimise ladder climbing</u>

As there was no ketene formation observed with 120 fs MIR pump pulses, a 25 mm LiF substrate was introduced into the MIR pump path. LiF possesses negative GVD around 5 µm, so that transmission through the LiF substrate results in a down-chirp imprinted on the pulse. A down-chirped pulse is supposed to be favourable for vibrational ladder climbing in an anharmonic potential, cf. Sec. IV. 2.3. 25 mm LiF introduce a GDD of -29×10^3 fs^2 at 4.8 µm. The pulse length of the MIR pump was increased from 120 fs to 840 fs, as was determined by an autocorrelation measurement. A comparison of normalised ΔA at several pump-probe delays τ with and without LiF in the pump path is shown in Fig. IV.20[1]. There is no substantial difference visible between the spectral cuts with and without LiF substrate, the normalised ΔA signals agree within the error. This means that the down-chirped pulses did not substantially improve the ladder climbing process.

One could argue that it might be the absorption of MeOH around 2040 cm^{-1} (cf. Fig. IV.11 c)) that hinders effective ladder climbing to higher vibrational levels, as this absorption lies in
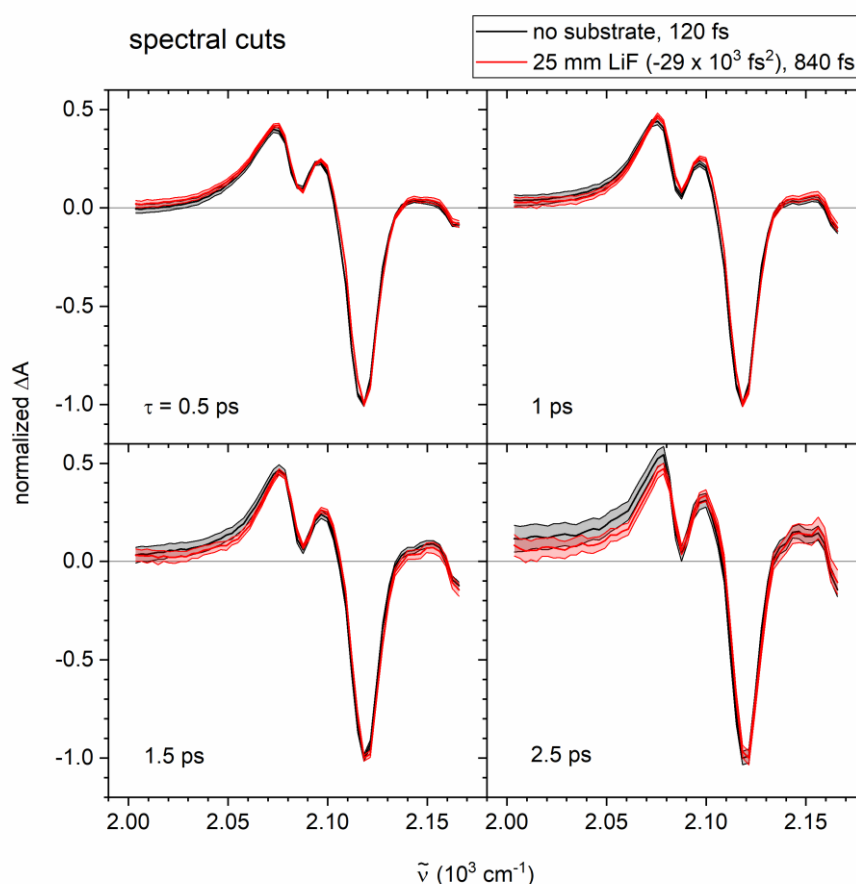
Figure IV.20: *Spectral cuts along several pump-probe delays τ for pulses without (black) and with (red) additional LiF substrate in the pump path. The shaded areas indicate the 1σ confidence level. For every τ, both curves overlap within the confidence level.*

---

[1] In contrast to all other measurements presented in this chapter, for the measurements shown in Fig. IV.20, MIR pump and probe were not focused by the same f = 75 mm spherical mirror, but by a f = 200 mm mirror for the pump and a f = 150 mm mirror for the probe.

the vicinity of the $v = 3 \rightarrow v = 4$ transition. Therefore, measurements with DNQ dissolved in a 4:1 mixture of 1-butanol/MeOH were performed. In that solvent mixture, the absorption dip around 2040 cm^{-1} is much less pronounced. However, a spectral cut for this experiment at $\tau = 0.5$ ps did not show any hints of enhanced population of higher vibrational levels compared to the experiments performed with DNQ dissolved in pure MeOH. Neither was any sign of emerging ketene around 2128 cm^{-1} observed. Moreover, the solubility of DNQ in the 4:1 1-butanol/MeOH mixture is highly decreased compared to pure MeOH. From FTIR measurements, the maximum achievable concentration of DNQ is determined to be less than 5 mM, i.e. less than 10% of the concentration used for the DNQ in MeOH measurements. The low solubility of DNQ in the 1-butanol/MeOH mixture lead to a poor signal-to-noise ratio (S/N) of the corresponding measurements.

Since enhanced ladder climbing efficiency was observed neither for a down-chirped pulse nor for DNQ dissolved in a solvent mixture with reduced absorption in the vicinity of the $v = 3 \rightarrow v = 4$ transition, both approaches were not pursued any further. In addition, the measurements without LiF substrate in the MIR pump path and with DNQ dissolved in pure MeOH gave the best S/N.

IV. 6.2 MIR pump/WL probe TA

In the TA trace with MIR pump and WL probe, the most prominent features are two bands in the region of the broad DNQ absorption around 400 nm (Fig. IV.21): One band of increased absorption with its maximum at 436 nm, another band of decreased absorption with its minimum at 394 nm. Above 500 nm, the TA trace shows no effect of MIR excitation on WL absorption. The bands at 394 nm and 436 nm decay with the same time constant (cf. Fig. IV.21 b)). Both bands vanish within 20 ps. This is consistent with the MIR pump/MIR probe measurements, in which the bleach at 2118 cm^{-1} also recovers within 20 ps (cf. Fig. IV.18 b)). Furthermore, there is only a small spectral shift of the ΔA minimum and maximum observable, their position remains nearly constant at 394 nm and 436 nm over the whole observed delay range and no other bands appear.

The behaviour observed in Fig. IV.21 can be qualitatively explained with the steady state UV/Vis absorption spectrum of DNQ, see Fig. IV.12 c): On the one hand, 436 nm ($\sim$22.940 cm^{-1}) lies at the edge of the UV/Vis absorption spectrum and vibrational pre-excitation by $\sim$2100 cm^{-1} shifts the absorption at 436 nm towards the absorption maximum at 400 nm (25.000 cm^{-1}). On the other hand, the absorption at 394 nm - close to the absorption maximum - is reduced by vibrational pre-excitation. These observations agree well with findings in the field of VIPER spectroscopy (VIPER: VIbrationally Promoted Electronic Resonance), where vibrational excitation of a molecule is used to red shift the UV/Vis absorption spectrum of the molecule, so that an initially off-resonant UV/Vis-pulse becomes resonant with the red shifted spectrum [24, 145].

The results of this section show that the effect of vibrational pre-excitation is largest if the subsequent UV pulse is around 394 nm or 436 nm. Thus, in Sec. IV. 6.4 an excitation of the C=N=N stretch mode is combined with UV excitation at these two wavelengths.
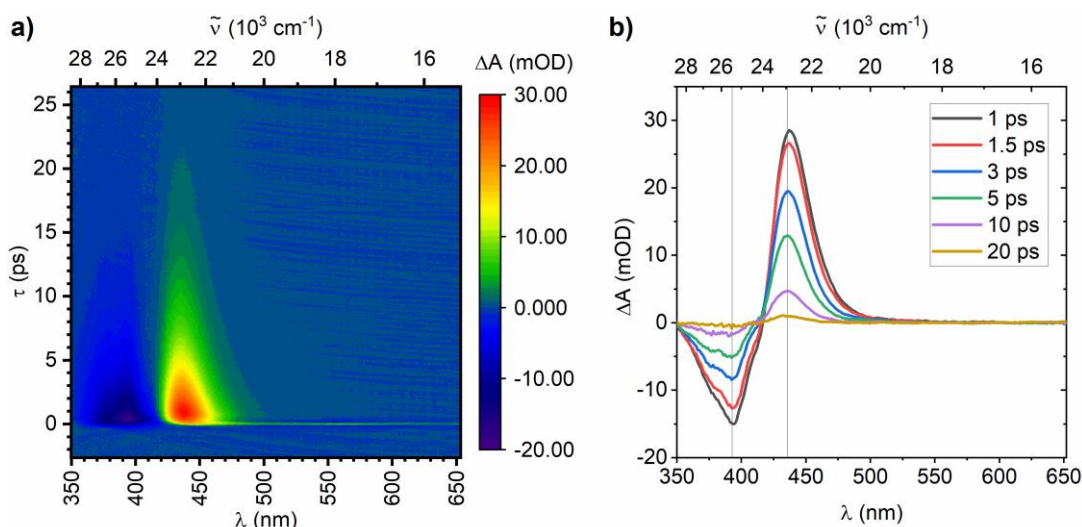
Figure IV.21: a) t_0 and post-pulse corrected MIR pump/WL probe TA trace. b) Spectral cuts along several delays of the TA trace. The vertical lines at 394 nm and 436 nm are a guide for the eye.

IV. 6.3 UV pump/WL probe TA

The TA trace of the UV pump/WL probe measurement in Fig. IV.22 a) shows a broad negative signal around 400 nm, i.e. around the region of maximum DNQ steady state absorption. That signal is thus attributed to bleach of DNQ. Up to 70 ps, the bleach does not recover, but reaches a constant value, see Fig. IV.22 b). This means that part of the DNQ molecules have undergone a photoreaction as described in Sec. IV. 2.1. From the information presented in Sec. IV. 2.1, it is also concluded that ketene is the only photoproduct that is present in a noticeable amount on the time scale of the experiment, i.e. on the timescale of several tens of picoseconds. Furthermore, electronic absorption spectra of ketene found in literature [129] show that there is virtually no absorption of
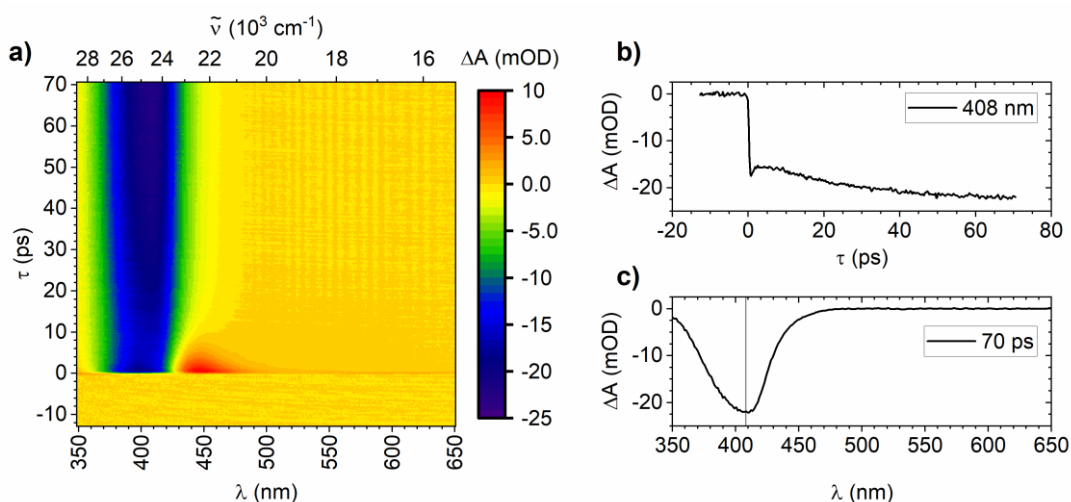
Figure IV.22: UV pump/WL probe TA experiment. a) t_0 corrected trace with clearly visible non-recovering bleach band around 400 nm. b) Transient at 408 nm. c) Spectral cut at 70 ps. The vertical line at 408 nm serves as guide for the eye.

ketene above 400 nm[1]. Hence, after several tens of picoseconds, the negative signal around 400 nm can be interpreted as a pure bleach signal of DNQ.

The trace in Fig. IV.22 might at early times include some contributions from vibrationally hot ketene - whose UV/Vis spectrum is unknown - or vibrationally excited DNQ - as was observed in Fig. IV.21. Vibrational excitation of both DNQ and ketene is expected according to Ref. [29]. However, for both DNQ and ketene, the vibrational excitation decays to $v = 0$ within 20 ps, cf. Sec. IV. 6.1 and Ref. [29]. The positive absorption at early times around 450 nm, which is observed in Fig. IV.22 a), is indeed also visible in the MIR pump/WL probe trace of Fig. IV.21 and is a signature of DNQ with $v > 0$. The features observed in Fig. IV.22 are in accordance with the previously presented experiments and with the model developed in Ref. [29]. In Ref. [29] it is stated that part of the UV excited DNQ molecules are converted to ketene, whereas the other part does not undergo a photoreaction, but returns to a hot electronic ground state of DNQ.

The non-recovering bleach around 400 nm is associated with permanent loss of DNQ, which directly implies formation of the ketene photoproduct. The bleach's amplitude is thus a measure for the efficiency of ketene formation. As can be seen from the spectral cut in Fig. IV.22 c), the bleach at long delay times is largest at 408 nm.

The equivalence between bleach level and ketene formation will be corroborated in Sec. IV. 6.5 by probing the emerging ketene directly at 2128 cm^{-1}.

IV. 6.4 MIR pre-pump/UV pump/WL probe

IV. 6.4.1 Excitation with UV pump off-resonant with DNQ absorption

For UV excitation at 433 nm – off-resonant with the DNQ steady state absorption and close to the maximum of the MIR induced absorption enhancement at 436 nm - Fig. IV.23 shows WL probed TA traces with (Fig. IV.23 left) and without (Fig. IV.23 middle) vibrational pre-excitation. The TA trace with pre-excitation looks qualitatively the same as the trace without pre-excitation. However, when the trace without MIR pre-pump is subtracted from the one
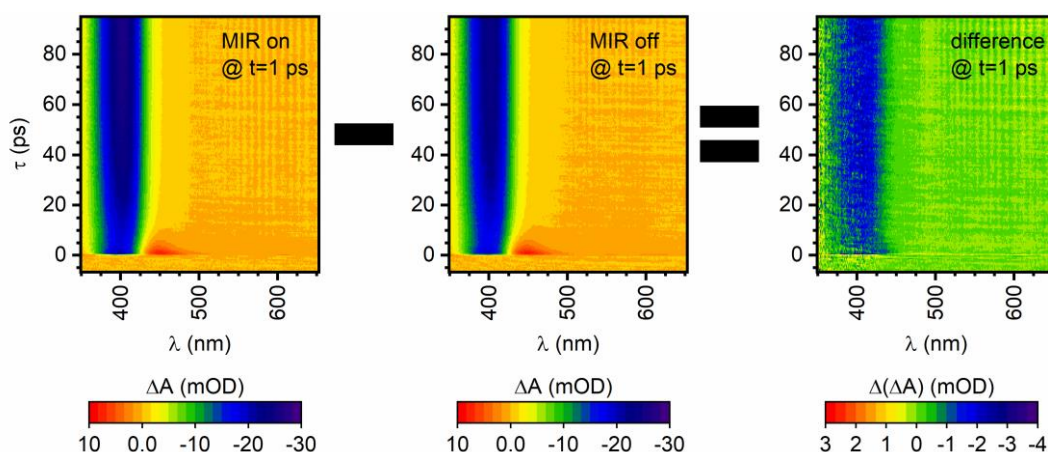
Figure IV.23: *Effect of vibrational pre-excitation on the UV induced photoreaction of DNQ. The trace with MIR pre-pump/UV pump ("MIR on", left) looks qualitatively the same as the trace with UV pump only ("MIR off", middle), but subtraction of the "MIR off" trace from the "MIR on" trace reveals a quantitative difference ("difference", right). The MIR-UV delay is $t = 1$ ps for the depicted traces. The traces with MIR on and MIR off are both t_0 and baseline corrected. Note the different colour scales for the TA traces and the difference trace.*

with MIR pre-pump, a clear difference in the bleach band around 400 nm becomes visible (Fig. IV.23 right). The level of the non-recovering bleach is larger when the UV pulse is preceded by a MIR pre-pump. Thus, vibrational pre-excitation of the C=N=N stretch mode favours formation of the photoproduct. The ratio of the bleach levels in the measurements with and without MIR pre-excitation allows to quantify the photoproduct enhancement. The dependence of the enhanced photoproduct formation on the delay t between MIR and UV pulse was further examined. For this purpose, transients at 408 nm at several delays t were considered, see Fig. IV.24. For these transients, the values of the non-recovering bleach levels were calculated (grey boxes in Fig. IV.24) and the ratio of the bleach levels for transients with and without MIR pre-excitation was determined by

$$\text{ratio } \Delta A = \frac{\overline{\Delta A} \, (75 - 94 \, ps) \text{ with MIR on}}{\overline{\Delta A} \, (75 - 94 \, ps) \text{ with MIR off}} \qquad \overline{\overline{\Delta A}}: \text{mean value of } \Delta A. \quad \text{(IV. 13)}$$
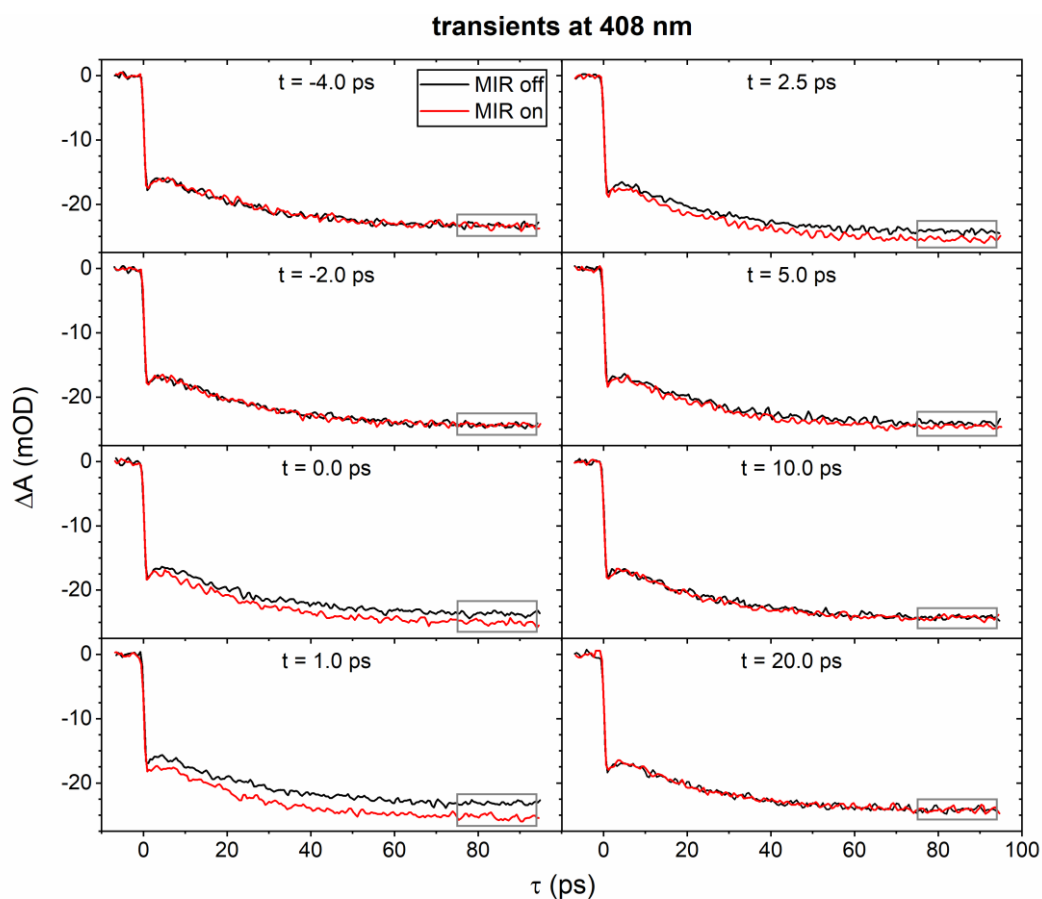
Figure IV.24: *Transients at 408 nm of the UV pump/WL probe measurement without (black) and with (red) additional MIR pre-excitation for several MIR-UV delays t. The UV pump spectrum was off-resonant with the DNQ absorption ($\lambda_{UV} = 433 \, nm$). For positive t, the MIR pulse precedes the UV pulse; for negative t, the MIR pulse arrives after the UV pulse. τ denotes the delay between UV pump and WL probe. The grey boxes (75-94 ps) indicate the range that were used to determine the level of the non-recovering bleach $\overline{\Delta A}$ by averaging each transient in this delay range.*
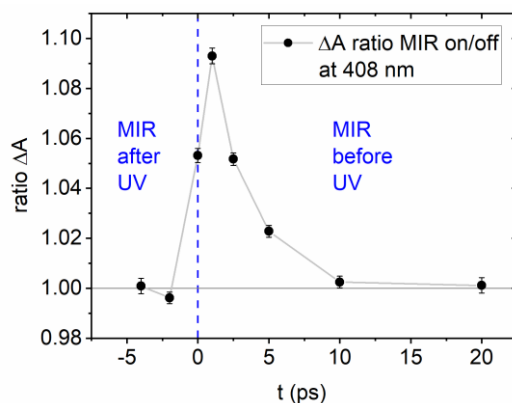
Figure IV.25: *Evolution of the ΔA ratio of MIR pre-pump on/off bleach values with MIR-UV delay t, cf. Eq. IV.13 . The UV pump spectrum was off-resonant with the DNQ absorption ($\lambda_{UV} = 433\ nm$). The error bars denote the 1σ confidence level, which was derived from the standard deviations of $\overline{\Delta A}$ values of the transients in Fig. IV.24. The horizontal line at 1.00 and the vertical line at $t = 0$ ps serve as guides for the eye.*

Figure IV.25 shows how the photoproduct enhancement calculated by Eq. IV.13 depends on t. The enhancement is highest when the MIR pulse precedes the UV pulse by 1 ps. Ketene formation is then enhanced by 9%. For larger MIR-UV delays, the enhancement decreases and at $t = 10$ ps, there is already no noteworthy enhancement observable. Furthermore, there is also no enhancement visible if the MIR pulse arrives after the UV pulse (i.e. $t < 0$).

IV. 6.4.2 Excitation with UV pump resonant with DNQ absorption

In analogy to the analyis of the results in the previous section, transients at 408 nm for the UV pump at resonance with the DNQ steady state absorption ($\lambda_{UV} = 393$ nm) are displayed in Fig. IV.26. Again, transients for the UV induced photoreaction with and without MIR pre-excitation are shown.

The deduced ΔA ratios of the bleach levels (cf. Eq. IV.13) for several MIR-UV delays t are shown in Fig. IV.27. Interestingly, the curve looks similar as the curve for non-resonant UV excitation, despite the opposite effect of MIR pre-excitation on the UV absorption, cf. Sec. IV. 6.2. Especially, there is an increase in photoproduct formation for $t > 0$, i.e. if the C=N=N stretch mode is vibrationally excited before the resonant electronic excitation. The photoproduct enhancement is again highest for $t = 1$ ps. The effect of MIR pre-excitation on the photoproduct formation will be further discussed in Sec. IV. 7.

transients at 408 nm
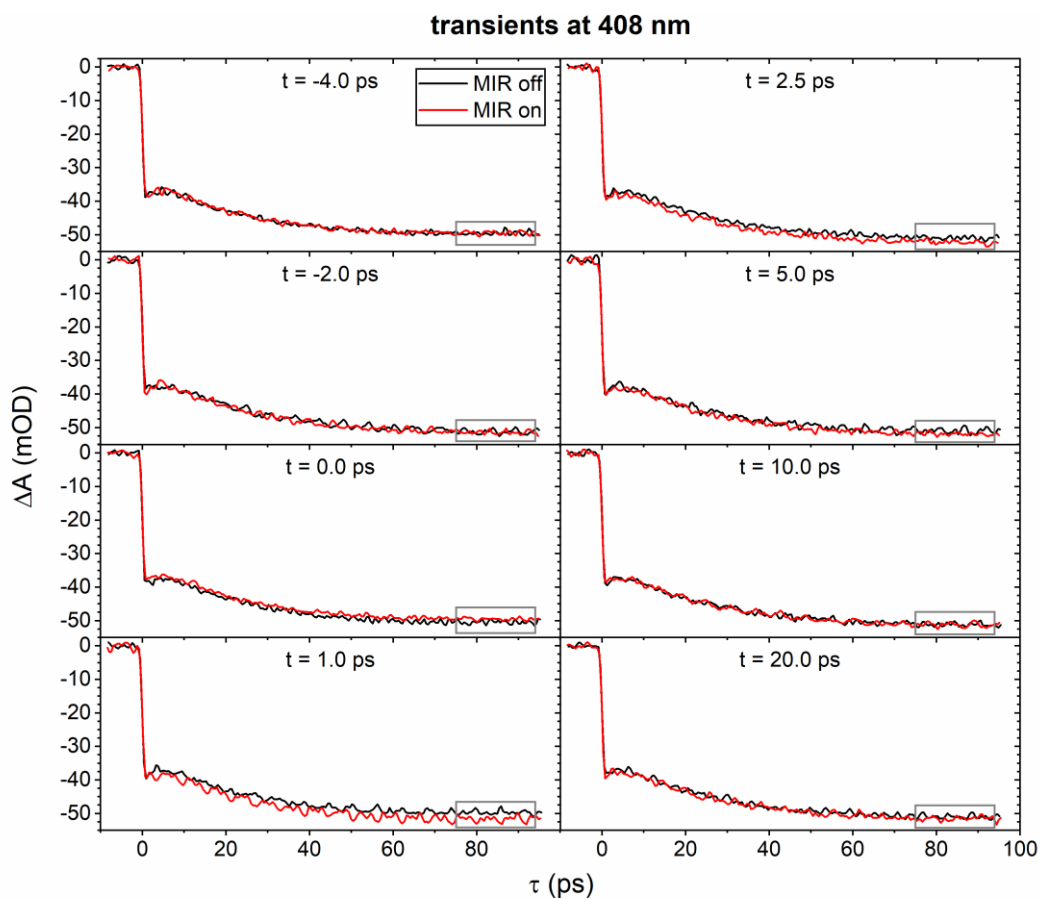
Figure IV.26: *Transients at 408 nm of the UV pump/WL probe measurement without (black) and with (red) additional MIR pre-excitation for several MIR-UV delays t. The UV pump spectrum was in resonance with the DNQ absorption. For positive t, the MIR pulse precedes the UV pulse; for negative t, the MIR pulse arrives after the UV pulse. τ denotes the delay between UV pump and WL probe. The grey boxes (75-94 ps) indicate the range that was used to determine the level of the non-recovering bleach by averaging each transient in this delay range. Note that the bleach level is now higher than for the off-resonant UV excitation (cf. Fig. IV.24).*
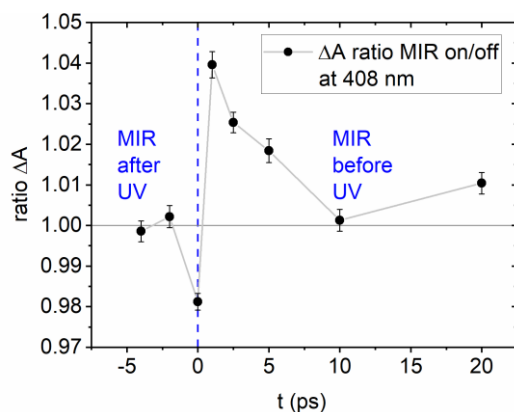
Figure IV.27: *Evolution of the ΔA ratio of MIR pre-pump on/off bleach values with MIR-UV delay t, cf. Eq. IV.13. The UV pump was resonant with the DNQ steady state absorption ($\lambda_{UV} = 393\ nm$). The error bars denote the 1σ confidence level, which was derived from the standard deviations of $\overline{\Delta A}$ values of the transients in Fig. IV.26. The horizontal line at 1.00 and the vertical line at $t = 0$ ps serve as guides for the eye. Note the different scale of the y-axis as compared to Fig. IV.25.*

IV. 6.5 MIR pre-pump/UV pump/MIR probe

Fig. IV.28 (middle) shows a TA trace with UV pump and MIR probe. After excitation of the DNQ sample with a UV pulse, there is a distinct band of increased absorption visible around 2128 cm^{-1} which persists throughout the timescale of the measurement (100 ps). Furthermore, non-recovering bleach bands at 2110 cm^{-1} and 2160 cm^{-1} are observed. The spectral positions of those coincide with absorption peaks of DNQ and are thus attributed to bleaching of DNQ molecules that were converted in the photoreaction. The measured
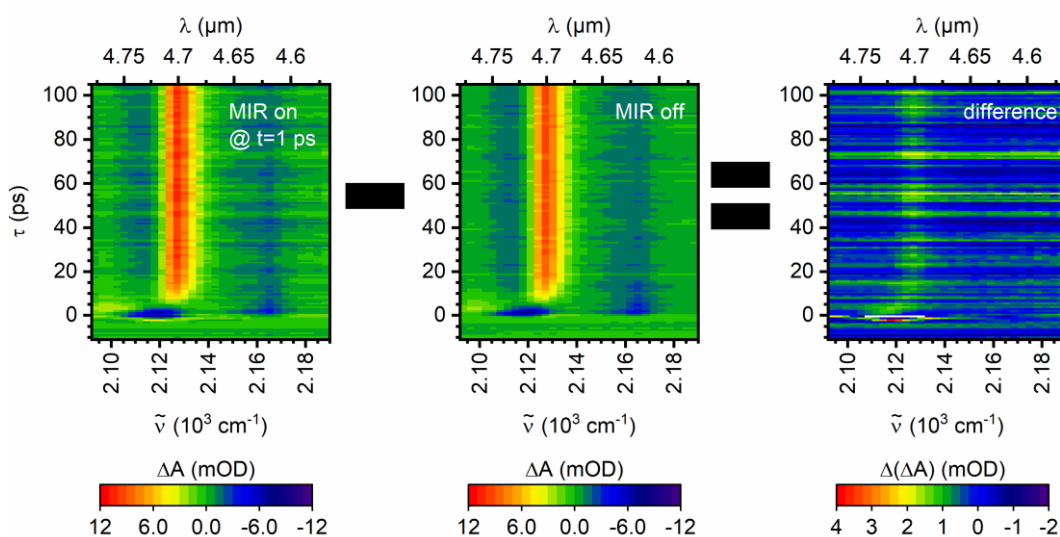
Figure IV.28: *Comparison of the t_0 and baseline corrected TA traces with (left, "MIR on") and without (middle, "MIR off") MIR pre-excitation before the UV pump pulse. Subtraction of those two traces show that MIR pre-excitation leads to a stronger ketene absorption band at 2128 cm^{-1} (right, "difference"). Note the different colour scales for the TA traces and the difference trace. For the displayed "MIR on" trace, the MIR pulse precedes the UV pulse by 1 ps. The "MIR off" trace is averaged for all measured MIR-UV delays t, cf. App. 0. For more details on the experiment, see Sec. IV. 6.5.*

trace in Fig. IV.28 (middle) is consistent with the traces measured in Ref. [29]. The same features are observed for the measurement with vibrational pre-excitation (Fig. IV.28 left). Subtracting the trace without pre-excitation of the C=N=N stretch mode from the trace with MIR pre-excitation reveals a difference in the amplitude of the ketene band at 2128 cm^{-1} (Fig. IV.28, right).

The level of the ketene transients at 2128 cm^{-1} was compared for measurements with and without MIR pre-excitation (Fig. IV.29), similar as it was done in Sec. IV. 6.4. The amplitude of the ketene band is larger if the UV pulse is preceded by a MIR pulse. The ratio of the levels $\overline{\Delta A}_{MIR\ on}/\overline{\Delta A}_{MIR\ off}$ vs. MIR-UV delay t is plotted in Fig. IV.30. It agrees with the values determined in Sec. IV. 6.4.1, where WL was used for probing. The agreement is even more pronounced when the WL probe measurement is scaled such that the ΔA ratios at $t = 1$ ps coincide for the measurements with MIR probe and WL probe[1]. From this agreement, it can be concluded that the non-recovering bleach at 408 nm in the previously presented experiments with WL probe (see Sec. IV. 6.3 and IV. 6.4) can indeed be interpreted as formation of ketene.

The results with respect to the photoproduct enhancement through vibrational pre-excitation obtained in this section (with MIR probing) are equivalent to the results obtained with WL probing, cf. Sec. IV. 6.4.1. In the further discussion, only the experiment with WL probing will be considered, as the WL probe measurements have a better S/N and more MIR-UV delays t are available. The noise in the experiment with MIR probe is discussed in App. C. 2.
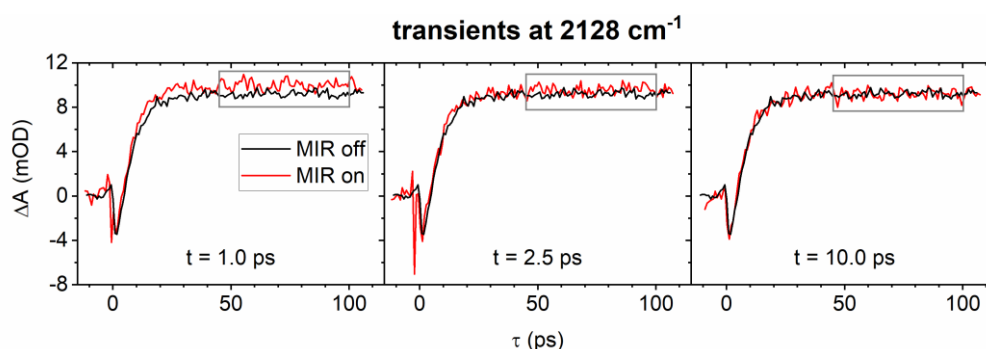
Figure IV.29: *Transients of the ketene photoproduct absorption at 2128 cm^{-1} without (black) and with (red) MIR pre-excitation for several MIR-UV delays t. For the transients with MIR pre-excitation, there is a MIR/MIR CA visible before the UV/MIR CA (for $t = 10\ ps$, only the tail of the MIR/MIR CA is visible). The grey boxes mark the range used to determine the mean level of the ketene absorption band. Those levels are used to determine the ratio $\overline{\Delta A}_{MIR\ on}/\overline{\Delta A}_{MIR\ off}$, cf. Fig. IV.30. The reference transient with MIR off is the same in all three graphs; for its computation the "MIR off" transients for all measured MIR-UV delays t were averaged to get a better S/N, cf. App. C. 2.*

---

[1] A minor deviation in the absolute values of the ΔA ratio between MIR probe and WL probe measurement is not surprising, as e.g. the ratio of MIR/UV pulse energies or the beam overlaps might slightly vary between both measurements.
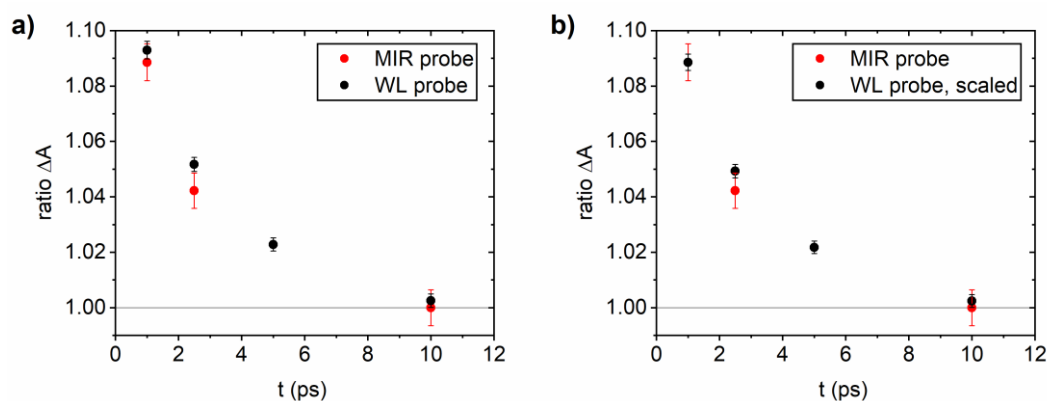
Figure IV.30: *Ratio $\overline{\Delta A}_{MIR\,on}/\overline{\Delta A}_{MIR\,off}$ of transients that are indicative of ketene formation, together with the 1σ confidence interval. The DNQ sample was excited by a UV pulse off-resonant with the DNQ steady state absorption. a) Comparison of two methods to determine the ΔA ratio vs. MIR-UV delay t. Red: MIR probe pulse used, transients of the ketene absorption band at 2128 cm^{-1} were taken to determine ΔA ratios, cf. Fig. IV.29. Black: WL probe pulse used, transients of the non-recovering bleach at 408 nm were used to determine ΔA ratios, cf. Fig. IV.24. For both methods, the error was derived from the standard deviations of the mean ΔA values. b) Same as a), but with ΔA ratios and errors of the WL probe measurement scaled such that the ΔA ratios of the MIR probe and WL probe method coincide at $t = 1\,ps$. The horizontal lines at 1.00 serve as guide for the eye.*

IV. 7   Discussion

IV. 7.1 MIR only excitation

IV. 7.1.1 Vibrational population in the CNN stretch mode

In the MIR pump/MIR probe TA measurements presented in Sec. IV. 6.1, the effect of an excitation of the C=N=N stretching vibration of DNQ was investigated, cf. Fig. IV.31 a). In this experiment, the enhanced absorption with pronounced peaks in the $\sim 2040 - 2100\ \mathrm{cm}^{-1}$ region gives clear evidence of ladder climbing with excitation of vibrational levels with $\nu > 1$. However, the steady state absorption of DNQ in MeOH is structured, cf. Fig. IV.31 b), and the signature of vibrationally excited states as seen in the MIR pump/MIR probe TA trace is superimposed by a *structured* GSB signal. In order to estimate to which level ν the C=N=N stretch mode is excited, the structured GSB contribution thus needs to be subtracted from the transient spectrum since the low frequency side peak of the GSB overlaps with the contributions of vibrationally excited modes with $\nu \geq 1$. To account for the structured GSB, a spectral cut at $\tau = 1.6$ ps was taken and further analysed. $\tau = 1.6$ ps was chosen because on the one hand, there is still substantial signal, on the other hand, it is well beyond any time where the signal might be contaminated by PFID or a CA.

Figure IV.32 a) displays the measured ΔA signal at $\tau = 1.6$ ps, normalised to -1 (blue line). Also shown in Fig. IV.32 a) is the measured steady state DNQ absorption spectrum, which is inverted and also normalised to -1 (red line). The measured ΔA was then corrected for the GSB contribution by subtracting the steady state absorption. This resulted in a GSB corrected signal (black line in Fig. IV.32 a)). The part below 2118 cm^{-1} of the GSB corrected signal was further analysed in Fig. IV.32 b). This spectral region is energetically lower than
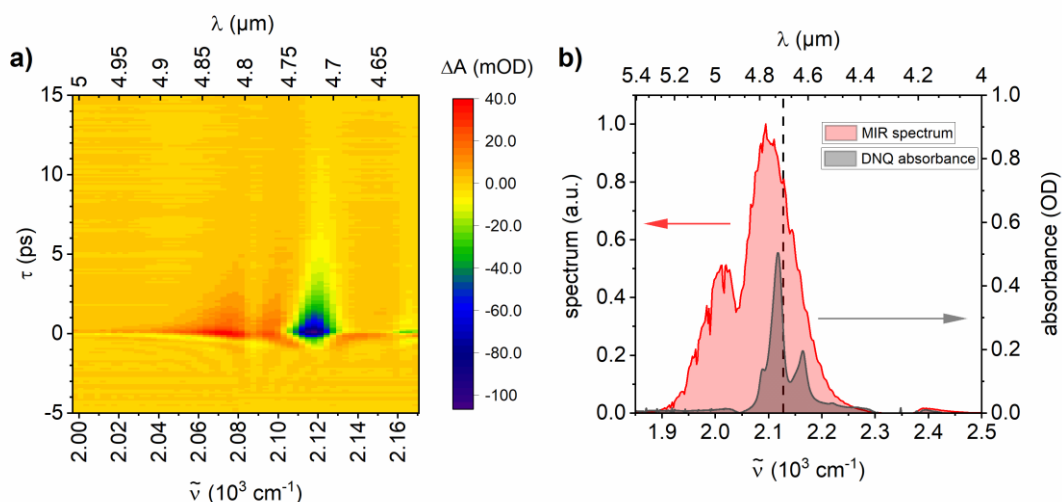
Figure IV.31: *a) TA trace of the MIR pump/WL probe measurement. b) MIR spectrum (red, left y-axis) and DNQ absorption spectrum (grey, right y-axis). The DNQ absorption is structured.*

the main absorption line of the $v = 0 \rightarrow v = 1$ transition of the C=N=N stretch mode and therefore carries information about vibrationally excited states, cf. Sec. IV. 2.2. The GSB corrected ΔA signal was fitted by a set of Gaussians (Fig. IV.32 b)). Three Gaussians were required to be able to reasonably fit the GSB corrected signal. Each Gaussian is interpreted as a vibrational transition of the C=N=N stretch mode. The highest transition that was probed in that way is $v = 3 \rightarrow v = 4$ (blue line in Fig. IV.32 b)), i.e. excitation up to $v = 3$ was induced by the MIR pump. Thus, a maximum of 3 vibrational quanta in the C=N=N mode
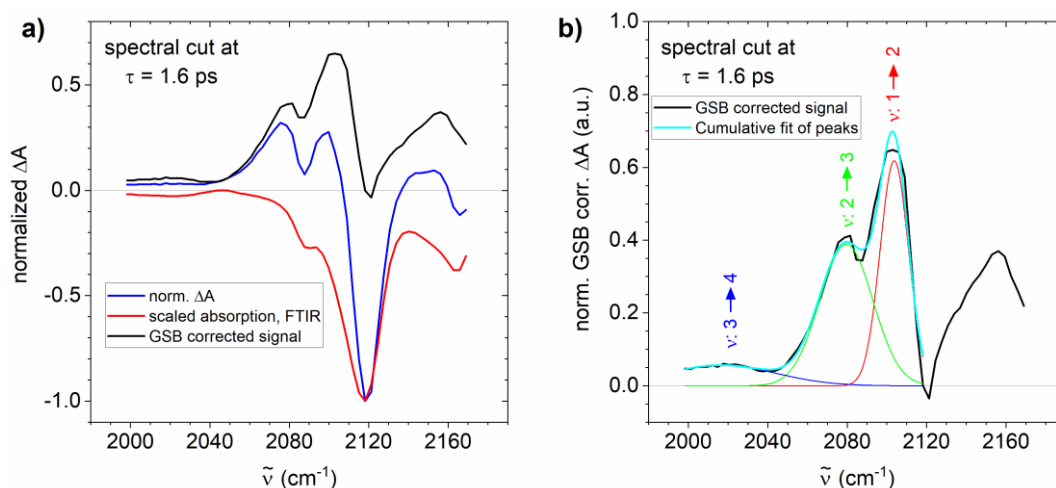
Figure IV.32: *Estimation of the highest populated vibrational state of the C=N=N stretch mode of DNQ. a) Correction of the measured ΔA for the structured GSB contribution: Subtraction of a scaled steady state absorption spectrum (red) from the normalised ΔA signal (blue) gives a GSB corrected ΔA signal (black). ΔA is taken at $\tau = 1.6\ ps$. b) The normalised GSB corrected ΔA from a) (black) is fitted by a set of 3 Gaussians (red, green and blue respectively) below 2118 cm^{-1}. The sum of the Gaussians is shown in cyan.*

was observed in the experiment[1], which is lower than the 5-6 quanta, that are estimated to be necessary for cleavage of the diazo group from the DNQ molecule.

The observed $\nu = 3$ should be viewed as lower bound of the highest excited vibrational state. It is well possible that there are more populated vibrational levels that were not resolved in the above analysis. This hypothesis is corroborated by the fact that the fitted Gaussians in Fig. IV.32 show for the transitions $\nu = 0 \rightarrow 1$, $\nu = 1 \rightarrow 2$ and $\nu = 2 \rightarrow 3$ a decrease in energy of ca. 20 cm^{-1} per excitation level ν. Thus the $\nu = 3 \rightarrow 4$ transition is expected around 2060 cm^{-1}. However, in the fit there is no Gaussian peaked at that position. On the other hand, the peaks at 2080 cm^{-1} (with FWHM: 31 cm^{-1}) and 2017 cm^{-1} (FWHM: 65 cm^{-1}) are significantly broader than the main peak at 2104 cm^{-1} (FWHM: 17 cm^{-1}). Thus, there might be additional transition peaks hidden in the transient spectrum that were not resolved in the measurement due to broadening and overlapping of the single transitions. In Ref. [147] it is shown that even for high excitation of a vibrational mode, the resulting ΔA spectrum might not show clear peaks for each populated ν, but that the single contributions from each ν might be smeared out.

It is interesting to note that the UV pump/MIR probe experiment presented in Ref. [29] also shows positive ΔA contributions in the range $\sim 2040 - 2100 \text{ cm}^{-1}$ that look very similar to the features observed in the MIR pump/MIR probe measurement of the present work (see Fig. IV.31 a)). The authors of Ref. [29] interpret those features as hot ketene photoproduct. However, they do not consider the possibility of hot DNQ in the electronic ground state. In contrast, the MIR pump/MIR probe measurement of the work at hand shows that the aforementioned features must result from hot DNQ and not ketene, as no ketene band was observed in the experiment with only a MIR pump employed.

Since in Ref. [29] the formation time of ketene is deduced from the most likely misinterpreted transient at 2055 cm^{-1}, the obtained value of below 300 fs does not directly reflect the formation time of ketene, but the lifetime of the electronically excited state of intact DNQ. Such an interpretation is in line with control experiments presented in Ref. [52], where a dwelling time of $\sim$200 fs was found for the DNQ population in the Franck-Condon region of the electronic excited state. These control experiments were performed by the same authors as the study in Ref. [29]. For a concerted reaction (cf. Sec. IV. 2.1) the lifetime of the DNQ electronic excited state should coincide with the ketene formation time. In contrast, if a carbene intermediate is involved, the actual formation time of ketene is expected to be retarded. The presumed misinterpretation of the 2055 cm^{-1} transient also explains that no kinetic contribution from the carbene intermediate to this alleged ketene transient was observed in Ref. [29].

---

[1] Evaluation of the MIR pump/MIR probe measurement at $\tau = 0.5\ ps$ gave also a maximum excitation of $\nu = 3$.

IV. 7.1.2 Rationalisation for absent DNQ dissociation in the electronic ground state

In the present work, there was no photoproduct formation observed by only selectively exciting the C=N=N stretch mode of DNQ with MIR pulses, i.e. without entering the electronically excited state. Several reasons are conceivable to explain this finding:

1. The initial estimation that 5 to 6 MIR photons are needed to induce the photoreaction of DNQ in the electronic ground state was based on a study on the dissociation of gaseous diazomethane (CH_2N_2) [20]. For that case, however, it was shown experimentally [20] and theoretically [148] that the CN bond scission is accompanied by a significant out-of-plane bending of the CH_2 moiety, see Fig. IV.33. The calculations in Ref. [148] show that for the dissociation the out-of-plane bending angle ϕ is larger than 75°. If there was no out-of-plane bending, an additional energy barrier of 9100 cm^{-1} (equivalent to 5 additional MIR photons) would need to be overcome. Thus the CNN mode had to be excited up to at least $v = 10$. It is possible that such an out-of-plane bending is hampered for the DNQ molecule in solution. In solution, the solvent cage might impede the out-of-plane bending of the N_2 moiety [149].
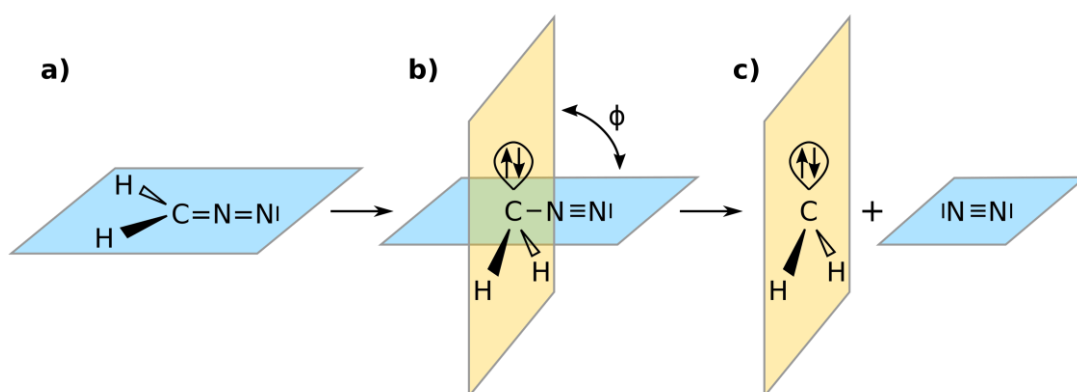
Figure IV.33: Out-of-plane bending of diazomethane. a) Planar configuration of diazomethane. b), c) Configuration at CN bond scission. The planes of the CH_2 and N_2 moieties are significantly tilted against each other. If there was no tilt between the planes of the CH2 and N2 moiety, a significant additional energy barrier needed to be overcome. According to Refs. [20, 148].

2. The projection of the C=N=N stretch mode on the actual reaction coordinate might be lower for DNQ than for CH_2N_2. In contrast to CH_2N_2, the desired reaction for DNQ not only includes cleavage of the diazo group from the rest of the molecule, but also Wolff rearrangement. Wolff rearrangement in turn involves large amplitude motion along many molecular coordinates [133]. In the experiment on gaseous diazomethane dissociation, it was found that the direct energy transfer from the C=N=N stretch mode into the reaction coordinate takes about 480 fs [20]. If that transfer time is longer in DNQ, energy transfer into the reaction coordinate might well be outcompeted by intramolecular energy redistribution together with energy loss to the solvent. That molecular dissociation via vibrational ladder climbing is much harder in the condensed phase than in the gaseous phase can be seen at the example of $W(CO)_6$: In Ref. [19], the dissociation of $W(CO)_6$ in the gas phase by

vibrational ladder climbing was successfully demonstrated. The same group performed a ladder climbing experiment with $W(CO)_6$ dissolved in n-hexane, employing MIR pulses with very similar parameters as before (spectrum, energy, focusing) [150]. However, for the experiment in the condensed phase, the group could not observe dissociation of $W(CO)_6$.

A similar issue is encountered for molecules with a Fe-CO bond. $Fe(CO)_5$ could be successfully dissociated by excitation of the CO vibration and subsequent IVR into the reaction coordinate [19]. In contrast, vibrational excitation of the CO bond did not lead to appreciable bond cleavage of the Fe-CO bond in the larger carboxyhemoglobin molecule [151]. This was later theoretically explained by insufficient coupling between the excited C-O vibration and the Fe-CO reaction coordinate, so that the energy deposited in the C-O vibration could not be efficiently guided into the reaction coordinate [152]. Thus, there is no significant Fe-CO bond breaking, even if the C-O vibration is initially excited above the Fe-CO dissociation limit [152].

3. In a recent theoretical study [153], it has been shown that for vibrational ladder climbing, the transition dipole moment for transitions between adjacent levels $v = n \rightarrow n + 1$ is not monotonically increasing[1], but can actually decrease and vanish for increasing n. Pictorially speaking, a vanishing dipole moment corresponds to a missing rung in the vibrational ladder. The position of the missing rung sensitively depends on the exact shape of the potential energy surface and highly accurate quantum chemical calculations are necessary to determine it [153]. A transfer of calculation results on the missing rung from one molecule to another is thus not straightforward.

IV. 7.2 Combination of vibrational pre-excitation with UV excitation

IV. 7.2.1 Enhancement of the quantum yield through vibrational pre-excitation

In Sec. IV. 6.4 it was shown that the *product yield* of the UV triggered photoreaction of DNQ is enhanced through vibrational pre-excitation for UV pump wavelengths λ_{UV}, both off-resonant ($\lambda_{UV} = 433\,\text{nm}$) and resonant ($\lambda_{UV} = 393\,\text{nm}$) with the DNQ steady state absorption. In contrast, vibrational excitation has an opposite effect on the DNQ *absorption* at these wavelengths, as was shown by the MIR pump/WL probe experiment in Sec. IV. 6.2. Absorption is decreased for resonant λ_{UV}, whereas it is increased for off-resonant λ_{UV}. The measured change in photoproduct yield is, therefore, a combined effect of a change in absorption of UV photons and a change in efficiency to undergo photoreaction, once a UV photon is absorbed. It is thus interesting to know how the quantum yield (QY) Φ with

$$\Phi = \frac{\#\ \text{molecules converted in photoreaction}}{\#\ \text{photons absorbed}} \qquad (\text{IV.}\,14)$$

is affected by vibrational pre-excitation.

---

[1] It is often assumed that the transition dipole moment monotonically increases with increasing v, like it does in a strictly harmonic potential, cf. e.g. Ref. [150].

	$\Phi_{v=0}$	$\Phi_{v>0}$	$\dfrac{\Phi_{v>0}}{\Phi_{v=0}}$
$\lambda_{UV} = 433$ nm	$0.22\,^{+0.06}_{-0.05}$	$0.25\,^{+0.06}_{-0.06}$	$1.11\,^{+0.01}_{-0.01}$
$\lambda_{UV} = 393$ nm	$0.29\,^{+0.04}_{-0.04}$	$0.32\,^{+0.05}_{-0.05}$	$1.10^{+0.00}_{-0.01}$

Table IV-1: *Obtained quantum yields Φ for off-resonant (λ_{UV}=433 nm) and resonant (λ_{UV}=393 nm) UV excitation. For both λ_{UV}, Φ is given for the case with ($v > 0$) and without ($v = 0$) vibrational pre-excitation. In the last column, the enhancement of Φ through vibrational pre-excitation is presented. Details on the calculation of Φ are given in App. C. 3.*

The QY can be estimated from the measured ΔA signal, the steady state absorption spectrum of DNQ and experimental parameters like the spot size, pulse energy and sample concentration. The actual calculation for the estimation of Φ is lengthy and only its results are relevant for the further discussion. Therefore, the calculation itself is presented in the appendix (App. C. 3). The estimated values for Φ are given in Tab. IV-1.

The values for the QY are likely to be underestimated, for reasons given in App. C. 3.5. This is in line with the reported QY in Ref. [29]: $\Phi_{v=0} = 0.32$ for $\lambda_{UV} = 400$ nm . The enhancement factors in the last column of Tab. IV-1 also rather give a *lower bound* for the QY enhancement through pre-excitation of the C=N=N stretch mode. Despite these shortcomings, the enhancement factors clearly indicate that the increased photoproduct formation observed in the experiments of Sec. IV. 6.4 is not only a consequence of a mere change in UV absorption, but also of a better coupling of vibrationally pre-excited molecules into the reaction coordinate by at least 10%. This holds for both resonant and off-resonant UV excitation and the QY enhancement is similar in both cases. Whether the QY substantially changes between $\lambda_{UV} = 433$ nm and $\lambda_{UV} = 393$ nm cannot be deduced from the values given in Tab. IV-1, as the error ranges overlap for both λ_{UV}.

IV. 7.2.2 Dynamics of the photoproduct enhancement

Vibrational pre-excitation enhances the photoproduct formation for both off-resonant and resonant UV excitation wavelengths, as was demonstrated in Sec. IV. 6.4.1 and IV. 6.4.2. It turns out that the dynamics of the photoproduct enhancement is similar for both λ_{UV}, as can be seen in Fig. IV.34 a). For better comparison, a normalised curve for the resonant UV wavelength ($\lambda_{UV} = 393$ nm) is shown in Fig. IV.34 a), too. The normalisation is done so that the value at 1 ps coincides with the value for the off-resonant excitation ($\lambda_{UV} = 433$ nm):

$$R_{norm}(393\ nm) = \big((R(393\ nm) - 1) \cdot \beta\big) + 1$$

$$with\ \beta = \frac{R(433\ nm, 1\ ps) - 1}{R(393\ nm, 1\ ps) - 1} \qquad and \qquad R = \frac{\overline{\Delta A}\ \text{with MIR pre} - \text{pump}}{\overline{\Delta A}\ \text{without MIR pre} - \text{pump}}\ .$$

$$(IV.\,15)$$

In Eq. IV. 15, the normalisation factor β relates the values of photoproduct enhancement at 1 ps of both curves. The ratio of ΔA values with and without MIR pre-excitation is abbreviated by R. The error bars of the normalised curve are also scaled by β.

Since the dynamics for both λ_{UV} is similar, in the following the dynamics of the photoproduct enhancement will be exemplified only for the off-resonant case with $\lambda_{UV} = 433$ nm. Fig. IV.34 b) shows the photoproduct enhancement dynamics together with the transient at 433 nm of the MIR pump/WL probe experiment. As can be seen, the 433 nm transient decays slower than the photoproduct enhancement. However, it is pointed out in literature that a transient at a single wavelength might be inappropriate to follow the vibrational cooling dynamics [154, 155]. This is because during the cooling process, the absorption spectrum is blue shifting and gets narrower. Thus following a transient along a single wavelength of the hot ground state might give an erroneous picture as the dynamics observed at the probed wavelength might be deteriorated by the contributions that sweep
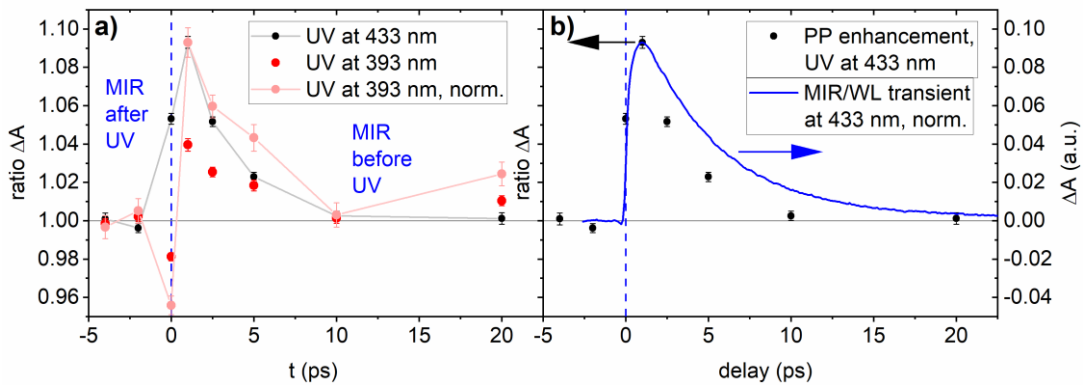
Figure IV.34: *a) R for several MIR pre-pump/UV pump delays t. Black: Off-resonant UV excitation ($\lambda_{UV} = 433\ nm$), red: Resonant UV excitation ($\lambda_{UV} = 393\ nm$), light red: $\lambda_{UV} = 393\ nm$, normalised; for better comparability, values and error bars are normalised so that the value at 1 ps coincides with the value for $\lambda_{UV} = 433\ nm$. The grey and light red lines serve as guide for the eye. b) Comparison of the photoproduct (PP) enhancement dynamics for $\lambda_{UV} = 433\ nm$ (left y-scale) and the 433 nm transient of the MIR pump/WL probe measurement (right y-scale). For the PP enhancement, the x-axis denotes the MIR pre-pump/UV pump delay t, for the 433 nm transient, it denotes the probe delay τ.*

through during the aforementioned blue shift. A better approach to follow the vibrational population dynamics is to use band integrals [155]. This is done in Fig. IV.35 b). Band integrals of the MIR pump/WL probe trace (Fig. IV.35 a)) over several spectral regions are compared with the dynamics of the photoproduct enhancement. The band integral that takes only into account the region where a bleach is observed (350-413 nm) agrees best with the observed photoproduct enhancement dynamics, whereas the band integral over the whole spectral region (350-600 nm) virtually shows no difference to the transient at 433 nm.

An even better agreement is found between the photoproduct enhancement and the transient at 400 nm, Fig. IV.35 c). At 400 nm, the DNQ UV/Vis absorption has a maximum (cf. Fig. IV.12 c)) and the MIR pump/WL probe TA trace shows a negative signal (cf. Fig. IV.35 a)). This means that the transient at 400 nm is a measure for the bleach induced by vibrational excitation and thus for the popuplation that has left the vibrational ground state and is in a vibrational excited state with $v > 0$.

A similar behaviour is observed in the MIR region around 2100 cm^{-1}. From the MIR
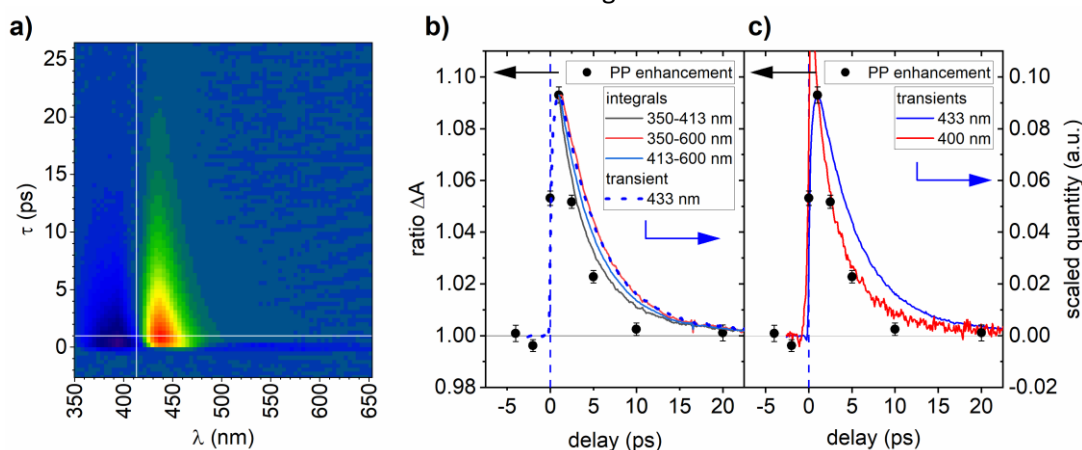
Figure IV.35: *Dynamics of vibrational cooling deduced from the MIR pump/WL probe measurement. a) MIR pump/WL probe TA trace, cf. Sec. IV. 6.2. The thin white lines are references for λ=413 nm and τ=1.0 ps, respectively. b) Photoproduct (PP) enhancement for pump wavelength $\lambda_{UV} = 433\ nm$ (black scattered, left y-axis) and band integrals of the MIR pump/WL probe TA trace for different wavelength ranges. The band integrals are scaled such that their maxima correspond to [R(433 nm, 1 ps)-1], cf. Eq. IV.15. Band integrals are evaluated only at delays above τ=1.0 ps. The transient at 433 nm is also shown for comparison. c) Scaled transients at 433 nm and 400 nm, together with the PP enhancement. The y-scales on the left and right side are the same for both b) and c). In b) and c), the x-axis denotes the MIR pre-pump/UV pump delay t for the PP enhancement and the MIR pump/WL probe delay τ elsewise.*

pump/MIR probe measurement presented in Sec. IV. 6.1, the dynamics of the bleach level of the fundamental $v = 0 \rightarrow 1$ transition around 2120 cm^{-1} is evaluated, cf. Fig. IV.36. To this end, spectral cuts are taken at each delay τ and the minimum value of $\Delta A(\tau)$ is determined, cf. Fig. IV.36 a). The normalised decay of the minima of $\Delta A(\tau)$ is shown in Fig. IV.36 b). It shows a better agreement with the dynamics of the photoproduct enhancement than the transient at 433 nm. Even if the measured signal around 2120 cm^{-1} contains contributions from both the actual GSB and stimulated emission from $v = 1 \rightarrow 0$, the agreement between measured photoproduct enhancement and decay of the bleach signal suggests that the probed bleach level of the fundamental $v = 0 \rightarrow 1$ transition indeed gives

a good indicator of the refilling of the vibrational ground state and therefore provides a measure for the number of vibrationally excited molecules with $v > 0$. However, it does not contain information about the population distribution of levels with $v > 0$. The slight deviations between the $\Delta A(\tau)$ minima and photoproduct enhancement dynamics seen in Fig. IV.36 b) might be caused by the mentioned superposition of GSB and stimulated emission. Another reason for the slight discrepancy could be that the coupling into the reaction coordinate is enhanced differently for different v.

From the above analysis of the bleach levels in both the MIR pump/WL probe and MIR pump/MIR probe TA traces, the photoproduct enhancement agrees well with the population in vibrational excited states with $v > 0$. The exact level of vibrational excitation only seems to play a minor role in photoproduct enhancement.
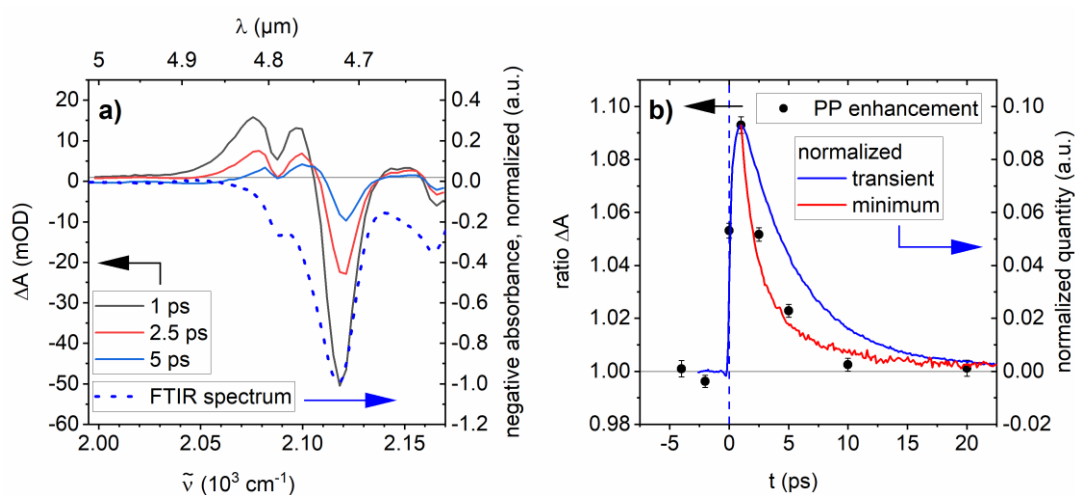
Figure IV.36: a) Spectral cuts of the MIR pump/MIR probe TA trace at several delays (left y-axis). The normalized inverted FTIR spectrum is shown as reference (dotted, right y-axis). b) Photoproduct (PP) enhancement for $\lambda_{UV} = 433\ nm$ (black, left y-axis) together with the normalised 433 nm transient (blue) and the normalised course of the minima of the transient spectra of the MIR pump/MIR probe measurement (red, both right y-axis). For the PP enhancement, the x-axis denotes the MIR pre-pump/UV pump delay t, for the 433 nm transient and the transient spectra minima, the x-axis denotes the probe delay τ.

IV. 8   Conclusion

In this chapter, the impact of excitation of the C=N=N stretching vibration of DNQ dissolved in MeOH on the molecule's photoreaction was investigated. It was found that the C=N=N stretch mode could be excited up to at least $v = 3$. The vibrational excitation decays within 20 ps. Cleavage of the N_2 group from the rest of the molecule by mere vibrational excitation of the C=N=N stretch mode was not observed. Possible reasons for the absence of electronic ground state dissociation were given. Excitation of the C=N=N stretch mode was found to influence the UV/Vis absorption spectrum. The UV/Vis absorption is reduced for wavelengths at resonance with the steady state UV/Vis absorption, whereas the absorption is increased at the long wavelength edge of the steady state UV/Vis absorption. These observations could be understood by findings in the field of VIPER spectroscopy [24, 145].
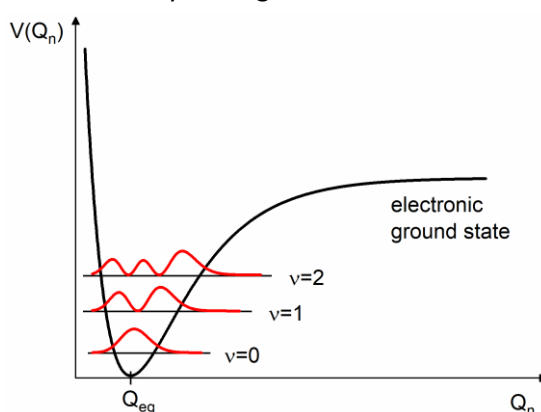
Figure IV.37: *Probability density of the vibrational wave function in the electronic ground state. Only for $v = 0$, the highest probability is at the centre of the potential, for $v > 0$, the highest probability shifts towards the edge of the potential.*

For a combination of vibrational pre-excitation and UV excitation in a VMP experiment, enhanced photoproduct formation was observed for both resonant and off-resonant UV wavelengths. The quantum yield for photoproduct formation was found to increase by at least 10% through vibrational pre-excitation for both resonant and off-resonant UV wavelengths. Good agreement was found between the evolution of the photoproduct enhancement with MIR/UV delay and the refilling of the vibrational ground state. This agreement also suggests that the increase in photoproduct formation is mostly due to excitation to *some* vibrational level with $v > 0$, whereas the *exact* number of vibrational quanta in the C=N=N stretch mode plays only a minor role for the photoproduct enhancement. This can be understood from Fig. IV.37. For $v = 0$, the highest probability of the vibrational wavefunction is around the centre of the molecular potential. For all $v > 0$, the highest probability shifts to the edge of the potential. The observed photoproduct enhancement is thus attributed to an increased Franck-Condon overlap between the reactive part of the electronic excited state's potential energy surface with the edge of the electronic ground state's potential energy surface. The increased Franck-Condon overlap of vibrationally excited molecules in the electronic ground state with the reactive part of the electronic excited state's potential energy surface then results in a better coupling to the actual reaction coordinate after UV excitation.

The results of this chapter provide a good qualitative understanding of how excitation of the C=N=N stretch mode impacts the photoreaction of DNQ. In order to get a better quantitative understanding as well, elaborate quantum chemical calculations are desirable. Such calculations should focus on the electronic ground state potential energy surface, since

already published calculations on DNQ focus on the transition between different electronic states [131-133]. If there was a possibility of DNQ dissociation in the electronic ground state, it might be identified by a thorough study of the electronic ground state potential energy surface. Such a study could also give hints on whether the excitation of the C=N=N stretch mode needed to be accompanied by excitation of an additional mode, for example a naphthalene ring mode, in order to achieve electronic ground state dissociation. After all, N_2 cleavage from DNQ is accompanied by a ring contraction (cf. Sec. IV. 2.1).

To investigate whether the missing rung in the vibrational ladder (cf. Sec. IV. 7.1.2) was the predominant cause that prevented ground state dissociation, a measurement employing vibrational excitation pulses at two frequencies, as is proposed in Ref. [153], could be performed. The excitation frequencies are on the one hand at the fundamental vibrational transition frequency and on the other hand at a frequency corresponding to a "double-stepping" transition. The latter is able to overcome the missing rung in the vibrational ladder.

V   Summary and outlook

The work at hand presents a source for broadband shapeable pulses in the mid-infrared (MIR) spectral region. The presented setup consists of a non-collinear optical parametric amplifier (NOPA) and an acousto-optic modulator (AOM) based pulse shaper. The NOPA is pumped by pulses from a Titanium:sapphire regenerative amplifier system and provides output pulses tunable between 2 and 5 µm. The novelty of the presented setup is that it comprises an implementation of dispersion scan (d-scan) for retrieval of the pulse's spectral phase. The all collinear, in-line characterisation of the spectral phase only demands for minimum additional alignment when a pulse shaper is involved anyway in the experiment, which is often the case for control experiments. The aspect of minimum additional alignment is especially important for the MIR spectral region, where alignment issues are more severe than in the visible or near-infrared range. The reliability of phase retrieval was demonstrated for rather narrowband pulses centred at 4.8 µm by successful reconstruction of the spectral phase introduced by various substrates that imprint group delay dispersions of different signs onto the pulses. Phase retrieval was shown to be successful also for the largest part of the spectrum of broadband MIR pulses centred at 3.2 µm. The bottleneck in the phase retrieval of the blue wing of the broadband pulses could be identified as the detector for the second harmonic spectrum available for this thesis and is in particular not intrinsic to the presented method itself. The setup's capabilities in broadband MIR pulse shaping have been demonstrated for spectral phases of increasing complexity, including a 2-colour double pulse that comprises a discontinuity of the group delay at the separation frequency.

The presented setup delivers shapeable, broadband MIR pulses centred at 3.2 µm with 400 nJ energy. The shapeable MIR pulses can be compressed to a duration below 50 fs FWHM autocorrelation. Strategies for further improvements of the presented setup were given. These concerned both the d-scan implementation and the output energy of the pulses from the NOPA.

Furthermore, this thesis investigated the impact of excitation of a specific vibration on a molecule's photoreaction. In the studied case, the C=N=N stretch mode of 2-diazo-1-naphthol-5-sulfonate (DNQ) dissolved in MeOH was excited by MIR pulses of 120 fs duration. Vibrational ladder climbing of the C=N=N stretch mode was observed up to at least $v = 3$. The vibrational excitation decays within 20 ps. Imprinting a negative chirp onto the MIR excitation pulse did not substantially improve the ladder climbing process. Dissociation of DNQ in the electronic ground state by sole excitation of the C=N=N stretching vibration was not observed. Several possible reasons for the absence of photodissociation in the electronic ground state were given.

An experiment on vibrationally mediated photodissociation (VMP) with a combination of vibrational pre-excitation of the C=N=N stretch mode and subsequent electronic excitation by an ultrafast ultraviolet (UV) pulse was also conducted on DNQ. The VMP experiment revealed that the quantum yield of the UV triggered photoreaction can be enhanced by at least 10% via vibrational pre-excitation of the C=N=N stretch mode. This holds true for both UV excitation wavelengths resonant ($\lambda_{UV} = 393$ nm) and off-resonant ($\lambda_{UV} = 433$ nm) with the steady state DNQ absorption. The lower bounds of the *absolute* values of the quantum yields are also estimated. The results are in good agreement with the values reported in literature (where available) [29].

The dynamics of the photoproduct enhancement in the VMP experiment agrees well with the dynamics of the refilling of the vibrational ground state of DNQ. This agreement

suggests that vibrational pre-excitation leads to a better coupling to the actual reaction coordinate via an increased Franck-Condon overlap of the molecular wave function in the electronic ground state with the reactive part of the potential energy surface of the electronic excited state.

Having a spectrally broad, well characterised and shapeable MIR pulse at hand, future experiments could combine such a MIR pulse with metal nanostructures. A feature of metal nanostructures is that if the incoming electromagnetic MIR field matches the resonance frequency of the metal nanostructure, the incoming electromagnetic MIR field is enhanced by orders of magnitude in the nanostructure's vicinity [156]. This in turn enhances vibrations of molecules in the proximity through resonant coupling between molecular vibrational excitation and plasmonic excitation of the metal nanostructure [156]. Resonant metal nanostructures thus compensate the often low MIR absorption cross-section. The metal nanostructures can be accordingly designed to match the vibrational frequency of interest and even to simultaneously match several vibrational bands [157]. On the one hand, due to its improved sensitivity, resonant surface-enhanced infrared spectroscopy, i.e. the combination of infrared radiation with suitable metal nanostructures, has found its application in the sensing of minute amounts of sampling material [156]. On the other hand, significant vibrational ladder climbing has been observed in surface-enhaced infrared spectroscopy, even in the case for weakly absorbing functional groups and moderate MIR pulse energies [158]. Furthermore, molecular dissociation in the electronic ground state succeeded by combination of a gold nanoantenna array with a MIR excitation pulse [22], where "traditional" ultrafast MIR excitation, i.e. without a nanoantenna array, did not [150]. The combination of shaped MIR pulses with suitably designed metal nanostructures, therefore, seems to be a promising path to achieve high excitation of the specific molecular vibration of interest and thus to steer a molecule's reaction via excitation of a particular molecular bond.

Appendix

A NOPA

A. 1   Alignment of the NOPA

This section provides some practical information on the alignment of the NOPA presented in Ch. II.

1st stage:

1. The compression of the Ti:Sa amplifier system is optimised for NOPA operation by maximising the energy of the 400 nm SH pulses that are generated in BBO 1.
2. An IR viewer can be used to check the spatial overlap of NIR signal and 400 nm pump in BBO 2.
3. Temporal overlap between pump and signal is easily noticed by the emergence of the well visible red idler on the diagnostic screen, cf. Fig. A.1 a).
4. The angle between pump and signal can be initially set by overlapping the WL seed with the yellow part of the pump-induced superfluorescent cone on the screen, see Fig. A.1 b). In order to see the WL signal on the screen with bare eye, the LP900 longpass filter needs to be removed and the D-mirror needs to be translated so that it also reflects the WL onto the screen.
5. The position of the $f = 50$ mm mirror after the WL generating sapphire window influences the spatial chirp of the pre-amplified signal beam, see Fig. A.2.
6. On top of the pre-amplified NIR signal beam, there is a weak green beam visible that originates from SHG of the NIR signal in BBO 2. The visible SH beam is very useful to guide the collimated pre-amplified NIR seed into the second stage.
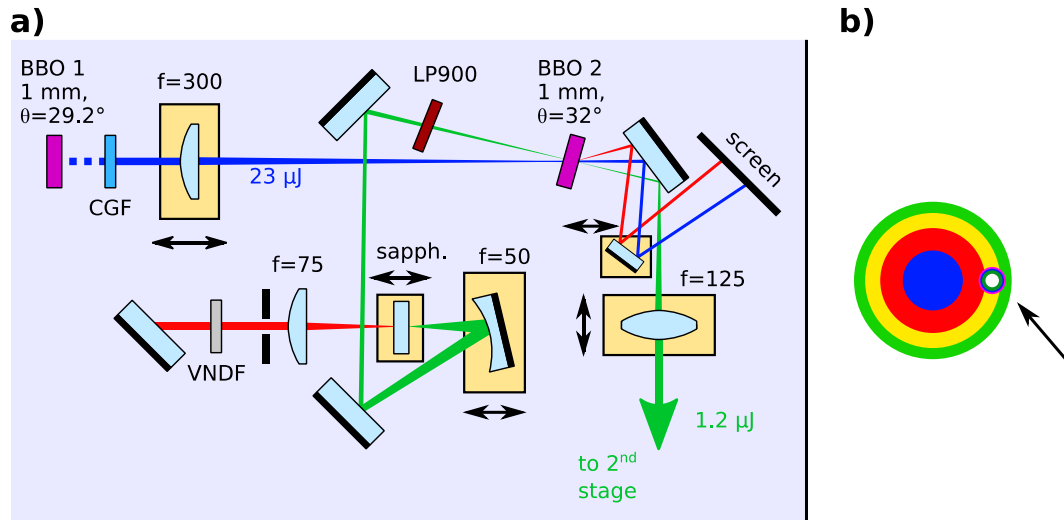
Figure A.1: *a) Part of the NOPA first stage for pre-amplification of the NIR seed. After pre-amplification in BBO 2, a diagnostic D-mirror reflects the idler and residual pump onto a screen. The D-mirror is mounted on a translation stage that allows to easily move the mirror into the signal path and to inspect the WL seed on the screen. b) Superfluorescent cone and WL as seen on the screen during alignment. For the WL to be visible on the screen, the LP900 longpass filter needs to be taken out of the beam path and the diagnostic D-mirror that reflects the residual 400 nm pump onto the screen needs to be moved into the signal beam path.*
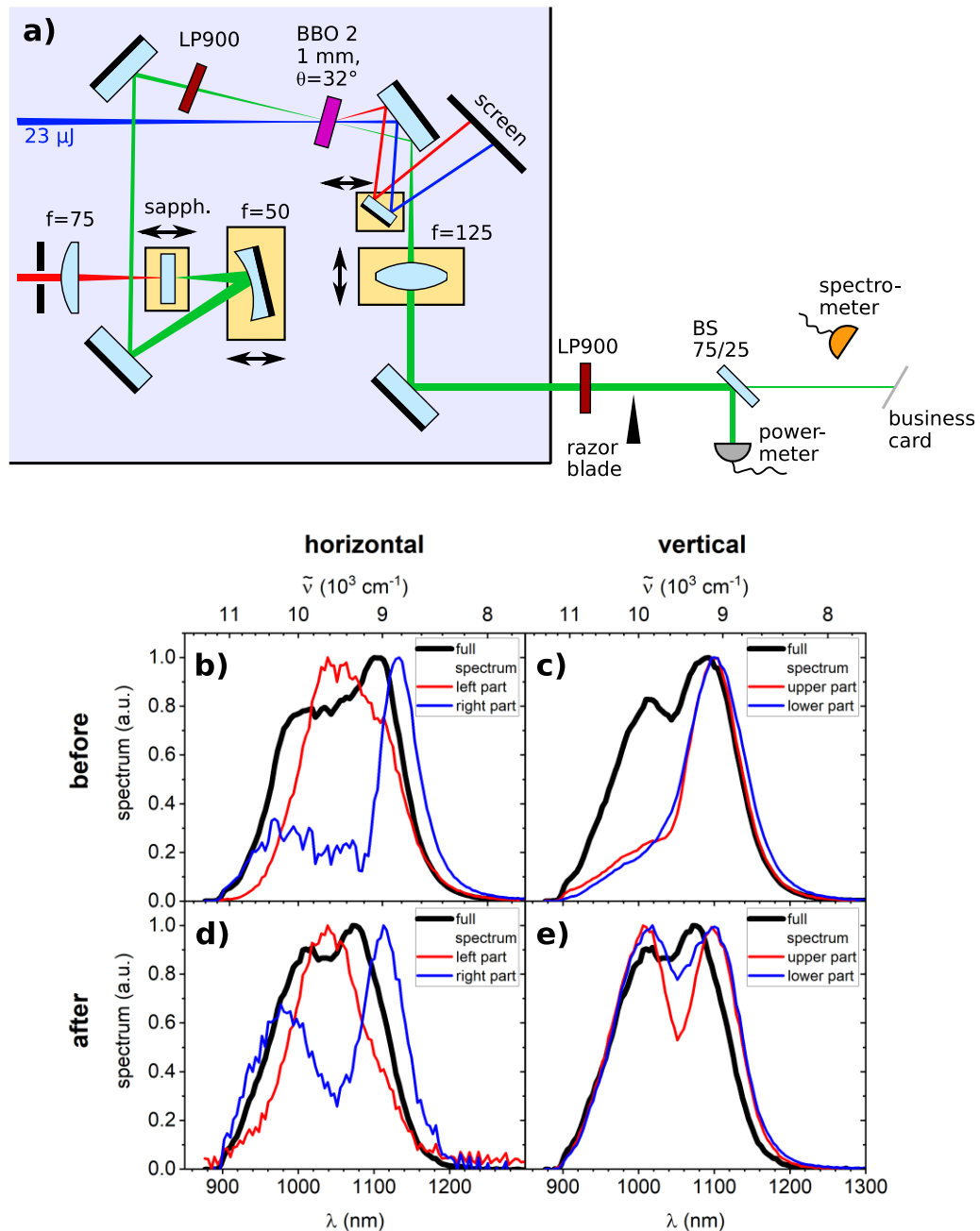
Figure A.2: *Spatial chirp of the pre-amplified NIR signal beam. a) Setup for spatial chirp measurement. After the collimation lens, the NIR pre-amplified seed is reflected out of the NOPA and passes a 900 nm longpass filter that filters out any visible component that is generated in the amplification process in BBO 2. A beamsplitter reflects 75% of the beam into a power meter and 25% are transmitted onto a business card. A spectrometer records the spectrum scattered from the business card. The beam can be gradually clipped by a razor blade. b)-e) Spectra before (top row) and after (bottom row) translation of the WL focus mirror by 0.70 mm away from the sapphire window. The spectra have been clipped in the horizontal (left column) and vertical (right column) direction by the razor blade. For the clipped spectra, ca. 14% of the energy pass the razor blade. The full spectrum is recorded without the blade clipping the beam. Translation of the WL focus mirror made the spectrum more uniform across the beam cross section.*

2nd stage:

1. The Ge window at the end of the NOPA transmits only spectral components above 2 µm. Visible components that are generated by wave mixing processes in the PPMCLN crystal are absorbed and reflected. The backreflection of the visible components can be guided onto some white adhesive tape placed on the PPMCLN crystal holder for inspection. The colour of the backreflection is a rough indicator for the MIR spectrum: For a broadband MIR spectrum around 3 µm, the backreflection is bright rose, whereas it is green-bluish for a rather narrowband MIR spectrum located between 4 µm and 5 µm.

2nd stage:

B AOM shaper and d-scan

B. 1 Position vs. frequency calibration of the AOM pulse shaper

The mapping of position on the AOM aperture vs. optical frequency follows the calibration procedure outlined in Ref. [159]. With the AWG, two amplitude masks are written on the AOM: One mask has a single peak at the centre of the AOM aperture, the other has multiple peaks distributed all over the AOM aperture, see Fig. B.1 a). From the respective spectra transmitted through the shaper (Fig. B.1 b)) and the information about the applied amplitude masks, each sampling point of the AWG can be mapped to an optical frequency f, as shown in Fig. B.1 c). The AWG generates the waveform with 1 GHz sampling frequency, i.e. every 1 ns a point of the waveform is created. The waveform over the whole AOM aperture (access time: 10 μs) is thus made up of 10.000 sampling points. Via the 1 GHz sampling frequency and acoustic velocity, it is straightforward to transform a sampling point n into a propagation time t_A or position x along the AOM aperture.

For the data shown in Fig. B.1, a quadratic fit of optical frequencies f vs. AWG sampling points n yields

$$f(n)[\mathrm{THz}] = 72.277 + 2.2396 \cdot 10^{-3} \cdot n + 4.0872 \cdot 10^{-7} \cdot n^2 \ . \qquad (B.1)$$
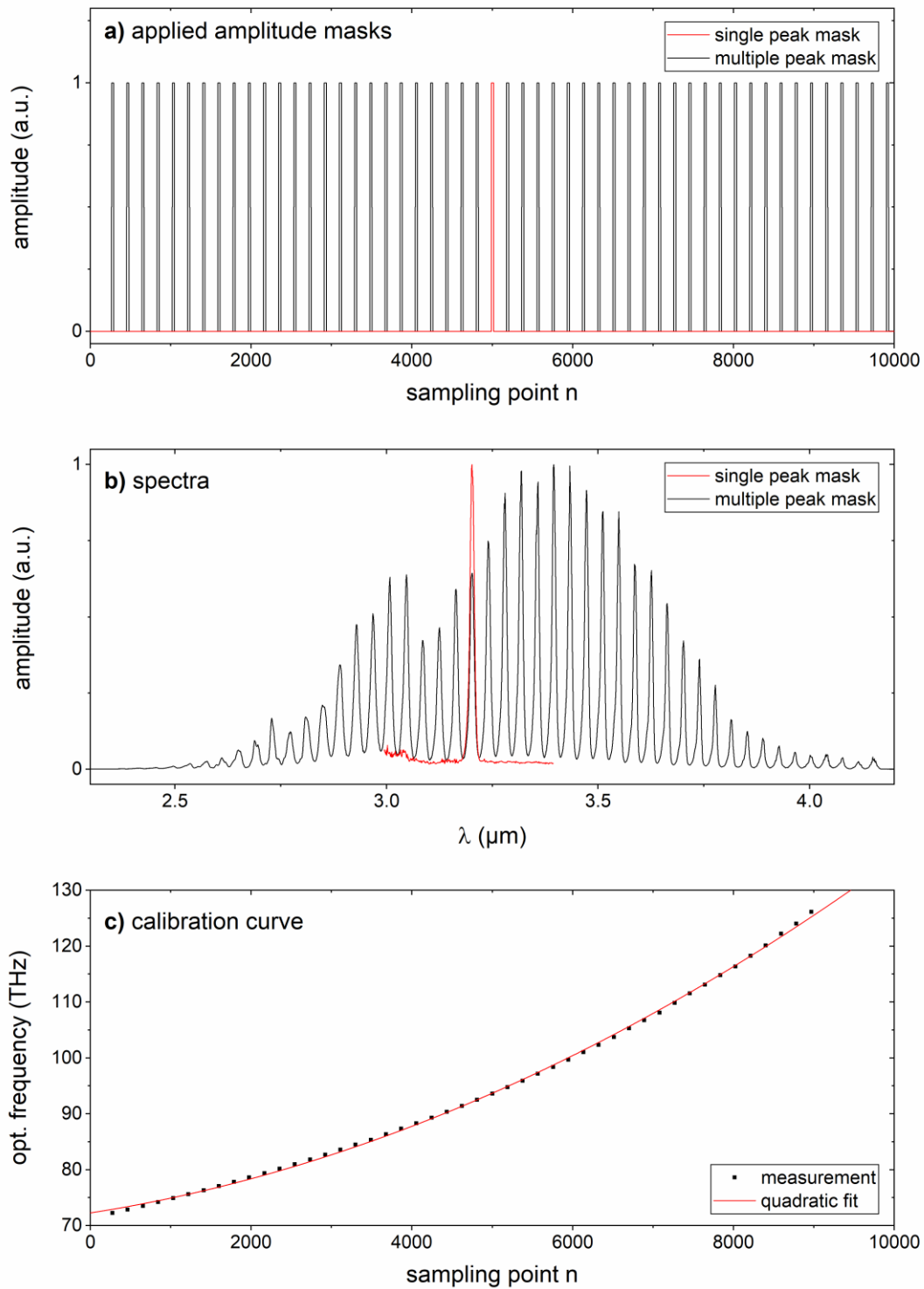
Figure B.1: *Calibration procedure of the shaper. a) Two amplitude masks are applied on the shaper, one with a narrow gate at the centre of the AOM aperture (red) and one with a series of narrow gates all along the aperture (black). b) Transmitted spectra corresponding to the applied amplitude masks. c) From the amplitude gate positions on the AOM aperture and the peak positions of the spectra, a calibration curve is obtained.*

B. 2   AOM shaper: Wavelength vs. position on second grating

The position of the several spectral components on the second grating of the AOM pulse shaper for a fixed acoustic frequency $f_{0,ac}$ can be approximated on the basis of ray optics. The approximation is done in the following way, cf. also Fig. B.2:

1) For a central wavelength λ_0, the Bragg angle in air $\theta_{B,air}(\lambda_0)$ is calculated. The incoming angle for all wavelengths on the AOM is taken as $\theta_{B,air}(\lambda_0)$.
2) All wavelengths are refracted when entering the AOM according to their refractive indices $n(\lambda)$: $\sin\theta_{B,air} = n(\lambda)\sin\theta_m$.
3) Diffraction of the optical wave at the acoustic wave (cf. [81]):

$$\sin\theta_m(\lambda) + \sin\theta_{diff}(\lambda) = \frac{\lambda_m f_{0,ac}}{v_{ac}}$$
(B.2)

with

θ_m:	angle of incoming beam inside the medium	λ_m:	optical wavelength inside the medium
θ_{diff}:	diffracted angle inside the medium	$f_{0,ac}$:	acoustic frequency
		v_{ac}:	sound velocity.

4) All wavelengths are refracted when exiting the AOM: $n(\lambda)\sin\theta_{diff} = \sin\theta_{air,out}$.
5) Use of ray matrices of free propagation and thin lens to calculate the position y_2 of each spectral component on the second grating, cf. Fig. B.2 b). The input values are $\theta_1(\lambda) = \theta_{air,out}(\lambda)$ and y_1 is taken from the position vs. frequency mapping as presented in App. B. 1. For y_1 the displacement due to the diffraction from the acoustic wave is neglected, as θ_B is small.

$$\begin{pmatrix} y_2(\lambda) \\ \theta_2(\lambda) \end{pmatrix} = M \begin{pmatrix} y_1(\lambda) \\ \theta_1(\lambda) \end{pmatrix}$$
(B.3)

with

$$M = \underbrace{\begin{pmatrix} 1 & d_2 \\ 0 & 1 \end{pmatrix}}_{\substack{\text{propagation} \\ \text{mirror}\rightarrow\text{grating}}} \underbrace{\begin{pmatrix} 1 & 0 \\ -\frac{1}{f} & 1 \end{pmatrix}}_{\text{cyl. mirror}} \underbrace{\begin{pmatrix} 1 & d_1 \\ 0 & 1 \end{pmatrix}}_{\substack{\text{propagation} \\ \text{AOM}\rightarrow\text{mirror}}} .$$

$d_1 = f - \frac{L}{2}$ is the distance between the output facet of the AOM and the cylindrical mirror, f is the focal length of the cylindrical mirror, L the width of the AOM and $d_2 = f$ the distance between cylindrical mirror and second grating.

a)

b)
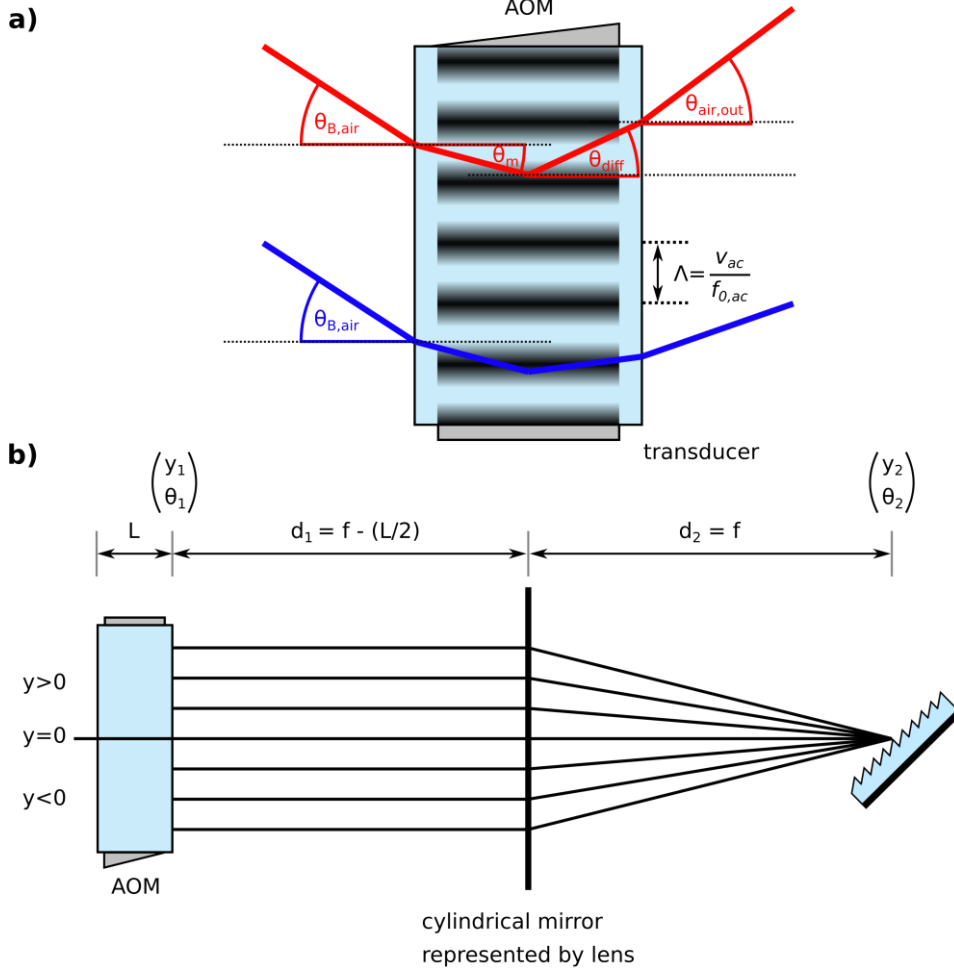
Figure B.2: *a) Scheme of the diffraction of different optical wavelengths in the AOM. The incoming angle $\theta_{B,air}$ is the same for all optical wavelengths, while the outgoing angle $\theta_{air,out}$ is not. b) Sketch of beam propagation after the AOM.*

B. 3   Implementation of evolutionary algorithm

The evolutionary algorithm used in this work is based on mutations of the individuals from one generation to the next. After evaluation of the fitness of all individuals within one generation, the fittest N_{par} individuals are chosen as parents for the next generation. Each parent individual then creates N_{mut} mutant individuals. This procedure follows the description of Ref. [93]. Let $\vec{x}_i$ be the vector containing the parameters describing parent i and $\vec{y}_i$ the vector of a descending mutant. In the case relevant for this work, $\vec{x}_i$ and $\vec{y}_i$ contain the GDD and TOD of the spectral phase. The entries of $\vec{y}_i$ of the mutant are generated form the parent $\vec{x}_i$ by

$$y_i = \begin{cases} x_i + \delta \cdot (x_{up} - x_{low}) \cdot m_i & \text{with probability } P_{mut} \\ x_i & \text{with probability } (1 - P_{mut}) \end{cases} \tag{B.4}$$

i.e. P_{mut} determines whether a mutation takes place or if the value of the parent is just inherited. If a mutation occurs, the value x_i of the parent is changed by $\delta(x_{up} - x_{low}) \cdot m_i$. x_{up} and x_{low} are the upper and lower bound of the parameter space given by the user, m_i is a random variable with a Gaussian probability distribution around 0:

$$P(m_i) = \frac{1}{\sqrt{2\pi\sigma^2}} e^{-\frac{m_i^2}{2\sigma^2}} \tag{B.5}$$

The variance is set as $\sigma^2 = 0.435$. The stepsize δ is adjusted each generation. If, on the one hand, mutation leads to a significant increase of the fitness compared to the previous generation, it means that the fittest individuals are still far away from the optimum. Thus the search space needs to be increased. On the other hand, if mutation does not lead to a significant increase of the fitness, i.e. the parent individuals had been already close to the optimum, it is advisable to further refine the search space around the current parameters. This can be expressed by [93]

$$\delta_t = \begin{cases} \dfrac{\delta_{t-1}}{q} & \text{if } \eta \geq \eta_c \\ \delta_{t-1} \cdot q & \text{if } \eta < \eta_c \end{cases} \tag{B.6}$$

t denotes the generation and q is th so-called convergence parameter. Whether the fitness is increased by mutations, is expressed by the ratio of successful mutations

$$\eta = \frac{n_{suc}}{n_{tot}} \tag{B.7}$$

n_{suc} is the number of successful mutations, i.e. the number of individuals of generation $t - 1$ that perform better than the median of generation $t - 2$. n_{tot} is the number of total mutations. η is compared to a threshold η_c.

The parameters for the evolutionary algorithm used in this work are given in Tab. B-1. For those parameters, convergence was observed well within the permitted number of generations t_{max}. Initial parameters for the first generation population are generated randomly between the bounds $\vec{x}_{up}$ and $\vec{x}_{low}$.

For each generation, the different individuals are successively tested in the experiment. This series of tests is repeated several times and the fitness of each individual is evaluated by taking the corresponding mean of the repeated test series. In this way, the influence of fluctuations of the laser power on the evaluation of the fitness is mitigated.

# individuals per generation	32	# survivors	0
# mutants	N_{mut} = 6	Mutation probability	P_{mut} = 0.5
# parents	N_{par} = 6	# generations	t_{max} = 30-40
Convergence parameter	q = 0.94	threshold	η_c = 0.8
Initial step size	δ_1 = 0.4		

Table B-1: *Parameters for the evolutionary algorithm used in this work. Each parent individual usually creates 6 mutants. As this would lead to $6 \cdot 6 = 36$ individuals for the next generation, the 6th parent only generates 2 mutants.*

B. 4 Optical d-scan setup for MIR at 4.8 μm

The d-scan optical setup for the narrowband MIR centred at 4.8 μm slightly deviates from the setup used for the broadband pulse centred at 3.2 μm, which was presented in Sec. III. 3. The differences for the narrowband 4.8 μm setup are listed in the following for the sake of completeness:

- Different AGS crystal for SHG: 200 µm thick with θ=32.6°, φ=45°.
- No 50 mm LiF rod in beampath.
- No Bragg compensation mask applied, the default waveform on the AOM was an unmodulated sine waveform.
- After the shaper, a 3 µm longpass was placed to block spectral components that might have been generated in the NOPA and could be misinterpreted as SH signal at 2.4 µm. The Ge substrate of the AOM only blocks components below 2 µm.
- The SH signal is not collimated by a CaF$_2$ lens after the AGS crystal, but by a N-BK7 lens. N-BK7 is only transmissive up to 4 µm and thus also acts as shortpass filter that blocks the fundamental.

Parameters of the AOM shaper deviating from the ones given in Sec. III. 3.2 are listed in Tab. B-2. The number of effective pixels over the active aperture is nearly the same as for the broadband spectrum around 3.2 µm. However, as the narrowband spectrum covers a smaller part of the AOM aperture, the spectral FWHM corresponds to only 25 pixels.

Centre optical wavelength	λ_0 = 4800 nm
Refractive index at λ_0	$n(\lambda_0)$ = 4.02
Bragg angle in medium	θ_B = 0.47°
Bragg angle in air	$\theta_{B,air}$ = 1.88°
Q parameter	Q = 9.3 π
Average horizontal spot size across interaction region ($\frac{1}{e^2}$ diameter)	$2\overline{w}_0$ = 290 µm
Effective number of pixels over active aperture	190
Time window available for shaping	T = 17.4 ps
Maximum displacement of FP due to FP tilt	0.9 mm
Rayleigh range	z_R = 2.7 mm

Table B-2: *Parameters of the AOM shaper for the narrowband MIR pulse around 4.8 µm.*
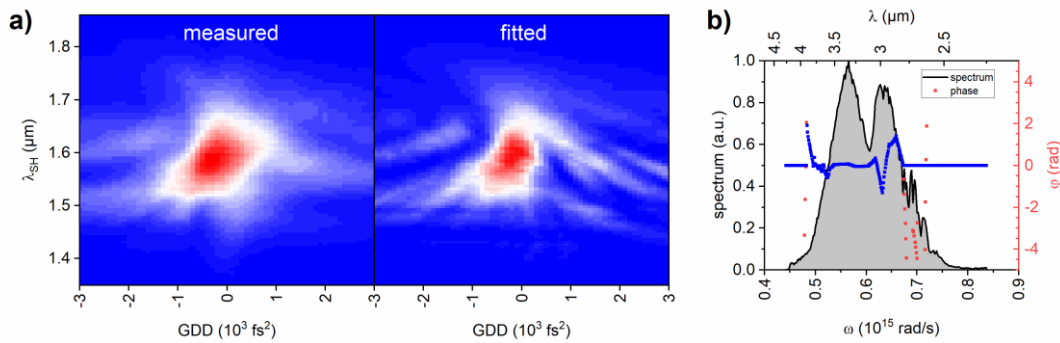
Figure B.3: *Phase retrieval of the compressed reference pulse. a) Measured and fitted d-scan trace, matrix size (frequency × dispersion): 339×61, G=0.0606. b) Retrieved phase (red scattered). Where the phase retrieval becomes unreliable, the reference is set to zero (blue scattered). Here, the retrieved phase is also displayed for spectral regions with intensity below 10% of the spectral maximum.*

B. 5   Reference phase of compressed broadband pulse

The reference phase of the compressed broadband pulse is given in Fig. B.3. From the measured d-scan trace it is seen that there is still some slight negative chirp present, as the trace is not centred at exactly zero GDD. The phase retrieval by d-scan (red in Fig. B.3 b)) becomes unreliable in the red part of the spectrum for regions with low spectral intensity (below 10% of the spectral maximum), in the blue region below 2.8 μm, for the reasons discussed in Sec. III. 6.2. Where the phase retrieval by d-scan is not reliable, the reference phase is set to zero (blue in Fig. B.3 b)). It is the zero padded reference phase that is subtracted from the retrieved phase of the tailored pulses in Sec. III. 5.3. The zero padding is justified because the phase in those regions is approximately compensated by the phase found by the evolutionary algorithm characterisation. Thus, zero phase is closer to the true phase than the diverging phase found by d-scan in those regions. Moreover, the zero padding of the reference phase only comes into effect for frequencies where the retrieval of the tailored phases is not reliable either.

B. 6   Spatial chirp measurement of the MIR beam after the shaper

The MIR beam after the shaper was checked for spatial chirp, i.e. it was examined whether the spectrum changes with position within the transverse plane perpendicular to the beam propagation direction, see. Fig. B.4 a). In order to do so, a slit between two razor blades was scanned along the beam profile and for each slit position, the spectrum transmitted through the slit was recorded, cf. Fig. B.4 b). Those spectra shall be referred as slit spectra in the following. The slit was scanned along the horizontal and vertical direction.

In addition, a reference spectrum without razor blades was taken, see Fig. B.5 f). The reference spectrum and the position dependent slit spectra were all normalised to 1. Then the normalised slit spectra were divided by the normalised reference spectrum. This gave a landscape as shown in Fig. B.5 a) and b) for the horizontal and vertical direction, where the relative deviations from the reference spectra are displayed. What can be seen from Fig. B.5 a) and b) is that the dominant colour is blue-green, which means that at most positions and wavelengths the ratio between normalised slit spectrum and the reference spectrum is around 1. Both horizontal and vertical directions do not exhibit obvious trends in wavelength evolution with position. For the horizontal component, there might be a shift towards higher wavelengths present for positions larger than 1 mm, indicated by the blue

a)   **b)**
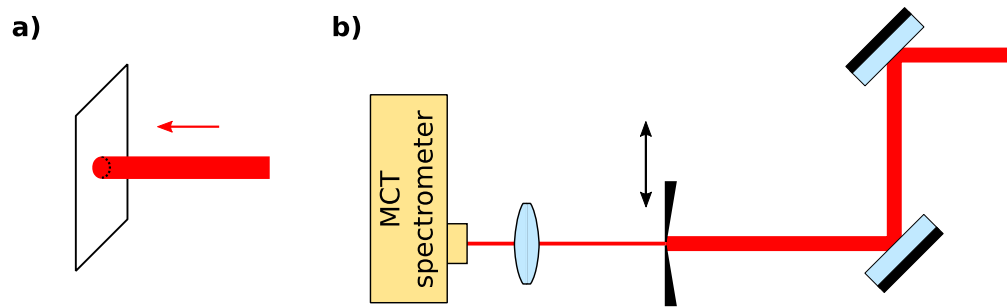
Figure B.4: *Spatial chirp measurement. a) The spatial chirp was examined in the transverse plane perpendicular to the beam propagation direction. b) To determine the spatial chirp, a slit between two razor blades was scanned along the transverse plane. The spectrum passing the slit was recorded for each slit position. Estimated slit width: 0.3 mm.*

skewed stripe in the lower right corner of Fig. B.5 a). This suspected shift is however already at the spatial edge of the beam profile and beyond the spatial FWHM (indicated by the white box in Fig. B.5 a)). The slit spectra of the vertical direction look very homogeneous (cf. Fig. B.5 b)) and there are hardly any structural differences to the reference spectrum visible in the FWHM region. Moreover, the centre of gravity wavelength was determined for each slit spectrum, as displayed in Fig. B.5 c) and d). From the central wavelength data, no obvious trend in spectral evolution with position can be observed, either. Again, the vertical component exhibits smaller fluctuations than the horizontal component. The maximum variation in central wavelength in the horizontal direction (Fig. B.5 c)) is circa one quarter of the FWHM of the reference spectrum.

From the data presented in this section, it can be inferred that spatial chirp poses no serious issue in characterisation of the shaped MIR pulse.
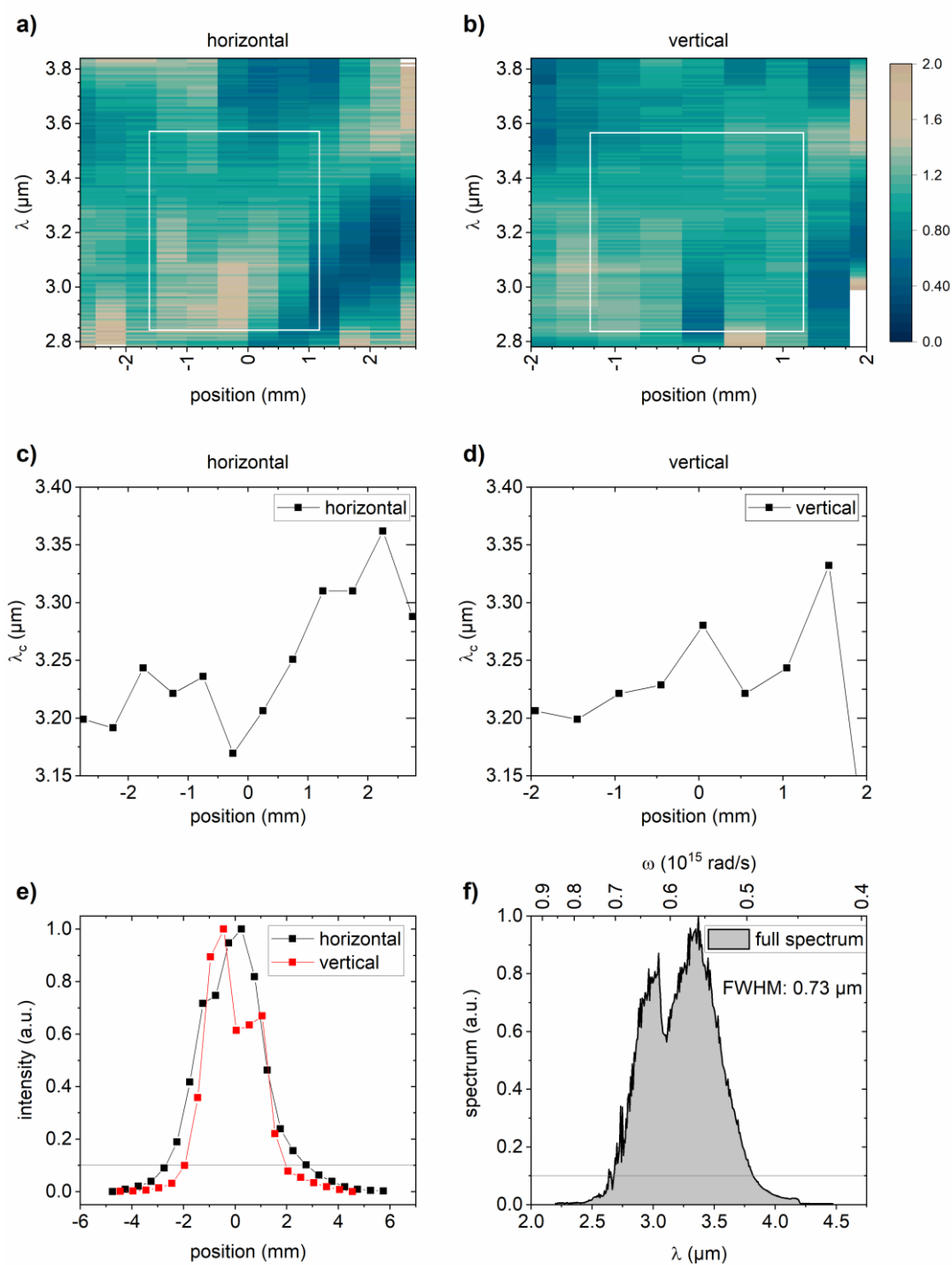
Figure B.5: *Top row: Spectra at different slit positions normalised to the reference spectrum for a) the horizontal direction and b) the vertical direction. Axes limits are the points beyond which the intensity drops below 10% of its maximum value. The white boxes indicate the region of FWHM for both the reference spectrum and the beam profile. Middle row: Central wavelength λ_c at several positions for c) the horizontal and d) the vertical direction. Bottom row: e) Spatial beam profiles obtained by integration of the measured spectra. f) Reference spectrum without slit. The horizontal lines indicate the 10% level that set the axes limits in a) and b).*

C AOM shaper and d-scan

C   Impact of excitation of the CNN stretch mode on the photoreaction of DNQ

C. 1   Normal coordinates

Consider a strictly harmonic potential V that is experienced by the nuclei of a molecule

$$V = V_0 + \sum_{i=1}^{3N} \left(\frac{\partial V}{\partial q_i} \right)_0 q_i + \frac{1}{2} \sum_{i,j=1}^{3N} \left(\frac{\partial^2 V}{\partial q_i \partial q_j} \right)_0 q_i q_j \;. \tag{C. 1}$$

q_i are the mass weighted displacements of each of the N nuclei that constitute the molecule from their respective equilibrium positions, cf. Sec. IV. 2.2. The last term in Eq. C. 1 shows that there is substantial coupling between the displacements. However, by a coordinate transformation from the Cartesian coordinates q_i to a new set of coordinates Q_i, the matrix $\frac{\partial^2 V}{\partial q_i \partial q_j}$ can be diagonalised and the coupling between different Q_i is removed [135, 160]. $Q_i = Q_i(q_1, q_2, \dots, q_{3N})$ are called normal coordinates. Each Q_i corresponds to an oscillation of *all N* nuclei around their respective equilibrium positions and all nuclei oscillate with the same frequency ω_i. In normal coordinates, the total vibrational energy of the molecule can the be written as the sum of the vibrational energies in each normal mode

$$E = \sum_{i=1}^{3N-6} \hbar \omega_i \left(v_i + \frac{1}{2} \right) \;. \tag{C. 2}$$

The summation runs up to $3N - 6$ ($3N - 5$ for linear molecules), since only *vibrational* degrees of freedom are considered in Eq. C. 2 and 6 (5 for linear molecules) out of the $3N$ degrees of freedom fall onto translational and rotational degrees of freedom. Furthermore, the total vibrational wave function of the system can be written as simple product of the wavefunctions of each single normal mode coordinate [160]

$$\psi_{vib} = \psi_{vib,v_1}(Q_1) \cdot \psi_{vib,v_2}(Q_2) \cdot \dots \cdot \psi_{vib,v_{3N-6}}(Q_{3N-6}) \;. \tag{C. 3}$$

The transition from Cartesian to normal coordinates thus allows to describe a system of coupled harmonic oscillators (the displacements of the nuclei from their equilibrium positions q_i) by uncoupled quantities (the normal coordinates Q_i comprising the movement of all nuclei). A harmonic vibration of the molecule with ω_i thus corresponds to a *1-dimensional* movement along the normal mode coordinate Q_i.

C. 2   Noise in MIR pre-pump/UV pump/MIR probe measurement

The S/N of the MIR pre-excitation/UV pump measurements with MIR probe is not as good as for the measurements with WL probe, cf. Sec. IV. 6.4 and IV. 6.5. This is due to the fact that the MIR pulse generation happened via a cascade of several non-linear processes in the commercial TOPAS/NDFG setup. In contrast, the WL was generated by simply focusing the 800 nm fundamental into a CaF_2 plate only once. Furthermore, the seed in the TOPAS was generated by parametric superflourescence [161], which inherently has larger shot-to-shot noise than WL [44]. To still have a decent S/N in the MIR probe measurement, less MIR-UV delays t were measured, with more scans taken at each t than for the measurement with WL probe. Moreover, in order to calculate the ratio $\overline{\Delta A}_{MIR\,on}/\overline{\Delta A}_{MIR\,off}$, the traces without MIR pre-pump (i.e. "MIR off") for all recorded t were considered in the

computation of the $\Delta A_{MIR\,off}$ reference trace, i.e. $\overline{\Delta A}_{MIR\,off}$ is the same value for all t. This is justified, firstly, since the MIR-UV delay t does not have any meaning if the MIR pre-excitation is blocked and, secondly, as the values of the MIR-UV delay t were scanned in the experiment in a symmetrically interleaved manner. The second point is explained in the following. The photoproduct enhancement by vibrational pre-excitation was determined for three MIR-UV delays t: $t = 1$ ps, $t = 2.5$ ps and $t = 10$ ps. In the experiment, however, not all scans for a certain t were taken right after each other, but only a quarter of the scans was taken at one t before the next t was set. This procedure was repeated four times. The t values were hence set in the order $t = 1$; 2.5; 10; 10; 2.5; 1; 1; 2.5; 10; 10; 2.5; 1 ps. For each value of t, the four single blocks of measurements were averaged to get the final $\Delta A_{MIR\,on}$ trace at that particular t. This implies, that for each t, the scans that were considered in the computation of the "MIR on" trace, were acquired over the whole course of the measurement. That is why the $\Delta A_{MIR\,off}$ reference trace can be calculated by considering the "MIR off" scans for all t, i.e. all "MIR off" scans over the whole course of the measurement. Considering all available "MIR off" scans and not only the ones for a particular t increases the S/N of the $\Delta A_{MIR\,off}$ trace.

C. 3   Estimation of the quantum yield for UV excitation of DNQ

In Sec. IV. 6.4 it was shown that a pre-excitation before the UV pulse enhances the ketene photoproduct formation. In this section, the quantum yield (QY) for the reaction with and without MIR pre-excitation is estimated. This helps to judge whether the vibrational pre-excitation of DNQ only causes a change in absorption of the UV pulse or also improves the coupling into the reaction channel. For the QY estimation, both the measurements with 433 nm and 394 nm UV excitation are evaluated, each with MIR-UV delay $t = 1$ ps.

The QY Φ of a photoreaction is defined as the ratio of the number of molecules that have been converted in the photoreaction and the number of photons that have been absorbed by the reactant [162]:

$$\Phi = \frac{\#\ \text{molecules converted in photoreaction}}{\#\ \text{photons absorbed}}\ . \qquad (C.4)$$

C. 3.1   Quantum yield without vibrational pre-excitation

In a first step, Φ for the photoreaction without MIR pre-excitation is assessed. To get the fraction of DNQ molecules converted to ketene, the change in absorption by UV excitation after several tens of picoseconds, $\overline{\Delta A}(75 - 94\ \text{ps})$, is evaluated from the $\lambda_{probe} = 408$ nm transient (cf. black curve in Fig. C.1 a)). The measured quantity is the absorbance change, with

$$A = \varepsilon \cdot d \cdot c\ . \qquad (C.5)$$
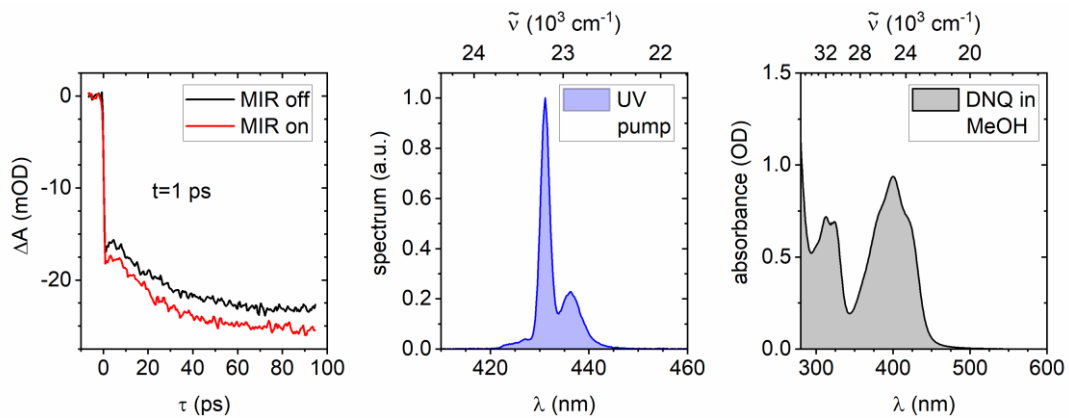
Figure C.1: *a) Transients at 408 nm of the UV pump/WL probe measurement without (black) and with (red) MIR pre-excitation. b) Off-resonant UV pump centred at 433 nm. c) Steady state UV/Vis absorbance of DNQ in MeOH (13 mM, 100 µm).*

The molar decadic absorption coefficient ε and thickness of the sample cell d do not change during the course of the measurement. The relative change in concentration can thus be calculated as

$$\frac{\Delta c}{c} = \frac{\Delta A}{A} = \frac{\overline{\Delta A}(75 - 94\ ps)}{\bar{c}_{DNQ} \cdot A_{DNQ}(\lambda_{probe})}\ . \tag{C.6}$$

In Eq. C.6, $A_{DNQ}(\lambda_{probe})$ denotes the DNQ steady state absorbance at the probe wavelength, see Fig. C.1 c). This absorbance spectrum is determined at a DNQ concentration corresponding to the concentration c_0 at the beginning of the measurement. However, DNQ is irreversibly converted during the course of the measurement. As the absorbance is a linear function of concentration, a correction factor $\bar{c}_{DNQ}$ is introduced to account for the decay of DNQ concentration during the measurement. It is determined as $\bar{c}_{DNQ} = 0.9286$. Details on the calculation of $\bar{c}_{DNQ}$ are given in App. C. 4. With that, the concentration change of DNQ can be determined as[1]

$$\frac{\Delta c}{c} = \frac{-23.1\ mOD}{0.9286 \cdot 0.842\ OD} = -2.96 \cdot 10^{-2}. \tag{C.7}$$

The number of photons absorbed by the DNQ molecules is determined from the total number of photons in the UV pulse and the DNQ steady state absorbance at the UV pump wavelength. In order to calculate the number of UV photons in the pulse from the measured pulse energy, the pulses wavelength needs to be known. The first moment (i.e. the centre of mass) of the UV pump spectrum is [145]

$$\lambda_{centre} = \int_{-\infty}^{\infty} \lambda \cdot f(\lambda) d\lambda = 433\ \text{nm}\ . \tag{C.8}$$

Here $f(\lambda)$ is the normalised spectrum, so that $\int_{-\infty}^{\infty} f(\lambda)\, d\lambda = 1$. The measured UV pulse energy before the sample cell was 1.4 µJ. Taking into account reflection at the CaF$_2$ entrance window, which was experimentally determined to ~5%, the energy available to excite the

---

[1] In the presented derivation, the numerical values given are for off-resonant UV excitation at $\lambda_{UV} = 433$ nm. Corresponding values for UV excitation at 394 nm are given at the end of the section.

sample is 1.3 µJ, corresponding to $2.9 \cdot 10^{12}$ photons. From the absorbance $A(\lambda_{pump}) = \bar{c}_{DNQ} \cdot 0.370\ \mathrm{OD}$, it follows that 57% of the photons are absorbed.

The total number of DNQ molecules in the excitation volume V_{exc} can be estimated by the concentration and the $1/e^2$-radius of the UV beam, which was measured to be $r_{UV} = 74\ \mathrm{µm}$

$$\text{\# DNQ molecules in } V_{exc} = \pi \cdot r_{UV}^2 \cdot d \cdot c \ . \tag{C.9}$$

With the thickness of the sample volume $d = 100\ \mathrm{µm}$ and the concentration $c = \bar{c}_{DNQ} \cdot 13\ \mathrm{mM}$. Under the assumption that a DNQ molecule can at maximum absorb one UV photon, this gives a fraction of excited DNQ molecules in the excitation volume of

$$\text{fraction UV excited DNQ molecules} = \frac{\text{\# absorbed photons}}{\text{\# DNQ molecules in } V_{exc}}$$

$$= \frac{1.67 \cdot 10^{12}}{1.25 \cdot 10^{13}}$$

$$= 0.13 \ . \tag{C.10}$$

The QY without vibrational pre-excitation $\Phi_{v=0}$ for the UV pump at 433 nm is thus estimated to be

$$\Phi_{v=0}(433\ \mathrm{nm}) = \frac{\dfrac{|\Delta c|}{c}}{\text{fraction UV excited DNQ molecules}} = 0.22 \ . \tag{C.11}$$

C. 3.2   Quantum yield with vibrational pre-excitation

After having evaluated $\Phi_{v=0}$, the QY with MIR pre-excitation $\Phi_{v>0}$ can be estimated in a next step. Again, the relative change in DNQ concentration is determined from the change in absorption

$$\frac{\Delta c}{c} = \frac{\overline{\Delta A}(75 - 94\ ps)}{\bar{c}_{DNQ} \cdot A_{DNQ}(\lambda_{probe})} = \frac{-25.3\ mOD}{0.9286 \cdot 0.842\ OD} = -3.24 \cdot 10^{-2} \ . \tag{C.12}$$

However, with a MIR pre-pulse, the measured Δc contains contributions from molecules with $v = 0$ and $v > 0$. This is because not all molecules in the probed sample volume that have been converted by a UV pulse have been previously excited by the MIR pre-pulse. It is thus necessary to know the fraction of MIR pre-excited DNQ molecules with $v > 0$ in the probed volume.

From the information at hand it is difficult, if not impossible, to properly deduce a population distribution of the various vibrational levels $v = 0$, $v = 1$, etc. upon MIR excitation. In the MIR pump/MIR probe transient spectra (cf. Sec. IV. 6.1), the features indicative of $v > 0$ contain contributions of both stimulated emission and excited state absorption. An analysis of the population distribution based on the band areas of the single transitions as presented in Ref. [150] is not applicable, as in the case of DNQ the bands corresponding to different v overlap significantly and are - judging from FTIR spectrum of the $v = 0 \rightarrow v = 1$ transition - most likely structured. The assignment of a certain band area to each v would thus be inevitably highly erroneous. Another complication that arises is that the absorption cross section is not known for transitions starting at $v > 0$. It is often assumed that the absorption cross section increases with increasing v like in a strictly

harmonic potential [150], but this assumption has been shown to be not valid in general [151].

For the reasons mentioned above, in the following it will only be distinguished between molecules with $v = 0$ and $v > 0$, irrespective of the concrete level of MIR excitation. It will be further assumed that most of the vibrationally excited DNQ molecules are in $v = 1$. So effectively, a 2-level-system with only $v = 0$ and $v = 1$ is considered for the estimation of the number of MIR excited molecules.

The estimation of $\Phi_{v>0}$ involves several steps. First, the number of MIR photons that are absorbed by the DNQ sample needs to be determined (Sec. C. 3.2.1). From this, the ratio of vibrationally excited DNQ molecules at $t = 1$ ps can then be concluded, cf. Sec. C. 3.2.2. Sec. C. 3.2.3 provides values for the absorption coefficients of DNQ in the vibrational ground and excited state, $\varepsilon_{v=0}$ and $\varepsilon_{v>0}$. These are deduced from the MIR pump/WL probe measurement and are necessary in order to finally estimate $\Phi_{v>0}$ from the MIR pre-pump/UV pump/WL probe measurement in Sec. C. 3.2.4. For the determination of $\Phi_{v>0}$, the contributions from DNQ molecules in a vibrational excited and in the vibrational ground state to the observed absorption change need to be separated.

C. 3.2.1 Number of absorbed MIR photons

The spectrum of the MIR pre-pump is spectrally much broader than the linewidth of the DNQ $v = 0 \rightarrow v = 1$ transition and a big part of the MIR spectrum will not be involved in that transition. It is, therefore, not appropriate to determine the number of absorbed photons by only calculating a centre wavelength and dividing the pulse energy by the energy of photons at that centre wavelength. Instead, the measured MIR spectrum $E(\omega)$ is first normalised to the pulse energy $E_{MIR} = 5.9$ µJ and subsequently converted into a photon density $n(\omega)$

$$n(\omega) = \frac{E(\omega)}{\hbar\omega} \qquad with \int_{-\infty}^{\infty} E(\omega)d\omega = E_{MIR} \; . \qquad (C.13)$$

The photon density $n(\omega)$ is shown in Fig. C.2 (black line) . What also needs to be considered in a quantitative analysis is that the solvent MeOH exhibits as well some absorbance in the MIR spectral region. The absorbance A_{MeOH} of a 100 µm thick cell filled with liquid MeOH is calculated from the imaginary part of the refractive index $\kappa(\omega)$, see App. C. 5. Values for $\kappa(\omega)$ are taken from literature [163]. From the photon density of the incoming MIR spectrum and the combined transmittance of DNQ and MeOH, the total density of absorbed photons $n_{abs,tot}(\omega)$ can be determined as

$$n_{abs,tot}(\omega) = n(\omega) \cdot \left(1 - T_{tot}(\omega)\right)$$
$$with \quad -\log\left(T_{tot}(\omega)\right) = \bar{c}_{DNQ} \cdot A_{DNQ}(\omega) + A_{MeOH}(\omega) \; . \qquad (C.14)$$

A_{DNQ} is the steady state absorbance of DNQ, known from the FTIR absorption spectrum at $c_0 = 13$ mM. The green line in Fig. C.2 corresponds to $n_{abs,tot}(\omega)$. In $n_{abs,tot}(\omega)$, there are both contributions from DNQ and MeOH accounted for. The photon density absorbed by DNQ only, $n_{abs,DNQ}(\omega)$, is calculated via the ratio of A_{DNQ} to the total absorbance

C Impact of excitation of the CNN stretch mode on the photoreaction of DNQ

$$n_{abs,DNQ} = n_{abs,tot}(\omega) \cdot \frac{\bar{c}_{DNQ} \cdot A_{DNQ}(\omega)}{\bar{c}_{DNQ} \cdot A_{DNQ}(\omega) + A_{MeOH}(\omega)} \quad . \tag{C. 15}$$

Finally, the number of absorbed MIR photons by only DNQ (blue area in Fig. C.2) is evaluated as

$$\text{\# absorbed MIR photons by DNQ} = \int_{-\infty}^{\infty} n_{abs,DNQ}(\omega)d\omega \quad . \tag{C. 16}$$
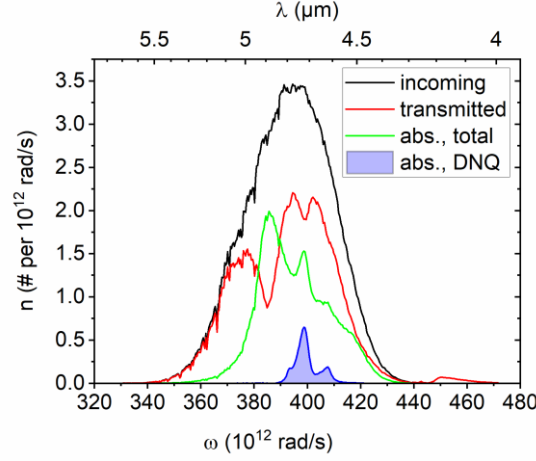
Figure C.2: *Photon densities $n(\omega)$ of the MIR pre-pump pulse spectra. Black: Incoming spectrum, red: transmitted $n(\omega)$, green: absorbed $n(\omega)$ by both MeOH and DNQ, blue: absorbed $n(\omega)$ by only DNQ. The shaded area corresponds to the number of absorbed photons by DNQ.*

C. 3.2.2 Ratio of vibrationally excited DNQ molecules

The absolute number of DNQ molecules in the MIR excitation volume is determined via the DNQ concentration and the spot size of the MIR beam at the sample, like in Eq. C. 9. The $1/e^2$-radius of the MIR beam was determined to be $r_{MIR} = 64$ µm. With that, the fraction of vibrationally excited molecules in the MIR excitation volume $V_{exc,MIR}$ is

$$\frac{\text{\# absorbed MIR photons}}{\text{\# DNQ molecules in } V_{exc,MIR}} = \frac{4.74 \cdot 10^{12}}{9.35 \cdot 10^{12}} = 0.506 \tag{C. 17}$$

The fraction of molecules in $v > 0$ is slightly larger than 0.5. This would be unphysical for a true 2-level-system, for which no population inversion is possible. However, the assumed 2-level-system is only an approximation to the real system. The real system also involves higher vibrational states. Therefore, the value in Eq. C. 17 slightly above 0.5 will be used in the further proceeding.

Furthermore, in the measurement the UV pulse arrived at $t = 1$ ps after the MIR pulse at the sample, so part of the initially vibrationally excited molecules will have fallen back to the ground state in the meantime. This is accounted for by multiplying the number of MIR excited molecules by a factor $\exp\left(-\frac{1 \text{ ps}}{8.7 \text{ ps}}\right)$, the time constant 8.7 ps is taken from Ref. [29].

With that, the fraction s of MIR excited molecules at the time the UV pulse arrives, reduces to $s = 0.45$.

C. 3.2.3 UV/Vis absorption coefficients for vibrationally excited and unexcited DNQ molecules

Moreover, one needs to consider that the absorption of the UV pump changes if the molecule is vibrationally pre-excited (cf. Sec. IV. 6.2). The molar decadic absorption coefficient ε of DNQ can be determined for $v = 0$ from the steady state absorption spectrum at known concentration

$$\varepsilon_{v=0}(433\text{ nm}) = \frac{A}{d \cdot c_0} = \frac{0.398\text{ OD}}{100\mu\text{m} \cdot 13\text{ mM}} = 0.31 \frac{\text{l}}{\text{mol} \cdot \mu\text{m}} \quad . \tag{C.18}$$

For $v > 0$, ε can be determined from the MIR pump/WL probe measurement presented in Sec. IV. 6.2. The total absorbance for $\lambda_{UV} = 433$ nm at $\tau = 1$ ps after MIR pulse excitation is $A + \Delta A_{MIR/WL} = (0.398 + 0.027)$ OD and has again contributions from $v = 0$ and $v > 0$. The fraction s_2 of MIR excited molecules at $\tau = 1$ ps in the MIR pump/WL probe experiment can be calculated as has been described in Eqs. C. 13 - C. 17 and Fig. C.2. Putting in the numbers of the experimental parameters of the MIR pump/WL probe experiment, gives $s_2 = 0.49$. The knowledge of $\varepsilon_{v=0}$, cf. Eq. C. 18, allows to determine $\varepsilon_{v>0}$

$$A + \Delta A_{MIR/WL} = \varepsilon_{v=0} \cdot c_{v=0} \cdot d + \varepsilon_{v>0} \cdot c_{v>0} \cdot d$$

$$with: \quad c_{v=0} = (1 - s_2)c_0 \qquad c_{v>0} = s_2 c_0$$

$$\Rightarrow A + \Delta A_{MIR/WL} = \frac{A}{d \cdot c_0} \cdot d \cdot (1 - s_2)c_0 + \varepsilon_{v>0} \cdot d \cdot s_2 c_0$$

$$\Rightarrow \qquad \varepsilon_{v>0} = \frac{\Delta A_{MIR/WL} + A \cdot s_2}{s_2 \cdot c_0 \cdot d} \quad . \tag{C.19}$$

Note that in the MIR pump/WL probe experiment there is no UV pulse involved and - if any - only a negligible amount of DNQ is converted. Therefore, the DNQ concentration does not change during the course of the measurement and is thus not corrected by $\bar{c}_{DNQ}$. Putting in numbers into Eq. C. 19 gives

$$\varepsilon_{v>0}(433\text{ nm}) = 0.35 \frac{\text{l}}{\text{mol} \cdot \mu\text{m}} \quad . \tag{C.20}$$

C. 3.2.4 Contribution of vibrationally excited DNQ molecules to the observed reactant concentration change

With the knowledge of $\varepsilon_{v=0}$ and $\varepsilon_{v>0}$, one can finally get back to the estimation of $\Phi_{v>0}$ from the MIR pre-pump/UV pump/WL probe experiment. The number of absorbed UV photons in the MIR excitation volume is calculated as

$$N_{UV,abs} = N_{UV} \cdot \left(\frac{r_{MIR}}{r_{UV}}\right)^2 \cdot \left(1 - T(\lambda_{UV})\right)$$

$$with: -\log T(\lambda_{UV}) = \bar{c}_{DNQ}\left(A(\lambda_{UV}) + \frac{s}{s_2}\Delta A_{MIR/WL}(\lambda_{UV})\right) . \qquad (C.21)$$

N_{UV} is the number of UV photons arriving at the sample and the transmission $T(\lambda_{UV})$ is calculated via the absorbance that changed due to the MIR pre-excitation. The latter is scaled by the mean DNQ concentration factor. The factor s/s_2 scales the value $\Delta A_{MIR/WL}$, which is obtained from the MIR pump/WL probe measurement, to the MIR pre-pump/UV pump/WL probe experiment[1]. $\left(\frac{r_{MIR}}{r_{UV}}\right)^2$ accounts for the slightly larger focus spot size of the UV pulse compared to the MIR pulse, so not all photons of the UV pulse will be contained in the volume excited by the MIR pulse.

The total number of absorbed UV photons $N_{UV,abs}$ is distributed over DNQ molecules with $v = 0$ and $v > 0$. In the following $N_{v=0}$ and $N_{v>0}$ denote the number of UV photons absorbed by DNQ molecules with $v = 0$ and $v > 0$, respectively. $N_{v=0}$ and $N_{v>0}$ can be determined from $N_{UV,abs}$ (Eq. C.21) and the ratio of $A_{v=0}$ and $A_{v>0}$ to the total absorbance A_{tot} of the MIR excited sample. $A_{v=0}$ and $A_{v>0}$ denote the absorbance induced by DNQ molecules with $v = 0$ and $v > 0$, respectively.

$$N_{v=0} = N_{UV,abs} \cdot \frac{A_{v=0}}{A_{tot}}$$

$$= N_{UV,abs} \cdot \frac{\varepsilon_{v=0} \cdot c_{v=0}}{\varepsilon_{v=0} \cdot c_{v=0} + \varepsilon_{v>0} \cdot c_{v>0}}$$

$$= N_{UV,abs} \cdot \frac{A \cdot (1 - s)}{A + \frac{s}{s_2} \cdot \Delta A_{MIR/WL}} , \qquad (C.22)$$

$$N_{v>0} = N_{UV,abs} \cdot \frac{A_{v>0}}{A_{tot}}$$

$$= N_{UV,abs} \cdot \frac{\varepsilon_{v>0} \cdot c_{v>0}}{\varepsilon_{v=0} \cdot c_{v=0} + \varepsilon_{v>0} \cdot c_{v>0}}$$

$$= N_{UV,abs} \cdot \frac{\frac{s}{s_2} \cdot \Delta A_{MIR/WL} + A \cdot s}{A + \frac{s}{s_2} \cdot \Delta A_{MIR/WL}} . \qquad (C.23)$$

All quantities are taken at the UV pump wavelength λ_{UV}. To finally be able to estimate $\Phi_{v>0}$, the measured change in DNQ concentration needs to be corrected for the

---

[1] s/s_2 is close to 1, as the experimental conditions of the MIR pump/WL probe and the MIR pre-pump/UV pump/WL probe experiments were very similar. Deviations from 1 come from small differences in MIR pulse energy between the measurements.

contribution that comes from molecules with $v = 0$. The number of molecules that are converted during the photoreaction, N_{conv}, is equivalent to the number of DNQ molecules lost

$$N_{conv} = \left(\text{# DNQ molecules in } V_{exc,MIR}\right) \cdot \frac{|\Delta c|}{c} = N_{v=0} \cdot \Phi_{v=0} + N_{v>0} \cdot \Phi_{v>0} \ . \quad \text{(C. 24)}$$

With that

$$\Phi_{v>0} = \frac{N_{conv} - N_{v=0} \cdot \Phi_{v=0}}{N_{v>0}} = 0.25 \ . \quad \text{(C. 25)}$$

C. 3.3 Values for quantum yields with resonant UV excitation

The estimation of the QY for excitation at resonant UV pump wavelength, $\lambda_{UV} = 393$ nm, works basically in the same way as described above for the off-resonant case with $\lambda_{UV} = 433$ nm.

The experimental parameters necessary for the QY estimation at $\lambda_{UV} = 393$ nm are given below. The UV energy available at the sample was $E_{UV} = 1.4$ µJ ($\triangleq 2.59 \cdot 10^{12}$ photons). The beam had a $1/e^2$-radius of $r_{UV} = 66$ µm, the available MIR energy was $E_{MIR} = 5.6$ µJ and the factor accounting for the mean DNQ concentration $\bar{c}_{DNQ} = 0.9139$. With that, one gets the following QYs:

$$\Phi_{v=0} = 0.29$$
$$\Phi_{v>0} = 0.32 \ .$$

C. 3.4 Summary of the results

Tab. C-1 summarises the values for the QYs obtained in this section. These results will be discussed in the next section, Sec. C. 3.5.

	$\Phi_{v=0}$	$\Phi_{v>0}$	$\dfrac{\Phi_{v>0}}{\Phi_{v=0}}$
$\lambda_{UV} = 433$ nm	$0.22\ ^{+0.06}_{-0.05}$	$0.25\ ^{+0.06}_{-0.06}$	$1.11\ ^{+0.01}_{-0.01}$
$\lambda_{UV} = 393$ nm	$0.29\ ^{+0.04}_{-0.04}$	$0.32\ ^{+0.05}_{-0.05}$	$1.10\ ^{+0.00}_{-0.01}$

Table C-1: *Obtained quantum yields Φ for UV excitation at 433 nm and 393 nm with ($v > 0$) and without ($v = 0$) vibrational pre-excitation. The errors are due to uncertainties in the beam spot size, see next section.*

C. 3.5 Discussion of the obtained quantum yield values

The estimation of the absolute values for the QY in Tab. C-1 represents a lower bound for the true values of the QY. The reason for this is that in the above QY estimation, the number of converted DNQ molecules is determined from the TA transients, whereas the total number of UV excited molecules is determined by independently measured parameters,

namely the steady state absorption spectrum of DNQ, the radii of the beam spot sizes in the focus (r_{UV} and r_{MIR}) and the pulse energies (E_{UV} and E_{MIR}).

In the calculation of the number of absorbed UV photons, a homogeneous beam profile across the excitation region is assumed and no saturation effects on the photon absorption are taken into account. The number of absorbed UV photons is thus rather overestimated since potential saturation effects (e.g. in the centre of the focal spot) will decrease the number of absorbed UV photons and hence increase the QY. Nevertheless, the estimated values for the QYs give the right magnitude: Ref. [29] reports $QY_{v=0} = 0.32$ for $\lambda_{UV} = 400$ nm. There, the QY was determined from the evolution of the bleach signal at a DNQ absorption transient probed in the MIR spectral region.

The errors for the absolute QY values given in Tab. C-1 are mainly due to the errors in the measured UV beam $1/e^2$-radii: $r_{UV} = 74 \pm 7$ µm for $\lambda_{UV} = 433$ nm and $r_{UV} = 66 \pm 3$ µm for $\lambda_{UV} = 393$ nm. The errors in r_{UV} affect the absolute values of the QY. However, the ratio $\Phi_{v>0}/\Phi_{v=0}$ is not affected by the values for r_{UV} as those cancel out in the ratio. The same is true for an error in E_{UV}, that also cancels out in the ratio.

Consequently, the errors in the ratio $\Phi_{v>0}/\Phi_{v=0}$ are smaller than the errors in $\Phi_{v>0}$ and $\Phi_{v=0}$ alone. The error in ratio comes from the uncertainties in the measured MIR beam $1/e^2$-radius ($r_{MIR} = 64^{+1}_{-2}$ µm) and MIR pump pulse energy (E_{MIR} error $\approx 5\%$). The uncertainties in MIR parameters have only a minor effect on the $\Phi_{v>0}/\Phi_{v=0}$ ratio.

A similar argument as for the absolute QY values reported in Tab. C-1 also holds for the QY enhancement ratios $\Phi_{v>0}/\Phi_{v=0}$. The latter should also be understood as lower bounds. In the determination of the fraction of MIR pre-excited DNQ molecules from the steady state MIR absorption (cf. Fig. C.2), a decrease in absorption due to saturation has been neglected. Moreover, multiphoton absorption was not taken into account in the above model. As the fundamental $v = 0 \rightarrow v = 1$ transition most likely spectrally overlaps with transitions at higher vibrational levels, part of the incoming MIR spectral photon density is spent for higher transitions and the photon density available for the $v = 0 \rightarrow v = 1$ transition decreases. The two aforementioned effects decrease the number of vibrationally pre-excited molecules and thus $\Phi_{v>0}$ will increase, because the observed photoproduct enhancement is caused by less pre-excited molecules.
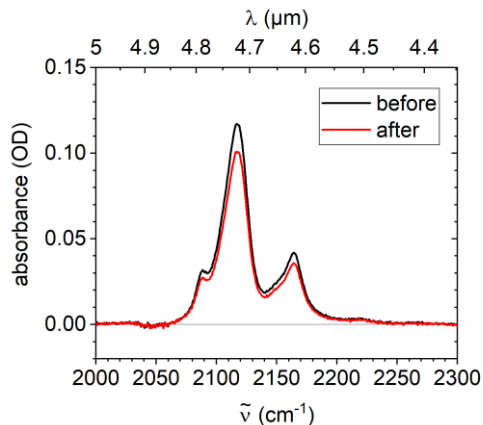
Figure C.3: *Absorbance of the sample before and after the measurement with MIR pre-excitation and 433 nm UV excitation. Shown is the region of the DNQ C=N=N stretching vibration around 2117 cm⁻¹.*

C. 4   Determination of mean DNQ concentration

In the experiments with UV excitation, part of the DNQ sample is irreversibly converted during the measurement. For the estimation of the quantum yield, the initial DNQ concentration c_0 is therefore corrected by a mean concentration $\bar{c}_{DNQ}$ that accounts for that sample degradation. The relative change in DNQ concentration during the whole measurement can be determined by FTIR spectra taken before and after the measurement, as is shown in Fig. C.3. In the experiment with MIR pre-excitation and UV excitation at $\lambda_{UV} = 433\ nm$, the amplitude of the peak at 2117 cm⁻¹ drops to ca. 86% of its initial value during the whole course of the measurement. That means also the DNQ concentration decreases by the same amount.

The number of converted DNQ molecules per UV pulse is proportional to the number of present molecules N_{DNQ} in the excitation volume

$$dN_{DNQ} \propto N_{DNQ}\ . \tag{C. 26}$$

From this it follows that the DNQ concentration c decreases exponentially during the course of the measurement

$$c(t) = c_0 \cdot e^{-\alpha \cdot t}\ . \tag{C. 27}$$

α can be determined from the duration of the whole measurement $t_{tot} = 209\ min$

$$e^{-\alpha \cdot 209\ min} = 0.86 \qquad \Rightarrow \qquad \alpha = 7.27 \cdot 10^{-4}\ min^{-1}\ . \tag{C. 28}$$

The measurements at MIR-UV delay $t = 1.0\ ps$ were taken ca. 20 and 189 min after begin of the measurement, so the factor $\bar{c}_{DNQ}$ is determined to be

$$\bar{c}_{DNQ} = \frac{1}{2}\left(e^{-\alpha \cdot 20\ min} + e^{-\alpha \cdot 189\ min}\right) = 0.9286\ . \tag{C. 29}$$

For $\lambda_{UV} = 393$ nm, the determination of $\bar{c}_{DNQ}$ works accordingly.

C. 5   Determination of MeOH absorbance

The absorbance A_{MeOH} of a 100 μm thick cell filled with liquid MeOH is calculated via the complex refractive index of MeOH, $n'(\omega) = n(\omega) - i\kappa(\omega)$. Values for $n'(\omega)$ of MeOH are

provided in Ref. [163]. A propagating optical E-field along the z-direction can be written as [47]

$$
\begin{aligned}
E(z,t) &= E_0 e^{i(\omega t - kz)} \\
&= E_0 e^{i\left(\omega t - \frac{2\pi}{\lambda_0}(n - i\kappa)z\right)} \\
&= E_0 e^{i\left(\omega t - \frac{\omega}{c_0}nz + \frac{i\omega}{c_0}\kappa z\right)} \\
&= E_0 e^{i\omega\left(t - \frac{nz}{c_0}\right)} e^{-\frac{\omega\kappa}{c_0} \cdot z} \quad .
\end{aligned}
\tag{C.30}
$$

c_0 and λ_0 denote the speed of light and wavelength in vacuum, respectively. For $n'(\omega)$, the argument ω has been omitted for better readability. The transmitted intensity after thickness d of the medium is proportional to the amplitude square of the E-field, so

$$
I(d) = I_0 e^{-\frac{2\omega\kappa}{c_0} \cdot d} \quad .
\tag{C.31}
$$

With that the absorbance can be calculated as

$$
A = -\log_{10}\left(e^{-\frac{2\omega\kappa}{c_0} \cdot d}\right) \quad .
\tag{C.32}
$$

List of publications

Publications included in this thesis

- o F. Nicolai, N. Müller, C. Manzoni, G. Cerullo, and T. Buckup, "Acousto-optic modulator based dispersion scan for phase characterization and shaping of femtosecond mid-infrared pulses," Optics Express **29**, 20970-20980 (2021), doi: 10.1364/OE.427154.
- o F. Nicolai and T. Buckup, "Effect of excitation of the CNN vibrational stretch mode on the photoreaction of 2-diazo-1-naphthol-5-sulfonate".
  Manuscript in preparation.

Additional publications

- o N. Müller, F. Nicolai, and T. Buckup, "Broadband mid-infrared phase retrieval for nonlinear microscopy," Optics Letters **46**, 5012-5015 (2021), doi: 10.1364/OL.440344.

Conference Contributions

- o F. Nicolai, N. Müller, C. Manzoni, G. Cerullo and T. Buckup, "Shaping and Phase Characterization of Ultrashort Pulses in the Mid-Infrared by AOM Shaper-Based D-Scan," *2021 Conference on Lasers and Electro-Optics Europe & European Quantum Electronics Conference (CLEO/Europe-EQEC)*, Munich, Germany, 2021, pp. 1-1, doi: 10.1109/CLEO/Europe-EQEC52157.2021.9541818.
- o F. Nicolai, T. Buckup and F.Deschler, "Effect of vibrational excitation on N_2 dissociation in DNQ", *28th IUPAC Symposium on Photochemistry*, Amsterdam, The Netherlands, 2022

References

References

1. W. Demtröder, *Laserspektroskopie 1: Grundlagen,* 6 ed. (Springer, Heidelberg, 2011).
2. W. Demtröder, *Laserspektroskopie 2: Experimentelle Techniken,* 6 ed. (Springer Spektrum, Berlin, Heidelberg, 2013).
3. M. J. Rosker, M. Dantus, and A. H. Zewail, "Femtosecond real-time probing of reactions. I. The technique," The Journal of Chemical Physics **89**, 6113-6127 (1988).
4. A. H. Zewail and R. B. Bernstein, "Real-Time Laser Femtochemistry - Viewing the transition from reagents to products," Chemical & Engineering News Archive **66**, 24-43 (1988).
5. A. H. Zewail, "Laser Femtochemistry," Science **242**, 1645-1653 (1988).
6. L. R. Khundkar and A. H. Zewail, "Ultrafast Molecular Reaction Dynamics in Real-Time: Progress Over a Decade," Annual Review of Physical Chemistry **41**, 15-60 (1990).
7. "Press release on the Nobel Prize in Chemistry 1999", Kungliga Vetenskapsakademien, 1999, https://www.nobelprize.org/prizes/chemistry/1999/press-release/
8. X. Hong, J. Kim, S.-F. Shi, Y. Zhang, C. Jin, Y. Sun, S. Tongay, J. Wu, Y. Zhang, and F. Wang, "Ultrafast charge transfer in atomically thin MoS2/WS2 heterostructures," Nature Nanotechnology **9**, 682-686 (2014).
9. C. Martín, M. Ziółek, and A. Douhal, "Ultrafast and fast charge separation processes in real dye-sensitized solar cells," Journal of Photochemistry and Photobiology C: Photochemistry Reviews **26**, 1-30 (2016).
10. F. Hainer, N. Alagna, A. Reddy Marri, T. J. Penfold, P. C. Gros, S. Haacke, and T. Buckup, "Vibrational Coherence Spectroscopy Identifies Ultrafast Branching in an Iron(II) Sensitizer," The Journal of Physical Chemistry Letters **12**, 8560-8565 (2021).
11. P. P. Roy, Y. Kato, R. Abe-Yoshizumi, E. Pieri, N. Ferré, H. Kandori, and T. Buckup, "Mapping the ultrafast vibrational dynamics of all-trans and 13-cis retinal isomerization in Anabaena Sensory Rhodopsin," Physical Chemistry Chemical Physics **20**, 30159-30173 (2018).
12. R. W. Schoenlein, L. A. Peteanu, R. A. Mathies, and C. V. Shank, "The First Step in Vision: Femtosecond Isomerization of Rhodopsin," Science **254**, 412-415 (1991).
13. Q. Wang, R. W. Schoenlein, L. A. Peteanu, R. A. Mathies, and C. V. Shank, "Vibrationally Coherent Photochemistry in the Femtosecond Primary Event of Vision," Science **266**, 422-424 (1994).
14. D. Polli, P. Altoè, O. Weingart, K. M. Spillane, C. Manzoni, D. Brida, G. Tomasello, G. Orlandi, P. Kukura, R. A. Mathies, M. Garavelli, and G. Cerullo, "Conical intersection dynamics of the primary photoisomerization event in vision," Nature **467**, 440-443 (2010).
15. R. van Grondelle, J. P. Dekker, T. Gillbro, and V. Sundstrom, "Energy transfer and trapping in photosynthesis," Biochimica et Biophysica Acta (BBA) - Bioenergetics **1187**, 1-65 (1994).
16. R. Berera, R. van Grondelle, and J. T. M. Kennis, "Ultrafast transient absorption spectroscopy: principles and application to photosynthetic systems," Photosynthesis Research **101**, 105-118 (2009).
17. P. Vöhringer, "Vibrations tell the tale. A time-resolved mid-infrared perspective of the photochemistry of iron complexes," Dalton Transactions **49**, 256-266 (2020).

18.   H. F. Shurvell, "Spectra– Structure Correlations in the Mid- and Far-Infrared," in *Handbook of Vibrational Spectroscopy*, J. M. Chalmers and P. R. Griffiths, eds. (John Wiley & Sons Ltd, 2002).

19.   L. Windhorn, T. Witte, J. S. Yeston, D. Proch, M. Motzkus, K. L. Kompa, and W. Fuß, "Molecular dissociation by mid-IR femtosecond pulses," Chemical Physics Letters **357**, 85-90 (2002).

20.   L. Windhorn, J. S. Yeston, T. Witte, W. Fuß, M. Motzkus, D. Proch, K.-L. Kompa, and C. B. Moore, "Getting ahead of IVR: A demonstration of mid-infrared induced molecular dissociation on a sub-statistical time scale," The Journal of Chemical Physics **119**, 641-645 (2003).

21.   T. Witte, T. Hornung, L. Windhorn, D. Proch, R. de Vivie-Riedle, M. Motzkus, and K. L. Kompa, "Controlling molecular ground-state dissociation by optimizing vibrational ladder climbing," The Journal of Chemical Physics **118**, 2021-2024 (2003).

22.   I. Morichika, K. Murata, A. Sakurai, K. Ishii, and S. Ashihara, "Molecular ground-state dissociation in the condensed phase employing plasmonic field enhancement of chirped mid-infrared pulses," Nature Communications **10**, 3893 (2019).

23.   M. Först, R. Mankowsky, and A. Cavalleri, "Mode-Selective Control of the Crystal Lattice," Accounts of Chemical Research **48**, 380-387 (2015).

24.   D. Kern-Michler, C. Neumann, N. Mielke, L. van Wilderen, M. Reinfelds, J. von Cosel, F. Santoro, A. Heckel, I. Burghardt, and J. Bredenbeck, "Controlling Photochemistry via Isotopomers and IR Pre-excitation," Journal of the American Chemical Society **140**, 926-931 (2018).

25.   C. J. Bardeen, V. V. Yakovlev, K. R. Wilson, S. D. Carpenter, P. M. Weber, and W. S. Warren, "Feedback quantum control of molecular electronic population transfer," Chemical Physics Letters **280**, 151-158 (1997).

26.   A. Assion, T. Baumert, M. Bergt, T. Brixner, B. Kiefer, V. Seyfried, M. Strehle, and G. Gerber, "Control of Chemical Reactions by Feedback-Optimized Phase-Shaped Femtosecond Laser Pulses," Science **282**, 919-922 (1998).

27.   P. Nuernberger, G. Vogt, T. Brixner, and G. Gerber, "Femtosecond quantum control of molecular dynamics in the condensed phase," Physical Chemistry Chemical Physics **9**, 2470-2497 (2007).

28.   G. Socrates, *Infrared and Raman characteristic group frequencies: tables and charts,* 3rd ed. (John Wiley & Sons Ltd., 2001).

29.   D. Wolpert, M. Schade, and T. Brixner, "Femtosecond midinfrared study of the photoinduced Wolff rearrangement of diazonaphthoquinone," Journal of Chemical Physics **129**, 094504 (2008).

30.   P. Tzankov, T. Fiebig, and I. Buchvarov, "Tunable femtosecond pulses in the near-ultraviolet from ultrabroadband parametric amplification," Applied Physics Letters **82**, 517-519 (2003).

31.   P. Baum, S. Lochbrunner, and E. Riedle, "Tunable sub-10-fs ultraviolet pulses generated by achromatic frequency doubling," Optics Letters **29**, 1686-1688 (2004).

32.   M. Beutler, M. Ghotbi, F. Noack, D. Brida, C. Manzoni, and G. Cerullo, "Generation of high-energy sub-20 fs pulses tunable in the 250-310 nm region by frequency doubling of a high-power noncollinear optical parametric amplifier," Optics Letters **34**, 710-712 (2009).

33.   R. B. Varillas, A. Candeo, D. Viola, M. Garavelli, S. De Silvestri, G. Cerullo, and C. Manzoni, "Microjoule-level, tunable sub-10 fs UV pulses by broadband sum-frequency generation," Optics Letters **39**, 3849-3852 (2014).

34. G. Cerullo, M. Nisoli, S. Stagira, S. De Silvestri, G. Tempea, F. Krausz, and K. Ferencz, "Mirror-dispersion-controlled OPA: a compact tool for sub-10-fs spectroscopy in the visible," Applied Physics B **70**, S253-S259 (2000).

35. D. Brida, C. Manzoni, G. Cirmi, M. Marangoni, S. Bonora, P. Villoresi, S. De Silvestri, and G. Cerullo, "Few-optical-cycle pulses tunable from the visible to the mid-infrared by optical parametric amplifiers," Journal of Optics **12**, 013001 (2010).

36. V. Petrov and F. Noack, "Mid-infrared femtosecond optical parametric amplification in potassium niobate," Optics Letters **21**, 1576-1578 (1996).

37. R. A. Kaindl, M. Wurm, K. Reimann, P. Hamm, A. M. Weiner, and M. Woerner, "Generation, shaping, and characterization of intense femtosecond pulses tunable from 3 to 20 μm," Journal of the Optical Society of America B **17**, 2086-2094 (2000).

38. G. Andriukaitis, T. Balčiūnas, S. Ališauskas, A. Pugžlys, A. Baltuška, T. Popmintchev, M.-C. Chen, M. M. Murnane, and H. C. Kapteyn, "90 GW peak power few-cycle mid-infrared pulses from an optical parametric amplifier," Optics Letters **36**, 2755-2757 (2011).

39. V. Kozich, A. Moguilevski, and K. Heyne, "High energy femtosecond OPA pumped by 1030nm Yb:KGW laser," Optics Communications **285**, 4515-4518 (2012).

40. D. Brida, C. Manzoni, G. Cirmi, M. Marangoni, S. De Silvestri, and G. Cerullo, "Generation of broadband mid-infrared pulses from an optical parametric amplifier," Optics Express **15**, 15035-15040 (2007).

41. D. Brida, M. Marangoni, C. Manzoni, S. D. Silvestri, and G. Cerullo, "Two-optical-cycle pulses in the mid-infrared from an optical parametric amplifier," Optics Letters **33**, 2901-2903 (2008).

42. G. M. Rossi, "Generation of broadband mid-infrared and ultraviolet pulses from optical parametric amplifiers," Master thesis (Politecnico di Milano, Milan, 2012/2013).

43. D. M. Gerz, "Shaping and characterization of tunable few-optical-cycle mid-infrared pulses," Master thesis (Ruprecht-Karls-Universität Heidelberg, Heidelberg, 2017).

44. C. Manzoni and G. Cerullo, "Design criteria for ultrafast optical parametric amplifiers," Journal of Optics **18**(2016).

45. R. W. Boyd, *Nonlinear optics,* Fourth ed. (Elsevier, AP Academic Press, London, 2020).

46. B. E. A. Saleh and M. C. Teich, *Fundamentals of photonics,* 2nd ed., Wiley series in pure and applied optics (Wiley-Interscience, Hoboken, New Jersey, 2007).

47. A. Yariv and P. Yeh, *Photonics: Optical Electronics in Modern Communications,* 6 ed., The Oxford Series in Electrical and Computer Engineering (Oxford University Press, 2007).

48. SNLO nonlinear optics code available from A. V. Smith, AS-Photonics, Albuquerque, NM.

49. A. Baltuška, T. Fuji, and T. Kobayashi, "Controlling the Carrier-Envelope Phase of Ultrashort Light Pulses with Optical Parametric Amplifiers," Physical Review Letters **88**, 133901 (2002).

50. G. Cerullo, A. Baltuška, O. D. Mücke, and C. Vozzi, "Few-optical-cycle light pulses with passive carrier-envelope phase stabilization," Laser & Photonics Reviews **5**, 323-351 (2011).

51. W. Wohlleben, T. Buckup, J. L. Herek, and M. Motzkus, "Coherent Control for Spectroscopy and Manipulation of Biological Dynamics," ChemPhysChem **6**, 850-857 (2005).

References

52. D. Wolpert, M. Schade, F. Langhojer, G. Gerber, and T. Brixner, "Quantum control of the photoinduced Wolff rearrangement of diazonaphthoquinone in the condensed phase," Journal of Physics B: Atomic, Molecular and Optical Physics **41**(2008).

53. D. B. Strasfeld, S.-H. Shim, and M. T. Zanni, "Controlling Vibrational Excitation with Shaped Mid-IR Pulses," Physical Review Letters **99**, 038102 (2007).

54. S. Ashihara, K. Enomoto, and J. Tayama, "Controlling Quantum Interferences in IR Vibrational Excitations in Metal Carbonyls," EPJ Web of Conferences **41**, 05024 (2013).

55. A. L. Serrano, A. Ghosh, J. S. Ostrander, and M. T. Zanni, "Wide-field FTIR microscopy using mid-IR pulse shaping," Optics Express **23**, 17815-17827 (2015).

56. J. E. Laaser, W. Xiong, and M. T. Zanni, "Time-Domain SFG Spectroscopy Using Mid-IR Pulse Shaping: Practical and Intrinsic Advantages," The Journal of Physical Chemistry B **115**, 2536-2546 (2011).

57. N. Müller, T. Buckup, and M. Motzkus, "Flexible pulse shaping for sum frequency microspectroscopies," Journal of the Optical Society of America B **37**, 117-126 (2020).

58. D. J. Kane and R. Trebino, "Characterization of arbitrary femtosecond pulses using frequency-resolved optical gating," IEEE Journal of Quantum Electronics **29**, 571-579 (1993).

59. R. Trebino, K. W. DeLong, D. N. Fittinghoff, J. N. Sweetser, M. A. Krumbügel, B. A. Richman, and D. J. Kane, "Measuring ultrashort laser pulses in the time-frequency domain using frequency-resolved optical gating," Review of Scientific Instruments **68**, 3277-3295 (1997).

60. C. Iaconis and I. A. Walmsley, "Spectral phase interferometry for direct electric-field reconstruction of ultrashort optical pulses," Optics Letters **23**, 792-794 (1998).

61. M. E. Anderson, A. Monmayrant, S. P. Gorza, P. Wasylczyk, and I. A. Walmsley, "SPIDER: A decade of measuring ultrashort pulses," Laser Physics Letters **5**, 259-266 (2008).

62. V. V. Lozovoy, I. Pastirk, and M. Dantus, "Multiphoton intrapulse interference. IV. Ultrashort laser pulse spectral phase characterization and compensation," Optics Letters **29**, 775-777 (2004).

63. B. Xu, J. M. Gunn, J. M. D. Cruz, V. V. Lozovoy, and M. Dantus, "Quantitative investigation of the multiphoton intrapulse interference phase scan method for simultaneous phase measurement and compensation of femtosecond laser pulses," Journal of the Optical Society of America B **23**, 750-759 (2006).

64. A. Monmayrant, S. Weber, and B. Chatel, "A newcomer's guide to ultrashort pulse shaping and characterization," Journal of Physics B: Atomic, Molecular and Optical Physics **43**, 103001 (2010).

65. S. Linden, J. Kuhl, and H. Giessen, "Amplitude and phase characterization of weak blue ultrashort pulses by downconversion," Optics Letters **24**, 569-571 (1999).

66. K. J. Kubarych, M. Joffre, A. Moore, N. Belabas, and D. M. Jonas, "Mid-infrared electric field characterization using a visible charge-coupled-device-based spectrometer," Optics Letters **30**, 1228-1230 (2005).

67. M. Tsubouchi and T. Momose, "Cross-correlation frequency-resolved optical gating for mid-infrared femtosecond laser pulses by an $AgGaGeS_4$ crystal," Optics Letters **34**, 2447-2449 (2009).

68. M. Miranda, T. Fordell, C. Arnold, A. L'Huillier, and H. Crespo, "Simultaneous compression and characterization of ultrashort laser pulses using chirped mirrors and glass wedges," Optics Express **20**, 688-697 (2012).

69. F. Silva, M. Miranda, S. Teichmann, M. Baudisch, M. Massicotte, F. Koppens, J. Biegert, and H. Crespo, "Near to mid-IR ultra-broadband third harmonic generation in multilayer graphene: few-cycle pulse measurement using THG dispersion-scan," in *CLEO: 2013*, OSA Technical Digest (online) (Optica Publishing Group, 2013), CW1H.5.

70. N. C. Geib, R. Hollinger, E. Haddad, P. Herrmann, F. Légaré, T. Pertsch, C. Spielmann, M. Zürch, and F. Eilenberger, "Discrete dispersion scan setup for measuring few-cycle laser pulses in the mid-infrared," Optics Letters **45**, 5295-5298 (2020).

71. P. Wnuk, H. Fuest, M. Neuhaus, L. Loetscher, S. Zherebtsov, E. Riedle, Z. Major, and M. F. Kling, "Discrete dispersion scanning as a simple method for broadband femtosecond pulse characterization," Optics Express **24**, 18551-18558 (2016).

72. N. Müller, F. Nicolai, and T. Buckup, "Broadband mid-infrared phase retrieval for nonlinear microscopy," Optics Letters **46**, 5012-5015 (2021).

73. V. Loriot, G. Gitzinger, and N. Forget, "Self-referenced characterization of femtosecond laser pulses by chirp scan," Optics Express **21**, 24879-24893 (2013).

74. F. Nicolai, N. Müller, C. Manzoni, G. Cerullo, and T. Buckup, "Acousto-optic modulator based dispersion scan for phase characterization and shaping of femtosecond mid-infrared pulses," Optics Express **29**, 20970-20980 (2021).

75. M. Wollenhaupt, A. Assion, and T. Baumert, "Short and Ultrashort Laser Pulses," in *Springer Handbook of Lasers and Optics,* 2. ed., F. Träger, ed. (Springer, Berlin; Heidelberg [u.a.], 2012).

76. U. Keller, *Ultrafast Lasers: A Comprehensive Introduction to Fundamental Principles with Practical Applications*, Graduate Texts in Physics (Springer, Cham, 2021).

77. J.-C. Diels and W. Rudolph, *Ultrashort Laser Pulse Phenomena,* 2nd ed. (Academic Press, 2006).

78. A. M. Weiner, "Femtosecond pulse shaping using spatial light modulators," Review of Scientific Instruments **71**, 1929-1960 (2000).

79. A. M. Weiner, "Ultrafast optical pulse shaping: A tutorial review," Optics Communications **284**, 3669-3692 (2011).

80. M. A. Dugan, J. X. Tull, and W. S. Warren, "High-resolution acousto-optic shaping of unamplified and amplified femtosecond laser pulses," Journal of the Optical Society of America B **14**, 2348-2358 (1997).

81. A. C. Jones, M. B. Kunz, I. Tigges-Green, and M. T. Zanni, "Dual spectral phase and diffraction angle compensation of a broadband AOM 4-f pulse-shaper for ultrafast spectroscopy," Optics Express **27**, 37236-37247 (2019).

82. "Application Note AN1022: All About Bragg Angle Errors in AO Modulators & Deflectors" (ISOMET Corp., 2007), retrieved 23.01.2017, 2017, https://isomet.com/App-Manual_pdf/Bragg%20Angle%20Errors.pdf.

83. J. M. Nite, J. D. Cyran, and A. T. Krummel, "Active Bragg angle compensation for shaping ultrafast mid-infrared pulses," Optics Express **20**, 23912-23920 (2012).

84. M. Hoffmann, T. Nagy, T. Willemsen, M. Jupé, D. Ristau, and U. Morgner, "Pulse characterization by THG d-scan in absorbing nonlinear media," Optics Express **22**, 5234-5240 (2014).

85. M. Canhota, F. Silva, R. Weigand, and H. M. Crespo, "Inline self-diffraction dispersion-scan of over octave-spanning pulses in the single-cycle regime," Optics Letters **42**, 3048-3051 (2017).

86. B. Schmidt, M. Hacker, G. Stobrawa, and T. Feurer, LAB2- A virtual femtosecond laser lab, http://www.lab2.de.

References

87. A. Catanese, B. Kaufman, C. Cheng, E. Jones, M. G. Cohen, and T. Weinacht, "Acousto-optic modulator pulse-shaper compression of octave-spanning pulses from a stretched hollow-core fiber," OSA Continuum **4**, 3176-3183 (2021).

88. J. A. Nelder and R. Mead, "A Simplex Method for Function Minimization," The Computer Journal **7**, 308-313 (1965).

89. M. Miranda, C. L. Arnold, T. Fordell, F. Silva, B. Alonso, R. Weigand, A. L'Huillier, and H. Crespo, "Characterization of broadband few-cycle laser pulses with the d-scan technique," Optics Express **20**, 18732-18743 (2012).

90. B. von Vacano, T. Buckup, and M. Motzkus, "Shaper-assisted collinear SPIDER: fast and simple broadband pulse compression in nonlinear microscopy," Journal of the Optical Society of America B **24**, 1091-1100 (2007).

91. J.-C. M. Diels, J. J. Fontaine, I. C. McMichael, and F. Simoni, "Control and measurement of ultrashort pulse shapes (in amplitude and phase) with femtosecond accuracy," Applied Optics **24**, 1270-1282 (1985).

92. L. Sarger and J. Oberlé, "How to Measure the Characteristics of Laser Pulses," in *Femtosecond laser pulses: principles and experiments*, C. Rullière, ed. (Springer, Berlin; Heidelberg [u.a.], 1998).

93. D. Zeidler, S. Frey, K. L. Kompa, and M. Motzkus, "Evolutionary algorithms and their application to optimal control studies," Physical Review A **64**, 023420 (2001).

94. T. Brixner, M. Strehle, and G. Gerber, "Feedback-controlled optimization of amplified femtosecond laser pulses," Applied Physics B **68**, 281-284 (1999).

95. J. Burnett, S. Kaplan, E. Stover, and A. Phenis, "Refractive index measurements of Ge," in SPIE Optical Engineering + Applications, (SPIE, 2016), Data retrieved from https://refractiveindex.info

96. I. C. Chang, "I. Acoustooptic Devices and Applications," IEEE Transactions on Sonics and Ultrasonics **23**, 2-21 (1976).

97. S.-H. Shim, D. B. Strasfeld, E. C. Fulmer, and M. T. Zanni, "Femtosecond pulse shaping directly in the mid-IR using acousto-optic modulation," Optics Letters **31**, 838-840 (2006).

98. S.-H. Shim, D. B. Strasfeld, and M. T. Zanni, "Generation and characterization of phase and amplitude shaped femtosecond mid-IR pulses," Optics Express **14**, 13120-13130 (2006).

99. J. Burnett, S. Kaplan, E. Stover, and A. Phenis, "Refractive index measurements of Ge," in *SPIE Optical Engineering + Applications*, (SPIE, 2016), Data retrieved via https://refractiveindex.info.

100. H. H. Li, "Refractive index of alkali halides and its wavelength and temperature derivatives," Journal of Physical and Chemical Reference Data **5**, 329-528 (1976), Data retrieved via https://refractiveindex.info.

101. E. Escoto, A. Tajalli, T. Nagy, and G. Steinmeyer, "Advanced phase retrieval for dispersion scan: a comparative study," Journal of the Optical Society of America B **35**, 8-19 (2018).

102. I. Sytcevich, C. Guo, S. Mikaelsson, J. Vogelsang, A.-L. Viotti, B. Alonso, R. Romero, P. T. Guerreiro, Í. J. Sola, A. L'Huillier, H. Crespo, M. Miranda, and C. L. Arnold, "Characterizing ultrashort laser pulses with second harmonic dispersion scans," Journal of the Optical Society of America B **38**, 1546-1555 (2021).

103. F. Silva, M. Miranda, B. Alonso, J. Rauschenberger, V. Pervak, and H. Crespo, "Simultaneous compression, characterization and phase stabilization of GW-level 1.4 cycle VIS-NIR femtosecond pulses using a single dispersion-scan setup," Optics Express **22**, 10181-10191 (2014).

104. D. Fabris, W. Holgado, F. Silva, T. Witting, J. W. G. Tisch, and H. Crespo, "Single-shot implementation of dispersion-scan for the characterization of ultrashort laser pulses," Optics Express **23**, 32803-32808 (2015).

105. M. Miranda, J. Penedones, C. Guo, A. Harth, M. Louisy, L. Neoričić, A. L'Huillier, and C. L. Arnold, "Fast iterative retrieval algorithm for ultrashort pulse characterization using dispersion scans," Journal of the Optical Society of America B **34**, 190-197 (2017).

106. V. V. Lozovoy, B. Xu, Y. Coello, and M. Dantus, "Direct measurement of spectral phase for ultrashort laser pulses," Optics Express **16**, 592-597 (2008).

107. S. Kleinert, A. Tajalli, T. Nagy, and U. Morgner, "Rapid phase retrieval of ultrashort pulses from dispersion scan traces using deep neural networks," Optics Letters **44**, 979-982 (2019).

108. N. C. Geib, M. Zilk, T. Pertsch, and F. Eilenberger, "Common pulse retrieval algorithm: a fast and universal method to retrieve ultrashort pulses," Optica **6**, 495-505 (2019).

109. A. H. Zewail, "Laser selective chemistry—is it possible?," Physics Today **33**, 27-33 (1980).

110. H. Rabitz, R. de Vivie-Riedle, M. Motzkus, and K. Kompa, "Whither the Future of Controlling Quantum Phenomena?," Science **288**, 824-828 (2000).

111. A. H. Zewail, "Femtosecond Transition-state Dynamics," Faraday Discussions of the Chemical Society **91**, 207-237 (1991).

112. D. J. Tannor, R. Kosloff, and S. A. Rice, "Coherent pulse sequence induced control of selectivity of reactions: Exact quantum mechanical calculations," The Journal of Chemical Physics **85**, 5805-5820 (1986).

113. A. M. Weiner, D. E. Leaird, G. P. Wiederrecht, and K. A. Nelson, "Femtosecond Pulse Sequences Used for Optical Manipulation of Molecular Motion," Science **247**, 1317-1319 (1990).

114. G. Vogt, P. Nuernberger, T. Brixner, and G. Gerber, "Femtosecond pump–shaped-dump quantum control of retinal isomerization in bacteriorhodopsin," Chemical Physics Letters **433**, 211-215 (2006).

115. T. Buckup, J. Hauer, C. Serrat, and M. Motzkus, "Control of excited-state population and vibrational coherence with shaped-resonant and near-resonant excitation," Journal of Physics B: Atomic, Molecular and Optical Physics **41**, 074024 (2008).

116. E. Brühl, T. Buckup, and M. Motzkus, "Experimental and numerical investigation of a phase-only control mechanism in the linear intensity regime," The Journal of Chemical Physics **148**, 214310 (2018).

117. C. R. Baiz, B. Błasiak, J. Bredenbeck, M. Cho, J.-H. Choi, S. A. Corcelli, A. G. Dijkstra, C.-J. Feng, S. Garrett-Roe, N.-H. Ge, M. W. D. Hanson-Heine, J. D. Hirst, T. L. C. Jansen, K. Kwac, K. J. Kubarych, C. H. Londergan, H. Maekawa, M. Reppert, S. Saito, S. Roy, J. L. Skinner, G. Stock, J. E. Straub, M. C. Thielges, K. Tominaga, A. Tokmakoff, H. Torii, L. Wang, L. J. Webb, and M. T. Zanni, "Vibrational Spectroscopic Map, Vibrational Spectroscopy, and Intermolecular Interaction," Chemical Reviews **120**, 7152-7218 (2020).

118. A. Reiser, J. P. Huang, X. He, T. F. Yeh, S. Jha, H. Y. Shih, M. S. Kim, Y. K. Han, and K. Yan, "The molecular mechanism of novolak–diazonaphthoquinone resists," European Polymer Journal **38**, 619-629 (2002).

119. R. Dammel, *Diazonaphthoquinone-based resists*, Tutorial texts in optical engineering (SPIE Optical Engineering Press, Bellingham, Wash., 1993), Vol. 11.

References

120. M. Mikulics, Z. Sofer, A. Winden, S. Trellenkamp, B. Förster, J. Mayer, and H. H. Hardtdegen, "Nano-LED induced chemical reactions for structuring processes," Nanoscale Advances **2**, 5421-5427 (2020).

121. P. Dimitrakellis, A. Smyrnakis, V. Constantoudis, D. Tsoutsou, A. Dimoulas, and E. Gogolides, "Atmospheric pressure plasma directed assembly during photoresist removal: A new route to micro and nano pattern formation," Micro and Nano Engineering **3**, 15-21 (2019).

122. L. Sun, Y. Yang, C. M. Dong, and Y. Wei, "Two-Photon-Sensitive and Sugar-Targeted Nanocarriers from Degradable and Dendritic Amphiphiles," Small **7**, 401-406 (2011).

123. K. N. Kim, K. S. Oh, J. Shim, I. R. Schlaepfer, S. D. Karam, and J.-J. Lee, "Light-Responsive Polymeric Micellar Nanoparticles with Enhanced Formulation Stability," Polymers **13**, 377 (2021).

124. R. L. Han, J. H. Shi, Z. J. Liu, Y. F. Hou, and Y. Wang, "Near-Infrared Light-Triggered Hydrophobic-to-Hydrophilic Switch Nanovalve for On-Demand Cancer Therapy," ACS Biomaterials Science & Engineering **4**, 3478-3486 (2018).

125. Y. Shin, P. Husni, K. Kang, D. Lee, S. Lee, E. Lee, Y. Youn, and K. Oh, "Recent Advances in pH- or/and Photo-Responsive Nanovehicles," Pharmaceutics **13**, 725 (2021).

126. N. K. Urdabayev and V. V. Popik, "Wolff Rearrangement of 2-Diazo-1(2H)-Naphthalenone Induced by Nonresonant Two-Photon Absorption of NIR Radiation," Journal of the American Chemical Society **126**, 4058-4059 (2004).

127. A. P. Goodwin, J. L. Mynar, Y. Ma, G. R. Fleming, and J. M. J. Fréchet, "Synthetic Micelle Sensitive to IR Light via a Two-Photon Process," Journal of the American Chemical Society **127**, 9952-9953 (2005).

128. J. L. Mynar, A. P. Goodwin, J. A. Cohen, Y. Ma, G. R. Fleming, and J. M. J. Fréchet, "Two-photon degradable supramolecular assemblies of linear-dendritic copolymers," Chemical Communications, 2081-2082 (2007).

129. J. J. M. Vleggaar, A. H. Huizer, P. A. Kraakman, W. P. M. Nijssen, R. J. Visser, and C. A. G. O. Varma, "Photoinduced Wolff-Rearrangement of 2-Diazo-1-naphthoquinones: Evidence for the Participation of a Carbene Intermediate," Journal of the American Chemical Society **116**, 11754-11763 (1994).

130. L. Wolff, "Ueber Diazoanhydride," Justus Liebigs Annalen der Chemie **325**, 129-195 (1902).

131. G. Cui and W. Thiel, "Photoinduced Ultrafast Wolff Rearrangement: A Non-Adiabatic Dynamics Perspective," Angewandte Chemie International Edition **52**, 433-436 (2013).

132. Q. Li, A. Migani, and L. Blancafort, "MS-CASPT2 assignment of the UV/vis absorption spectrum of diazoquinones undergoing the photoinduced Wolff rearrangement," The Journal of Physical Chemistry A **113**, 9413-9417 (2009).

133. Q. Li, A. Migani, and L. Blancafort, "Wave Packet Dynamics at an Extended Seam of Conical Intersection: Mechanism of the Light-Induced Wolff Rearrangement," The Journal of Physical Chemistry Letters **3**, 1056-1061 (2012).

134. M. Ladinig, M. Ramseier, and J. Wirz, "Photo-Wolff Rearrangement of 2-Diazo-1,2-naphthoquinone: Stern-Volmer Analysis of the Stepwise Reaction Pathway," Photochemistry and Photobiology **91**, 678-683 (2015).

135. H. Haken and H. C. Wolf, *Molekülphysik und Quantenchemie,* 5th ed. (Springer, Berlin, Heidelberg, New York, 2006).

136. W. Demtröder, *Molekülphysik,* 2 ed. (Oldenbourg, München, 2013).

137. B. H. Bransden and C. J. Joachain, *Physics of Atoms and Molecules,* 2nd ed. (Prentice Hall, Harlow, Munich, 2003).

138. M. Sánchez-Castellanos, C. A. Amezcua-Eccius, O. Álvarez-Bajo, and R. Lemus, "A local–normal description of vibrational excitations of pyramidal molecules in terms of Morse oscillators," Journal of Molecular Spectroscopy **247**, 140-159 (2008).

139. W. Demtröder, *Atoms, Molecules and Photons: An Introduction to Atomic-, Molecular- and Quantum Physics,* 3rd ed., Graduate texts in physics (Springer, Berlin, Heidelberg, 2018).

140. C. Ruckebusch, M. Sliwa, P. Pernot, A. de Juan, and R. Tauler, "Comprehensive data analysis of femtosecond transient absorption spectra: A review," Journal of Photochemistry and Photobiology C: Photochemistry Reviews **13**, 1-27 (2012).

141. M. Lorenc, M. Ziolek, R. Naskrecki, J. Karolczak, J. Kubicki, and A. Maciejewski, "Artifacts in femtosecond transient absorption spectroscopy," Applied Physics B **74**, 19-27 (2002).

142. P. Hamm, "Coherent effects in femtosecond infrared spectroscopy," Chemical Physics **200**, 415-429 (1995).

143. S. Yan, M. T. Seidel, and H.-S. Tan, "Perturbed free induction decay in ultrafast mid-IR pump–probe spectroscopy," Chemical Physics Letters **517**, 36-40 (2011).

144. "Safety Data Sheet, 2-Diazo-1-naphthol-5-sulfonic acid sodium salt monohydrate" (AK Scientific, Inc., 2021), retrieved 13.12.2022, 2022, https://aksci.com/item_detail.php?cat=P681.

145. J. von Cosel, J. Cerezo, D. Kern-Michler, C. Neumann, L. van Wilderen, J. Bredenbeck, F. Santoro, and I. Burghardt, "Vibrationally resolved electronic spectra including vibrational pre-excitation: Theory and application to VIPER spectroscopy," The Journal of Chemical Physics **147**, 164116 (2017).

146. J. Pacansky and J. R. Lyerla, "Photochemical Decomposition Mechanisms for AZ-Type Photoresists," IBM Journal of Research and Development **23**, 42-55 (1979).

147. P. Hamm, S. M. Ohline, and W. Zinth, "Vibrational cooling after ultrafast photoisomerization of azobenzene measured by femtosecond infrared spectroscopy," The Journal of Chemical Physics **106**, 519-529 (1997).

148. A. Papakondylis and A. Mavridis, "A Theoretical Investigation of the Structure and Bonding of Diazomethane, CH_2N_2," The Journal of Physical Chemistry A **103**, 1255-1259 (1999).

149. M. Kasha, A. Sytnik, and B. Dellinger, "Solvent cage spectroscopy," Pure and Applied Chemistry **65**, 1641-1646 (1993).

150. T. Witte, J. S. Yeston, M. Motzkus, E. J. Heilweil, and K. L. Kompa, "Femtosecond infrared coherent excitation of liquid phase vibrational population distributions (v>5)," Chemical Physics Letters **392**, 156-161 (2004).

151. C. Ventalon, J. M. Fraser, M. H. Vos, A. Alexandrou, J.-L. Martin, and M. Joffre, "Coherent vibrational climbing in carboxyhemoglobin," Proceedings of the National Academy of Sciences **101**, 13216-13220 (2004).

152. O. Kühn, "Multidimensional vibrational quantum dynamics of CO–heme compounds: ultrafast IVR mediated Fe–CO bond-breaking after CO excitation?," Chemical Physics Letters **402**, 48-53 (2005).

153. T. Horiba, S. Shirai, and H. Hirai, "Missing-rung problem in vibrational ladder climbing," Physical Review A **105**, 013117 (2022).

154. F. O. Koller, C. Sobotta, T. E. Schrader, T. Cordes, W. J. Schreier, A. Sieg, and P. Gilch, "Slower processes of the ultrafast photo-isomerization of an azobenzene observed by IR spectroscopy," Chemical Physics **341**, 258-266 (2007).

155. T. Schmierer, W. J. Schreier, F. O. Koller, T. E. Schrader, and P. Gilch, "Impact of vibrational excitation on the kinetics of a nascent ketene," Physical Chemistry Chemical Physics **11**, 11596-11607 (2009).

References

156. F. Neubrech, C. Huck, K. Weber, A. Pucci, and H. Giessen, "Surface-Enhanced Infrared Spectroscopy Using Resonant Nanoantennas," Chemical Reviews **117**, 5110-5145 (2017).

157. H. Aouani, H. Šípová, M. Rahmani, M. Navarro-Cia, K. Hegnerová, J. Homola, M. Hong, and S. A. Maier, "Ultrasensitive Broadband Probing of Molecular Vibrational Modes with Multifrequency Optical Antennas," ACS Nano **7**, 669-675 (2013).

158. J. P. Kraack and P. Hamm, "Vibrational ladder-climbing in surface-enhanced, ultrafast infrared spectroscopy," Physical Chemistry Chemical Physics **18**, 16088-16093 (2016).

159. C. T. Middleton, A. M. Woys, S. S. Mukherjee, and M. T. Zanni, "Residue-specific structural kinetics of proteins through the union of isotope labeling, mid-IR pulse shaping, and coherent 2D IR spectroscopy," Methods **52**, 12-22 (2010).

160. I. V. Hertel and C.-P. Schulz, *Atoms, Molecules and Optical Physics 2 : Molecules and Photons - Spectroscopy and Collisions*, Graduate Texts in Physics (Springer, Berlin, Heidelberg, 2015).

161. "TOPAS-800: User's Manual," (Light Conversion, 2015).

162. IUPAC, "Compendium of Chemical Terminology" (Blackwell Scientific Publications, 2014), retrieved 17.03.2023, 2023, https://goldbook.iupac.org/.

163. T. L. Myers, R. G. Tonkyn, T. O. Danby, M. S. Taubman, B. E. Bernacki, J. C. Birnbaum, S. W. Sharpe, and T. J. Johnson, "Accurate Measurement of the Optical Constants n and k for a Series of 57 Inorganic and Organic Liquids for Optical Modeling and Detection," Applied Spectroscopy **72**, 535-550 (2018), Data retrieved via https://refractiveindex.info.

Danksagung

Danksagung

Bei Prof. Dr. Giulio Cerullo und Dr. Cristian Manzoni vom Politecnico di Milano möchte ich mich für die Unterstützung bezüglich des NOPAs bedanken.

Bedanken möchte ich mich auch bei Angelika Neuner und Marina Sommer für ihre stets freundliche Art und die Unterstützung bei jeglichen organisatorischen Fragen.
Das selbe gilt für die HGSFP. Auch von dieser Seite wurde mir bei organisatorischen Fragen immer weiter geholfen. Außerdem gewährte mir die HGSFP großzüge finanzielle Unterstützung während der Zeit, in der es noch nicht feststand, wie die Arbeitsgruppe künftig geleitet wird.

Klaus Schmitt und seinem Team von der Feinmechanischen Werkstatt danke ich für die gute Zusammenarbeit bei ansteheneden kleineren und größeren Konstruktionen.

Meinen Mitstreitern im Studium Dr. Pirmin Kükelhan, Dr. Sven Sauerland, Dr. Ole Schmidt und Dr. Andreas Weu danke ich dafür, dass wir uns gemeinsam durch Übungszettel, Klausurvorbereitungen und Praktika geschlagen haben und dabei einander geholfen und gegenseitig erklärt haben, sodass am Ende jeder davon profitierte.

Der größte Dank allerdings geht an meine Familie, die mich bisher in allen Lebenslagen so gut es ging unterstützt hat und mir mit Rat und Tat zur Seite steht. Auch möchte ich meiner Freundin Réka Illés meinen Dank aussprechen, dass sie mir mit den Formulierungen im Englischen in dieser Arbeit geholfen hat. Ich möchte ihr außerdem von ganzem Herzen dafür danken, dass sie mir den Rücken stärkt und die Höhen und Tiefen der vergangenen Jahre gemeinsam mit mir durchgemacht hat. Danke, dass Ihr immer für mich da seid!